DOCTOR OF PHILOSOPHY

A new proxy for constraining Palaeotidal simulations for the Northwest European Shelf Seas

Ward, Sophie

Award date:
2016

Awarding institution:
Bangor University

[Link to publication](#)

A NEW PROXY FOR CONSTRAINING PALAEOTIDAL SIMULATIONS FOR THE NORTHWEST EUROPEAN SHELF SEAS

Sophie L. Ward

PRIFYSGOL

BANGOR

UNIVERSITY

A thesis presented for the degree of

Doctor of Philosophy

School of Ocean Sciences

Bangor University

Wales, UK

July 2014

Acknowledgments

Abstract

Past major changes in sea level have had significant implications for global and shelf sea tidal dynamics. Changing shelf sea tidal dynamics impact on tidal elevation amplitudes, the location of tidal mixing fronts, dissipation, shelf sea biogeochemistry and sediment transport. Some of these major changes are reflected in the geological records of shelf seas and therefore proxy data may be used to constrain tidal model outputs.

This study explores a new geological proxy for northwest European shelf sea (NWESS) tidal dynamics by quantifying the relationship between modelled tidally-modulated bed shear stress (BSS) and observed seabed sediment grain size. A grain size tidal current proxy (GSTCP) has been developed by comparing tidal model output of BSS with observational data on present-day grain size data from the Irish Sea. This new proxy is shown to reproduce large-scale sediment distribution in the present-day Irish Sea, and the relationship is applied to the NWESS to predict sediment distribution across the shelf, over a range of (palaeo) time slices.

A new three-dimensional palaeotidal model has been developed, which incorporates dynamic palaeotopography from the latest glacial-isostatic adjustment model for the region (Bradley, 2011). The tidal evolution of the NWESS is simulated using 1 ka time slices, from 21 ka BP (taken to be the approximate time of the Last Glacial Maximum) to present-day. Model outputs of BSS from the new palaeotidal model were compared with outputs from existing palaeotidal models, which were developed using different glacial-isostatic adjustment models (Peltier, 1994; Lambeck, 1995). The new glacial-isostatic adjustment model produced significantly different relative sea level signals across the shelf, and hence there were differences in the timing of the major changes in modelled BSS between simulations.

Sediment grain size evolution profiles were generated for five BGS UK shelf sediment cores, using laser particle diffractometry and radiocarbon dating techniques. Predictive grain size profiles were generated by applying the GSTCP to the modelled evolution of BSS at the sediment core locations, and were compared with the observed grain size profiles. In general, the GSTCP reproduced the observed trends in grain size variations in three of the four sediment cores, although tended to over-predict the grain size in all core locations. Despite the limitations of the GSTCP for reproducing observed sediment classifications at specific sites, the GSTCP was applied to the regional model output of BSS to generate predictive maps of seabed sediment types on the shelf, in 1 ka time slices from 21 ka BP to the present-day. Such maps of sediment distribution are useful for a number of

applications, including for physical (e.g. morphodynamic) modelling and biological studies (e.g. habitat mapping).

The new palaeotidal model was also used to estimate changes in the position of the shelf sea tidal mixing fronts with sea-level rise since 21 ka BP. Prior to this work, the only proxy data used to constrain palaeotidal model simulations was from one sediment core from the Celtic Deep. The timing of stratification at the core location had been used to validate a palaeotidal model; however, considerable variation in the timing of onset of stratification at the core locations considered here was predicted by different palaeotidal model simulations. Further, since the position of the tidal mixing front is very sensitive to the value used for the critical contour, it is suggested that using the timing of stratification at an isolated site is too sensitive a parameter for validating palaeotidal models.

The GSTCP does not fully resolve the changes in observed grain size at the core locations, thus the proxy is considered unsuitable for constraining palaeotidal model output in this context. The main limitations are the lack of consideration of sediment availability and supply, the limited spatial extent of the geological data (i.e. few sediment cores) and the absence of wave-induced BSS. Future work should consider combined wave and current induced sediment transport, and the feedbacks between evolving morphodynamics and hydrodynamics, over a range of timescales.

The new proxy can be used to approximate the large-scale sediment distribution over the NWESS for the present-day, and has been applied to palaeotidal model output to predict the evolution of large-scale patterns in sediment dynamics across the shelf over the last 21 ka. The predictive map of the large-scale distribution of seabed sediment grain size is useful for a number of applications, including for considering the marine aggregate resource, for marine habitat mapping, and for including spatially-varying bed roughnesses in hydrodynamic- and morphodynamic models.

Contents

List of Figures

List of Tables

Abbreviations and notation

BIIS	British-Irish Ice Sheet
BGS	British Geological Survey
BSS	Bed shear stress(es)
d_{50}	Median grain size
GIA	Glacial-isostatic adjustment
GSTCP	Grain size tidal current proxy
ka BP	Thousand years before present
LGM	Last Glacial Maximum
NWESS	Northwest European shelf seas
RMSE	Root mean square error
ROMS	Regional Ocean Modeling System

1 Introduction

Past changes in climate have resulted in major changes in sea levels, which have implications for global and shelf sea tidal dynamics. Over geological time-scales, global (eustatic) sea-level changes are driven by the exchange of water between expanding and contracting ice sheets and the global oceans. Relative, or regional sea-level change, reflects the interplay between eustasy and isostasy. Ocean-land loading and unloading by ice, referred to as glacial-isostatic adjustment (GIA), influences the spatial and temporal variability of relative sea level. The effects of GIA can be both local and far-field, although it is particularly pertinent in formerly glaciated regions such as the British Isles.

There have been rapid advances in palaeoclimate research in recent years, with strong motivation to understand the drivers behind natural climate variability. Understanding how the shelf seas have responded to past changes in sea level is useful for predicting the likely impacts of future sea level rise. Although projections of future (eustatic) sea level rise contain considerable uncertainties, ranging from 2-10 mm y^{-1} until 2100 (Church et al, 2013), post-glacial sea-level change provides us with an analogue of how these changes are likely to affect shelf sea tidal dynamics. A number of studies (e.g. Belderson et al, 1986; Thomas and Sündermann, 1999; Uehara et al, 2002; Egbert, 2004; Hall and Davies, 2004; Uehara et al, 2006) of the period since the Last Glacial Maximum (LGM), which occurred between *ca.* 26 and 20 ka BP (Clark et al, 2009), and when global sea levels were up to 130 m lower than they are today (Lambeck et al, 2002), consider the evolution of tides and the hydrodynamics of shelf seas as sea levels have changed. The numerical modelling of both tides and GIA has progressed significantly in the last few years with advances in observational and computational techniques. Recent advances have supported the development of multi-proxy approaches, an improved understanding of processes, higher accuracy chronological control and enhanced model-data comparison. The shallow shelf seas of northwest Europe are well-suited to such studies due to the evolution of the highly energetic tidal regimes of the region, and due to the response to ice loading and unloading. To date, the only proxy available for constraining palaeotidal model outputs is one vibrocore from the

Celtic Sea, which has been used to constrain the timing of onset of seasonal stratification in the area (Scourse et al, 2002) and has been compared with palaeotidal model outputs of Uehara et al (2006). Seasonal stratification has significant influence over biological productivity and carbon dioxide fluxes on shelf seas (e.g. Austin, 1991; Rippeth et al, 2008). The use of geological proxy data for verifying the accuracy of tidal model outputs need not be confined to investigating long-term stratification dynamics and could be extended to other model outputs.

1.1   Research question and rationale

Sediment dynamics over the northwest European shelf seas (NWESS) have been subject to considerable change over the recent geological past, due to the evolution of tidal dynamics and wave climates resulting from significant sea-level change since the LGM. It is likely that existing tidal models do not reflect all of the changes in sediment dynamics that have occurred since the LGM. With advancements in tidal modelling, such as three-dimensional and higher resolution models made possible by better computational capacity, it becomes increasingly important to validate and constrain output with observational data. The outputs of such models can be used for a number of applications, including estimating how changing tidal regimes impact upon large-scale sediment distribution on the shelf seas.

Model-data comparisons for past changes provide important constraints on the accuracy of model outputs, with implications for model predictions of future changes. Increasing model confidence via observational sedimentary constraints ("validation") is not limited to the constrained variable only and applies to other model outputs; thus the use of observational data to constrain model outputs is potentially a powerful tool for progressing this area of palaeotidal modelling. Recent developments in palaeotidal model inputs, such as more advanced GIA models, facilitates inter-model comparison in addition to model-data comparison, which is useful for establishing whether particular model set-ups have consistently better fit with geological observational data.

1.2   Aims and Objectives

The principal aim of this work is to investigate whether seabed sediment grain size can be used as a proxy for past tidal current conditions. Validating model outputs of bed shear stress (BSS) at discrete locations has the potential to greatly improve the accuracy of studies of large-scale sediment dynamics, by applying the relationship to model output

across entire domains.

In the first instance, the aim is to examine the relationship between present-day seabed sediment type and modelled bed shear stress, in the Irish Sea. It is considered that, to the first order, as bed shear stress increases, the size of the sediment grain size which can be transported also increases. Prior to this work, no attempt had been made to quantify the relationship between modelled bed shear stress and observed sediment grain size, in the field, and on a regional scale. A high resolution tidal model for the Irish Sea is developed, using the Regional Ocean Modelling System (ROMS). This modelled tidal-induced bed shear stress is compared with the observed median grain size of present-day seabed sediment samples, and the relationship is quantified. This relationship is subsequently applied to regional model outputs of bed shear stress to predict the large-scale distribution of seabed sediment type in the Irish Sea.

The overall aim of the project is to explore whether the present-day relationship between modelled bed shear stress and observed seabed sediment grain size can be applied to past tidal current conditions. To achieve this, a new palaeotidal model for the NWESS is developed, which is an advancement of existing palaeotidal models for the region as it is higher resolution, three-dimensional, and incorporates the latest GIA model for the region (Bradley et al, 2011). This new palaeotidal model is compared with existing palaeotidal models for the region, which were developed using earlier GIA models (Peltier, 1994; Lambeck, 1995). Furthermore, new seabed sediment sequences are developed, by conducting laser particle size analysis on several vibrocores from the NWESS, for which age-depth models are also predicted. The relationship between changes in simulated tidal bed shear stress at the core locations, from the LGM to the present-day, and the observed evolution of grain size in the cores is compared.

1.3   Thesis outline

In Chapter 2, the background and motivation of this project are outlined, and the methods and techniques employed are described in Chapter 3. The development of the new proxy for tidal currents is described and defined in Chapter 4. This proxy is developed for the present-day Irish Sea, using seabed sediment grain size data and a high-resolution, comprehensive, three-dimensional tidal model. Grain size data of five shelf sea sediment cores are presented in Chapter 5. The shelf sea sediment core data are developed using laser particle analysis, and age-depth models are constructed for deducing the temporal grain size evolution of each core.

The focus of the palaeotidal model is on the tidal evolution of the NWESS during the last 21 ka. Incorporated into the shelf-scale tidal model set-up is dynamic palaeotopography from the latest GIA model for the region. Initial outputs from this new regional palaeotidal model are given in Chapter 6, where the changes to the position of the shelf sea tidal mixing front with time are outlined. The timing of the movement of tidal mixing fronts is interesting since previously proxy data has been used to constrain their positions (Scourse et al, 2002; Uehara et al, 2006). Further palaeotidal model output, and the results of applying the new proxy to the outputs of BSS are presented in Chapter 7. In Chapter 8, the implications and conclusions of the study are synthesised. A discussion of the implications of the work is given, along with suggestions for future work.

2 Scientific background

The focus of this study is on the impact of the evolving hydrodynamics of the northwest European shelf seas (NWESS) during the last 21 ka on large-scale sediment dynamics. In this chapter, background to the research question is given, by introducing processes that influence global and regional sea levels, tidal modelling, sediment transport theory, and the study domain.

2.1 The Last Glacial Maximum

The EPILOG programme defined the LGM of Marine Isotope Stage (MIS) 2 as *"the most recent interval when global ice sheets reached their maximum integrated volume during the last glaciation"*, and was the interval centred on *ca.* 21 ka BP (Mix et al, 2001). Clark et al (2009) concluded that nearly all ice sheets reached their maximum extent between 26.5 and 20 – 19 ka BP, since the glacial maxima were not in phase globally. During the LGM, global ice volumes and areal extent were more than twice those of present-day (Clark and Mix, 2002). Glaciation typically takes a lot longer than deglaciation, e.g. approximately 90 ka versus 10 ka, respectively (Peltier, 1994), and there was considerable variation in the rates of deglaciation of different ice margins. Generally, the global deglaciation occurred between *ca.* 20 and 7 ka BP (Milne et al, 2006) although it is likely that the deglaciation occurred in stages and was interrupted by stillstands or re-advance episodes (e.g. McCabe et al, 2007).

2.1.1 The Last British-Irish Ice Sheet

In the area of the British Isles, the maximum volume of the BIIS occurred between 27 and 21 ka BP (Chiverrell and Thomas, 2010; Clark et al, 2012); more specifically, Scourse et al (2009a) used deep-sea ice-rafted detritus records to constrain the maximum advance of the BIIS to 24 ka BP. Large parts of the BIIS were marine-based, extending into the present-day North Sea and the shelves of Britain and Ireland (Figure 2.1). The chronology

of the BIIS still requires further research as there is some variation in the maximum limits for various ice streams and lobes and much of the offshore limits are still poorly constrained (Chiverrell and Thomas, 2010). A recent study by Everest et al (2013) age-constrained the offshore northwestern sector of the BIIS at its maximum thickness to between 27 and 25 ka BP.
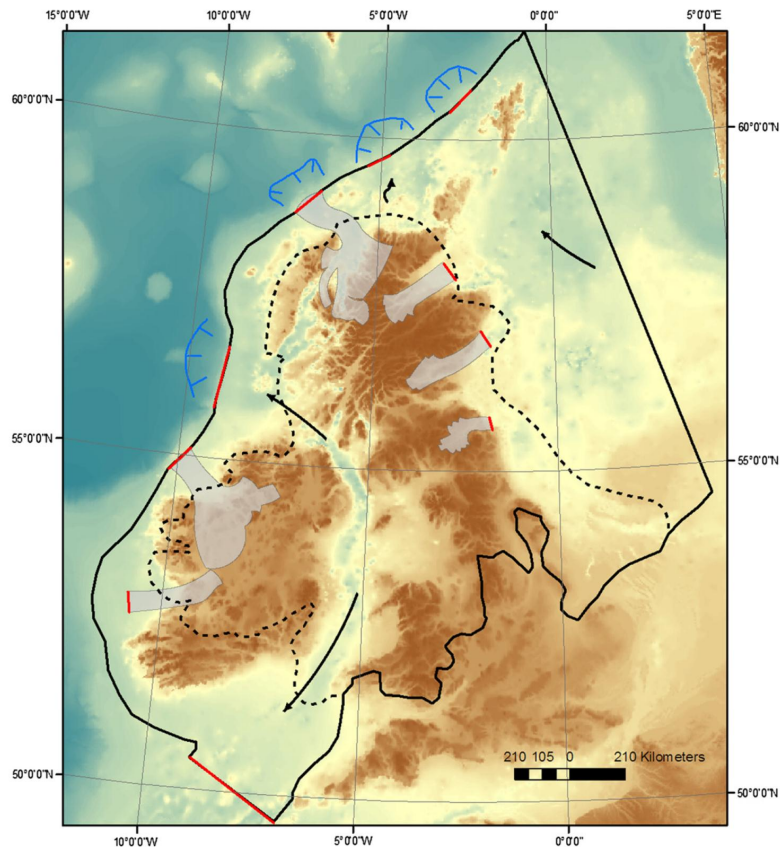
Figure 2.1: Two reconstructions of the maximum extent of the BIIS, from Clark et al (2012). The dashed line is the smaller extent which was accepted for many years. This is the more traditional view (here shown as the assessment of Bowen et al (1986)) and included parts of Scotland and Ireland being ice free at the LGM. The solid line is the larger extent (and included ice of Scotland and Ireland), which extended to the continental shelf edge and covering the North Sea. The solid line was reconstructed using evidence from landforms and ice-rafted detritus, and included data from a number of studies, including for example Sejrup et al (2005), Ó Cofaigh and Evans (2007), Bradwell et al (2008) and Scourse et al (2009a). The blue lines show trough mouth fans, the grey lines (or black arrows) indicate ice stream tracks and the red marks indicate their marine-terminating margins.

The results of the study by Scourse et al (2009a) suggest that the BIIS was present from 46 ka BP until its final deglaciation before the Younger Dryas (*ca.* 12.9 – 11.7 ka BP), which was a period of global ice re-advance (Rasmussen et al, 2006; Lowe et al, 2008). A

period of re-advance of the BIIS between *ca.* 19 − 17 ka BP was detailed by Chiverrell and Thomas (2010), although a longer period of re-advance between 22 ka BP and 16 ka BP was found in the study by Scourse et al (2009a), which followed rapid retreat of the ice sheet at 23 ka BP. The extent of this re-advance was treated with caution by Clark et al (2012), who stated that the evidence suggests only a small distance of re-advance (hundreds of metres to kilometres, rather than many kilometres). Uncertainties in the extent and timing of the BIIS remain, but mounting field evidence is facilitating increasingly high-resolution reconstructions.

2.2   Sea-level change

Understanding spatial and temporal changes in sea level is a difficult physical problem as a number of complex mechanisms, which work over varying timescales, interact (Figure 2.2). Changes in both absolute sea level (i.e. those relative to the Earth's centre of mass) and relative sea level (i.e. those relative to the sea floor) can occur on very short (e.g. semi-diurnal) to millennial timescales. Climate-driven sea-level changes are caused by interactions between components of the Earth system - predominantly oceans, ice sheets and the solid Earth (Milne, 2008). The main contributor to long-term changes in sea levels is mass exchange between ice sheets and the oceans. Medium-term changes in sea level, occurring over decades and centuries, result from variations in ocean water density (thermosteric and halosteric changes) caused by changing atmospheric temperature, ice melt, anthropogenic or natural land-water storage and by changes in ocean circulation (Milne et al, 2009).
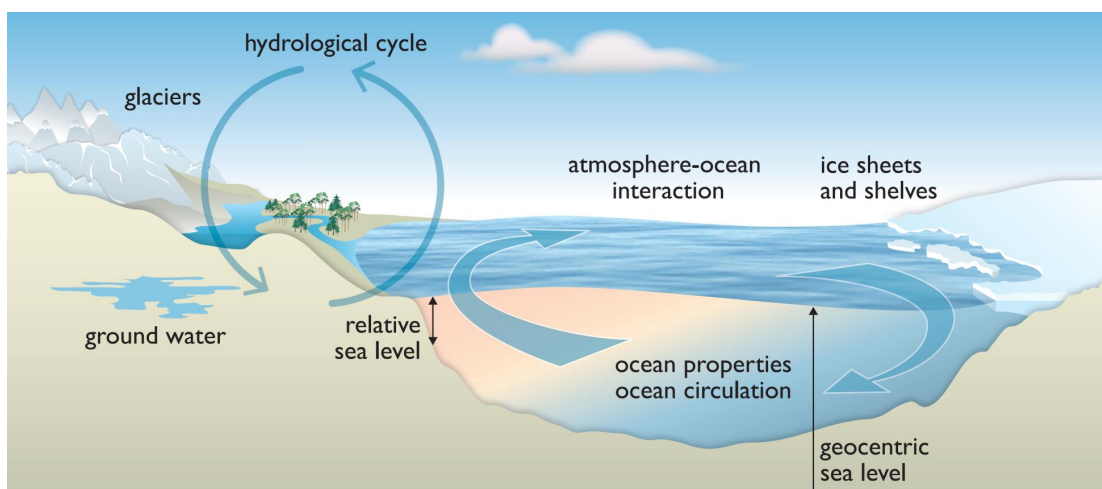
Figure 2.2: Processes that can impact on regional and global sea-level change. 'Ocean properties' include temperature, density and salinity (from Church et al, 2013).

Global, or 'eustatic', changes in sea level are caused by processes such as changes in the volume of water in the ocean basins (due to tectonics), changes in temperature of the ocean water and glacio-eustasy, resulting from the storage or release of water from glaciers and ice sheets (Milne, 2008) and by departure from the geoid, resulting from local variations in gravity (Barnett, 1990; Nicholls et al, 1999; Church et al, 2013). Relative sea level changes are spatially variable and can be caused by factors such as compaction of sediments, subsidence, glacio-isostasy (loading by ice sheets, the influence of which can also extend globally) and hydro-isostasy (loading and unloading of ocean basins) (Lambeck and Chappell, 2001; Church et al, 2013). Tectonic processes can contribute to both eustatic or regional changes in sea levels through processes such as tectonic uplift and subsidence (regional sea-level change) and sea-floor spreading (eustatic sea-level change). Changes in relative sea level tend to continue after the increase in eustatic sea level, even once ice melting has ceased, since isostatic responses have a very slow lag, giving the Earth system 'memory' (see Section 2.3). Glacio-hydro-isostatic contributions to sea level that cause spatial variability are the result of combined deformation-gravitational effects and in formerly glaciated and immediately extra-glacial areas, it is this term which dominates during and after glaciation (e.g. Lambeck and Chappell, 2001; Gehrels, 2010).

Increasing sea levels have considerable environmental, societal and economic implications (Stern, 2007), including increased coastal flooding, coastal erosion, loss of wetlands and wildlife habitat and hence ecosystem changes, increased cost of coastal protection and decreased freshwater availability due to saltwater intrusion (e.g. Stern, 2007; Nicholls, 2011). A number of modelling studies have been carried out into the impacts of past changes in sea level on the hydrodynamic regimes of shelf seas (e.g Egbert, 2004; Uehara et al, 2006; Rippeth et al, 2008; Van Landeghem et al, 2009; Neill et al, 2010), and these are discussed in more detail in Section 2.5. Although such changes have direct impacts, they also feed back into the climate system, for example through changes to carbon dioxide fluxes (e.g. Rippeth et al, 2008) and the impact of tidal changes on the Meridional Overturning Circulation (e.g. Green et al, 2009). Consideration of past changes in sea level, and the subsequent changes in tidal dynamics (through palaeotidal modelling), is important for considering how the shelf seas will respond to future predicted sea-level rise.

2.2.1 Sea level history

During the Quaternary (ca. 2.8 million years BP to present, Gibbard et al, 2010), the main contributor to changes in sea levels has been the cyclical growth and decay of ice sheets (Lambeck and Chappell, 2001). Cycles of glaciation affect the world's radiation budget, atmospheric and ocean circulation and ocean-ice mass flux. This periodic exchange of mass between the ice sheets and the ocean has resulted in the complex spatial and temporal pattern of sea-level change. In areas previously covered by ice sheets, during deglaciation a monotonic decrease in sea levels occurred, whereas in equatorial regions or those distant from the areas of major deglaciation, monotonic sea-level rise occurred (Milne et al, 2006).
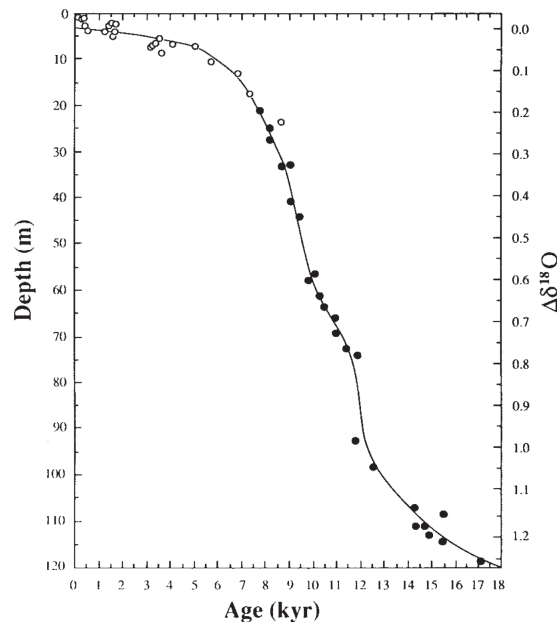
Figure 2.3: Barbados sea level curve from Fairbanks (1989). The sea level curve was based on radiocarbon-dated (filled circles) and age-depth data (open circles) from a coral species from four other Caribbean island locations. Fairbanks (1989) corrected the Barbados sea level data for the estimated mean uplift of the area (34 cm yr^{-1}). Note that the time-scale is in radiocarbon years BP.

Lambeck et al (2002) estimated that global mean sea level rose by ∼130 m between 20 and 7 ka BP, and relative sea level records suggest that between 7 and 3 ka BP, global mean sea level likely rose a further 2-3 m, and have not changed considerably since (Lambeck et al, 2004, 2010). The results of Fairbanks (1989) suggest that there was a period of rapid eustatic sea-level rise (∼ 25 m) at *ca.* 14 ka BP (shown in Figure 2.3 as *ca.* 12 kyr BP in radiocarbon age), which is referred to as Meltwater Pulse 1A (MWP-1A). This sea-level rise has been constrained more recently by Deschamps et al (2012) to ∼ 20 m between 14.65 and 14.3 ka BP. Various studies have estimated that the rate of eustatic sea level

rise during the Holocene was between 0.1 and 0.2 m per century (Lewis et al, 2008), with higher rates during the early Holocene than during the mid-Holocene. Relative sea level records indicate that in the last 7000 years, global mean sea level *"likely increased by 2-3 m"*, to near present-day levels (Church et al, 2013).

The Barbados sea level curve developed by Fairbanks (1989) (Figure 2.3) is considered a benchmark for sea level history, being one of the most cited papers in all Quaternary science; however, there is some discussion over the treatment of the sea-level curve as 'eustatic' (Gehrels, 2010, and references therein) due to the tectonic instability of Barbados and the treatment of the uplift rate applied by Fairbanks (1989). As pointed out by Gehrels (2010), it is generally not considered good practice to compile sea level data from a wide region into a single curve due to differential isostatic movements and regionally variable sea-level and thus the concept of 'eustasy' is a difficult one to quantify; that said, the discovery of rapid sea-level rise evident from the Barbados curve is a significant one.

2.2.2 Present and projected rates of sea-level change

There is still considerable uncertainty regarding quantification of the sea-level response to climate forcing and to the likely climate forcing of the coming decades. It is, however, widely acknowledged that current eustatic sea-level rise is a consequence of climate change, resulting in melting of land ice and the thermal expansion of ocean water (e.g. Stern, 2007; Milne et al, 2009; Vermeer and Rahmstorf, 2009; Nicholls, 2011; Church et al, 2013). Observations of changes in sea level are becoming progressively comprehensive and since 1992, satellite altimetry has provided near-global maps (66°S to 66°N) of absolute sea level at ten-day intervals.

In the past century, global mean sea-level rise has departed significantly from late Holocene trends (e.g. Gehrels et al, 2004; Church et al, 2013). In recent decades, the rate of sea level rise has increased dramatically to a few decimetres per century, up from a rate of a few centimetres per century over the past few millennia (Milne et al, 2009). A global mean sea level rise of 3.2 ± 0.4 mm yr^{-1} was found by satellite altimetry for the period 1993-2012 (Church et al, 2013). Thermal expansion and the melting of glaciers and ice sheets continue to be the dominant contributors to current global mean sea level rise (Church et al, 2013). Within IPCC's AR5 (Church et al, 2013), the estimate for 'likely' range in global mean sea level rise by 2100 is 0.44-0.74 m above the 1986-2005 average; these are higher than the estimates in AR4 because of improved modelling of land-ice contributions.

There remain significant uncertainties regarding future sea level predictions (Milne et al, 2009; Vermeer and Rahmstorf, 2009; Gehrels, 2010; Church et al, 2013), attributable to uncertainties in ice flow dynamics, contribution of terrestrial water sources and anthropogenic water storage, and contributions of land ice due to lack of information regarding the total amount of ice and the rate at which it is likely to melt. The greatest uncertainty is in the likely response of the Greenland Ice Sheet and the West Antarctic Ice Sheet to increasing global temperatures.

2.2.3   Sea-level index points (SLIPs)

Past sea levels can be reconstructed using sediment records, as well as using morphological features, the formation of which depend upon palaeo sea levels (Fairbanks, 1989; Peltier, 1994; Lambeck and Chappell, 2001; Clark and Mix, 2002; Shennan et al, 2002, 2006b). These observations, from known locations and which can be age-constrained (usually using radiocarbon dating) are useful for providing information on past sea levels. Such observations of relative sea level provide the primary observational evidence for constraining GIA models (Section 2.3), and are referred to as 'sea level index points' (SLIPs). A rigorous protocol for screening and classifying relative sea level observations exists, which helps to eliminate potentially erroneous data (see Shennan et al, 2002). Knowledge of the age (which is defined in radiocarbon years), location, (present) altitude and tendency (i.e. the level of marine influence) of such sediments or features allows the records to be used as SLIPs (Shennan et al, 2006b). The indicative meaning of the SLIP must also be known, which relates its vertical relationship to a former tide level using two parameters (Figure 2.4), since few SLIPs formed exactly at palaeo-mean sea level (Shennan et al, 2006b). The first of the two parameters is the reference water level, which is the midpoint of the indicative range, and which allows for calculation of the sea-level change relative to present by comparing the reference water level and the altitude of the reference point to the national datum. The second parameter considered is the indicative range, which is the vertical range over which the accumulating sediment could occur (Shennan et al, 2006b). The data points which have a reference water level at, or close to, mean high water spring tides are most useful for constraining GIA model predictions, as they are most easy to quantify the changes in past relative sea level. If it is not possible to quantitatively define a relationship between the reference level and the field evidence then the sea-level information is considered a 'limiting date'. Individual SLIPs may vary due to localised effects such as changes in tidal regimes, sediment accumulation and sediment compaction

(Shennan and Horton, 2002), but must not have been eroded or transported since the time of accumulation to be reliable for the reconstruction of relative sea level rise (Shennan et al, 2006b).
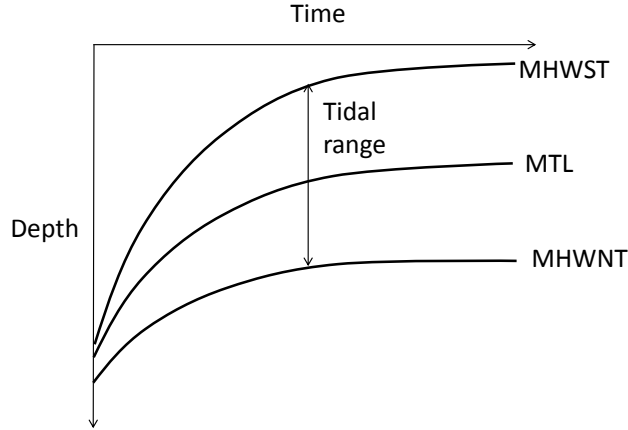
Figure 2.4: Diagram to illustrate how changes in tidal range, plotted here on an age/altitude graph, need to be accounted for when establishing the indicative meaning of SLIPs (from Gehrels et al, 1995).

There is a high quality dataset of relative sea level change for the British Isles region, which now contains over 1250 SLIPs, as it has been added to considerably in recent years (Shennan et al, 2002; Milne et al, 2006; Roberts et al, 2011). A sea-level database was developed for Ireland by Brooks and Edwards (2006), before which there were only limited observations of relative sea level to constrain the GIA models generated by Lambeck (1996) and Lambeck and Chappell (2001). The SLIPs have been rigorously evaluated in order to determine their individual accuracy and precision as relative sea level markers (Shennan et al, 2002) and are separated into 'primary' and 'secondary' SLIPs depending on how well the indicative meaning of a sample is quantified. These SLIP databases are critical for determining estimations of GIA-induced land motion as well as for constraining the key input parameters in geophysical modelling of GIA processes (Bradley et al, 2009) and ice sheet thicknesses (Brooks et al, 2008b).

2.3 Glacial isostatic adjustment (GIA)

The term 'glacial isostatic adjustment' (GIA) is often given to the isostatic deformation of the solid Earth and the geopotential associated with mass distribution (both solid Earth and ice/ocean). The response of the mantle to surface loading occurs on timescales of thousands- to hundreds of thousands of years and the earth response-function is both

depth-dependent and spatially variable (Lambeck and Chappell, 2001). It is well known that this climate-induced ice/ocean mass redistribution causes a spatial and temporal response in sea levels (see Figure 2.5). At the ice margin, the rebound due to ice unloading is smaller than at the centre of the load and dominates initially, however, it is the ice-equivalent sea level rise from (what can be more distant) ice sheets that becomes more important later during deglaciation (Lambeck and Chappell, 2001).
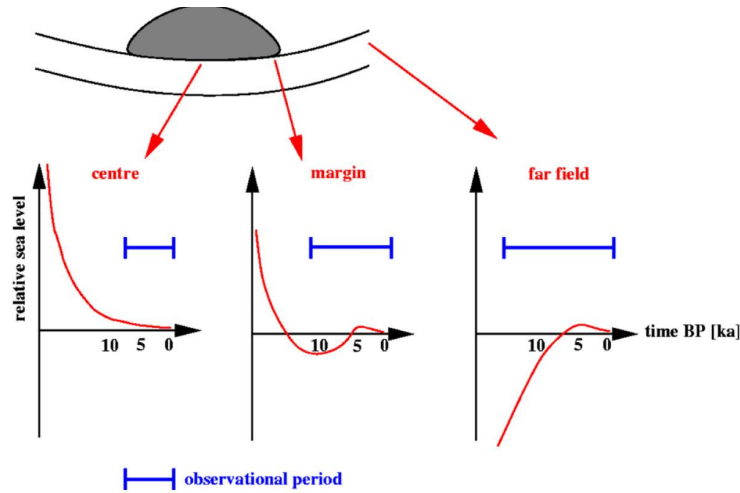
Figure 2.5: Anatomy of sea-level records with distance from the ice sheet (from Steffen and Wu, 2011).

In the region of the British Isles, relative sea level change since the LGM has largely been a function of crustal rebound due to ice-unloading of the BIIS as well as due to meltwater loading of the adjacent seas and the North Atlantic in relation to the global glacio-eustatic term. The unloading of distant ice sheets, including the Fennoscandian and Laurentide ice sheets, has also had an effect (Lambeck, 1995). A number of studies (e.g. Shennan et al, 2006b; Bradley et al, 2009; Teferle et al, 2009) have shown from comparison of observations of former sea levels with modelled GIA, long-term vertical motion in the area of the British Isles is dominated by GIA, whereas the (relatively very small) horizontal motion component is dominated by motion of the Eurasian plate.

2.3.1 GIA modelling

GIA models essentially consist of three key elements: an ice loading model to define the global distribution of land ice over time, an Earth model to reproduce the solid earth deformation resulting from surface mass redistribution, as well as a model of eustatic sea-level change to calculate the redistribution of the ocean mass (e.g. Farrell and Clark, 1976; Lambeck, 1995; Peltier, 1996; Bassett et al, 2005; Shennan et al, 2006b).

Because of the complex pattern of relative sea level, and the extensive SLIP database, the British Isles have been a focus of many studies of modelling GIA following the LGM (e.g Lambeck, 1993, 1995, 1996; Shennan et al, 2000b; Peltier, 2002b; Shennan et al, 2006b; Bradley et al, 2011). The spatially variable sea-level changes can be combined with observational data from further afield to produce a rigorous test for quantitative models of local ice sheet history, global meltwater influx as well as GIA.

2.3.2   GIA model advancements: Great Britain and Ireland

Models of GIA are continuously being revised and improved as more observational data of increasing quality become available for constraining the models and also as understanding of the GIA and glaciation-deglaciation processes improves. Earlier models of GIA only considered the sea level aspect (e.g. Lambeck, 1996; Lambeck et al, 1998; Shennan et al, 2000b; Peltier, 2002a; Shennan and Horton, 2002); however, with the use of continuous global positioning system (CGPS) measurements, which are important for constraining the Earth component of the GIA model, more recent GIA modelling studies have been able to consider the summation of both the near- and far-field effects (e.g. Lambeck and Chappell, 2001; Milne et al, 2006, 2009; Bradley et al, 2009; Teferle et al, 2009). Despite considerable advancements in GIA modelling in recent years and with growing observational databases being made available, there still remain significant differences in model fits.

Two early GIA models were developed by Peltier (1994, 1996) (global model) and Lambeck (1995) (British Isles and North Sea model). A significant advancement was made by Shennan et al (2006b), who further-constrained the ICE-4G model of Peltier (1996), which has subsequently been renamed BIM-1. Using new SLIPs, Brooks et al (2008b) improved the fit of BIM-1 for Ireland. Furthering the work of Shennan et al (2006b) and Milne et al (2006), Bradley et al (2009) studied 16 sites for vertical motion and 21 sites for horizontal motion, using CGPS measurements to perform a much more complete Earth model parameter study, again using BIM-1. A longer time-series of observational data as well as improved techniques were available to Bradley et al (2009). Both Milne et al (2006) and Bradley et al (2009) found good agreement between observational data from CGPS and GIA model data for vertical motion, and hence they concluded that GIA is the dominant vertical geodynamic process in the region.

Bradley et al (2011) were the first to consider the entire and most up-to-date dataset of relative sea level for both Great Britain and Ireland in the context of developing GIA modelling; the locations of their SLIPs can be seen in Figure 2.6. The study complemented

and collated a number of aspects from recent work on GIA modelling of parts of the BIIS, including papers by Milne et al (2006); Shennan et al (2006b); Brooks et al (2008b) and Bradley et al (2009), by combining regional ice sheet reconstruction with a new global ice model. Their work incorporated the most recent advances in the sea level component of GIA modelling such as coastal evolution, an accurate treatment of sea-level change in areas of ablating marine-based ice as well as the influence of GIA perturbations on the Earth's rotation vector (Milne and Mitrovica, 1998; Mitrovica et al, 2001). They used the BIIS ice model of Brooks et al (2008b) and the global ice model of Bassett et al (2005) and although the revised model produced a reasonable fit with observations, there were still regional misfits, which included a Holocene highstand that was too high and too late, an under-prediction of the magnitude of the sea-level fall of the late Devensian, and a late Holocene sea level rise which was too rapid at 6 ka BP and which contradicts trends from observational evidence. An attempt was made to address these misfits by modifying the eustatic model by continuing global ice melting through the late Holocene; this alteration provided an improvement by reducing the late Holocene misfits, although not entirely. The study highlighted the importance of considering the spatial variation in sensitivity to earth model parameters, best done by considering the full set of relative sea level data points to produce their optimal ice-earth model set.

In an attempt to make GIA models more realistic, Kuchar et al (2012) were the first to incorporate a numerical geological model into a GIA model for the British Isles. Prior to this work, the ice in the GIA models of the region simply overlay flat topographies, which were at sea level. Although the geological model was constrained using ice flow data, and was combined with the BIIS ice sheet model of Hubbard et al (2009) (which was combined with the global model of and Bradley et al (2011)), the overall fit with the relative sea level curves obtained by Kuchar et al (2012) was not as good as that obtained by the BIIS GIA model of Bradley et al (2011).

GIA models are used for a number of applications, including for palaeotidal modelling studies, as detailed in Section 2.5 (e.g. Uehara et al, 2006; Rippeth et al, 2008; Neill et al, 2009b, 2010). For such applications, the GIA model outputs of shelf palaeotopography are critical as input parameters.

2.4 The tides and the shelf seas

Although dominated by the Moon (Darwin, 1880; Baker, 1991), temporal and spatial changes in tides are a result of the combined effect of multiple influences that act over
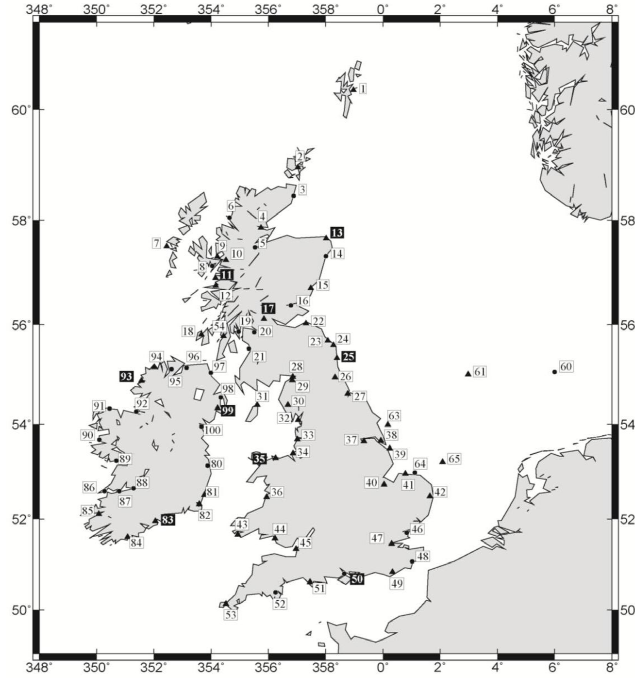
Figure 2.6: Map showing the locations of the 80 data points used by Bradley et al (2011).

varying timescales. The observed tides can thus be broken down into a number of 'harmonic constituents', or 'partial tides', which are added together to include the effects of topography, rotation and other bodies on the tides (Table 2.1).

The maximum tidal amplitude in the open ocean is about 1 m and in accordance with the law of energy conservation, tidal amplitudes increase substantially as the tidal wave approaches the coast, i.e. as water depths decrease (Arbic et al, 2009). Tidal amplitudes can be particularly high in estuaries due to the shelving of the seabed and the 'funnelling' effect of the channel on the water, such as in the Bristol Channel (Uncles, 1983). Further amplification of the tidal range can occur if the tides are reflected by the coastline or are in- or near-resonance. Rather than being a direct response to the gravitational forces of the Moon and the Sun on the shelf sea waters themselves, the tides of the NWESS are a co-oscillating response of the shelf seas to the tides generated in the Atlantic Ocean. Results of previous studies (e.g. Hinton, 1995; Uehara et al, 2006) have concluded that semi-diurnal tidal forcing of shelf models is very sensitive to changes in ocean tides and changing bathymetry (see Section 2.5).

Since the work of Jeffreys (1920), the shelf seas have been regarded as the likely principal sink of tidal energy in the world's oceans, due to the increased friction associated with the bottom boundary layer in the shallower water. Dissipation of tidal energy also occurs in

the deep ocean over rough topography, a result of barotropic tides being converted into baroclinic waves, and the dissipated energy contributes to abyssal mixing (Egbert and Ray, 2000; Egbert and Erofeeva, 2002). Some of the tidal energy incident from the open ocean is reflected back into the deep ocean at the edge of the continental shelf and the remainder is transmitted onto the shelf where the energy is dissipated as turbulence (e.g. Green et al, 2008; Arbic et al, 2009). The numerical modelling study of Arbic and Garrett (2010) indicated that when the open ocean and shelf tides are near resonance, even the small mass (i.e. the shelf) can significantly affect the oscillations of the larger mass (i.e. the open ocean). Total global dissipation on the shelf seas at present is thought to be on average 2.7 TW of the total global dissipation of 3.5 TW, or 70% (Egbert, 2003, 2004; Green et al, 2009), a figure which includes direct estimates from satellite altimetry (Egbert and Ray, 2001) and from hydrodynamic models (e.g. Provost and Lyard, 1997; Egbert, 2004; Uehara et al, 2006; Arbic and Garrett, 2010).

Table 2.1: Principle tidal constituents (from Brown et al, 2006)

Period	Tidal Constituent	Symbol	Period in Solar hours	Approximate mean elevation amplitude on the NWESS (m)
Semi-diurnal	Principle lunar	M_2	12.42	0.77
	Principle solar	S_2	12.00	0.26
	Large lunar ecliptic	N_2	12.66	0.16
	Luni-solar	K_2	11.97	0.07
Diurnal	Luni-solar	K_1	23.93	0.07
	Principle lunar	O_1	25.82	0.06
	Principle solar	P_1	24.07	0.02
(Longer)	Lunar fortnight	Mf	327.86	0.02
	Lunar monthly	Mm	661.30	0.01

2.4.1   Shelf sea seasonal stratification

Tidal mixing fronts are an important feature of many shelf seas that delineate stratified and well-mixed (or sporadically-stratified) waters. The mixing, due to tidal stirring, and the stratification, due to solar heating of the water column, are in balance at the shelf sea tidal mixing fronts, the positions of which vary with the spring-neap tidal cycle, as well as

seasonally (Simpson and Bowers, 1981).

In shelf seas, the transition from stratified to tidally-mixed waters tends to occur rather abruptly; the region of transition is termed the tidal mixing front and is typically around 5 km wide (Simpson et al, 1974) and exhibits large gradients in temperature and other physical properties. The shelf seas are highly biologically productive and biogeochemically active due to intense inputs of terrestrial nutrients and carbon through rivers and from the open ocean at continental margins. Stratified continental shelf seas are thus significant sinks for atmospheric carbon dioxide (CO_2). Rippeth et al (2008) demonstrated that with significant sea level rise since the LGM, the impact of the continental shelf seas on the atmosphere-ocean interaction of CO_2 increased as their ability to draw down CO_2 increased with significant increases in the tidally-mixed regions. Simpson et al (1974) determined that the location of the tidal mixing front lies on a critical contour, $\chi_{\text{simpson}} = 70 \text{ m}^{-2}\text{s}^{-3}$ (where χ is the 'stratification parameter'), which depends upon the water depth, h, and the spring-neap tidal current speed at the surface, u_s, such that:

$$\chi_{\text{simpson}} = \frac{h}{|u_s|^3} \qquad (2.1)$$

Although seasonal stratification has important implications for carbon dioxide exchange in shelf seas, it is also interesting in this context since the only existing proxy for constraining palaeotidal model simulations was developed on the grounds of using the transition between seasonally stratified and well-mixed waters for validating palaeotidal model outputs (Section 2.5.2).

2.5   Palaeotidal modelling

Over geological timescales, tidal conditions on both global and shelf scales have been considerably different to those at present. Numerical modelling studies have demonstrated that global tides have changed significantly since the LGM (Belderson et al, 1986; Thomas and Sündermann, 1999; Uehara et al, 2002; Egbert, 2004; Hall and Davies, 2004; Uehara et al, 2006). A number of attempts have been made to estimate evolving tidal regimes on various continental shelves since the LGM, including the NWESS (e.g. Austin, 1991; Scourse and Austin, 1995; Uehara et al, 2006), the East China Sea (e.g. Uehara et al, 2002) and the Bay of Fundy and the Gulf of Maine (e.g. Scott and Greenberg, 1983).

2.5.1   Developments in palaeotidal modelling

Scott and Greenberg (1983) conducted an early palaeotidal modelling study into the evolving tides in the Bay of Fundy over the last 7000 years. Due to limited observational data at the time, Scott and Greenberg (1983) assumed that the tides in the North Atlantic have been constant throughout time; subsequent modelling studies have shown that this is not the case (e.g. Thomas and Sündermann, 1999; Egbert, 2004; Uehara et al, 2006), as shown in Figure 2.7. For example, Uehara et al (2006) found incorporating changes in palaeo ocean tides in a palaeotidal model of the NWESS greatly increased tidal amplitudes (and hence tidal currents) prior to 10 ka BP, a result of the North Atlantic mega tides. Other early modelling studies, such as that by Austin (1991), implemented changes in sea levels by simply reducing water depth uniformly across the model domain to simulate eustatic sea-level change. At the time, no dynamic GIA-derived palaeotopographies were available and Austin (1991) attempted no validation of the palaeotidal model results. Austin (1991) identified the need for development of the technique by use of palaeotopographies/bathymetries, inclusion of more tidal constituents and consideration of ocean tides for setting more realistic boundary conditions. A number of studies have found that changing the area or the dynamics of the shelf seas can impact upon global tides by varying dissipation and resonance (e.g. Egbert, 2004; Arbic et al, 2009; Green et al, 2009; Arbic and Garrett, 2010). It is clearly important to consider any feedbacks of changing sea levels or tidal dynamics on the shelf seas on the ocean tide.

Unprecedented work on developing tidal models was carried out by Egbert (2004); their study was the first time an entirely unconstrained (i.e. no data assimilation) global tidal model was run with any accuracy. The model used by Egbert (2004) was Oregon State University's Tidal Inversion System (OTIS), a barotropic tidal model which assumes shallow water dynamics (Egbert, 2004). The model uses knowledge of the bathymetry and astronomical forcing, with no additional forcing or boundary conditions. The modelled M_2 elevation amplitudes were within 5 cm accuracy of present-day elevations from satellite altimetry (averaged across the domain) and were found to be in agreement with TOPEX/Poseidon altimetric estimates of energy dissipation.

Uehara et al (2006) conducted a detailed numerical modelling study into the tidal evolution on the NWESS during the last 20 ka. A two-dimensional finite-difference palaeotidal model, which was a development of the Princeton Ocean Model (POM) (Blumberg and Mellor, 1987), was used to test the differences in incorporating the rebound model of Peltier (1994) and a revised version of Lambeck (1995) into the palaeobathymetries. Outputs of
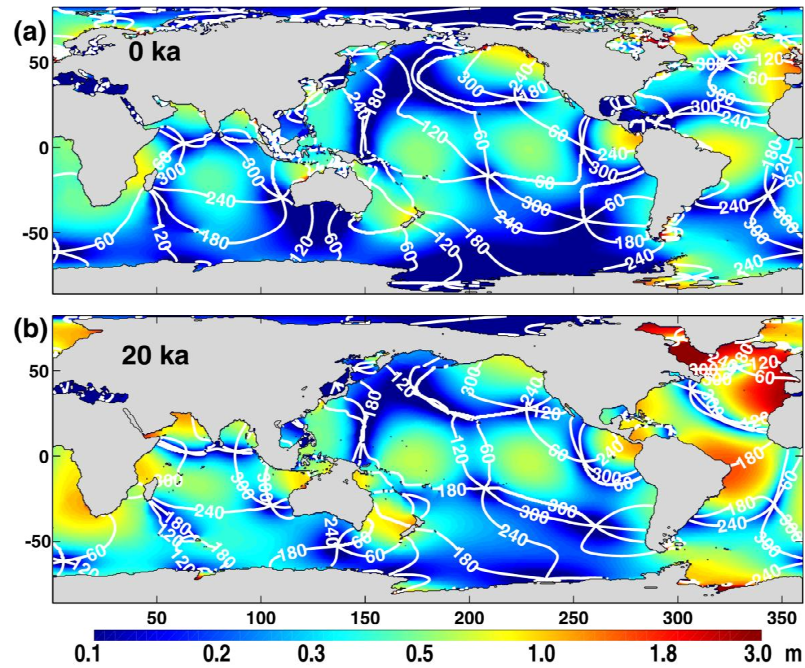
Figure 2.7: Modelled M$_2$ amplitude and phase for a) present-day and b) 20 ka BP (from Egbert, 2004).
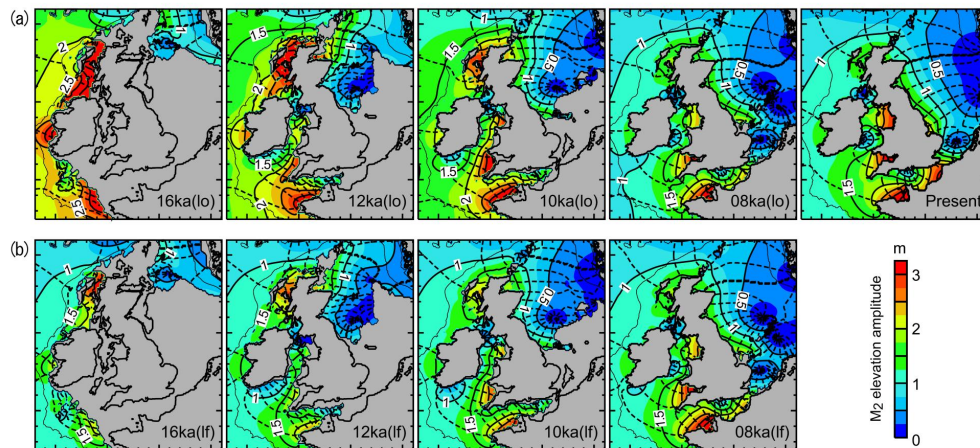
Figure 2.8: Modelled M$_2$ elevation amplitude and phase for various time slices using the Lambeck GIA model (from Uehara et al, 2006).

tidal amplitudes (Figure 2.8), dissipation, tidal currents, mean high water spring tide, seasonal stratification and peak BSS vectors (and hence sediment transport paths) from both model set-ups were compared. Further, they investigated the impact of setting the boundary conditions of the domain to be fixed to present-day tides ('fixed') or to vary ('open-ocean'), where the latter accounted for changes in ocean tides caused by changes in eustatic sea level and ice-sheet extent. According to Uehara et al (2006), the timing of the changes was sensitive to the local isostatic effects, however the variability of offshore tides ('open-ocean') since the LGM had the most profound impact. It should be noted at

this point that Figure 2.8 shows changes in modelled M_2 elevation amplitudes and phases only, where the M_2 elevation amplitude is only about 50% of the total tidal elevation, as indicated in Table 2.1. This suggests that if all tidal constituents were considered, the total changes in elevation amplitude could be twice those shown in Figure 2.8.

Amplitudes of the M_2 constituent are thought to have changed considerably since the LGM, in particular in the North Atlantic (Thomas and Sündermann, 1999; Egbert, 2004; Griffiths and Peltier, 2008) and in the Arctic Ocean (Griffiths and Peltier, 2008). Modelled tidal amplitudes of up to double present-day amplitudes were observed by Egbert (2004) in the glacial North Atlantic and were coupled with a 50% increase in global dissipation compared with the present and almost triple the present dissipation in the deep ocean. The results for the global model runs conducted by Uehara et al (2006) were convergent with those of Egbert (2004) in the observation of mega tides in the glacial North Atlantic. These large changes in M_2 tides in the eastern North Atlantic during the early phase of deglaciation are thought to be due to increasing sea levels and due to quasi-resonant conditions of the basin with respect to the semi-diurnal frequency. Tidal changes are thought to have generally been small in the last 8 ka (e.g. Thomas and Sündermann, 1999; Uehara et al, 2006) with the exception of in Antarctica, where there were still noticeable modifications along the coast over the last 8 ka (Thomas and Sündermann, 1999).

2.5.2 Constraining palaeo-model simulations

Prior to this work, limited work has been carried out into the 'validation' of palaeotidal model outputs, which comprises constraining model outputs using observational data. Austin and Scourse (1997) compared the palaeotidal model outputs from Austin (1991) with faunal, isotopic and geochemical data from a sediment core from the Celtic Sea basin in order to investigate the seasonal thermocline development in the region during the Holocene. It was the first study of the long-term dynamics of seasonal stratification; the outputs of the model provided a hypothesis to be tested with the first data on the long-term dynamics of seasonal stratification from any shelf sea. The results of Austin and Scourse (1997) verified the model predictions of Austin (1991) for the position of the tidal mixing front in the Celtic Sea, although only the M_2 tidal constituent was considered and, more significantly, the model palaeotopography was not isostatically corrected. This problem was revisited by Scourse et al (2002), to whom more sophisticated dating methods were available with which to refine the model further. The combined, more extensive faunal assemblages, provided a dataset from the LGM to the late Holocene, and were used by

Scourse et al (2002) to estimate the evolution of stratification at the core site. This palaeo-data point was subsequently compared with the modelled timing of stratification onset in the Celtic Sea (Uehara et al, 2006). One data point for constraining palaeotidal models is clearly insufficient, and work needs to be done on finding a proxy which can be used on a regional scale to validate and/or constrain palaeotidal model output. The geological data record potentially holds powerful information for developing this aspect of palaeotidal modelling.

2.5.3 Implications for sediment dynamics

On the shelf seas, changes in sea level (and the associated changes in tidal dynamics) impact upon sediment transport, sediment type and bedform distribution, primary production and hence carbon dioxide uptake, and tidal energy dissipation. The melting of the BIIS and the Fennoscandian Ice Sheet, which had ablated by 9 ka BP (Boulton et al, 1985; Scourse et al, 2009a), was a major source of sediment supply to the NWESS and played a significant role in the formation of large bedforms and in bathymetric evolution (Boulton et al, 1985; Neill et al, 2009b; Scourse et al, 2009a).

Further to early two-dimensional tidal modelling of the NWESS (e.g. Pingree and Griffiths, 1979; Aldridge, 1997), Hall and Davies (2004) used a three-dimensional tidal model to investigate the effect of changing water depth on the magnitude and direction of tidal-induced BSS. Hall and Davies (2004) also used the recognised method of using the direction of peak BSS as an indicator of sediment movement (e.g. Pingree and Griffiths, 1979; Aldridge, 1997) and forced the model with M_2 only and subsequently with five tidal constituents, namely M_2, S_2, N_2, K_1 and O_1. They simulated the tidal conditions in the region when the sea level was 35 m lower than at present, which corresponds to *ca.* 10 ka BP. The *"coarse-grid model"* assumed solely eustatic sea level rise and did not take into account GIA. They found that while the distribution of peak BSS were similar to those computed with M_2 when forcing with a number of constituents, the magnitude of the BSS was modified.

Modelling over a larger area, Neill et al (2010) found that waves generally had a more significant contribution to BSS at 12 ka BP than at present (compare Figures 2.9 and 2.10). In some areas where large tidal sand-ridges or banks are seen, e.g. in the East China Sea (Uehara et al, 2002) and in the Celtic Sea (Belderson et al, 1986; Scourse et al, 2009a), modern tidal current conditions do not appear to be sufficiently energetic for their generation, indicating the changes in the hydrodynamics in these areas as sea levels have

risen. For example, an early modelling study by Belderson et al (1986) considered sea level 100 m lower than at present in the outer Celtic Sea and found that tidal currents in the area were around twice as strong than they are at present, thus suggesting that these higher tidal currents were the origin for the northeast-trending sandbanks in the area, although they could have formed at even lower sea levels.
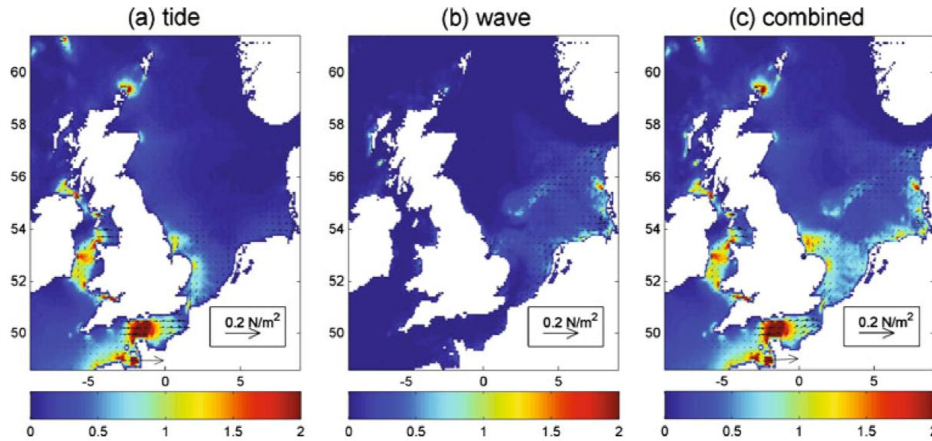
Figure 2.9: Mean annual BSS for present-day, a) tidal-induced, b) wave-induced and c) combined tide and wave (from Neill et al, 2010). The colour scale is BSS in N m^{-2}.
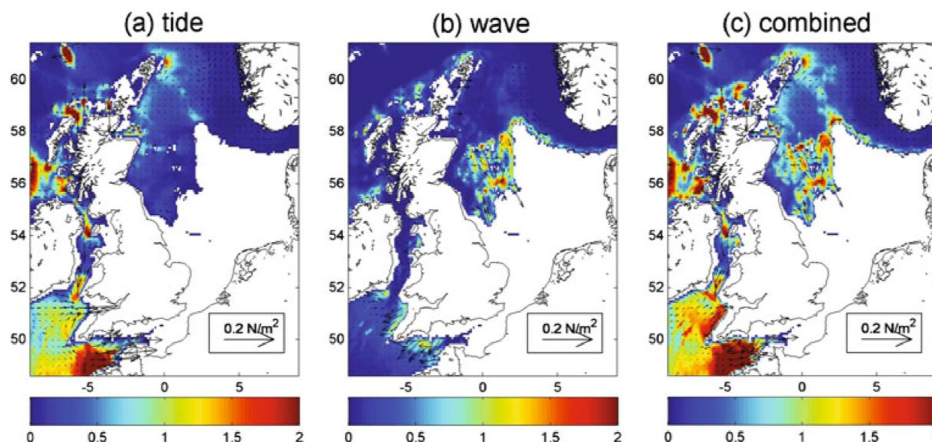
Figure 2.10: Mean annual BSS for 12 ka BP, a) tidal-induced, b) wave-induced and c) combined tide and wave (from Neill et al, 2010). The colour scale is BSS in N m^{-2}.

Scourse et al (2009b) used the palaeotidal model outputs of Uehara et al (2006) to revisit the question of the formation of the linear tidal sand ridges in the Celtic Sea. They coupled the model output data with published observational data and the results supported previous interpretation that the sand ridges are moribund tidally remobilised sediments representing the transgressive system tract. The timing of the formation of the sand ridges

predicted by the model outputs of BSS could not be validated using observational data due to limitations of field testing at such depths of water; however, model predictions of sand transport vectors and the overall direction of sandbank growth were in agreement with seismic stratigraphic data. Van Landeghem et al (2009) also found that outputs of modelled BSS of Uehara et al (2006) compared well with cross-sectional profiles over asymmetrical sediment waves in the Irish Sea. Interestingly, during the period $15 - 10$ ka BP, the direction of predicted bedload transport and those inferred from the bedforms were opposite and they speculated that the reversal of the direction to present-day tidal vectors would have played a mayor role in the build-up of some of the large bedforms in the Irish Sea.

To investigate the formation and maintenance of headland/island sandbanks in the English Channel, Neill and Scourse (2009) used existing relative sea level and radiocarbon data and field data (ADCP flow data) over the sandbanks to constrain a morphological model. The morphological model contained three components - hydrodynamic, bedload transport and bed level change. Considering that bed level change was the main contributor to the formation of the sandbanks, Neill and Scourse (2009) attempted to apply the morphological model to palaeo time slices using idealised domains for the model simulations. Neill and Scourse (2009) concluded that sea level rise can affect the magnitude and location of primary sandbanks, as it has done in the vicinity of the Isle of Portland, the area of focus for their study. Understanding the formation of such headland/island sandbanks is significant because of their role in dissipating wave energy and hence in coastal protection (Neill and Scourse, 2009).

2.6 Sediment transport

2.6.1 Sediment transport theory and formulae

Large-scale redistribution of sediments by hydrodynamical processes occurs in shelf seas which has direct implications for basin and coastal evolution. Sediments are important as they comprise the seabed, determine the turbidity of water, provide a substrate for marine benthic organisms, carry organic matter and are involved in biogeochemical exchanges. In the majority of shelf sea and coastal regions, both waves and currents play a role in sediment dynamics; however, the combined effect is not simply a linear addition of the two independent effects (Soulsby, 1997). The effects of currents, waves or by combined current and wave motion on sediment dynamics take place primarily through the friction they exert on the seabed (Soulsby, 1997). This frictional force is referred to as the bed shear stress (BSS, τ_0) and is expressed as the force exerted by the flow per unit area of bed in terms of the density of water (ρ) and the frictional velocity (u_*) such that:

$$\tau_0 = \rho {u_*}^2 \tag{2.2}$$

Sediment transport (of non-cohesive sediments) occurs when the BSS exceeds the threshold of motion, τ_{cr}, or threshold Shields parameter (θ_{cr}), which is a dimensionless form of the BSS and is dependent upon the median grain size, d_{50}:

$$\theta_{cr} = \frac{\tau_{cr}}{g(\rho_s - \rho)d_{50}} \tag{2.3}$$

where g is the gravitational acceleration and ρ_s is the grain density. The threshold Shields parameter can be plotted against the dimensionless grain size, D_*, to produce the well-known Shields Curve (Figure 2.11), to show the threshold of motion beneath waves and/or currents. The dimensionless grain size is given by:

$$D_* = [\frac{g(s-1)^{1/3}}{\nu^2}]d_{50} \tag{2.4}$$

where υ is the kinematic viscosity of water and s is the ratio of grain to water density. An improved threshold BSS formula was developed by Soulsby and Whitehouse (1997) which accounts for overestimation of the data for fine grain sizes in the Shields parameter equation:

$$\theta_{cr} = \frac{0.3}{(1+1.2D_*)} + 0.55[1 - exp(-0.020D_*)] \tag{2.5}$$
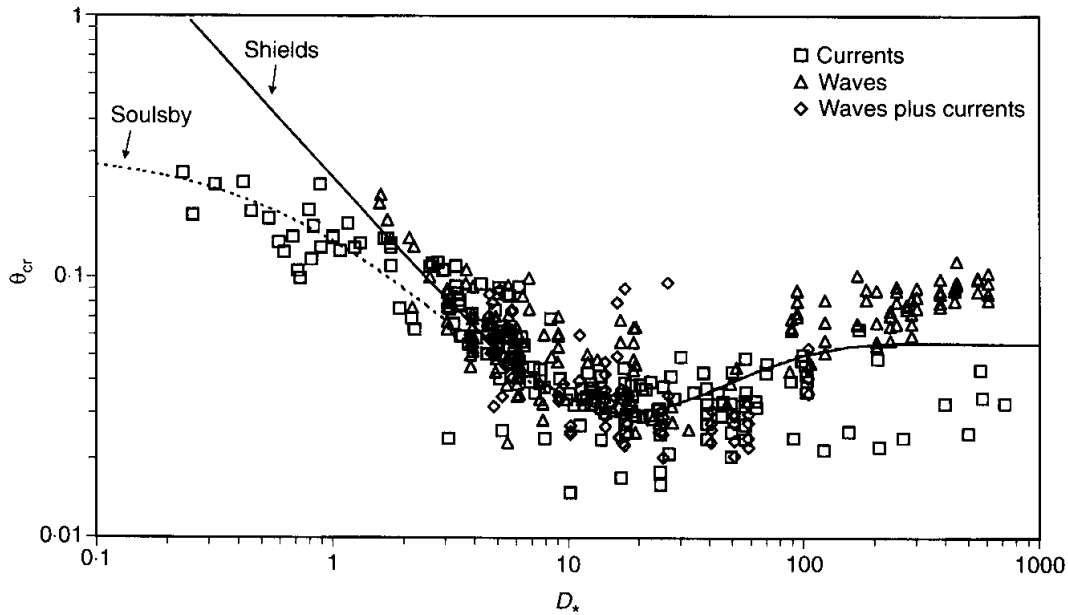
Figure 2.11: Critical Shields Curve for threshold of motion (from Soulsby, 1997).

Sediment transport occurs through bedload and suspended load transport and varies depending on the forcing e.g. whether it is wave-, current-, wind-induced motion or a combination of mechanisms inducing the motion. Quoting Soulsby (1997), *"for combined waves and currents, the waves provide a stirring mechanism which keeps the sediment grains mobile, while the current adds to the stirring and also provides a mechanism for net transport"* and hence the combined wave and current motion tends to (non-linearly) enhance the sediment motion in comparison to individual transport mechanisms. In general, bedload transport involves the sliding, rolling (both defined as 'traction') or hopping ('saltation') of grains along the bed, whereas for grains to be transported as suspended load they are entrained off the bed and into the water column. Suspended load transport tends to occur when the threshold of motion is exceeded significantly and the contribution of suspended load transport to the *total* sediment transport rate tends to be greater than that of bedload transport (Soulsby, 1997). At lower current velocities and/or for large grain sizes, bedload is the dominant form of sediment transport (Campbell, 2005). The overall residual current field, comprising tidal currents and wind-driven surface and (near-surface) currents, is significant in terms of the direction and magnitude of sediment transport.

Numerous sediment transport formulae are available, which consider many different environments in which sediment transport might occur, including over rippled beds, in oscillatory flows, as bedload transport only, in varying water depths and for different grain sizes. However, these empirically-derived equations have inherent limitations, such as restrictions on applicable water depths, or ranges of grain sizes, and as such are not

suitable for application to regional or shelf scales. One example is the Soulsby-Van Rijn formulation, which can be used to calculate the change in total (i.e. bedload plus suspended load) instantaneous sediment transport rate by currents in waters up to around 20 m depth, q_t, such that:

$$q_t = q_b + q_s \tag{2.6}$$

where bedload transport is:

$$q_b = 0.005Uh \left\{ \frac{U - U_{cr}}{((s-1)gd_{50})} \right\}^{2.4} \left(\frac{d_{50}}{h} \right)^{1.2} \tag{2.7}$$

and suspended load transport is:

$$q_s = 0.005Uh \left\{ \frac{U - U_{cr}}{((s-1)gd_{50})} \right\}^{2.4} \left(\frac{d_{50}}{h} \right) D_*^{1.2} \tag{2.8}$$

where d_{50} is the median grain size and U_{cr} is the depth-averaged current speed at the threshold of sediment motion:

$$U_{cr} = 0.19(d_{50})^{0.1} log(\frac{4h}{d_{90}}) \qquad \text{for } 100 \leq d_{50} \leq 500 \mu m \tag{2.9}$$

$$U_{cr} = 8.5(d_{50})^{0.6} log(\frac{4h}{d_{90}}) \qquad \text{for } 500 \leq d_{50} \leq 2000 \mu m \tag{2.10}$$

where d_{90} is the grain size for which 90% of the grains by mass are finer.

It is important to consider the threshold of motion of sediments on the seabed for a number of calculations, including for seabed mobility calculations, bedload transport and the entrainment of finer sediments into suspension (Soulsby, 1997). A number of studies have used the distribution of peak BSS vectors from tidal models to infer the path of sediment transport and the location of bedload partings including Pingree and Griffiths (1979); Austin (1991); Harris and Collins (1991); Aldridge (1997); Hall and Davies (2004); Neill and Scourse (2009); Mitchell et al (2010) as well as for the evolution of bathymetric features such as tidal sand ridges (e.g. Scourse et al, 2009b). Sediment transport paths originate in zones of divergence, referred to as bedload partings, which tend to be located in narrow straits where tidal currents are strong (Pingree and Griffiths, 1979). Conversely, bedload convergences are found in areas where sediment transport paths meet and the rate of deposition exceeds the rate of erosion. It is the phase relationship between the semi-diurnal (M_2 and S_2) and quarter-diurnal (M_4 and S_4) constituents which determines differences between maximum BSS on flood and ebb tides, as well as differences in current

direction at these times (Pingree and Griffiths, 1979; Hall and Davies, 2004). Where the strength of the flood and the ebb tides are equal (and opposite), no net sand transport is anticipated.

As an example of sand transport on a larger scale, van der Molen (2002) used a number of equations to investigate the combined influence of tides, wind and waves on the net sand transport in the North Sea. By comparing the individual contributions as well as the combined effect, large-scale sand transport was investigated by incorporating outputs from a hydrodynamic model into sediment transport equations. As an example, Van der Molen (2002) used Bailard's formulation for total flow (Bailard, 1981) i.e. for the instantaneous total volumetric sediment transport per unit width (q_t), given by:

$$\vec{q}_t = \vec{q}_b + \vec{q}_s = \frac{f_{cw}\varepsilon_b}{g(s-1)tan\phi_i}\|\vec{u}\|^2\vec{u} + \frac{f_{cw}\varepsilon_s}{g(s-1)w_s}\|\vec{u}\|^3\vec{u} \qquad (2.11)$$

where $\vec{q}_b$ and $\vec{q}_s$ are the bedload and suspended load transports (as before), f_{cw} is the friction factor for combined currents and waves, $\varepsilon_b = 0.10$ and $\varepsilon_b = 0.20$ are the efficiency factors for bedload and suspended load transport, respectively, ϕ_i is the angle of internal friction of the sediment with $tan\phi_i = 0.63$, w_s is the setting velocity of sand grains in water and $\vec{u}$ is the total near-bed flow-velocity vector.

2.6.2   Modelling sediment dynamics

Understanding long-term and large-scale geological processes that have formed coasts and the surrounding bathymetry is important for the appropriate management of the present-day coastline as well as for predicting the impact of future climate and sea level change. Although long-term sediment dynamics in shelf seas are dominated by tidal currents, waves also contribute significantly (e.g. van der Molen, 2002; Neill et al, 2009b). Waves are the primary mechanism for inter-annual variability, due to sensitivity to variability in atmospheric (wind) forcing (Neill et al, 2009b). Thus, consideration of both tide- and wave-induced BSS is preferable for more accurate representation of sediment transport processes.

Pingree and Griffiths (1979) were the first to model the correlation between sand transport paths and the maximum BSS vectors caused by the combined $M_2 + M_4$ tidal currents for many areas on the UK shelf. Pingree and Griffiths (1979) found that the direction of bedload transport correlates with the maximum bottom BSS vectors ($M_2 + M_4$), although most sand transport occurs in response to the maximum current velocity over a tidal cycle.

A study of sand transport in the Bristol Channel by Harris and Collins (1991) found

that there is no simple correlation between the direction of maximum BSS and bedload transport in this area, particularly in near-shore regions. In the Bristol Channel, large spatial variations in tidal asymmetry occur along the length of the channel (e.g. Neill et al, 2009b) with both convergences and divergences along its length (Harris and Collins, 1991; Neill et al, 2009b). Numerical modelling of sediment dynamics using such models is inherently crude since processes such as bed level change due to erosion and deposition, which involve many complex variables, including grain orientation and the turbulence structure, are often not accounted for. Three-dimensional models are required for description of the turbulence and three-dimensional currents, and hence are essential for consideration of sediment transport as suspended load, since vertical variations in current profile and changes in turbulence intensity are responsible for keeping sediments in suspension.

The ability to predict the morphodynamic evolution of the seabed is important for a number of applications; such as for engineering, coastal management, habitat mapping, and sea level studies. Morphodynamic modelling has also progressed in recent years, with the advancement of coupled modelling techniques and the increasing computational capacity for modelling complex processes (e.g. van der Molen et al, 2004; Roelvink, 2006; Warner et al, 2008b). Sediment models can include cohesive and non-cohesive sediment categories, which account for attributes such as grain size, density, settling velocity and the critical shear stress for erosion. A recent example of such a system is the Coupled-Ocean-Atmosphere-Wave-Sediment Transport (COAWST) Modeling System (Warner et al, 2008b, 2010), which uses a module to represent sediment transport processes in coastal environments (the Community Sediment Transport Modeling System, CSTMS). The sediment and hydrodynamic components of COAWST can feed back to each other, thus changes in the hydrodynamics and the evolving sediment bed are sent to, and received by, the separate model components at predefined intervals during the simulation, and are subsequently taken into consideration during later time steps.

2.6.3 Inferring changes in ocean dynamics from seabed sediment grain size

The focus of using seabed sediment grain size as a proxy for current flows has been on the use of the fine fraction. Sediment grain sizes have been used to infer past deep bottom current speeds, using what is known as the 'sortable silt proxy'. For example, McCave et al (1995a,b, 2006) used the silt fraction (10-63 µm) as an indicator of changes in bottom current speed in western North Atlantic over the last 30,000 years. The sediment grain

sizes considered were from sediment cores taken in waters between approximately 1000 and 4000 m deep, where the currents are considered to be deep currents. Michels (2000) used sediment settling velocities to infer present-day geostrophic current speeds (and the associated critical shear velocities) in the Norwegian-Greenland Sea. Current speeds were determined from the sediment grain size (generally <300 μm) using the critical curve for the threshold of motion of Miller et al (1977).

Gyllencreutz et al (2010) carried out particle size analysis on three dated cores from the southeastern Brazilian shelf to infer environmental changes on the southwestern Atlantic Margin since 7 ka BP. The currents in the region are dominated by wind stress (i.e. wind waves) and thus Gyllencreutz et al (2010) assumed that variations in seabed sediment grain size in the area reflect changes in wind-driven currents. The grain size characteristics within the sediment cores support the theory of the southward shift of the Inter Tropical Convergence Zone at 5 ka BP, which would have influenced the wind-driven currents in the area.

Using the relationship explained above, whereby as bed shear stress increases, so too does the sediment grain size which can be mobilised/transported, the geological data on the shelf seas potentially holds a record of changes in past tidal current conditions. Examining this relationship on a tidally-dominated shelf sea is the first step towards determining whether grain size can be used as a proxy for tidal current conditions.

2.7 Study area: the northwest European shelf seas (NWESS)

The focus of this study is on the NWESS, shown in Figure 2.12. Exposed to Atlantic waters are the Celtic Sea, the Malin Shelf and the northern North Sea. In the North Sea, depths are generally between 100 m and 200 m, although a maximum depth of around 700 m can be found in the Norwegian Trench, located in the northeastern North Sea, adjacent to the Fennoscandian landmass. The Irish Sea is a semi-enclosed body of water with a north-south trending channel of depth 250 m, bordered to the south by the Celtic Sea and it is linked north to the Malin Shelf by the North Channel. The English Channel, which has a depth of less than 50 m and contains various large sandbanks, connects the eastern Celtic Sea to the southern North Sea.

The tides on the NWESS are predominantly semi-diurnal (Pingree and Griffiths, 1978), and are dominated by the M_2 (lunar) and S_2 (solar) tidal constituents. Tidal energy propagates from the North Atlantic onto the shelf into the Celtic Sea. Some of the tidal wave propagates into the English Channel and through into the North Sea, while some

passes into the the Bristol Channel and into the Irish Sea (Pugh, 1987). Part of the semi-diurnal wave is diffracted south and east by northern Scotland, and enters the North Sea. In the Celtic Sea, the Bristol Channel and English Channel, the diurnal tide behaves as a standing wave, but without any tendency to resonance (Pugh, 1987). The tidal amplitudes in the Severn Estuary, which reaches a maximum of ∼12 m, are the second largest in the world, after the Bay of Fundy. It has long been realised that higher-than-average intensity of energy dissipation occurs in the shallow shelf seas around the UK (Flather, 1976; Simpson and Bowers, 1981), with approximately 5 to 6% of the total global tidal dissipation occurring on the NWESS, making it the second most energetic shelf on the planet, second only to Hudson Bay (Egbert and Ray, 2001; Egbert, 2004).
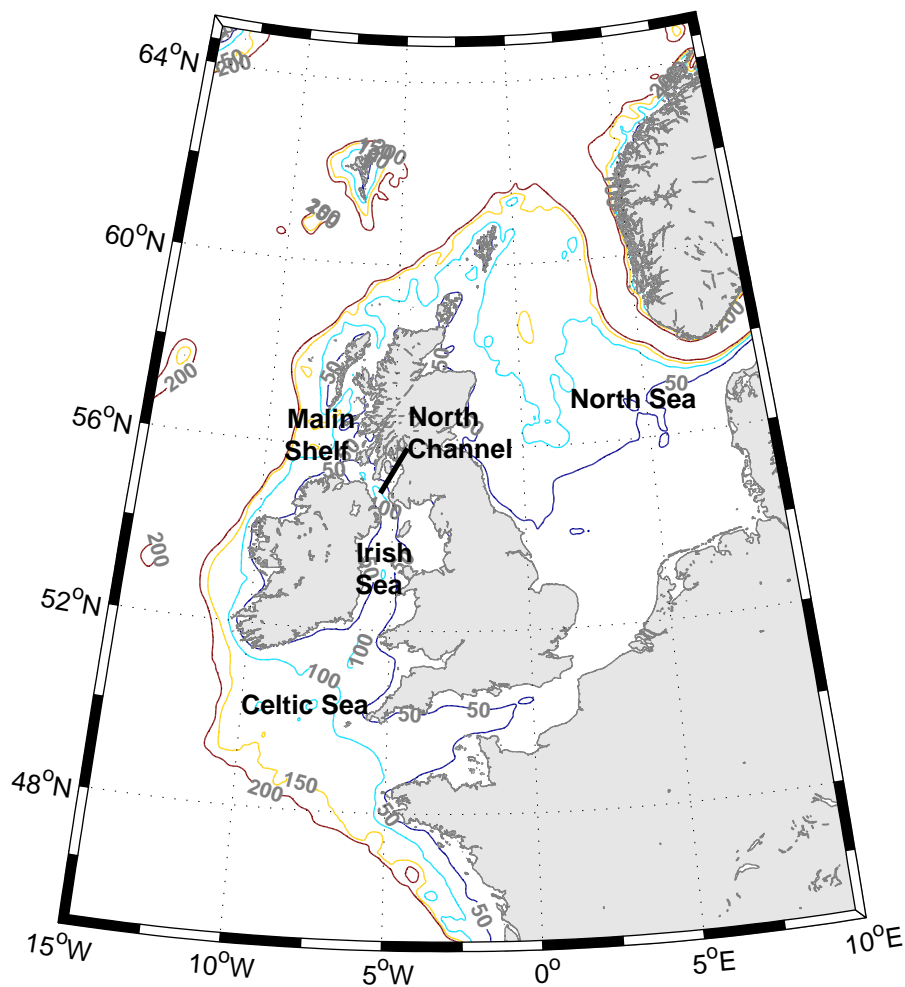
Figure 2.12: present-day bathymetry of the NWESS - the model domain. Water depth contours are plotted at 50 m (dark blue), 100 m (light blue), 150 m (yellow) and 200 m (red).

In the North Sea, the seabed mainly consists of fine to medium sands (grain sizes 125-500 µm) (e.g. van der Molen, 2002), showing a general fining trend towards the northeast (Jarke, 1956). In addition to this sand, there is substantial gravel content, often overlying bed rock, in the Strait of Dover and along the eastern British Coast. Much of the Celtic Sea and the English Channel are comprised of mixtures of sand and gravel, with a large area of gravel in the eastern and central English Channel Uncles and Stephens (2007). The deglaciation of the Fennoscandian and British-Irish Ice Sheets, both of which had ablated by 9 ka BP, was a major source of sediment supply to the NWESS (Boulton et al, 1985; Scourse et al, 2009b), in particular acting as a source of mixed sediments (diamicton). Both ice sheets also played a significant role in the formation of large sand banks, such as Dogger Bank in the North Sea (Carr et al, 2006).

In Chapter 4 the focus is on the Irish Sea, which is an ideal case study given the abundance of existing research and information on the constitution of the seabed sediment distribution (e.g. Wilson et al, 2001; Holmes and Tappin, 2005; Blyth-Skyrme et al, 2008; Robinson et al, 2009; Van Landeghem et al, 2009), as well as extensive surveys by the British Geological Survey (BGS). There is a significant diversity of seabed sediment classifications within the Irish Sea, including areas of exposed bedrock (mostly limited to the northwest of Anglesey) and patches of semi-consolidated Pleistocene deposits, both covered in places only by thin transient patches of unconsolidated sediment. The majority of the seabed consists of sands and gravels, which are largely reworked glacial sediments. In the southern Irish Sea, sandy gravel is the predominant sediment type. Coarse sediments of glacial and glaciofluvial origin occupy both Cardigan Bay and St George's Channel. In St George's Channel there are several areas of exposed till, covered only by thin transitory sediment. Along the coast of Cardigan Bay is a belt of (mainly) sand, which gets increasingly muddy towards the mouth of rivers. In the northern Irish Sea, there is a band of gravelly sediment lying to the south and north of the Isle of Man, which separates areas of muddy and sandy sediments to the east and west. West of the Isle of Man is a large area of mud, known as the Western Irish Sea Mud Belt, almost entirely surrounded by sandy mud, which itself is surrounded by muddy sand. The muddy sediments in the Irish Sea are largely confined to the northwest Irish Sea Mudbelt and the Celtic Deep (e.g. Jackson et al, 1995).

The complex glacial origin of NWESS seabed sediments has led to the formation of a range of morphological features, including drumlins (e.g. Eyles and Marshall McCabe, 1989), large linear tidal sand ridges in the Celtic Sea (e.g. Scourse et al, 2009b,a), and

evidence of ice streaming and calving in the Irish Sea (van Landeghem et al, 2009).

2.8 Summary points

- Quantifying the extent and timing of the BIIS, as well as far-field ice sheets, is on-going work. As developments in understanding of the ice sheets extents and timings are made, changes to glacial isostatic modelling are made (GIA modelling, Section 2.3), as a model of the ice sheets is a key input parameter to GIA models. For studies such as this, where a new palaeotidal model is developed, it is important to use the most up-to-date, and well-constrained GIA model available (Bradley et al, 2011).

- Patterns of relative sea level change over the NWESS have varied considerably since the LGM. Significant advancements in GIA modelling of the region have been made in recent years, and GIA model output can be used as input to generate palaeobathymetric grids in palaeotidal models.

- Because of the complex isostatic response of the NWESS to the deglaciation following the LGM, it is an interesting region for modelling tidal changes resulting from significant sea level rise (~ 130 m), as there are regions which display contrasting responses to the sea level rise.

- Modelling sediment transport is a complex problem, as many different factors play significant roles over various spatial and temporal scales.

- Limited work has been carried out into constraining palaeotidal model output using proxy data. There is only one existing data point that has been used to constrain palaeotidal model outputs (Austin and Scourse, 1997; Scourse et al, 2002; Uehara et al, 2006).

3 Methods and Techniques

The two main aspects of this model-data comparison study were the analysis of observational data (in the form of sediment cores) and the development of a tidal (and palaeotidal) model. The cores were first selected from the British Geological Survey (BGS) archives (Section 3.1) before being subsampled (Section 3.1.1), analysed for grain size (Section 3.2) and corresponding samples sent for radiocarbon analysis (Section 3.3). A high resolution regional tidal model and a shelf-scale palaeotidal model were developed (Section 3.4) for comparing modelled outputs of tidally-modulated parameters with observed grain size parameters (Chapters 4 and 7).

3.1 Sediment core selection

A criterion for core selection was developed by first examining the modelled evolution of tidal-induced BSS on the NWESS using outputs from the existing palaeotidal model simulations of Uehara et al (2006). The model outputs were available between approximately -15°E and 15°E and 45°N and 65°N, at a resolution of 1/12 degree and for 1 ka time slices from 21 ka BP to present-day.

The cumulative absolute change in BSS between time slices from the early Holocene (using model output of 13 ka BP) to the present-day is presented in Figure 3.1, and was used for highlighting regions of the shelf in which there have been significant temporal changes in tidal currents. It was anticipated that such areas were more likely to display gradients in grain size evolutions for comparison with modelled changes in tidal current over time than areas that had undergone small changes in BSS. A number of key regions were identified; namely areas within the Bristol Channel, the Irish Sea, off the north coast of Anglesey, the North Channel, west of Scotland, northeast of the Shetland Isles and around Orkney.

Using the online BGS database tool ('Offshore GeoIndex'), it was possible to identify all vibrocore samples within areas of interest. An obvious constraint was that they had
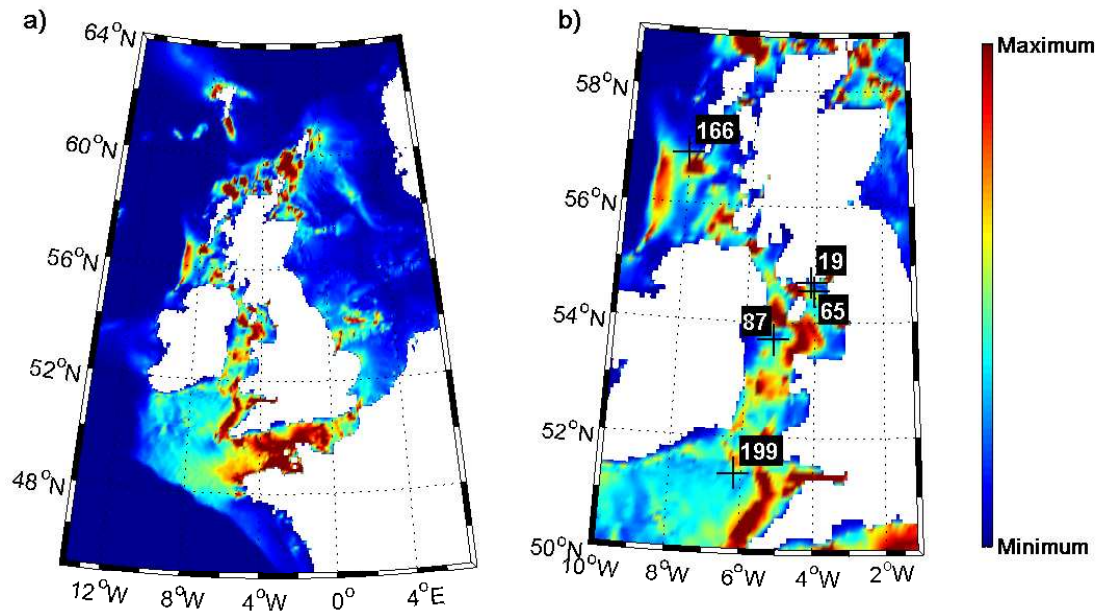
Figure 3.1: a) Cumulative absolute change in BSS on the NWESS from 13 ka BP to present, using 1 ka time slices modelled by Uehara et al (2006). The location and number (where 19=BGS19) of the marine sediment cores used in this study are marked in panel b). The colour scale indicates the (relative) range in cumulative change in BSS with time, where dark blue shows the areas of minimum (or no) change and the red represents maximum change.

to be within British waters in order for them to be available from the BGS. An initial visit to BGS in Keyworth, Nottingham, was made in order to view the core logs for each of the 250 vibrocores selected within areas of interest. This preliminary selection took into consideration water depth, core length, the logged stratigraphy and location in proximity to other cores. The selection of cores was narrowed down to 21 potential cores. During subsequent visits to BGS, the selected cores were inspected and four were selected. These four cores, namely BGS vibrocores 54/-05/19, 54/-05/65, 53/-06/87 and 56/-09/166 (hereafter referred to as cores BGS19, BGS65, BGS87 and BGS166) were subsampled for later grain size analysis and radiocarbon dating. All four cores were transferred to the School of Ocean Sciences for the remainder of the project, ensuring that they were available for additional analysis if necessary. The core locations are plotted in Figure 3.1 and further details of the cores are presented in Chapter 5. It should be noted here that core 51/-07/199 from the Celtic Deep had been examined previously (Austin and Scourse, 1997; Scourse et al, 2002), and was already on-site and available for sampling.

3.1.1   Sediment core subsampling

To obtain grain size information for the five sediment cores, samples were taken at various depths down each core. Each sample was 1 cm thick and spanned the diameter of the core. The positions of the samples were recorded as depth down core, with the depth recorded from the end of the 1 cm sample nearest to the core top. The core subsamples were extracted using chisel, palette knife and spatula. Care was taken to remove the parts of each subsample from the edge of the core which may have been 'smeared' down during the vibrocoring process. Vibrocore samples were preferred over cores collected by other methods, e.g. gravity or piston coring methods since the latter employ inertia to push the core tube into the sediments, thus tending to disturb the sample more (Emery and Dietz, 1941). In contrast, vibrocoring techniques utilise vibrations to rearrange the sediments, allowing the core tubing to penetrate the sediment under the static weight of the apparatus.

The core depth from which these samples were taken depended upon visually-identified changes in grain size, positions of previous samples and the integrity of the vibrocore. Efforts were made to obtain samples that would highlight sequences of significant grain size evolution. With the exception of BGS166 which remained moist, the cores were dry, hard and consolidated. These samples were separated into subsamples for particle size analysis (PSA, Section 3.2), and in preparation for AMS radiocarbon dating (Section 3.3). Samples from BGS199 for PSA were taken from as close as possible to the locations of previous samples (Austin and Scourse, 1997; Scourse et al, 2002).

3.2   Laser particle size analysis (PSA)

The grain size evolution of the five BGS vibrocores was determined using a laser particle sizer. Laser particle diffractometry has been used for measuring particle size since the early 1970s. Early instruments had a much narrower size detection range (typically 0.5-550 µm) than the modern instruments such as the Malvern Mastersizer 2000 (hereafter referred to as the Mastersizer) used in this study (range 0.02-2000 µm).

A prepared sample (see Section 3.2.1) added to a volume of distilled (deiononised) water, passes through the measurement area, where a laser beam illuminates the particles, and the scattered light (Figure 3.2) is measured by a series of detectors (Figure 3.3). An accuracy of better than 1% is possible using the Mastersizer (Sperazza et al, 2004). Mie theory of light scattering, developed by Gustav Mie in 1908 (see Horvath, 2009) is used to calculate the particle size distribution. It is necessary to know the optical properties

(complex refractive indices) of both the sample and the dispersant for application of Mie theory. The Mastersizer has a built-in database of common dispersants - in this study, distilled water was used as the dispersant.
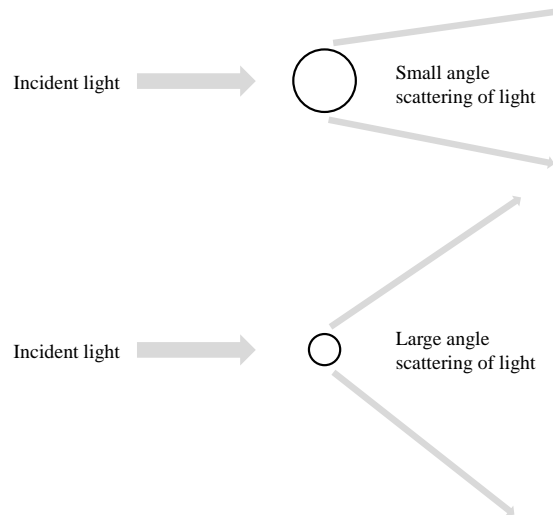
Figure 3.2: Scattering of light from a large (upper) and small (lower) particle (from Malvern Instrument Wordwide, 2012).
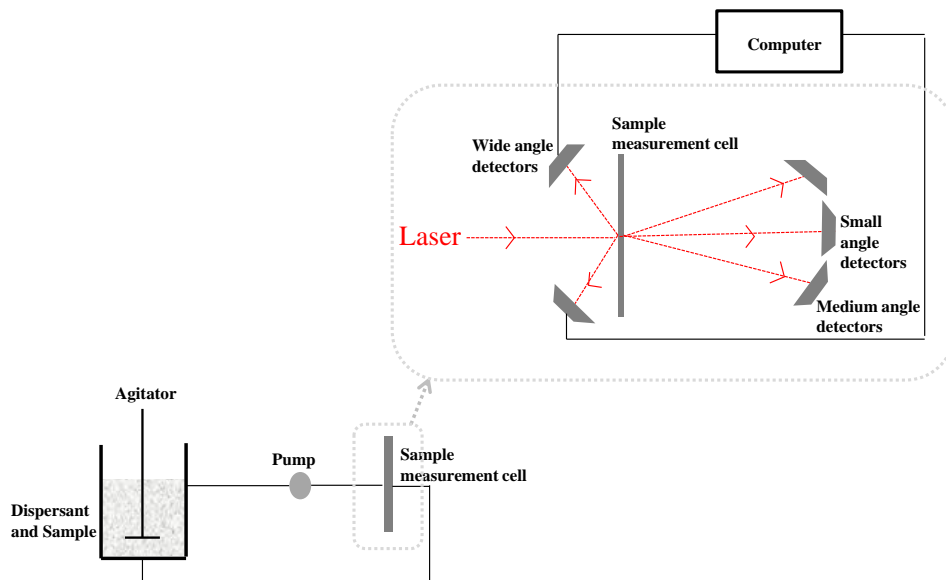
Figure 3.3: Optical layout of a modern laser diffraction instrument (from Malvern Instrument Wordwide, 2012).

3.2.1 PSA sample preparation

Preparation of the samples was required, particularly for those which were dry and consolidated. Although samples from BGS166 were moist, for consistency, every sample from each core was placed in a dispersive solution, made up of 1 litre distilled water, 33 g sodium hexametaphosphate and 7 g sodium carbonate. A small volume of dispersant was added to each of the subsamples and, where necessary, the samples were gently broken up using a spatula before adding 100 ml dispersant. The sample and dispersant were then stirred using a commercial milkshake mixer for 15 minutes, to break up any remaining consolidated material. The samples were then left for 24 hours before analysis.

3.2.2 Laser particle sizing

Directly prior to PSA, each sample was agitated for a further 5 minutes using a magnetic stirrer. This was to ensure that that any floccs that might have formed during the 24 hours dispersion time were broken down. Mixing the samples vigorously at this stage also prevented settling during the extraction of an aliquot of the suspension for addition to the Mastersizer solution. For removing the aliquot to be analysed from the dispersed sample, a pipette was used (see Sperazza et al (2004) for details). The aliquot was drawn from the agitated sample by raising the pipette through the depth of the sample. It was found that extracting sample from only the bottom or the top of the beaker containing the sample (i.e. without raising the pipette through the sample), preferentially sampled coarser or finer particles, respectively. Further, before addition of aliquots to the Mastersizer system, the dispersed sample was passed through a 2 mm (2000 μm) sieve, thus ensuring that all the samples were below the maximum particle size suitable for the Mastersizer. Only shell fragments were removed during this sieving, and so this did not affect the grain size distribution results.

The volume of sample needing to be withdrawn from the sample solution varied depending on the grain size distribution within the sample - the sample was added to the distilled water in the Mastersizer until laser obscuration was within 10 - 20%. This is standard sampling protocol for the Mastersizer. Once the correct volume of sample had been added, the integrated ultrasonics probe was used for 60 seconds (set at 20%) to further aid dispersion of any cohesive particles, a recommendation for very fine materials or strongly bound agglomerates. The pump speed was set to 2000 rpm (Sperazza et al, 2004).

For each aliquot, three measurements were taken; the sampling time of each of these three measurements was 10 s. An average was then taken for each aliquot. The aliquots

were repeated until the measured average d_{10}, d_{50} and d_{90} were within 0.1 ɸ (Krumbein phi scale) of another subsample, a criterion developed by Poizot et al (2008). The ɸ value was calculated using the following equation:

$$\phi = -\frac{\log_{10}(D)}{\log_{10}(2)} \tag{3.1}$$

where D is the diameter of the particle (in mm). This resulted in between two and seven aliquots being analysed for each sample, where more aliquots were needed for poorly sorted samples.

3.2.3 PSA sample post-processing

The results of the PSA were post-processed using the GRADISTAT software (Blott and Pye, 2001) for more detailed analysis of grain size statistics. The granulometric analysis used here for calculating the sample statistics was the graphical method of Folk and Ward (1957), which output statistics on sediment classification, including mean, mode, sorting and cumulative percentile values (e.g. d_{10}, d_{50} and d_{90}). The focus of this study was on the cumulative percentile values, in particular the d_{50} (i.e. the median grain size), as this is commonly used in sediment transport equations, such as in the Shields parameter (Shields, 1936) and in the Soulsby-Van Rijn formulation for total load transport by waves and currents (Soulsby, 1997). Furthermore, d_{50} is a widely-recognised parameter for application of spatially-varying sediment classifications within hydrodynamic models, e.g. for inputting spatially-varying drag coefficients.

3.3 Radiocarbon dating

The primary aim of the ^{14}C analysis was to establish age models for the cores. Initially, range-finder samples were analysed for four cores (BGS19, BGS65, BGS87 and BGS166); BGS199 had an existing age-depth model (Austin and Scourse, 1997; Scourse et al, 2002).

3.3.1 Basic principles of radiocarbon dating

Carbon is made up of three isotopes; ^{12}C and ^{13}C are stable isotopes and [14]C (radiocarbon) is an unstable and weakly radioactive isotope. Nitrogen nuclei in the upper atmosphere capture neutrons from cosmic radiation, forming [14]C. This is rapidly oxidised to form [14]CO_2 and thus enters the global carbon cycle. All organisms assimilate ^{14}C from CO_2 throughout their lifetimes; when they die they cease exchanging carbon with the biosphere

and the amount of ^{14}C decreases at a rate determined by the law of radioactive decay (Figure 3.4), since ^{14}C is a long-lived radioisotope with a half-life of 5730 years. By observing the relative abundance of ^{14}C in an organism, it is possible to relate the residual radioactivity to the time of death of the organism (Figure 3.4).
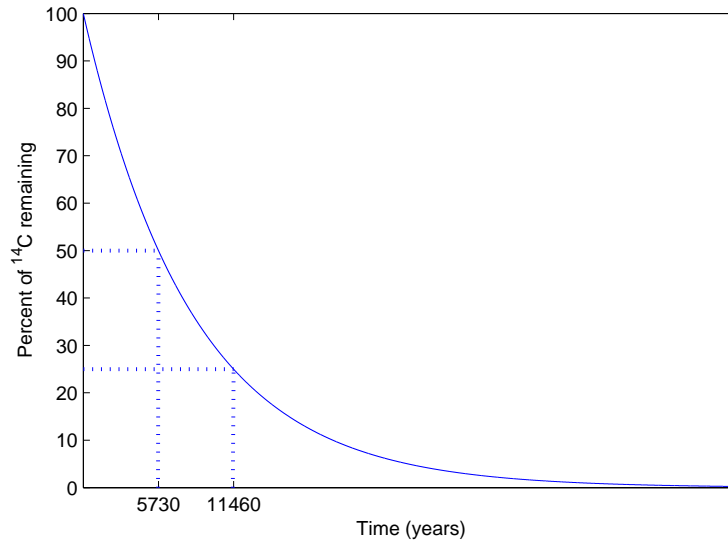
Figure 3.4: Radioactive decay curve for ^{14}C.

3.3.2 Sample preparation

The remainders of the 1 cm core subsamples not used for PSA were prepared for radiocarbon dating. Firstly, each sample was dried in an oven (40°C) and were then weighed once dry. The samples were then submerged in distilled water for 24 hours to unconsolidate the material, before being wet-sieved through a 63 μm sieve to remove any fines and salt. The final stage in the wet-sieving was to rinse the sample thoroughly with distilled water and retain the coarse fraction by filtration. The samples were then returned to the oven and re-weighed once dry. Each sample was then passed through a nest of 500, 250, 125 and 63 μm sieves (1, 2, 3, 4 and 5 ϕ, respectively) to separate the size fractions.

3.3.3 Sample selection

The 250 and 125 μm fractions were examined for foraminifera (foram) content and the 500 μm fraction for molluscs. All molluscs picked were bivalves and were cleaned again in distilled water to minimise any contamination from sediment. The bivalves were identified using Tebble (1966) as well as using the online database of the National Museum Wales (Oliver et al, 2010). Bivalves with taxodont dentitions (rows of interlocking teeth) were

avoided since taxodont dentition is characteristic of deposit feeders, which are likely to contain detrital carbon which would impact on the accuracy of a radiocarbon date. Mollusc species known to burrow (e.g. *Turritella*) were also avoided. Only one bivalve per sample was submitted for radiocarbon dating. Due to limited variety and availability, it was necessary to use various bivalve species per core. Efforts were made to take the largest sample possible; for example, whenever possible, foram samples were picked to be over 5 mg in weight and larger bivalves were preferred over multiple small bivalves. Foram samples of suitable species, such as *Ammonia batavus* and *Cibicides lobatulus* were picked under a microscope. Each foram sample was monospecific.

In the first instance, the top and bottom of the remaining cores were sampled, in accordance with the grant awarded by the the NERC Radiocarbon Facility-Steering Committee (Radiocarbon Analysis Allocation Number 1659.1012). A mixture of both bivalve and foram samples were submitted to the NERC Radiocarbon Facility (Environment) at The Scottish Universities Environmental Research Centre (SUERC) AMS Laboratory in East Kilbride. This first batch of samples contained 12 samples and was submitted on 23/01/2013 (results were received on 14/06/2013), and included four foram-bivalve pairs chosen from the same horizon to test for possible reworking (see Table 5.3). The opportunity arose for subsequent samples to be analysed at the Atmosphere and Ocean Research Institute (AORI), University of Tokyo. Further samples from BGS19 (3 samples) and BGS87 (5 samples) were sent for analysis, to attempt to constrain significant features in the grain size evolution of these two cores.

3.3.4 Radiocarbon analysis

Bivalve samples weighing more than 10 mg were etched by controlled hydrolysis with dilute hydrochloric acid to remove outer and possibly contaminated surface carbonate. The samples were then rinsed in distilled water, dried, crushed and weighed. The pre-treated sample was hydrolysed to CO_2 using 85% orthophosphoric acid (at room temperature). The samples were then converted to graphite by Fe/Zn reduction and pressed into cathode targets. This graphite sample was compressed into a small cavity in an aluminium target, which acts as a cathode in the ion source. The ions produced by sputtering (bombarding) the graphite surface with heated caesium were extracted and accelerated in the AMS. The ^{12}C and ^{13}C positive ions were separated magnetically by mass and measured in Faraday Cups. Simultaneously, a gas ionisation counter was used to record the ^{14}C and thus instantaneous ratios of ^{12}C, ^{13}C and ^{14}C were recorded. A known weight of the CO_2

samples were measured for δ^{13}C on a dual inlet stable isotope mass spectrometer (Thermo Fisher Delta V).

3.3.5 Correction and calibration of radiocarbon dates

It is necessary to apply a calibration to all radiocarbon dates because the calculation of a conventional ^{14}C age assumes constant ^{14}C content in the atmosphere over time (Stuiver and Polach, 1977). In reality the rate of atmospheric production of ^{14}C has varied over time. Results from radiocarbon analysis of marine organisms must also be corrected for the Global Marine Reservoir Effect. The oceans, atmosphere and biosphere are radiocarbon reservoirs of varying concentrations and radiocarbon in the ocean is dissolved from the atmosphere in the form of CO_2. Dates of terrestrial and marine organisms obtained through radiocarbon analysis have a difference of around 400 radiocarbon years (marine samples being older), and this constitutes the mean global modelled surface ocean reservoir correction that must be applied. In addition, not all marine organisms contain the same concentrations of ^{14}C since ^{14}C concentrations, along with CO_2 concentrations, vary depending on water depth, location, and levels of upwelling and stratification. A localised marine carbon reservoir correction (ΔR) must thus also be applied to results for marine carbonates (Stuiver et al, 1986), in addition to the global correction.

The results of the radiocarbon analysis were reported as conventional radiocarbon years BP (relative to AD 1950) and modern ^{14}C, both expressed as $\pm 1\phi$ for overall analytical confidence (Chapter 5). The carbon content (percent by weight) and δ^{13}C$_{\text{VPDB}}$ ‰ were also reported (where VPDB is short for Vienna Pee Dee Belemnite, which is the international reference standard for carbon isotope ratios). For calibration and correction of the report dates, the IntCa13 and Marine13 Radiocarbon Calibration Curve were used (Reimer et al, 2013).

3.4 Tidal modelling

Numerical models of the ocean tides generally contain two fundamental components: the input data (mainly as bathymetry and boundary conditions) and the equations describing ocean dynamics. Since the tides have considerably long wavelengths in comparison to water depths, they can be modelled numerically assuming shallow water dynamics (e.g. Blumberg and Mellor, 1987; Egbert and Ray, 2001). The shallow water equations are non-linear partial differential equations that can be used to represent conservation of both mass and momentum, and are applicable where the water depth is much less than the

horizontal scale of motion (in this case the length of the tidal wave). The equations can be used to estimate the water height (tidal elevation) and water velocity (tidal current speed) within a region, at any specific time in the tidal cycle. For open-ocean tidal modelling, the forcing comes only from the tidal potential forcing within the interior of the model domain. For regional or shelf-scale tidal modelling, the forcing comes from setting tidal boundary conditions at the open boundaries of the domain; such conditions include changes in sea-surface height and ocean currents due to the tides.

Advancements in tidal modelling have seen early tidal models, which were simple barotropic models (two-dimensional, depth-averaged), progress into comprehensive three-dimensional models, which incorporate and feed back between both barotropic and baroclinic signals and motions (e.g. Shchepetkin and McWilliams, 2005), and which can be coupled with other numerical models (e.g. Warner et al, 2010). Such developments have been made possible by developments in computing power and capacity, which has changed the way these models can be applied (e.g. through increased temporal and spatial resolution of simulations).

3.4.1   Hydrodynamic model: ROMS

The Regional Ocean Modeling System (ROMS) is an open-source model, developed by Rutgers University and the University of California, Los Angeles (www.myroms.org). ROMS has a large user community that contributes to its active development, and is suitable for investigation of a broad range of processes on various scales, including regional and coastal domains. There are options for coupling ROMS with sub-models, for example for biogeochemical, bio-optical, sediment, and sea ice applications. There are also many user-defined parameters within ROMS, such as options for advection, bottom friction and horizontal mixing schemes, making it a versatile model choice.

ROMS is a three-dimensional free-surface, terrain-following, primitive equations model (e.g. Haidvogel et al, 2000; Marchesiello et al, 2001; Shchepetkin and McWilliams, 2005). There is a choice of linear (density as a function of temperature, which is mainly used for highly idealised applications) or non-linear (density as a function of temperature, salinity and depth) equations of state. The finite-difference approximations of the Reynolds-averaged Navier-Stokes equations are implemented using the hydrostatic and Boussinesq assumptions. The governing dynamical equations (from Haidvogel et al, 2008) - using Cartesian coordinates in the horizontal, and sigma vertical coordinates - are written a follows:

$$\frac{\partial(H_z u)}{\partial t} + \frac{\partial(u H_z u)}{\partial x} + \frac{\partial(v H_z u)}{\partial y} + \frac{\partial(\Omega H_z u)}{\partial s} - f H_z v = -\frac{H_z}{\rho_0}\frac{\partial p}{\partial x} - H_z g \frac{\partial \zeta}{\partial x} - \frac{\partial}{\partial s}\left(\overline{u'w'} - \frac{\nu}{H_z}\frac{\partial u}{\partial s}\right)$$
$$(3.2)$$

$$\frac{\partial(H_z v)}{\partial t} + \frac{\partial(u H_z v)}{\partial x} + \frac{\partial(v H_z v)}{\partial y} + \frac{\partial(\Omega H_z v)}{\partial s} + f H_z u = -\frac{H_z}{\rho_0}\frac{\partial p}{\partial y} - H_z g \frac{\partial \zeta}{\partial y} - \frac{\partial}{\partial s}\left(\overline{v'w'} - \frac{\nu}{H_z}\frac{\partial v}{\partial s}\right)$$
$$(3.3)$$

$$\frac{1}{\rho_0}\frac{\partial p}{\partial s} = -\frac{g}{\rho_0}H_z\rho \tag{3.4}$$

with the continuity equation (for an incompressible fluid):

$$\frac{\partial(H_z u)}{\partial x} + \frac{\partial(H_z v)}{\partial y} + \frac{\partial (H_z \Omega)}{\partial s} = 0 \tag{3.5}$$

scalar transport:

$$\frac{\partial(H_z C)}{\partial t} + \frac{\partial(u H_z C)}{\partial x} + \frac{\partial(v H_z C)}{\partial y} + \frac{\partial(\Omega H_z C)}{\partial s} = -\frac{\partial}{\partial s}\left(\overline{c'w'} - \frac{\nu_\theta}{H_z}\frac{\partial C}{\partial s}\right) + C_{source} \quad (3.6)$$

and (non-linear) equation of state:

$$\rho = \rho(T, S, z) \tag{3.7}$$

The variables used in these equations are given in Table 3.1. Note that the prime represents turbulent fluctuations and the over-bar represents time-averaging (e.g. $\overline{v'w'}$).

For efficiency, a split-explicit time-stepping scheme is used for solving the hydrostatic primitive equations for momentum. A user-defined number of barotropic (fast) steps are carried out within each baroclinic (slow) step to evolve the vertically-integrated momentum equations and the free surface (Shchepetkin and McWilliams, 2005). The model is written in Fortran90/95, using C-preprocessing to activate the various numerical and physical options. The ROMS code can be run either in serial mode or on parallel computing systems, using either shared-memory (openMP) or distributed-memory (MPI) architectures. The model input and output files are written in network common data form, NetCDF, commonly used for array-orientated scientific data.

Table 3.1: Variables used in the description of ROMS

Variable	Description
x, y	horizontal coordinates
s	vertical coordinates
t	time
H_z	vertical stretching factor
C	scalar quantities, e.g. temperature, salinity
f	Coriolis parameter
g	gravitational acceleration
ζ	wave-averaged free-surface elevation
u, v, Ω	the horizontal (u, v) and vertical (Ω) components of velocity
ν, ν_θ	molecular viscosity and diffusivity
p	pressure
ρ, ρ_0	total and reference densities

Orthogonal curvilinear coordinates are staggered on an Arakawa C-grid, allowing for Cartesian, polar and spherical grid systems. The free-surface, density and tracer variables are stored cell-centred (known as 'rho-points'), whereas horizontal velocities are staggered and stored at the edges of a cell ('psi-points'). An orthogonal curvilinear coordinate system aids grid design of complicated regions such as coastlines. Land/sea masking is required to identify land. The bathymetry is measured as positive downwards and cannot contain zero depth; for model stability, a minimum depth must be set and all land points (and water depths less than the minimum depth) set to this minimum depth. In the vertical, the model uses a stretched s-coordinate (sigma) system. This system in ROMS allows the adjustment of vertical resolution, rather than layers being a fixed percentage of the water column (Haidvogel et al, 2000). As in the horizontal, the model state variables are vertically staggered.

3.4.2 NWESS model set-up

Widely-used forcing and bathymetry datasets were used for model optimisation before forcing the model using the relatively low resolution interpolated palaeotidal model outputs of Uehara et al (2006) (Section 3.5). The latter was also available for the present-day, facilitating direct comparison of the palaeotidal model set-up with the ROMS outputs from the optimised present-day runs. A number of sensitivity tests were carried out to interro-

gate the impact of changing key model parameters on the accuracy of the model outputs (see Section 3.4.4). At each stage, the ROMS outputs were analysed (Section 3.4.3) and compared with observations (Section 3.4.5) and the root mean square errors (RMSE) and scatter index (which is the RMSE normalised by the mean of the data) are considered. The final model set-up is described in this section and the optimisation tests in Section 3.4.4.

The NWESS model was set up with a spatial resolution of approximately 1/24 degree longitude and 1/40 degree latitude, (2-3 km grid spacing). The domain was set to cover 15°W to 11°E and 45°N to 65°N, as shown in Figure 2.12. It was not considered necessary to have a larger spatial domain, since the core sites were located at considerable distances from the model boundaries.

The model was forced at the boundaries using surface elevation and the u and v components of depth-averaged tidal current velocities. The tidal constituents considered in the derivation of the boundary conditions were M_2, S_2 and N_2, these being the three dominant constituents of the region. For initial model development, the boundary values of the model were derived from the harmonic constants of the OSU TOPEX/Poseidon Global Inversion Solution 7.2 (TPXO7.2, 1/4 degree resolution globally). The methods used to compute this global model of tides were described by Egbert et al (1994) and further by Egbert and Erofeeva (2002). The tidal forcing data were linearly interpolated onto the computational grid.

The present-day bathymetry was derived from the freely-available GEBCO (General Bathymetric Chart of the Oceans). The topography dataset was available at a 30 arc second spatial resolution, and was compiled using combined datasets of various products, including ship depth soundings and satellite-derived gravity data. The minimum depth was set to 10 m, resulting in water depths of between 0 and 10 m to be set at 10 m. It should be noted that the model assumes a solid wall along the entire land/sea boundary, and hence sea-level regression and land inundation (with tidal cycles) is not accounted for, i.e. alternate wetting and drying of land cells is not included. The minimum water depth of 10 m ensures sufficient water depth for model grid cells not to dry out. Given the model resolution (i.e. since inter-tidal zone are not resolved), the lack of consideration of wetting and drying is considered reasonable in this application. The land/sea mask was defined in the grid file, masking out all areas that were land. To check for any offset of model grid (Marks and Smith, 2006) and to facilitate more precise land-masking, the GSHHG present-day coastline (Wessel and Smith, 1996) for the region was extracted using the GSHHG coastline extraction software and was compared with the land/sea mask. The

land/sea mask could thus be manually edited to account for any spatial offset or to remove any single grid cell embayments for the present-day grid.

Due to the terrain-following coordinate system used in ROMS, it was also necessary to smooth the bathymetry. Grid smoothing helps to minimise possible errors in the pressure gradient term arising from excessively large gradients in the sea bed (e.g. from steep features). The option for smoothing of deep sea mounts was not used for this application. Two passes of a single hanning filter were used to minimise two-dimensional noise. The slope parameter for the topography smoothing was set to 0.25, which is the gradient of depth change between adjacent cells, considering the water depth, i.e. gradient(depth)/depth (Beckmann and Haidvogel, 1993). This value of the slope parameter was used in accordance with the recommendations for the model, and hence a smoothing function was applied to the bathymetry for the required number of passes to achieve this ratio.

The model was run with analytical expressions for surface momentum stress, bottom and surface salinity fluxes, bottom and surface temperature flux, free-surface boundary conditions, initial conditions and two-dimensional momentum boundary conditions. A list of the CPP (C preprocessing) options for this model are given in Appendix 1, and the physical input parameters are given in Appendix 2. The coefficients of vertical harmonic viscosity and diffusion were set to be computed using the generic lengthscale (GLS) turbulence closure scheme model tuned to $K - \varepsilon$ (Umlauf and Burchard, 2003; Warner et al, 2005; Hashemi and Neill, 2014). The water temperature and salinity were set constant at 12.5 °C and 32 PSU, respectively. The tidal model was thus effectively 'three dimensional barotropic', set to have ten layers in the sigma (vertical) coordinate. As much as was possible without compromising the accuracy of the model, the resolution of the layers was increased towards the bed by changing the values of the sigma-coordinate bottom/surface control parameters in the model runtime options. The option for quadratic bottom drag scheme was used, using a bottom drag coefficient of 0.003. Runs with a reasonable range of values (0.002 - 0.003) did not provide any significant difference (Table 3.2); the value used was similar to the 0.0026 value used by Uehara et al (2006) and Neill et al (2010) and was found to give the best fit of model output in comparison to observational data (see 3.4.4).

The shelf runs were integrated for 30 days using a barotropic time step of 10 seconds, and a baroclinic time-step of 1 minute. Each run was initiated from rest and run for 30 days. For stability, the boundary conditions were set to linearly 'ramp up' from stationary, a process which took approximately two simulated days to complete. The first 48 hours

Table 3.2: RMSE and scatter index for M$_2$ and S$_2$ amplitudes and phases for varying drag coefficient values, compared with 10 tide gauges (as in Table 3.3).

Drag	RMSE M$_2$		RMSE S$_2$		Scatter index M$_2$		Scatter index S$_2$	
	h (m)	g (°)	h (m)	g (°)	h (%)	g (%)	h (%)	g (%)
0.0020	0.20	10	0.04	8	10	5	6	4
0.0025	0.12	10	0.03	8	6	5	4	4
0.0030	0.10	10	0.05	8	5	5	7	4
0.0050	0.25	10	0.12	8	12	5	17	5

of model output were thus removed before analysis to ensure that the model reached a state of statistical equilibrium under the applied forcing. The length of this spin-up time was tested and found to be sufficient. The length of model run incorporated two full spring-neap cycles and was sufficient to meet the Rayleigh Criterion for separation of the constituents (Pugh, 1987). For example, to separate M$_2$ and S$_2$ constituents, which have periods of 12.42 and 12.00 hours, respectively, a period of at least 14.8 days needs to be considered:

$$\frac{1}{|\frac{1}{T_{M2}} - \frac{1}{T_{S2}}|} = \frac{1}{|\frac{1}{12.42} - \frac{1}{12.00}|} \text{ hours} = 14.8 \text{ days} \tag{3.8}$$

3.4.3   Model outputs and analysis

The selection of outputs from ROMS is user-defined. The model was set to output surface elevation, depth-averaged velocities, bottom current velocity and BSS at hourly intervals. The internal calculation of BSS is automatically set to compute this variable at the mid-depth of the bottom computational cell. This BSS is hereafter referred to as 'near-bed BSS', as opposed to BSS calculated using depth-averaged tidal currents, which is also an option in ROMS and is the method used for two-dimensional tidal modelling. The equations for computing the northwards and eastwards components of the BSS are shown in equations 3.9 and 3.10:

$$\tau_x = C_D(\sqrt{u^2 + v^2})u \tag{3.9}$$

$$\tau_y = C_D(\sqrt{u^2 + v^2})v \tag{3.10}$$

where τ is the BSS, C_D is the user-defined drag coefficient and u and v are the modelled tidal current velocities in the east and north directions, respectively. Output BSS could be

compared with those calculated directly from tidal velocities (uv, either depth-averaged or from the lowest vertical layer) using the equation:

$$\tau = \rho C_D |uv|^2 \tag{3.11}$$

Harmonic analysis of the model outputs of surface elevation and currents was carried out using 'T_TIDE', a MATLAB toolbox for performing harmonic analysis on combined tidal signals (Pawlowicz et al, 2002). T_TIDE was set-up to separate all of the forcing constituents, as well as M_4, which is a non-linear overtide generated by the self-interaction of M_2. It is the differences between the phase of the semi-diurnal and quarter-diurnal constituents which determine differences between maximum stresses on flood and ebb tides, as well as the differences in velocity direction at these times (Pingree and Griffiths, 1979; Hall and Davies, 2004). Through analysis of the time series output by ROMS, it was possible to extract the mean and peak tidal current velocities at any location within the domain.

The input, computation and output of velocity was on a staggered grid; thus, whenever output model velocities were considered, the u (positive west-east) and v (positive south-north) velocity components were adjusted to be cell-centred. In keeping with the staggered velocity grid, the u and v landmasks were also staggered (and shifted on output) and thus also had to be taken into consideration. For example, the u for a grid centre was found by averaging the two values of east-west velocity on the eastern and western grid sides. Equations 3.12 and 3.13 show how the velocity components were combined and calculated to be at the centre of the grid. The variables u_1, u_2, v_1 and v_2 are the staggered u and v velocity components, respectively; (ii, jj) are the co-ordinates for which the combined and cell-centred velocity is calculated. The $mask_u$, $mask_v$ are the u- and v landmasks, the values being 1 and 0 over water and land points, respectively.

$$U = 0.5 \times [(u_1 \times mask_u(ii-1, jj)) + (u_2 \times mask_u(ii, jj))] \tag{3.12}$$

$$V = 0.5 \times [(v_1 \times mask_v(ii, jj-1)) + (v_2 \times mask_v(ii, jj))] \tag{3.13}$$

and in order to combine the two components to give an absolute magnitude of velocity at the cell centre:

$$UV = \sqrt{(U^2 + V^2)} \tag{3.14}$$

3.4.4 Model calibration

Increasing the domain size did not significantly alter the model outputs, and thus for computational efficiency it was not deemed necessary to use the precise 15°W to 15°E and 45°N to 65°N domain used in previous NWESS modelling studies (e.g Uehara et al, 2006; Neill et al, 2010; Ward et al, 2012). Model runs using the 30 arc second GEBCO bathymetry were compared with runs using 2-minute resolution ETOPO2 Global Relief Model Smith (1997), a freely-available product from the National Geophysical Data Center (2001). See Marks and Smith (2006) for a review of the bathymetric data. It was found that using the GEBCO bathymetry dataset gave the most accurate outputs of modelled tidal elevation amplitudes and phases. The model was run with various minimum water depths and the minimum water depth found to give the most accurate results while maintaining model stability was 10 m and thus this was used for all subsequent runs. The bottom friction coefficient was set to 0.003, found to be the optimum for this set-up (Table 3.2). The model was found to be very sensitive to the values of the surface and bottom control parameters, i.e. to where in the water column the model was set to have higher resolution. A smaller RMSE could be achieved by increasing the resolution at the surface; however for this application higher resolution nearer the seabed was more desirable to resolve the near-bed tidal currents. It was found that it was necessary to increase the value of the drag coefficient and associated BSS when increasing the vertical resolution near the bed (keeping the number of sigma levels constant). The transformation equations of Shchepetkin and McWilliams (2005) were used. Using these parameters, the depth of the lowest vertical layer on the shelf sea (i.e. water depths less than 200 m) remained less than 20 m.

3.4.5 Model validation

The M_2 and S_2 tidal constituents separated using harmonic analysis (T_TIDE) were compared with 10 tide gauges within the UK tide gauge network (National Tidal and Sea Level Facility, 2012), and the results are given in Table 3.3. Data on the N_2 tidal constituent were not available for validation. The nearest model water grid point to the location of each tide gauge was determined; the exact location could not always be considered due to the land/sea mask. The location of the tide gauges is shown in Figure 3.5, and the comparisons between the modelled and observed tidal amplitudes and phases are given. The RMSE in M_2 and S_2 amplitude of 10 cm and 5 cm, respectively, and the RMSE in phase were 10° (M_2) and 8° (S_2). Given the uncertainties associated with the model set-up, such as using model output of Uehara et al (2006) for boundary forcing and errors associ-

ated with the palaeotidal model set-up (Section 3.5), the model was considered to validate well. The focus of this study was on the use of the forcing of Uehara et al (2006) for the palaeotidal model runs, the present-day model set-up being a model optimisation exercise. The accuracy of using various combinations of forcing constituents was investigated, and it was shown that the model performed well when forced with the three dominant tidal constituents for the shelf: M_2, S_2 and N_2.

Figure 3.6 shows the co-tidal charts for the model outputs of the M_2 and S_2 tidal constituents. Further, the outputs were compared with FES2012 (Finite Element Solution) which is the latest data assimilation product of Aviso (2012), available globally at a resolution of 1/16 degree. In reality, significant inundation of land occurs in the Bristol Channel during the flood tide; since this is not accounted for in ROMS due to the lack of wetting and drying, there is a discrepancy in the amount of tidal energy dissipation that occurs, and hence there is significant over-estimation of modelled tidal amplitude in this area. Further, the model parameterisation of the bottom drag may be too low for this region. In reality, the Bristol Channel and Severn Estuary are highly complex and energetic regions that may not be adequately resolved by the (relatively coarse resolution) shelf-scale model. The greatest difference (i.e. largest scatter index) between the FES2012 and simulated elevation amplitudes were in the Bristol Channel and in The Wash (eastern England).

The modelled depth-averaged M_2 current amplitudes and phases were validated using offshore current meter data, presented in Davies and Jones (1990), again using T_TIDE. The RMSE of tidal current speed (average of u and v) amplitudes and phases were 6 cm s^{-1} and 14°, respectively. The modelled tidal current speed validation is shown in Table 3.4 and in Figure 3.7.
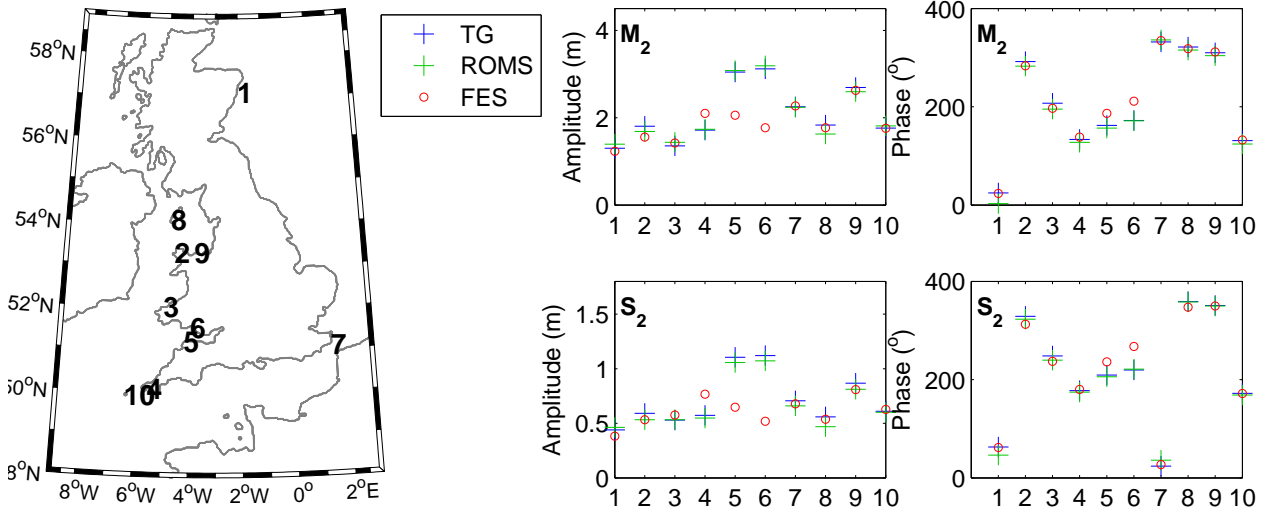
Figure 3.5: Left panel: Tide gauge (TG) locations and numbers, which correspond with the numbers given on the amplitude and phase plots. Modelled (ROMS, green crosses) and observed (tide gauges, blue crosses) amplitudes and phases (M_2 and S_2) at the 10 tide gauges. Also shown are the corresponding amplitudes and phases of the FES2012 product, which was interpolated onto the ROMS grid.

Table 3.3: Observed and modelled amplitudes (h, in metres) and phases (g, in degrees) of the M_2 and S_2 tidal constituents for the 1/24 degree ROMS set-up, using KUTM tidal forcing and GEBCO bathymetry. The amplitudes and phases of the separate tidal constituents were calculated using 'T_TIDE' (Pawlowicz et al, 2002), and the associated amplitude error estimates of the harmonic analysis are also given. Phase errors were all <1°. RMSE=root mean square error and SI=scatter index. The tide gauges are numbered, and the locations are shown in Figure 3.5.

Tide Gauge	Observed				Modelled			
	M_2		S_2		M_2		S_2	
	h	g	h	g	h	g	h	g
Aberdeen (1)	1.30	25	0.44	63	1.39 ± 0.004	3	0.46 ± 0.004	46
Holyhead (2)	1.81	292	0.59	329	1.68 ± 0.006	283	0.53 ± 0.006	323
Fishguard (3)	1.35	207	0.53	248	1.44 ± 0.005	195	0.53 ± 0.006	240
Newlyn (4)	1.72	133	0.57	178	1.73 ± 0.010	128	0.55 ± 0.01	174
Ilfracombe (5)	3.04	162	1.10	209	3.08 ± 0.015	157	1.06 ± 0.015	206
Mumbles (6)	3.12	172	1.12	220	3.19 ± 0.021	171	1.07 ± 0.025	222
Dover (7)	2.25	332	0.71	24	2.24 ± 0.029	336	0.66 ± 0.028	36
Port Erin (8)	1.83	322	0.56	1	1.62 ± 0.010	315	0.47 ± 0.01	2
Llandudno (9)	2.69	310	0.87	351	2.59 ± 0.012	304	0.81 ± 0.012	350
St Mary's (10)	1.76	131	0.61	172	1.81 ± 0.006	124	0.6 ± 0.007	169
RMSE					**0.10**	**10**	**0.05**	**8**
SI (%)					**5**	**5**	**7**	**4**
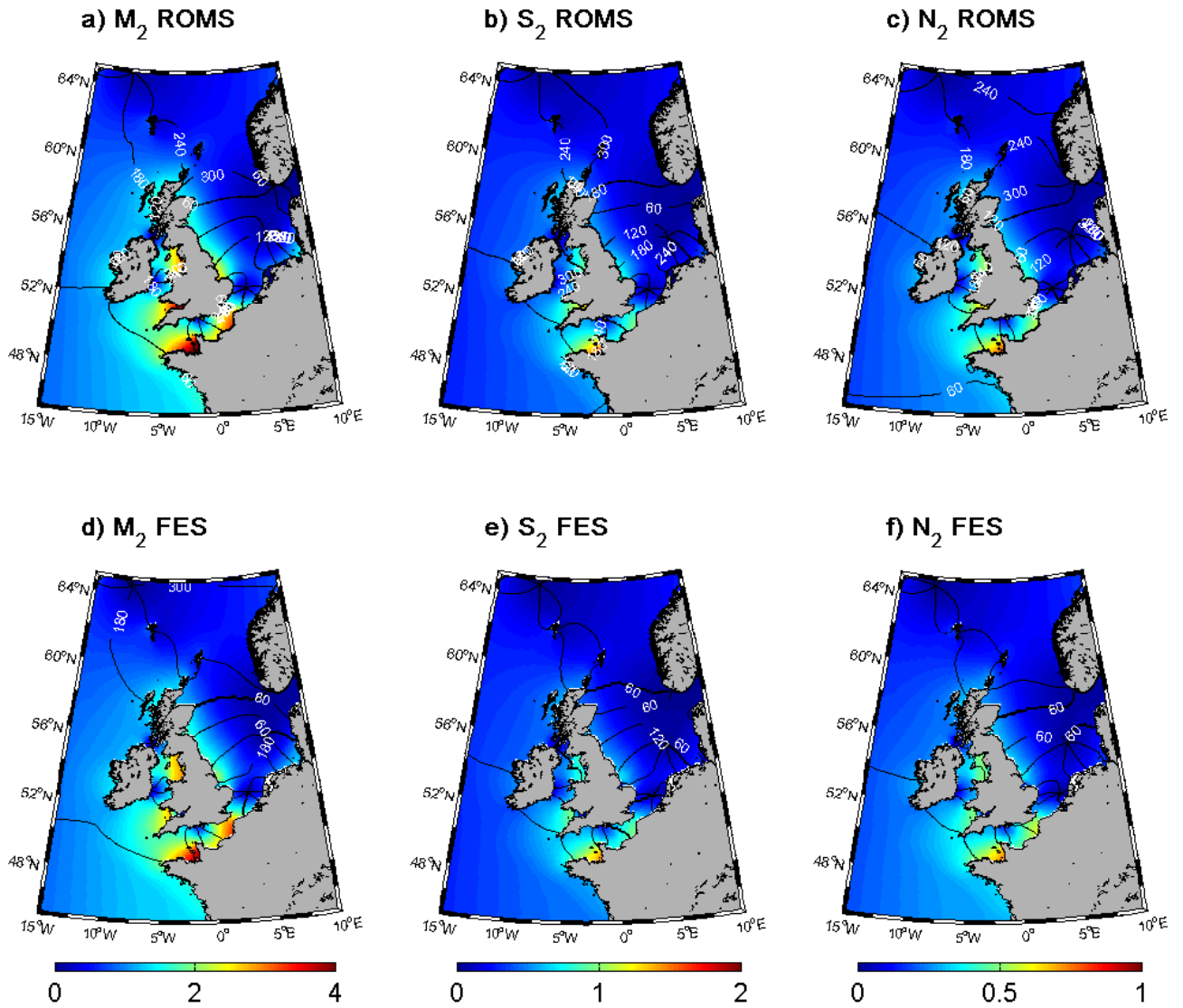
Figure 3.6: Cotidal charts of the M_2, S_2 and N_2 tidal constituents from ROMS (a,b,c) and from FES2012 (d,e,f), respectively. The colour scale denotes the amplitude and the lines indicate the phases, which are plotted at 60° intervals.
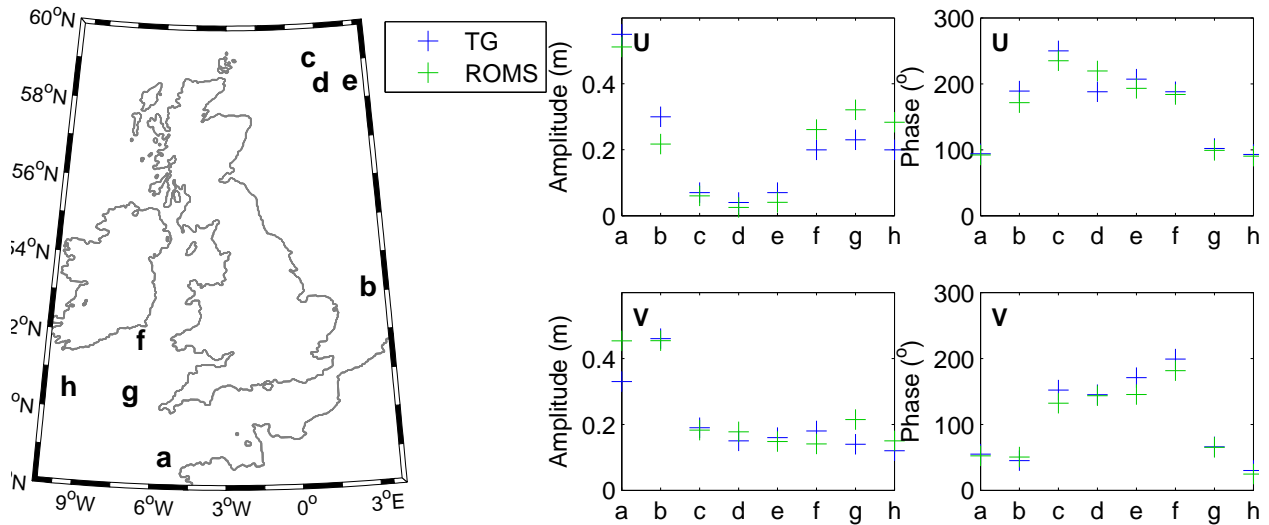
Figure 3.7: Left panel: Offshore tide gauge locations, which correspond with the numbers given on the u and v current amplitude and phase plots. Modelled (ROMS, green crosses) and observed (tide gauges, blue crosses) amplitudes and phases (M_2) at the 8 offshore tide gauges.

Table 3.4: Observed and modelled M_2 current speeds (h=current amplitude, in m s^{-1} and g=phase, in degrees) at offshore tide gauges for the 1/24 degree ROMS model, using KUTM tidal forcing and GEBCO bathymetry. RMSE=root mean square error. The tide gauges locations are shown in Figure 3.7.

Offshore Tide Gauge	Observed				Modelled			
	U		V		U		V	
	h	g	h	g	h	g	h	g
a	0.55	94	0.33	55	0.51	92	0.45	52
b	0.30	189	0.46	45	0.22	171	0.45	50
c	0.07	250	0.19	152	0.06	235	0.18	132
d	0.04	188	0.15	145	0.03	220	0.18	144
e	0.07	207	0.16	171	0.04	193	0.15	146
f	0.20	188	0.18	199	0.26	184	0.14	182
g	0.23	102	0.14	66	0.32	99	0.21	65
h	0.20	93	0.12	30	0.28	90	0.15	25
RMSE					**0.06**	**15**	**0.05**	**13**

3.4.6 High resolution Irish Sea model

A high resolution ROMS model of the Irish Sea was set up for use in Chapter 4. The domain extent was 7°W to 2.7°E and 51°N to 55°N at a resolution of approximately 1/60 degree longitude and 1/100 degree latitude, i.e. approximately 1.1 km grid spacing. Model parameters (e.g. minimum depth, value of bottom drag coefficient, vertical coordinate set-up) and CPP options were unchanged from the shelf-scale runs. As with the shelf-scale model, the Irish Sea simulation was run for 30 days, with two days spin-up time and 28 days of model output analysed. Due to the increased spatial resolution it was necessary to decrease the length of the time step from that used in the shelf model to ensure the Courant-Friedrichs-Lewy condition (CFL, Courant et al, 1928) was not violated. Barotropic and baroclinic time-steps of 2 s and 10 s, respectively, were used. The model was forced at the boundaries using elevations and currents speeds derived from TPXO7.2. As with the other models developed in this study, the forcing tidal constituents were M_2, S_2 and N_2. The validation of the tidal current amplitudes is shown in Table 3.5.

Table 3.5: Observed and modelled amplitudes (h, in metres) and phases (g, in degrees) of the M_2 and S_2 tidal constituents for the 1/60 degree ROMS set-up for the Irish Sea, using tidal forcing from TPXO7.2 and GEBCO bathymetry. The amplitudes and phases of the separate tidal constituents were calculated using 'T_TIDE' (Pawlowicz et al, 2002), and the associated amplitude error estimates of the harmonic analysis are also given. Phase errors were all $<1°$. RMSE=root mean square error and SI=scatter index. The tide gauges are numbered, and the locations are shown in Figure 3.5.

Tide Gauge	Observed				Modelled			
	M_2		S_2		M_2		S_2	
	h	g	h	g	h	g	h	g
Holyhead (2)	1.81	292	0.59	329	1.66 ± 0.007	297	0.58 ± 0.009	331
Fishguard (3)	1.35	207	0.53	248	1.36 ± 0.004	212	0.55 ± 0.004	255
Ilfracombe (5)	3.04	162	1.10	209	3.03 ± 0.012	174	1.07 ± 0.011	221
Mumbles (6)	3.12	172	1.12	220	3.03 ± 0.016	186	1.06 ± 0.018	233
Port Erin (8)	1.83	322	0.56	1	1.54 ± 0.009	329	0.46 ± 0.008	4
Llandudno (9)	2.69	310	0.87	351	2.47 ± 0.010	317	0.83 ± 0.010	356
St Mary's (10)	1.76	131	0.61	172	1.80 ± 0.002	139	0.62 ± 0.002	180
RMSE					**0.15**	**9**	**0.05**	**8**
SI (%)					**7**	**4**	**6**	**4**

3.5   Palaeotidal model development

The new palaeotidal model was developed by incorporating palaeotopographic data and palaeotidal forcing into the present-day regional model (i.e. 15°W to 11°E and 45°N to 65°N, approximate domain size 1200 km x 2220 km). Palaeotopography from the latest GIA model for the region was used, developed by Bradley et al (2011). Further details regarding GIA modelling can be found in Section 2.3.1, and of this specific GIA model in Bradley et al (2011). This new palaeotidal model is referred to here as *ROMS+Bradley*. This tidal model is a significant advancement on the existing palaeotidal models of the region (e.g. Uehara et al, 2006) as it is twice the spatial resolution of Uehara et al (2006), is three-dimensional, as well as incorporating the more recent palaeotopographies of Bradley et al (2011). Furthermore, the output of Uehara et al (2006) is used as model boundary forcing, and hence it is an incremental development on the model presented by Uehara et al (2006).

3.5.1   Palaeotopographic grid generation

The palaeotopography for the region was available for 20°W to 20°E and 40°N to 70°N, at a resolution of 1/12 degree, for 1 ka time slices from 21 ka BP to present. The dataset for the domain of interest was extracted from this more extensive dataset and was linearly interpolated onto the computational grid. Sensitivity tests were conducted using various interpolation methods, e.g. linear and cubic spline, but the difference in final model outputs was not significant. These GIA model outputs of Bradley et al (2011) were incorporated into the model grid by addition to the present-day water depths, thus constructing 22 separate palaeotopographic grids. For example, where the sea level was lower in the past, a negative value of GIA was added to the water depth, since water depths were positive in ROMS. Where the land was depressed by loading of ice sheets, such as under the BIIS and the Fennoscandian Ice Sheet, a positive value of GIA output was added, since this results in a relative sea level increase (to the present-day) in those areas (Figure 3.8). Dynamic changes and spatially-varying patterns of relative sea level were thus accounted for.

By incorporating the GIA model into the bathymetry grid, some regions loaded by former ice sheets were apparently flooded, since the isostatic loading was greater than the global reduction in sea level. Knowledge of the ice sheet extents (British-Irish and Fennoscandian Ice Sheets) was thus needed in order to mask out areas that would have been ice. The ice sheet model used was consistent with that used by Bradley et al (2011),
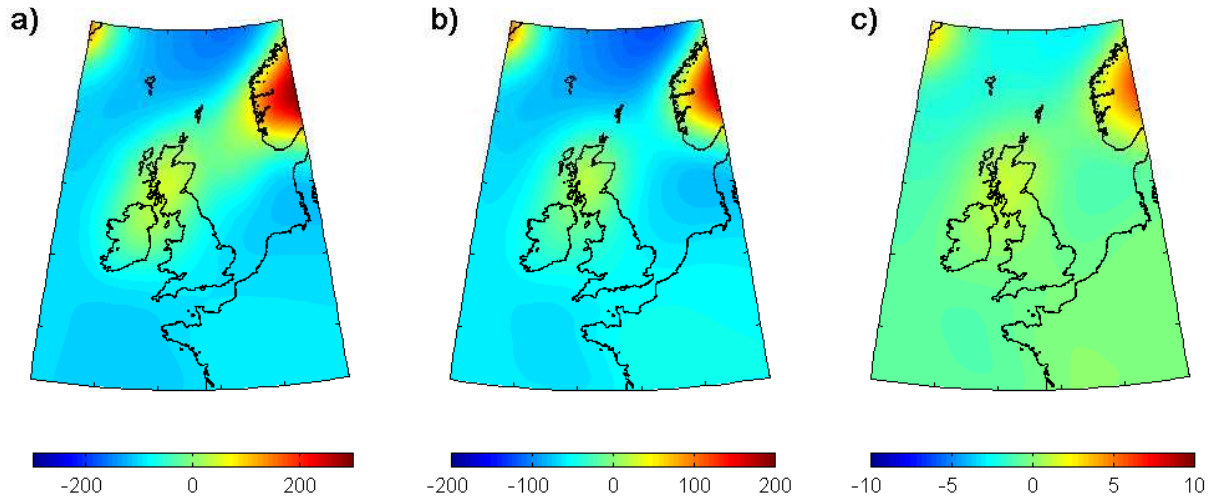
Figure 3.8: GIA model outputs of Bradley et al (2011) for the region, interpolated to the ROMS computational grid. Shown is GIA (metres) from present-day for (a) 21 ka BP, (b) 13 ka BP and (c) 1 ka BP. Note the different colour scales. The present-day coastline is given for reference (black line).

and was developed by Bassett et al (2005). Incorporated into this global model were recent constraints on regional ice by Shennan et al (2006a) and Brooks et al (2008a). This dataset was available at a resolution of half a degree (global) and again, it was necessary to linearly interpolate the regional dataset to the ROMS computational grid.

The areas covered by ice were masked out as land, as for the land/sea mask in the present-day ROMS set-up. Due to the limitations of interpolating the coarse ice model data onto the higher resolution computational grid, the resulting land/sea (or ice-sea) masks were highly unrealistic. For every model time slice where the ice cover extended over water, and hence affected the land/sea mask in the computational grid, only ice thicker than half the thickness of the thinnest ice was used. This removed some of the unrealistic thinning out of ice at the ice sheet margin due to the interpolation. For model stability and for consistency, a minimum water depth of 10 m was used. The various steps of generating the palaeobathymetry grid are outlined in Figure 3.9.

3.5.2 Palaeotidal forcing

It has been shown that for regional tidal modelling studies, it is necessary to consider changes in the ocean tide over time, as described in Section 2.5. Global model outputs of Uehara et al (2006) were used as forcing for the palaeotidal model runs. The palaeotidal
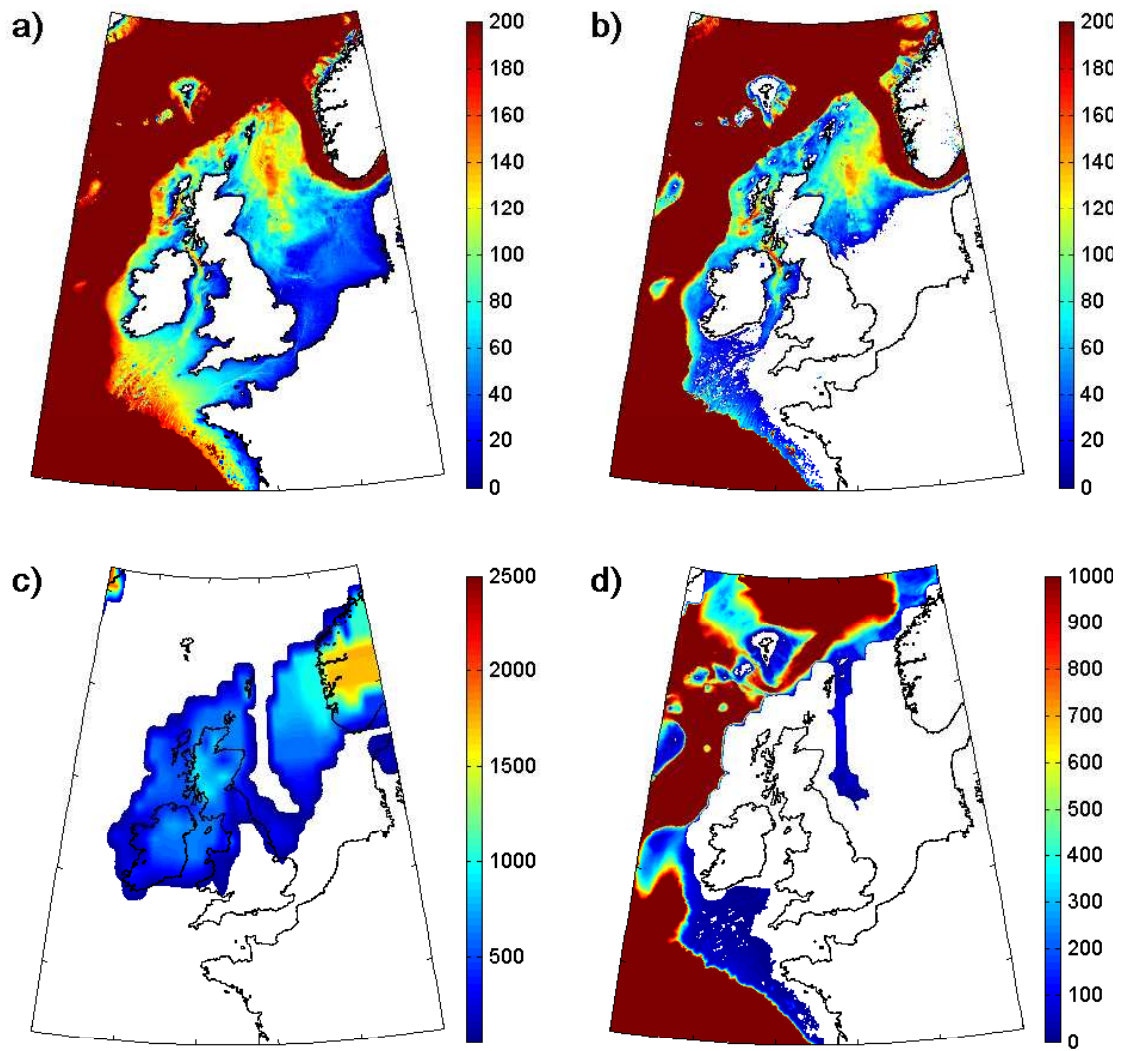
Figure 3.9: The steps used to prepare palaeobathymetry grids for the palaeotidal model. a) Present-day bathymetry (GEBCO), showing positive water depths up to 200 m; b) present-day bathymetry plus the GIA adjustment for 21 ka BP showing glaciated areas as being inundated because of the glacio-isostatic loading; c) the interpolated ice sheet extent and thickness for 21 ka BP, extracted at ice thickness contour 100 m; d) combined present-day bathymetry, GIA model and ice sheet extent for 21 ka BP. Note the varying colour scales.

model was forced with the M_2, S_2 and N_2 constituents, these three being the dominant tidal constituents on the shelf. The palaeotidal model forcing (amplitude, phase and currents) was available at 1/2 degree resolution ($\sim 25 \times 50$ km grid size), and was linearly interpolated onto the computational grid. Any discrepancies in the palaeotidal model land/sea mask and the ROMS mask were not of concern since ROMS reads the forcing from the domain boundaries only. The interpolation of the coarser palaeotidal model outputs onto the higher resolution ROMS grid was thus reasonable.

Before incorporating the forcing for the palaeo time slices, the model was run with the

outputs of the model of Uehara et al (2006) for 0 ka BP, i.e. the present-day, to validate the interpolation of the forcing onto the higher resolution grid. As for the present-day model, the model outputs were validated against the same tide gauge data. The scatter index for M_2 and S_2 amplitudes compared with 10 tide gauges were 5% and 7% respectively, and for phases were 5% and 4% respectively. The present-day 1/2 degree palaeotidal model forcing thus provided comparable fit with observational data as the 1/4 degree TPXO7.2 forcing did.

3.5.3 Additional palaeotidal models

A second ROMS palaeotidal model (*ROMS+Lambeck*) was developed for direct comparison with existing palaeotidal models of Uehara et al (2006) and Neill et al (2010), which are referred to as *KUTM+Lambeck* and *POLCOMS+Lambeck*, respectively. These three models incorporated a revised version of the GIA model of the region developed by Lambeck (1995), which is described in Uehara et al (2006). The two GIA models used are hereafter referred to as Lambeck and Bradley; the differences between these models are described in Section 7.1. For consistency with existing palaeotidal models, *ROMS+Lambeck* was set up at a resolution of 1/12 degree longitude and 1/20 degree latitude, covering 15°W to 15°E and 45°N to 65°N. The palaeotidal forcings were the global model outputs of Uehara et al (2006), the same forcings used in *ROMS+Bradley*. Details of the set-ups of each model are given in Table 3.6.

Table 3.6: Model set-up for the new and existing palaeotidal model simulations.

	Hydrodynamic Model	GIA model	Description	Reference
ROMS+ Bradley	ROMS	Bradley et al (2011)	Three-dimensional, near-bed BSS output, 0-21 ka BP in 1 ka time slices	[new simulations]
ROMS+ Lambeck	ROMS	revised Lambeck (1995)	Three-dimensional, near-bed BSS output, 0-21 ka BP in 1 ka time slices	[new simulations]
KUTM+ Lambeck	POM	revised Lambeck (1995)	Two-dimensional, depth-averaged currents used to compute BSS, 0-21 ka BP in 1 ka time slices	Uehara et al (2006)
POLCOMS+ Lambeck	POLCOMS	revised Lambeck (1995)	Three-dimensional, depth-averaged currents used to compute BSS, available for 0, 6, 8, 10, 12 and 20 ka BP	Neill et al (2010)

4 Relationship between modelled BSS and seabed sediment grain size

Shelf sea sediment motion under the influence of tides, waves and wind-driven currents is a complex phenomenon. Many laboratory and field experiments have been conducted in attempts to understand each contributing process. In the coastal zone, where water is particularly shallow and waves shoal and break, sediment transport tends to be dominated by wave action. Further offshore however, the characteristics of seabed sediment distribution can be indicative of the tidal current conditions of a region.

Various studies have examined the relationship between near-bed hydrodynamics and seabed sediment textures in tidally dominated areas (e.g. Uncles, 1983; Knebel and Poppe, 2000; Signell et al, 2000). Several attempts have been made to link grain size parameters to the magnitude of tidal currents; however, there remains a need to define a first-order relationship between modelled current speed and seabed sediment type. Interpreting bedform geometries (which can be used to infer current conditions) from small diameter core samples is very difficult, thus grain size is the only parameter obtained from the sediment core sections used in this study. Near-bed tidal currents (i.e. currents output from the lowest vertical layer in the model) as well as depth-averaged current speeds are taken into consideration. The focus of the study is the UK sector of the NWESS, due to the availability of digital maps and observational data. These observational data are compared with output from a tidal model of the Irish Sea, where there are large variations in both seabed sediment type and the magnitude of tidal current speeds. In this chapter, an attempt is made to identify which grain size parameter best correlates with modelled tidal current speed (and BSS), i.e. the development of a seabed sediment grain size proxy for tidal currents.

4.1 Seabed sediment on the UK shelf

There is a significant range in seabed sediment classifications on the UK sector of the NWESS (Figure 4.1), including areas of exposed bedrock and patches of semi-consolidated Pleistocene deposits, both covered in places only by thin transient patches of unconsolidated sediment. In the southern Irish Sea, sandy gravel is the predominant sediment type. Coarse sediments of glacial and glaciofluvial origin occupy both Cardigan Bay and St George's Channel. In St George's Channel there are several areas of exposed till, covered only by thin transitory sediment. Along the coast of Cardigan Bay is a belt of mainly sand, which gets muddier towards the mouth of rivers. In the northern Irish Sea, there is a band of gravelly sediment lying to the south and north of the Isle of Man which separates areas of muddy and sandy sediments to the east and west. West of the Isle of Man is a large area of mud, known as the Western Irish Sea Mud Belt, almost entirely surrounded by sandy mud, which itself is surrounded by muddy sand.

The UK seabed sediment have been mapped and made available by the BGS as a 1:250,000 scale digital map product called DigSBS250 (Figure 4.1). The map is based on seabed samples from grabs of the top 0.1 m, combined with core and dredge samples. For sediment classification, the standard Folk triangle was used (Figure 4.2) based on the percentage gravel and the sand:mud ratio (Folk, 1954). A list of the sediment classification abbreviations used in DigSBS250 is shown in Table 4.1. Over the NWESS, sediment distribution by classification is typically patchy, with isolated areas of one category surrounded by another sediment type in some places, and with irregular boundaries between categories; such boundaries are generalisations. The size of these patches vary from a few metres to many kilometres. The DigSBS250 map does not contain data for several areas of the UK sector, such as Morecambe Bay and the north Wales coast. Despite these limitations, the maps show general distribution of sediments in the Irish Sea.

4.2 Seabed sediment data preparation

Data on observed seabed sediment were available from a number of projects, namely HabMap (Robinson et al, 2009), the South West Irish Sea Survey (SWISS, Wilson et al, 2001), the Irish Sea Aggregates Initiative (IMAGIN, Kozachenko et al, 2008), Application of Seabed Acoustic Data in Fish Stocks Assessment and Fishery Performance (ADFISH, Coastal and Marine Research Centre, 2008), and the Joint Nature and Conservation Committee (JNCC, e.g., Blyth-Skyrme et al, 2008). Sediment samples from around the Isle of
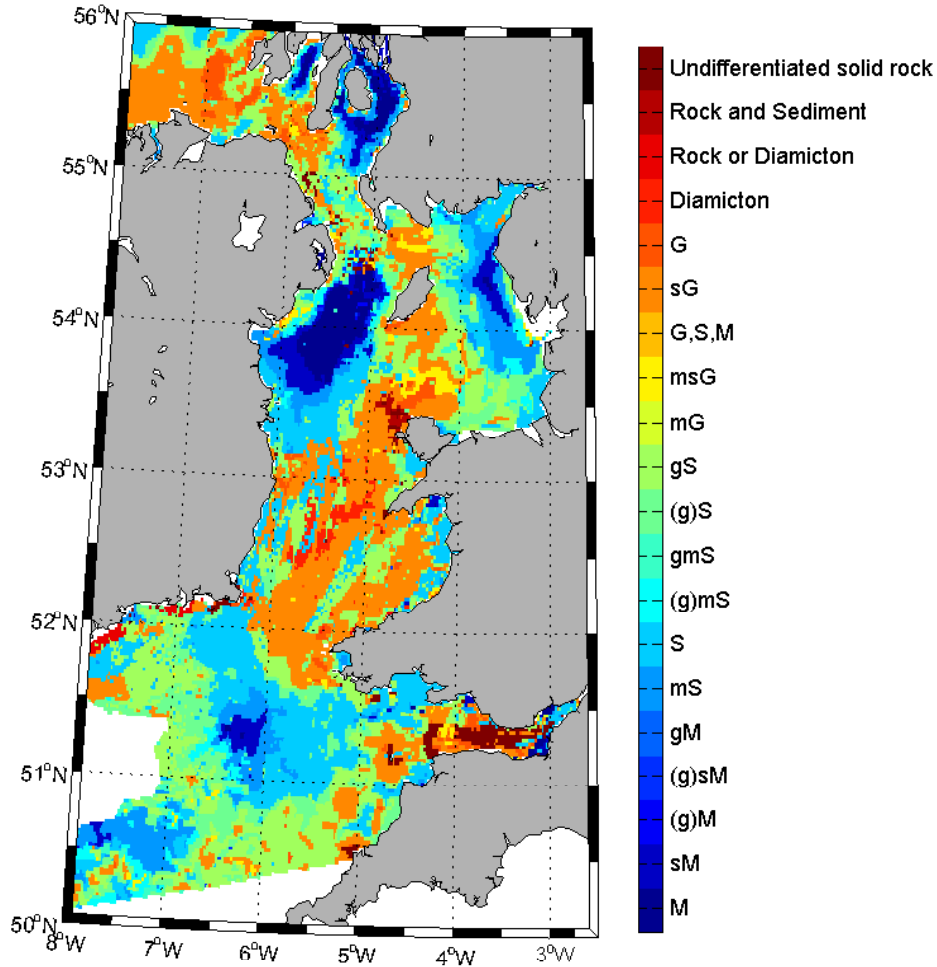
Figure 4.1: Digital map of the seabed sediment of the UK waters in the Irish Sea, taken from DigSBS250. The figure shows the 20 sediment categories used in the digital map, which are identified in Figure 4.2 and detailed in Table 4.1. Grey areas are land and white areas indicate where data are not available.
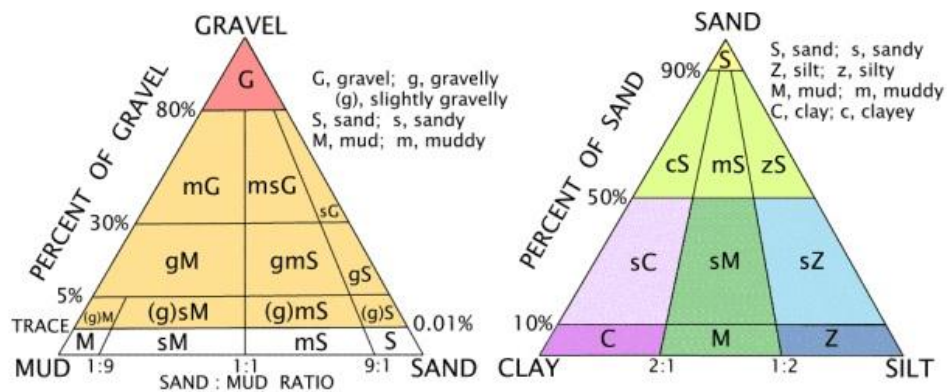
Figure 4.2: Folk ternary diagram (from U.S. Geological Survey, 2013).

Table 4.1: Folk sediment classifications

Folk Class	Abbreviation
Mud	M
Sandy mud	sM
Slightly gravelly mud	(g)M
Slightly gravelly sandy mud	(g)sM
Gravelly mud	gM
Sand	S
Muddy sand	mS
Slightly gravelly sand	(g)S
Slightly gravelly muddy sand	(g)mS
Gravelly muddy sand	gmS
Gravelly sand	gS
Gravel	G
Muddy gravel	mG
Muddy sandy gravel	msG
Sandy gravel	sG

Table 4.2: Wentworth sediment classifications and size ranges

ϕ scale	Size range	Wentworth Class	Folk Class
< -8	> 256 mm	Boulder	
-6 to -8	64-256 mm	Cobble	
-5 to -6	32-63 mm	Very coarse gravel	
-4 to -5	16-32 mm	Coarse gravel	**Gravel**
-3 to -4	8-16 mm	Medium gravel	
-2 to -3	4-8 mm	Fine gravel	
-1 to -2	2-4 mm	Very fine gravel	
0 to -1	1-2 mm	Very coarse sand	
1 to 0	0.5-1 mm	Coarse sand	
2 to 1	0.25-0.5 mm	Medium Sand	**Sand**
3 to 2	125-250 μm	Fine sand	
4 to 3	62.5-125 μm	Very fine sand	
8 to 4	3.90625-62.5 μm	Silt	
<8	<3.90625-1 μm	Clay	**Mud**
<10	<1 μm	Colloid	

Man were collected and analysed as part of work funded by the Isle of Man, Department of Environment, Food and Agriculture (unpublished data).

The combined dataset consists of 1105 samples, ranging in grain size from mud to boulders. The samples were originally collected by grab sampler and were then analysed using wet sieving, and a range of mesh sizes was used between the different data sources. The results of the wet sieving were analysed using the GRADISTAT software (Blott and Pye, 2001) for more detailed analysis of grain size statistics. The granulometric analysis used here for calculating the sample statistics was the graphical method of Folk and Ward (1957). A subset of the data did not include any information on water depth at the sample

location. To ensure that these were not included in the analysis if they were near-shore samples, all samples from locations with water depths ≤ 10 m in the model bathymetry were removed, which was consistent with the minimum water depth set in the model bathymetry grid.
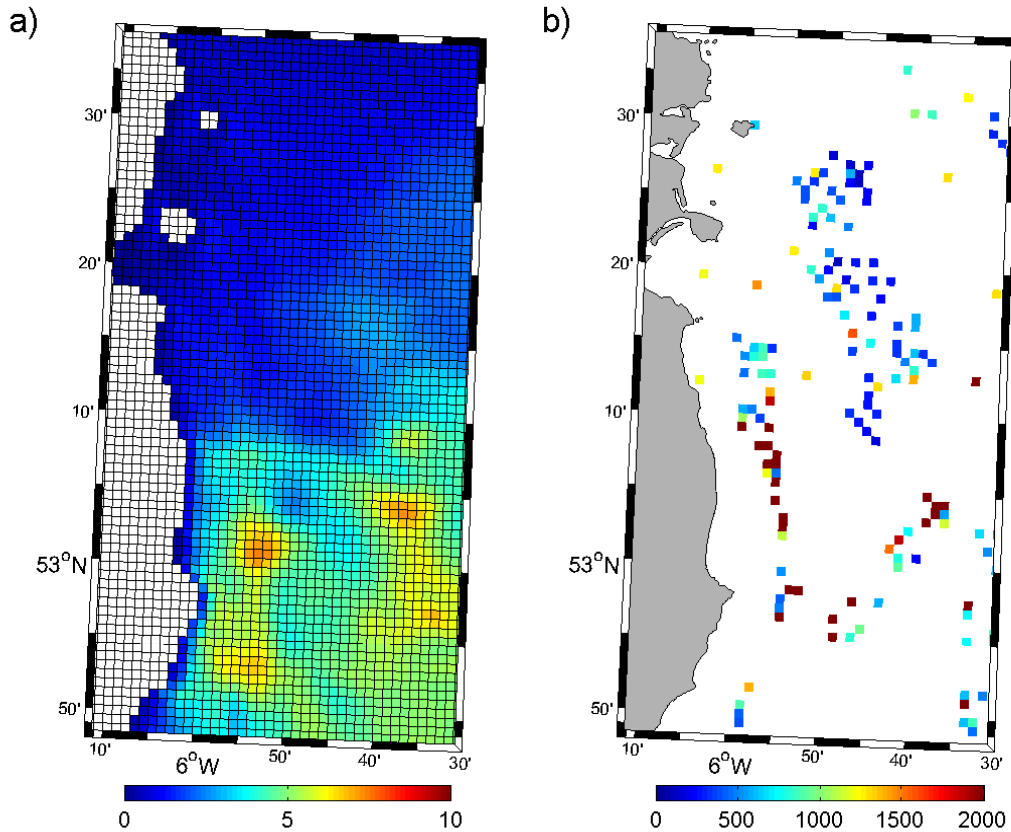
Figure 4.3: a) The computational grid overlaying the model output of BSS on the east coast of Ireland (white areas are land), b) selection of the gridded sediment data for the same area, displaying the median grain size (d_{50}, μm) and grey areas are land.

For comparison with model output, the seabed sediment data were sorted by location and fitted to the computational grid, where each grid cell represented approximately 1 km^2. Samples taken from locations within the same grid cell were combined (Figure 4.3) and the mean, minimum, maximum, and range of various grain size parameters (e.g. d_{50}) were calculated for each grid cell containing data.

4.3   Results: Irish Sea tidal model

A high resolution (approximately 1/60° longitude × 1/100° latitude) tidal model was set up for the Irish Sea using ROMS. The components of the west-east ($\mathbf{u}$) and south-north ($\mathbf{v}$) velocities were output, and these were combined to give an absolute magnitude of the peak current speed. The focus was on the magnitude of the tidal current, i.e. current speed, rather than on the magnitude and direction, i.e. current velocity. More details of the set-up and output are described in Section 3.4.

Various model outputs were considered in the first instance, including depth-averaged and near-bed current speeds and BSS (see Figures 4.4, 4.5 and 4.6). The model was set to use a constant drag coefficient of 0.003 across the entire domain. The near-bed BSS (τ), which is the focus of the 'grain size tidal current proxy' (GSTCP), is computed at the mid-depth of the bottom computational cell, i.e. in the lowest of the 10 vertical layers.

In plots of the model output, areas where the tidal range exceeded the water depth have been masked. Of most interest with regards to sediment transport is peak near-bed BSS, resulting from tidal currents at peak spring tide, and neither the direction of the flow nor the difference between the ebb and the flood tides are considered. While M_2 tidal currents are representative of the peak current for a mean tide, adding together M_2 and S_2 is representative of the peak currents during a spring tide.

4.4   Interpretation: model-data relationship

Deducing which grain size parameter correlates best with the model output was an iterative process. To deduce limitations of the GSTCP, various criteria were investigated and applied to the seabed sediment dataset, including grain size limits and degree of sediment sorting. This process is described in the following section. The total gridded seabed sediment dataset consisted of 718 combined data points (locations shown in Figure 4.7), ranging in grain size between mud and boulders. Figure 4.8 shows the degree of sediment sorting within each model grid cell containing seabed sediment data.

4.4.1   Determining significance of a relationship

The statistical significance of the correlation between the seabed sediment grain size parameter and model output was based on the Pearson product-moment correlation coefficient, r. A value of $r = 0$ indicates no correlation and a value of $+1$ indicates a perfect positive correlation. The correlation coefficient assumes a linear relationship between the two variables
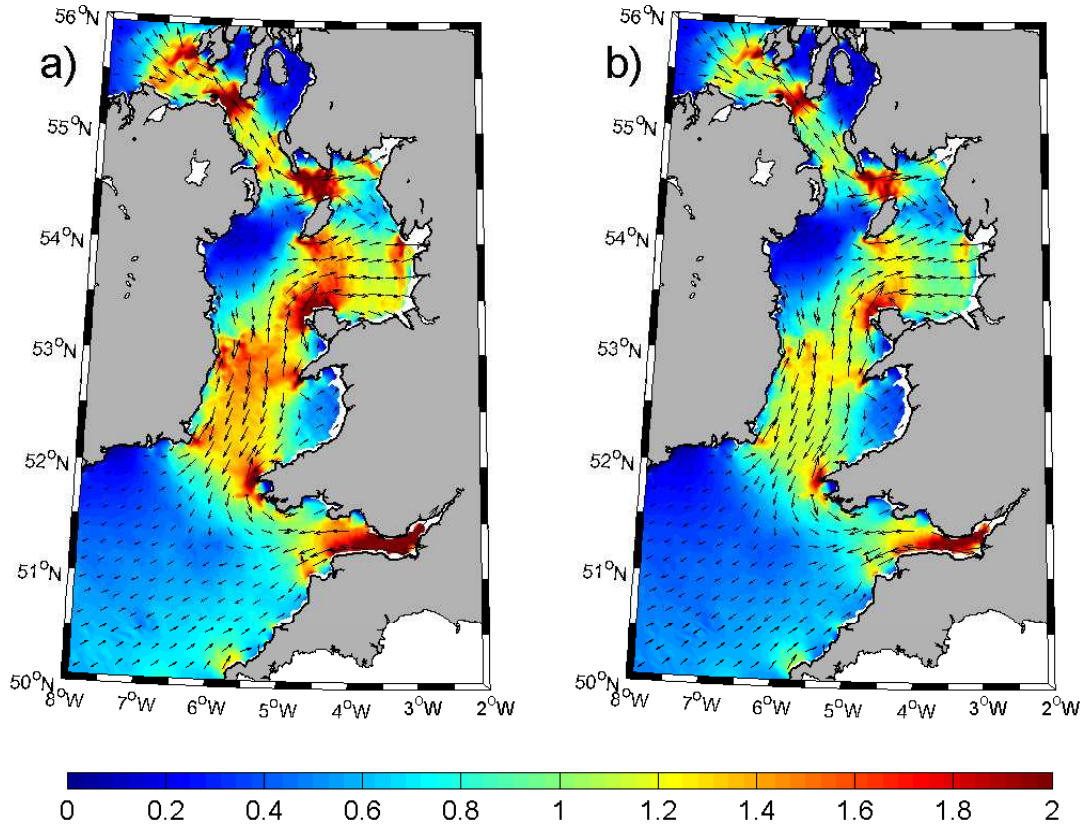
Figure 4.4: Modelled peak ($M_2 + S_2$) tidal currents in the Irish Sea (in m s^{-1}), a) depth-averaged and b) near-bed. Colour scale denotes the current magnitude and vectors denote the direction. Grey areas are land and white areas show additional masked areas.

under consideration, and was initially used to confirm a correlation between grain size and tidal current speed. The significance of a correlation coefficient ('t-test for significance') is dependent upon the sample size, N, and can be calculated as follows:

$$t = \frac{r}{\sqrt{\dfrac{N-2}{1-r^2}}} \tag{4.1}$$

For a relationship to be statistically significant, the value of r must be greater than the critical value for the correlation coefficient for that sample size. A table of critical values by Rohlf and Robert (1936) was used, which presents the calculated critical value for the 5 % and 1 % levels of significance. The correlation between seabed sediment parameter and model output was less significant when d_{90} was considered, or when seabed sediment data were compared with mean tidal current speeds rather than peak current speeds or peak BSS.
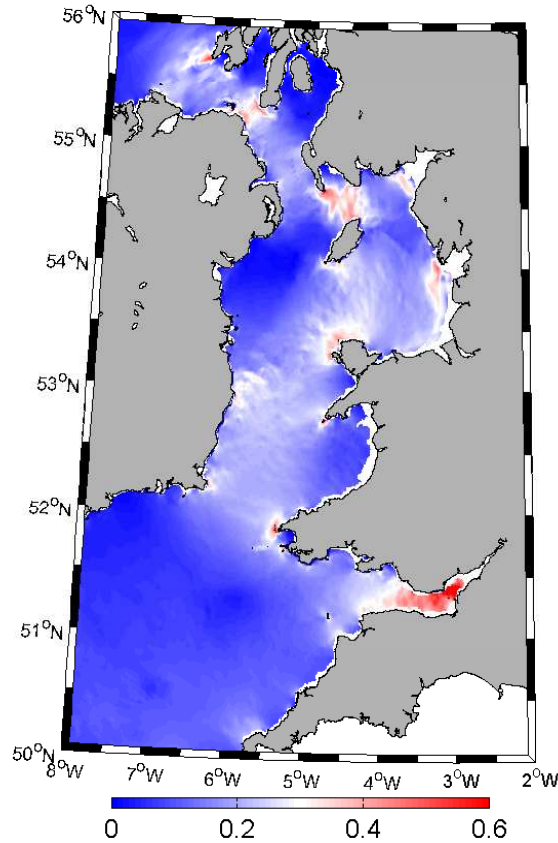
Figure 4.5: Difference between model outputs of depth-averaged and near-bed tidal current speeds, plotted as depth-averaged minus near-bed. Colour scale shows difference in m s^{-1}. Grey areas are land and white areas show additional masked areas.

4.4.2 Considering seabed sediment sample sorting

The first grain size parameter to be considered was sorting since the accuracy of the calculations of median grain size increases with the degree of sorting of a sample. All *extremely poorly sorted*, *very poorly sorted* and *poorly sorted* samples were removed from the seabed sediment dataset. This reduced the sample size considerably, from 718 to 273, consisting of only *moderately sorted*, *moderately well sorted*, *well sorted* and *very well sorted* samples. The *poorly sorted* samples were scattered across the sampling sites (Figure 4.8), with no bias towards any particular region of the Irish Sea. The seabed sediment-current correlation for the remaining 273 samples is displayed in Figure 4.9.

4.4.3 Considering seabed sediment grain size

Consideration of the mean, minimum or maximum d_{50} within each grid containing data did not alter the correlation considerably, but adjusted the value of the y-intercept of the line of best fit which corresponds to the grain sizes at low tidal current speeds.

70
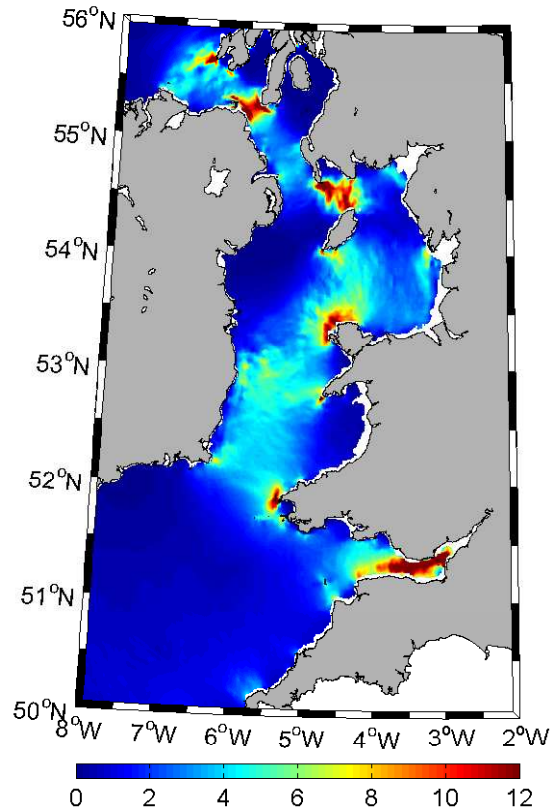
Figure 4.6: Model output of peak near-bed BSS (in N m^{-2}). Grey areas are land and white areas show additional masked areas.

Of the 273 *moderately-* to *very well sorted* samples, 12 had d_{50} >64 mm (larger than pebbles), and only 8 had d_{50} <4 µm (very fine silt). These very fine seabed sediment samples were randomly distributed, on the north coast of the Lleyn Peninsula, in the western Irish Sea and north west of Anglesey. There was no significant seabed sediment-current correlation when these very coarse and very fine sediments were included; they were so few that they appeared as outliers. These 20 samples were removed from the dataset, and hence the remaining 256 seabed sediment samples were all finer than gravel and coarser than clay.

Fourteen significant outliers remained which were fine sands (or finer) found in areas containing high tidal current speeds. Specifically these were in the Bristol Channel and off the north coast of Pembrokeshire, where modelled BSS were >10 N m^{-2} (see Section 4.5.1 for further discussion). Removing these samples improved the seabed sediment-current correlation considerably and decreased the value of the y-intercept, from a medium sand to a fine sand. The correlation between the set of 242 seabed sediment samples was >0.6 for each of the model outputs considered, as shown in Figure 4.10. For N=242 critical values for the 5 % and 1 % correlation coefficients were 0.181 and 0.138, respectively,
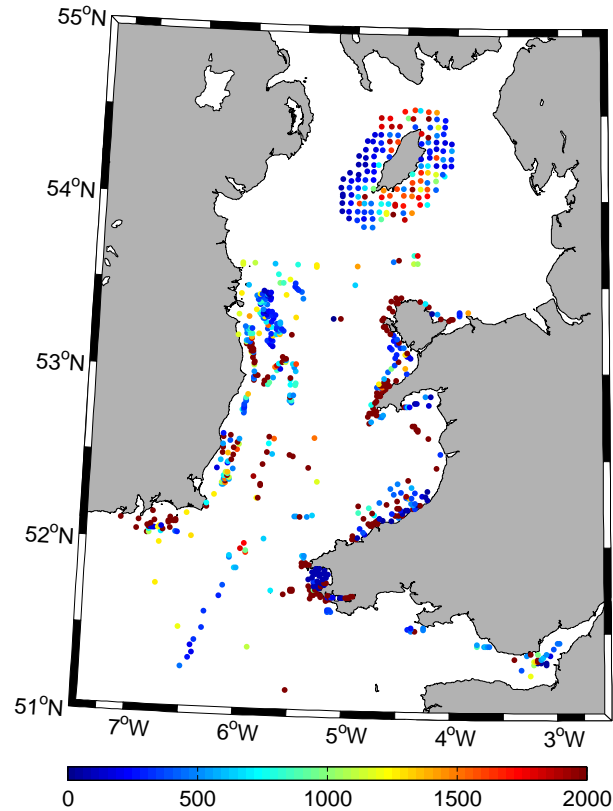
Figure 4.7: Gridded averaged median grain size, d_{50} (µm), of all seabed sediment samples within any one computational grid cell. Grey areas are land.

hence these correlations were significant. All of the subset of 242 gridded seabed sediment samples (shown in Figure 4.11) were from water depths between 10 and 100 m. Almost half of the samples (118) were from water of 10-15 m depth and 216 of the samples were taken in water shallower than 50 m.

4.5 Results: grain size tidal current proxy (GSTCP)

To quantify the relationship between the sediment grain size and the magnitude of the tidal current speed, the squared and cubed tidal current speeds (proportional to the BSS and sediment transport, respectively), as well the model outputs of BSS were considered in the first instance. No significant difference in the pattern of predicted grain size was found using the various model output, thus only the results for the near-bed BSS are presented and were used to develop the GSTCP. There was a clear positive correlation between BSS and seabed sediment grain size when the median grain size was considered (Figure 4.10). This relationship was not clearly linear in nature, as expected from the characteristics of the Shields curve (Figure 2.11), which describes the non-linear variation in the threshold of motion of sediments between currents (and/or waves), or the Hjulström
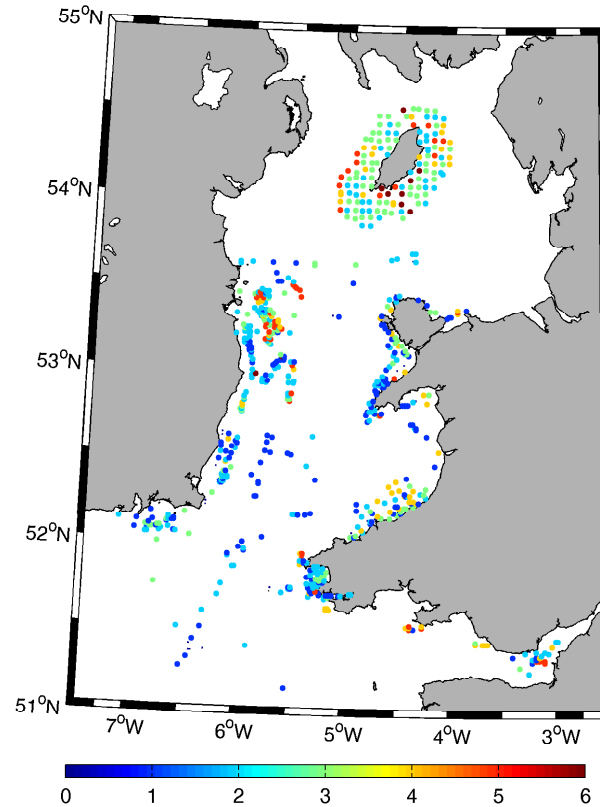
Figure 4.8: Variation in the degree of sorting of the gridded sediments data, a variable output by the GRADISTAT software. The numbered colour scale represents the following: 0 = *extremely poorly sorted*, 1 = *very poorly sorted*, 2 = *poorly sorted*, 3 = *moderately sorted*, 4 = *moderately well sorted*, 5 = *well sorted*, 6 = *very well sorted*. Grey areas are land.
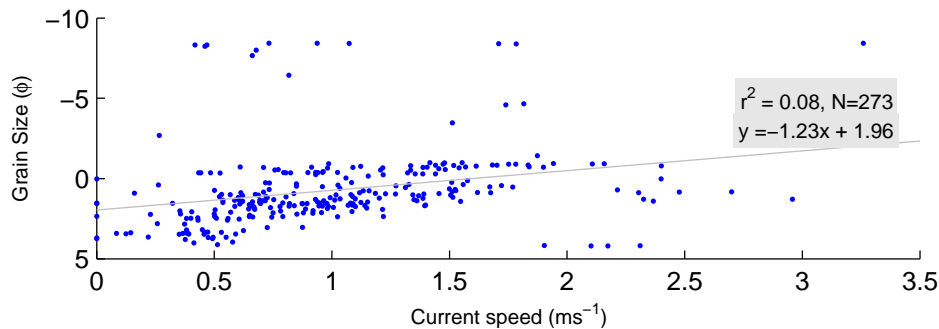
Figure 4.9: Correlation between mean d_{50} (in ɸ to show the large size range) and depth-averaged peak tidal current speed for seabed sediment samples that were *moderately well sorted* and higher. The text indicates the correlation (r^2), the equation of the line of best fit (y) and the number of gridded seabed sediment samples considered (N). The critical correlation coefficient for 273 samples is $r = 0.138$ ($r^2 = 0.02$) and $r = 0.181$ ($r^2 = 0.03$) for the 5 % and 1 % coefficients, respectively.

curve (Hjulstrom, 1935), which describes erosion, deposition or transport of sediment in rivers (i.e. uni-directional flows).
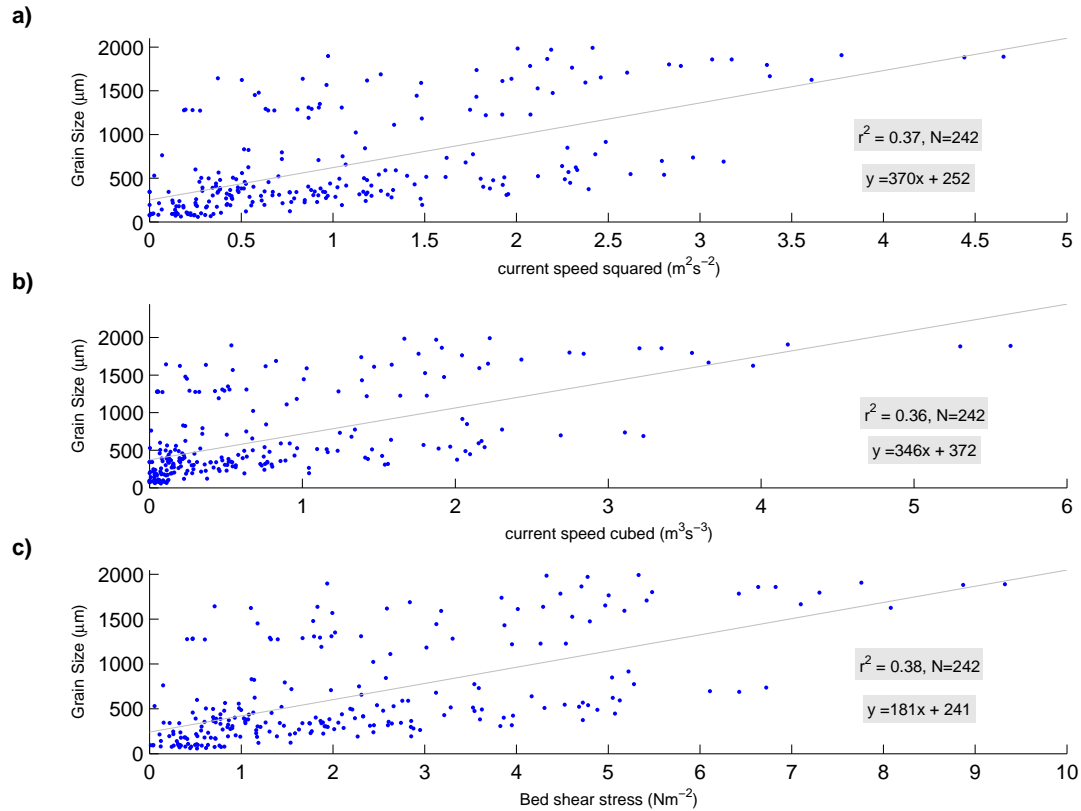
Figure 4.10: Correlation between gridded seabed sediment samples (mean d_{50} in µm) and ROMS tidal model output: a) depth-average tidal current speed cubed, b) near-bed current speed cubed, c) near-bed BSS. Samples removed from this dataset included those that were less well sorted than *moderately sorted*, very fine samples ($<$63 µm) in areas of very strong tidal currents and samples from areas with BSS $>$10 N m^{-2}.

To quantify the relationship between BSS and observed grain size, the model outputs of peak BSS were binned into a range of very low through to high BSS; specifically 0-0.5, 0.5-1, 1-1.5, 1.5-2, 2.5-3, 3-4, 4-5, 5-8 and 8-10 N m^{-2}. The observed d_{50} from the model grid cells with BSS within each range were combined and plotted against the corresponding mid-point of the BSS range (Figure 4.12a). The minimum and maximum of the gridded median d_{50} were also noted for each of the BSS ranges, and are also shown in Figure 4.12a.

A number of sediment classes from the Wentworth scale (Table 4.2) were considered, namely very fine sand and mud ($<$125 µm), fine sand (125-250 µm), medium sand (250-500 µm), coarse sand (500-1000 µm), very coarse sand (1000-2000 µm) and gravel ($>$2000 µm). The BSS ranges in which observations of these sediment classes were recorded are shown in Figure 4.12b. For example, for all model grid cells with BSS between 0.6 and 3.2 N m^{-2} the seabed sediment sediment predicted by the GSTCP was medium sand (250-500 µm). The values used in the GSTCP are given in Table 4.3. These seabed sediment size ranges have been applied to the Irish Sea tidal model output of BSS, thus developing a
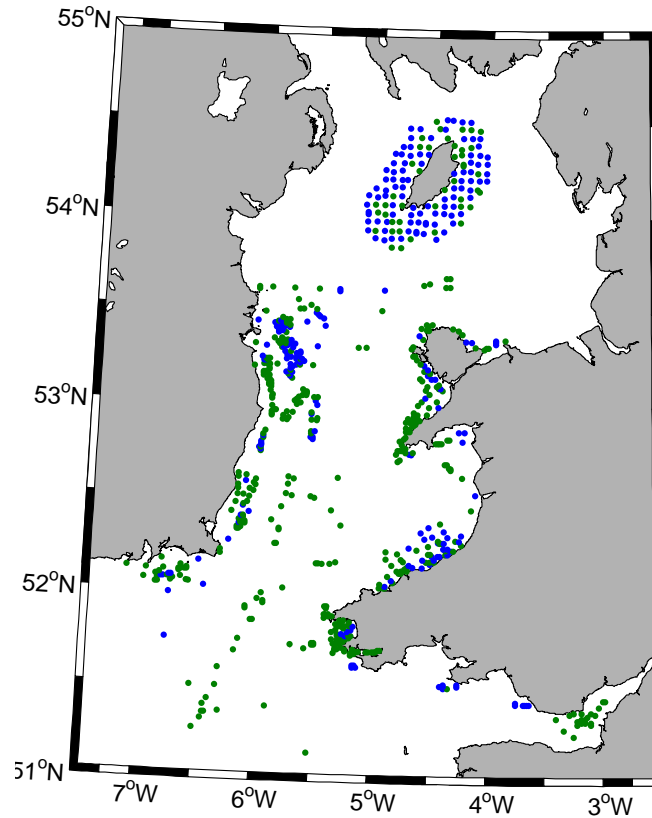
Figure 4.11: Distribution of gridded seabed sediment samples: blue = 242 samples remaining after application of the various selection criteria, green = 476 samples removed.

method for predicting sediment classification for specific modelled BSS values, as presented in Figure 4.13, and a reduced version of the DigSBS250 map is given for comparison (Figure 4.14).

Table 4.3: Details of the GSTCP

Modelled BSS range (N m^{-2})	GSTCP grain size range (μm)	GSTCP sediment classification
<0.25	<125	very fine sand and mud
0.25 - 0.6	125 - 250	fine sand
0.6 - 3.2	250 - 500	medium sand
3.2 - 4.1	500 - 1000	coarse sand
4.1 - 9	1000 - 2000	very coarse sand
>9	>2000	gravel
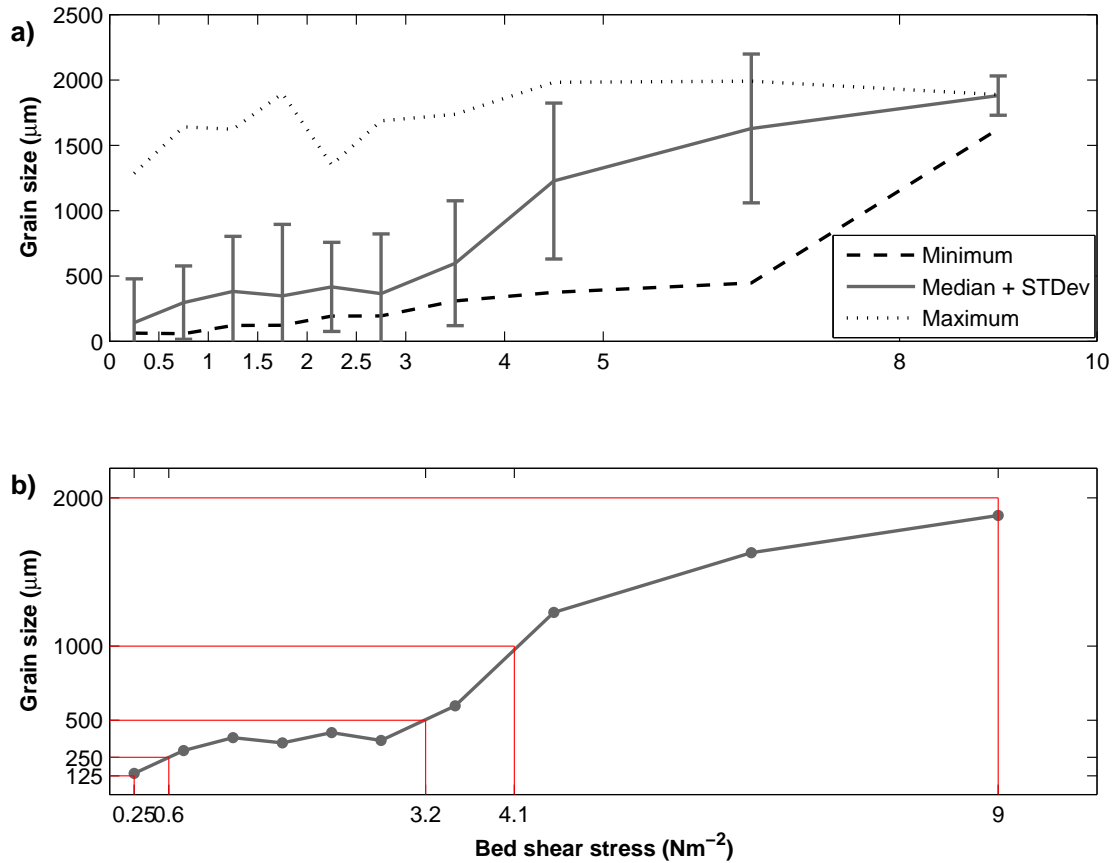
Figure 4.12: a) Median d_{50} and associated standard deviations of observed seabed sediment samples within specified ranges of modelled BSS (grey line), plotted at the mid-point of the BSS range (shown on the x-axis). The minimum and maximum gridded median grain sizes are also given (dashed and dotted black lines, respectively). b) The red lines on the median grain size curve indicate the range of BSS for the different sediment classifications (shown on the y-axis), the BSS range values are given on the x-axis. The sample sorting and grain size selection criteria have been applied to these data.
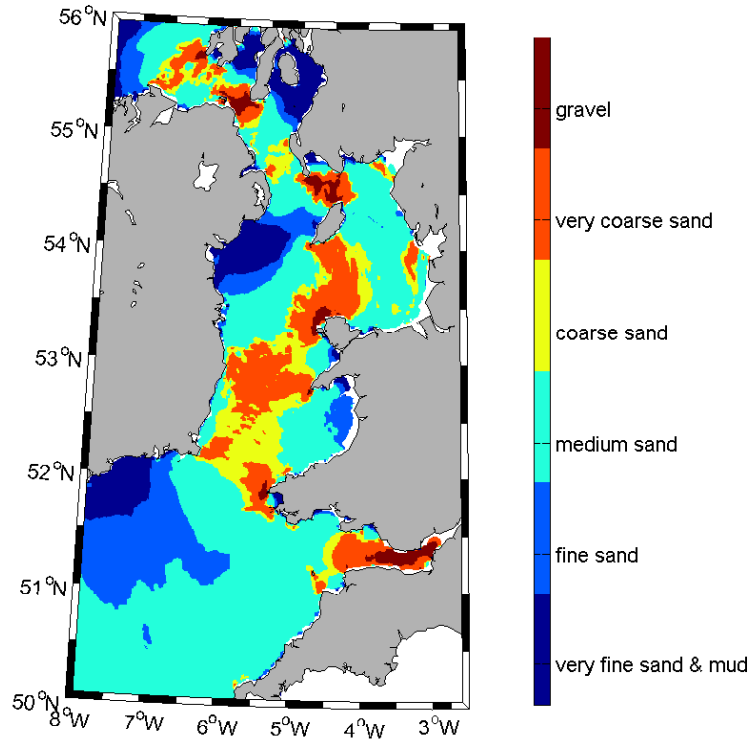
Figure 4.13: Irish Sea seabed sediment distribution predicted by the GSTCP, using modelled near-bed BSS.
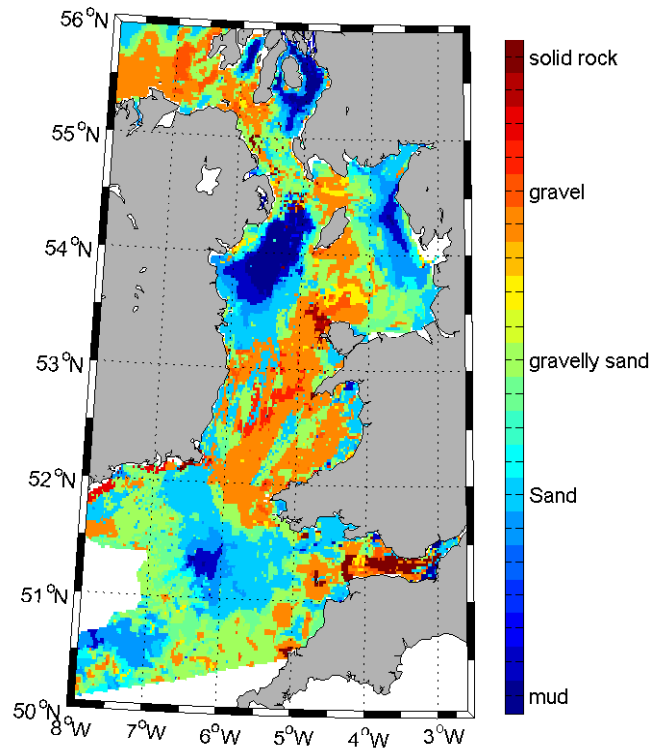
Figure 4.14: Seabed sediment from DigSBS250, for comparison with Figure 4.13. Only selected grain size classifications are identified on the colour scale, which indicates a general coarsening of seabed sediment from blue to red.

4.5.1   Validating the GSTCP

It was necessary to be selective with the seabed sediment data used to develop the proxy. All seabed sediment samples taken in the shallow near-shore were omitted in the first instance, due to the tendency of such areas to be wave-dominated. When poorly-sorted seabed sediment samples were retained in the dataset, the relationship was unrealistic due to the erroneously high d_{50} of mixed (bimodal) sediment samples. It was not possible to resolve such poorly-sorted samples and hence they were removed from the dataset. Further, it was important to remove the fine-grained samples in the Bristol Channel from the seabed sediment-current correlation. This area is highly energetic and it is likely such samples are either a result of a local fine-grained sediment source or are highly cohesive and thus resistant to current-induced sediment transport, as demonstrated in the values of the threshold of motion in the Shields curve (Figure 2.11). Harris and Collins (1991) concluded that in the Bristol Channel, there is no simple correlation between the direction of maximum BSS and bed load transport, particularly in near-shore regions. In the Bristol Channel, large spatial variations in tidal asymmetry occur along the length of the channel with both convergences and divergences along its length (Harris and Collins, 1991; Neill et al, 2009a). The focus of the study by Harris and Collins (1991) was on M_2 and M_4 tidal constituents and the numerical model output suggested dominant ebb-direction sand transport along the central axis of the estuary, with flood-directed transport within narrow in-shore zones, i.e. 'mutually evasive'. Harris and Collins (1991) questioned the use of peak BSS vectors as indicators of net bed load transport, since in some in-shore areas it is the mean stress which is important due to interactions between the tidal wave and local geometry. An attempt was made to account for this by eliminating near-shore (<10 m deep) regions.

The GSTCP did not fully resolve the extent of the Western Irish Sea Mud Belt. This is the main area where there was an over-predication of seabed sediment classification by the proxy. The proxy did not predict some of the isolated patches of gravel, such as northeast of Anglesey, and in the North Channel. The actual seabed sediment sediments south of Ireland are coarser than the very fine sand and mud predicted by the proxy, as indicated by the red patch south of Ireland in Figure 4.14. There was particularly poor fit between observed seabed sediment classifications and predicted grain sizes south of Ireland (Figure 4.13) and hence confidence in the results of the GSTCP for this area is low. Although the model output for this region does not display strong tidal currents, in reality it is influenced considerably by wave action (e.g. Neill and Hashemi, 2013).

Cardigan Bay (west coast of mid Wales) is also strongly affected by wave action (e.g. Neill and Hashemi, 2013) and hence the GSTCP under-predicts the grain size, as the modelled peak tidal current speeds in this area are not high. The area of mud in the western Irish Sea corresponds with low tidal current speeds, suggesting this accumulation is strongly controlled by low hydrodynamic energy. However, other factors likely influence this muddy area, since the upper few metres of seabed sediment appear to date back several thousand years (e.g. Kershaw, 1986). It is thus not accurate to assume these sediments have accumulated as a direct result of the present-day hydrodynamic regime, which could account for the discrepancy in the predicted and observed seabed sediment in this area. There is a narrow band of sandy sediment between the Cumbrian coast and the eastern mud belt which has been identified by Pantin (1991) as having formed at a lower sea level, but remains exposed due to wave action preventing later deposition. The grain size in the area of the mud belt east of the Isle of Man is over-predicted by the GSTCP and is defined as fine sand.
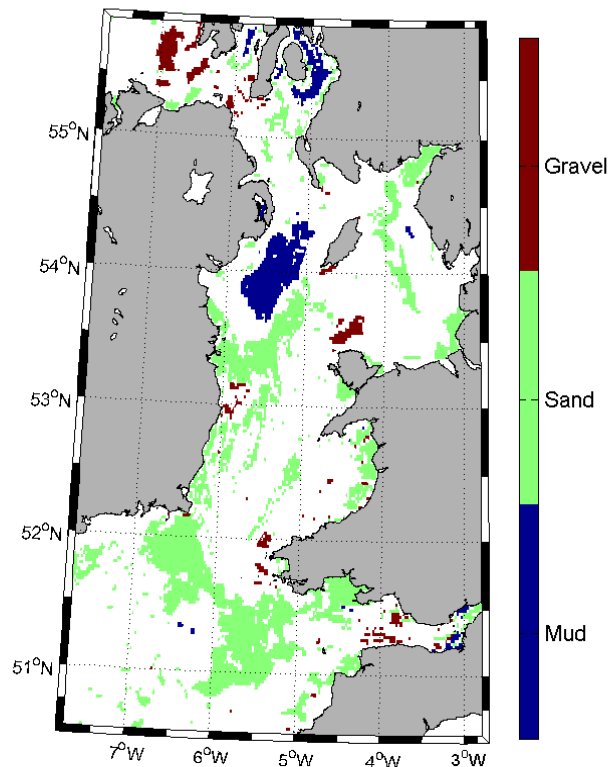
Figure 4.15: Selected seabed sediment classes from DigSBS250 for comparison with the sediment classes predicted by the GSTCP (Figure 4.13). Only mud (blue), sand (green) and gravel (red) are shown, mixed sediment classifications are white.

An attempt was made at a more quantitative validation of the GSTCP, a significant constraint being the difficulty of estimating a median grain size of Folk sediment classifi-
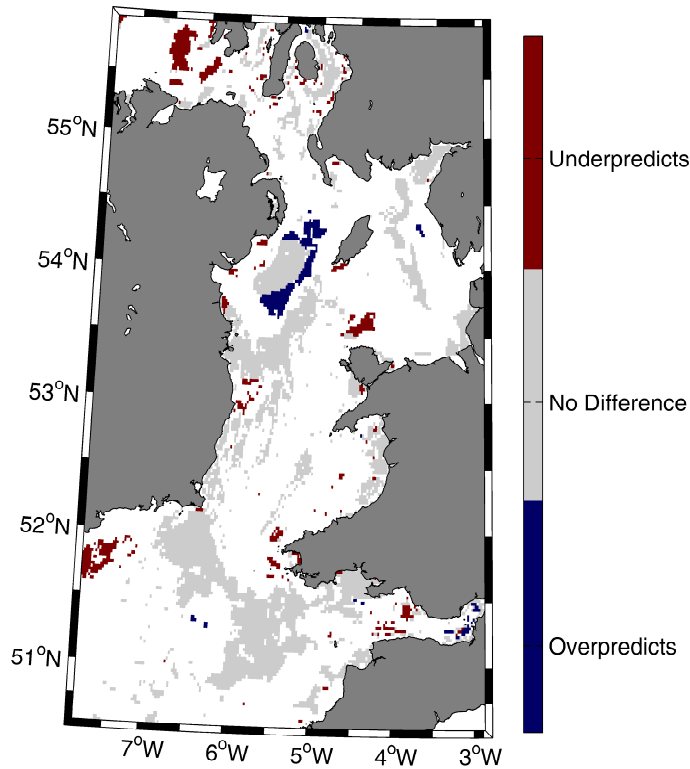
Figure 4.16: Difference between the observed and estimated grain size classifications, plotted as the observed minus the estimated. The white areas indicate where seabed sediment was classified as mixed or where there was no seabed sediment data, the light grey areas show areas of agreement between estimated and observed sediment classifications. The red and blue areas indicate where the GSTCP under- and over-estimate the seabed sediment classification, respectively.

cations. To this end, a quantitative assessment is made by comparing only the mapped areas of mud, sand and gravel from the DigSBS250 (Figure 4.15) with the mud, sand and gravel regions predicted by the proxy, rather than considering mixed samples. The fine, medium and coarse sands predicted by the GSTCP were combined and simply classified as sands. The predicted very fine sand and muds (grain size <125 μm) were classified as mud. Predicted grain sizes >2000 μm are shown to be gravel. The spatial differences in areas of mud, sand and gravel are shown in Figure 4.16. The white areas in Figure 4.16 show areas where either the seabed sediment in the DigSBS250 was mixed, or where the predicted and observed seabed sediment classification were in agreement. The red and blue patches indicate where the GSTCP is under- and over-estimating the seabed sediment grain size, respectively. The differences in the predicted and observed seabed sediment classification were only between mud and sand, or sand and gravel, and not between gravel and mud.

This attempt at quantifying the accuracy of the proxy also has limitations, by excluding mixed seabed sediment sediments. For example, the Eastern Irish Sea Mud Belt, east of

the Isle of Man, is comprised of fine mixed sediments (such as sandy mud), the latter is omitted from the comparison and hence the proxy over-prediction of the grain size in this area (medium sand) is not highlighted in the proxy validation. Although tidal asymmetry is not accounted for within the GSTCP, there is no correlation between modelled regions of BSS convergence and divergence and regions where there were discrepancies between observed and predicted grain sizes.

4.6 Limitations of the GSTCP

Several key limitations and assumptions of the GSTCP include:

- **Tidal currents only:** the GSTCP assumes tidal current-induced sediment transport only and does not account for wave action (which is particularly high during storm events), nor wave-current interaction. Further, other sediment transport mechanisms including fluvial processes, wind drift, storm-surge currents, biological mechanisms, gravitational currents and eddy-diffusive transport of suspended sediment are not considered. On regional scales such as the NWESS, the dominant influence on sediment transport is the tide; however, in shallower, in-shore regions, wave action becomes more important than tidal-induced currents for transporting sediments, hence areas with water depths less than 10 m were omitted from the proxy.

- **Sediment source:** at no point are the sediment sources in the Irish Sea identified or considered, a potential source of error when comparing the output of the GSTCP with the DigSBS250 map. Winnowing and sediment sorting could, for example, deposit coarser sediments in tidally quiescent areas and hence the GSTCP would underestimate the grain size in such regions. These samples tend to be poorly-sorted, and are likely to be of glacial origin.

- **Bedforms:** the tidal model assumes a constant drag coefficient (0.003) and does not take into account spatially-varying seabed texture, grain roughness or bedforms (e.g. upstanding rock outcrops in mud belts).

- **Cohesive and mixed sediments:** the GSTCP does not resolve cohesive or mixed sediment classifications.

- **Peak tidal currents:** the model outputs considered are the peak tidal currents identified during a spring-neap cycle. In reality, strong mean currents in varying directions might produce little or no net sediment transport.

- **Gravitational settling:** this is not taken into account, but can have a consider-able effect in some areas, whereby deeper areas tend to receive more fine sediments winnowed from shallower areas.

4.7   Recommendations for improving the GSTCP

- Coupled tide and wave modelling would increase the accuracy of the GSTCP by considering wave-induced sediment transport. This would omit the need to remove regions likely to be dominated by wave action, which in this case were defined as model grid cells with water depths <10 m.

- The GSTCP would be improved by having more observed seabed sediment data, with better spatial coverage of the Irish Sea, and from a greater range of water depths. In the dataset used here, there are clusters of samples and hence some grid cells contained a combined dataset of seabed sediment samples. Further, almost 90 % of the samples were taken in water <50 m deep.

- A higher resolution tidal model would decrease the need for combining clustered seabed sediment sample data, and would better-resolve spatial variations in peak BSS.

4.8   Summary points

- The aim was to develop a first-order proxy for seabed sediment classification (grain size tidal current proxy, GSTCP) using tidal model output. The model output used in the proxy is the tidal-induced near-bed BSS from a tidal model of the Irish Sea ($M_2 + S_2 + N_2$).

- The DigSBS250 map of the Irish Sea was interpreted for comparison with the grain sizes predicted by the proxy. The GSTCP is able to identify the main areas of coarse sediments in regions of stronger peak tidal currents speeds (and hence high BSS). Since net sediment transport is not always in the same direction as the mass transport of water, a GSTCP for model output of near-bed tidal current speeds is preferable over a proxy for depth-averaged currents.

- A number of recommendations are made for future work on the GSTCP, including coupled tide and wave modelling, for consideration of wave-induce bed sediment transport.

5 Marine sediment core data

Five marine vibrocores were investigated in this study, all of which were collected and curated by the BGS. The cores are referred to as BGS19, BGS65, BGS87, BGS166 and BGS199, and details of the cores are given in Table 5.1. In this chapter, basic lithostratigraphic logs of the five BGS cores are given. Each of the cores was sampled and particle size analysis (PSA, Section 5.1) was carried out using laser particle diffractometry, and a number of subsamples was used for radiocarbon dating (Section 5.2). BGS199 had an existing age-depth model, developed by Austin and Scourse (1997) and Scourse et al (2002). The age-depth models constructed from the corrected, calibrated radiocarbon (^{14}C) dates are shown in Section 5.3, along with the grain size profiles plotted against age.

Table 5.1: Details of the five BGS vibrocores.

BGS core ID	Latitude	Longitude	Water Depth (m)	Collection date	Length (m)	Units (* = core top unit)
+54/-05/19	54°42.80′N	−4°05.60′E	26	09/06/1969	6.10	A-H*
+54/-05/65	54°30.74′N	−4°00.08′E	48	10/06/1969	6.10	A-H*
+53/-06/87	53°44.11′N	−5°11.95′E	72	11/11/1980	5.93	A*-F
+56/-09/166	56°52.46′N	−4°00.08′E	131	11/11/1985	3.71	A*-D
+51/-07/199	51°21.23′N	−8°01.98′E	118	08/09/1982	5.68	A*-F

Prior to the sampling for this work, each of the cores had been split length-ways, and halved lengths of the cores were available for sampling, stored in the original plastic coring tubes (of internal diameter 8 cm) which were inserted into plastic sleeves for storage. With the exception of BGS166, which was still moist, the cores were dry at the time of sampling. Each of the cores had been divided into units, which were labelled alphabetically and varied in length between approximately 0.6 and 1 m.

The five core sites (locations of which are shown in Figure 5.1) were selected by us-
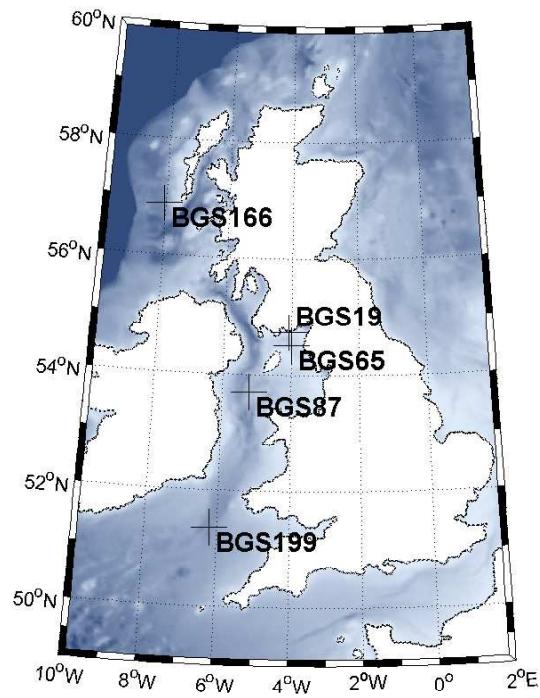
Figure 5.1: Locations of the five BGS vibrocores.

ing existing palaeotidal model output of Uehara et al (2006) to identify regions of the NWESS which displayed significant net change in BSS over the past 21 ka. The grain size profiles and age-depth models were developed for the purpose of model-data comparison (Chapter 5), i.e. comparing the GSTCP (developed in Chapter 4 and applied to the grain size profiles) with the evolution of tidal-induced BSS since the LGM at the core sites (Chapter 7).

5.0.1 Lithostratigraphy: vibrocore +54/-05/19 (BGS19)

BGS19 displayed a general coarsening-upwards sequence, from uniform mud at the base to muddy fine sand at the core top. Shell fragments and bivalves were present throughout the core. There were indications of bioturbation within the lowest metre section. The core was very fragmented between ~5.1 and 4.4 m and several gaps of up to 10 cm were present, which are indicated on Figure 5.2.
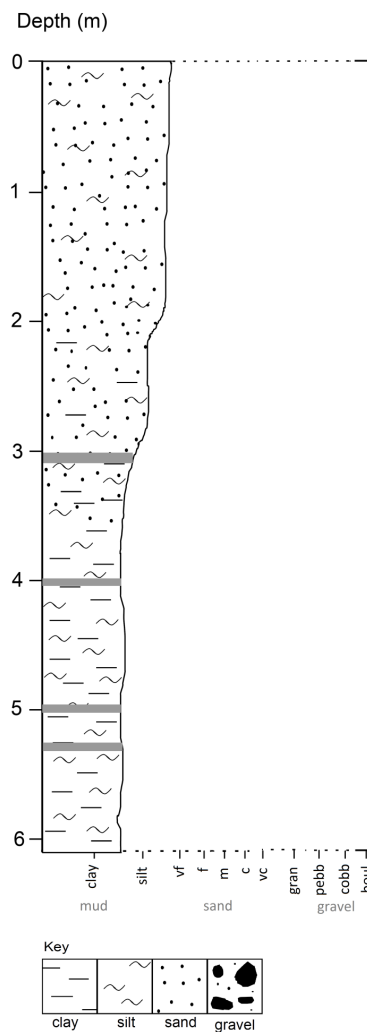
Figure 5.2: Lithostratigraphic log for vibrocore +54/-05/19 (BGS19). The grey bands indicate where there were gaps in the core record. The horizontal scale shows mud (clay and silt), sand (very fine, fine, medium, coarse and very coarse) and gravel (granules, pebbles, cobbles and boulders).

5.0.2 Lithostratigraphy: vibrocore +54/-05/65 (BGS65)

From the base of BGS65 to ~1 m core depth were laminations of mud and very fine sands and sandy mud. Above this finer section, extending to the top, the core consisted of unconsolidated, gravelly shelly sand, containing bivalves, *Turritella* and shell fragments. Sections of BGS65 were strongly bioturbated.
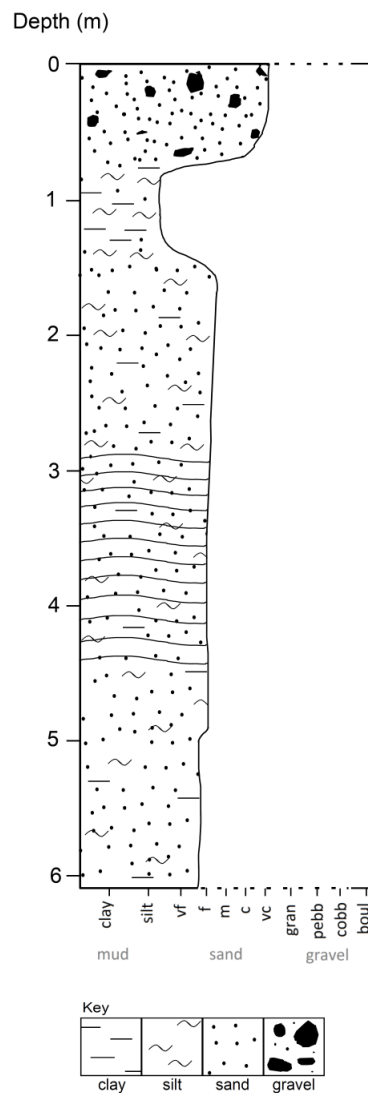
Figure 5.3: Lithostratigraphic log for vibrocore +54/-05/65 (BGS65). The horizontal scale shows mud (clay and silt), sand (very fine, fine, medium, coarse and very coarse) and gravel (granules, pebbles, cobbles and boulders).

5.0.3 Lithostratigraphy: vibrocore +53/-06/87 (BGS87)

BGS87 displayed a coarsening-upwards sequence throughout the core length. Mud with some silty, sandy laminations were present from the base up to 1.4 m. From 1.4 m to the core top was muddy sand. There was evidence of bioturbation and *Turritella* were present from the base to 1.4 m. This core had previously been heavily sampled (in ∼4 cm sections).
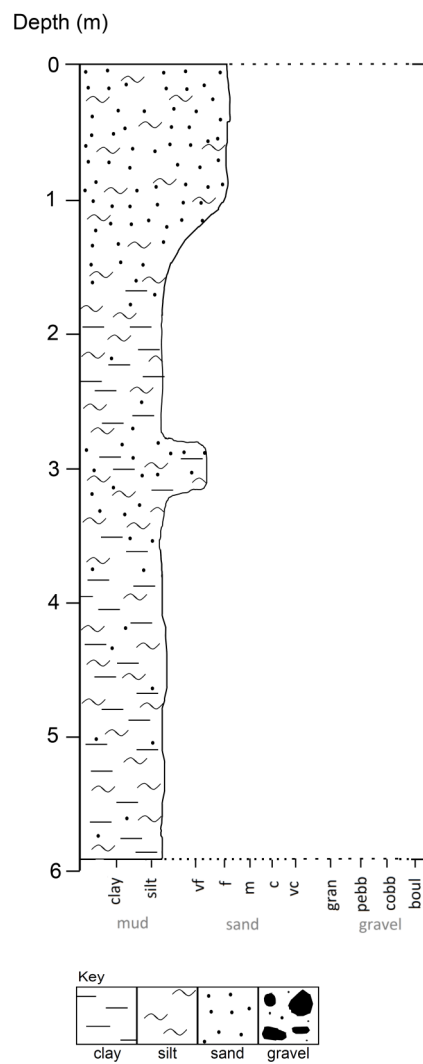
Figure 5.4: Lithostratigraphic log for vibrocore +53/-06/87 (BGS87). The horizontal scale shows mud (clay and silt), sand (very fine, fine, medium, coarse and very coarse) and gravel (granules, pebbles, cobbles and boulders).

5.0.4   Lithostratigraphy: vibrocore +56/-09/166 (BGS166)

BGS166 displayed a coarsening-upwards sequence. From the core base up to around 2.0 m was relatively uniform mud, coarsening to a sandy mud up to approximately 0.8 m, above which was muddy fine (well-sorted) sand to the core top. Shell fragments were scattered throughout the length of the core.
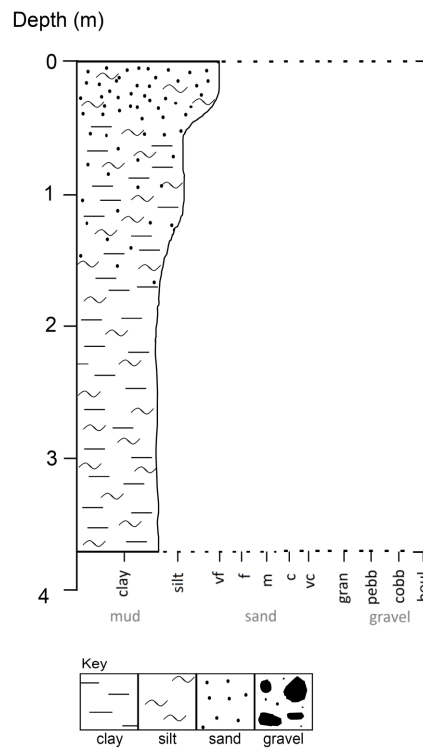
Figure 5.5: Lithostratigraphic log for vibrocore +56/-09/166 (BGS166). The horizontal scale shows mud (clay and silt), sand (very fine, fine, medium, coarse and very coarse) and gravel (granules, pebbles, cobbles and boulders).

5.0.5   Lithostratigraphy: vibrocore +51/-07/199 (BGS199)

BGS199 could be divided into three main stratigraphic units. The bottom and top units were sand/mud units, which sandwiched a coarse shelly sand and gravel sequence (from ~4.9-3.3 m). The bottom and middle units display a progressive fining-upwards sequence; from sandy gravel, through coarse shelly sands, ending in fine silt and clay-rich mud at the core top. This core had previously been sampled and analysed by Austin and Scourse (1997) and Scourse et al (2002).
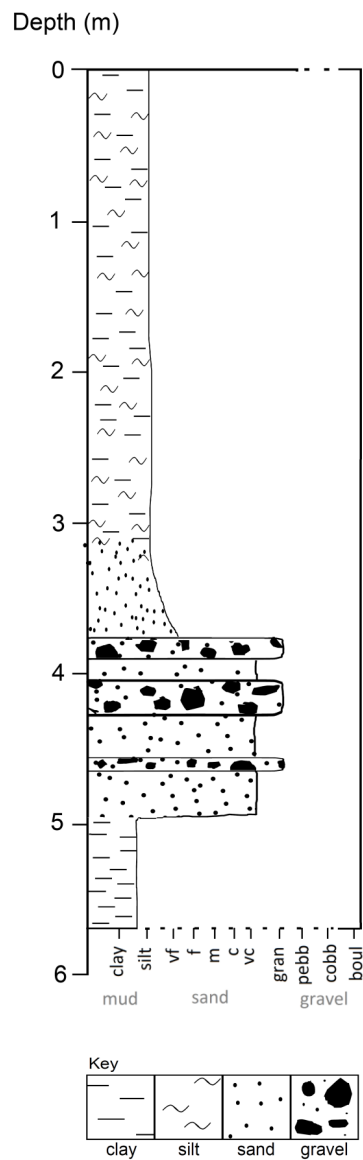
Figure 5.6: Lithostratigraphic log for vibrocore +51/-07/199 (BGS199). The horizontal scale shows mud (clay and silt), sand (very fine, fine, medium, coarse and very coarse) and gravel (granules, pebbles, cobbles and boulders).

5.1 Particle size analysis (PSA)

A number of samples from each core were taken for PSA using the Malvern Mastersizer 2000 (laser particle sizer). The sample positions, presented in Table 5.2, depended on a number of factors; including the integrity of the cores, positions of previous samples and perceived changes in grain size. Between 17 and 25 samples were taken from each of the cores, and subsamples of some of these were used for ^{14}C dating. The position of these ^{14}C dating samples are also given in Table 5.2, although these samples and results are presented in more detail in Section 5.2.

Table 5.2: Position of PSA and radiocarbon dating samples taken from the five cores, given as depth below core top. The samples extended 1 cm down the core from the positions given, unless stated otherwise.

Core ID	PSA sample positions (m down core)	[14]C sample positions (m down core)
+54/-05/19	0.00, 0.46, 0.74, 1.24, 1.49, 1.69, 2.09, 2.25, 2.46, 2.81, 3.18, 3.34, 3.70, 3.93, 4.16, 4.48, 4.79, 5.08, 5.23, 5.70	0.46, 2.09, 3.18, 3.70, 3.93
+54/-05/65	0.00, 0.35, 0.60, 0.76, 1.07, 1.35, 1.61, 1.77, 2.33, 2.60, 3.10, 3.21, 3.65, 3.81, 4.10, 4.46, 4.79, 5.21, 5.46, 5.89	0.00, 5.89
+53/-06/87	0.08, 0.20, 0.45, 0.67, 0.79, 1.19, 1.32, 1.67, 1.88, 2.18, 2.42, 2.67, 2.87, 3.16, 3.39, 3.65, 3.85, 4.12, 4.39, 4.64, 4.85, 5.10, 5.35, 5.60, 5.82	0.20, 0.79, 1.32, 2.42, 5.82
+56/-09/166	0.04, 0.20, 0.49, 0.66, 0.71, 0.94, 1.25, 1.52, 1.82, 1.95, 2.17, 2.41, 2.62, 2.85, 3.00, 3.45, 3.63	0.04, 1.52
+51/-07/199	0.20, 0.42, 0.58, 0.76, 1.10, 1.29, 1.64, 1.84, 2.10, 2.40, 2.70, 2.98, 3.10, 3.36, 3.75, 4.70, 4.93, 5.11, 5.30	0.50, 1.05, 1.55, 2.05, 2.45, 2.75, 3.05, 3.35, 4.20-4.30

5.1.1 PSA results

The PSA results are summarised in the following section, but more detailed PSA presented in tables in Appendix 3. Cores BGS19, BGS87 and BGS166 displayed general upwards-coarsening sequences, whereas in BGS65 there was no significant change in grain size until the top ~0.6 m and BGS199 displayed a significant coarsening below ~3 m. Figure 5.7 shows the grain size evolution of each of the cores (d_{50} and d_{90}). Using the PSA results, the proportion of sand, silt and clay fractions of the core samples was calculated and these are plotted as percentages in Figure 5.8.
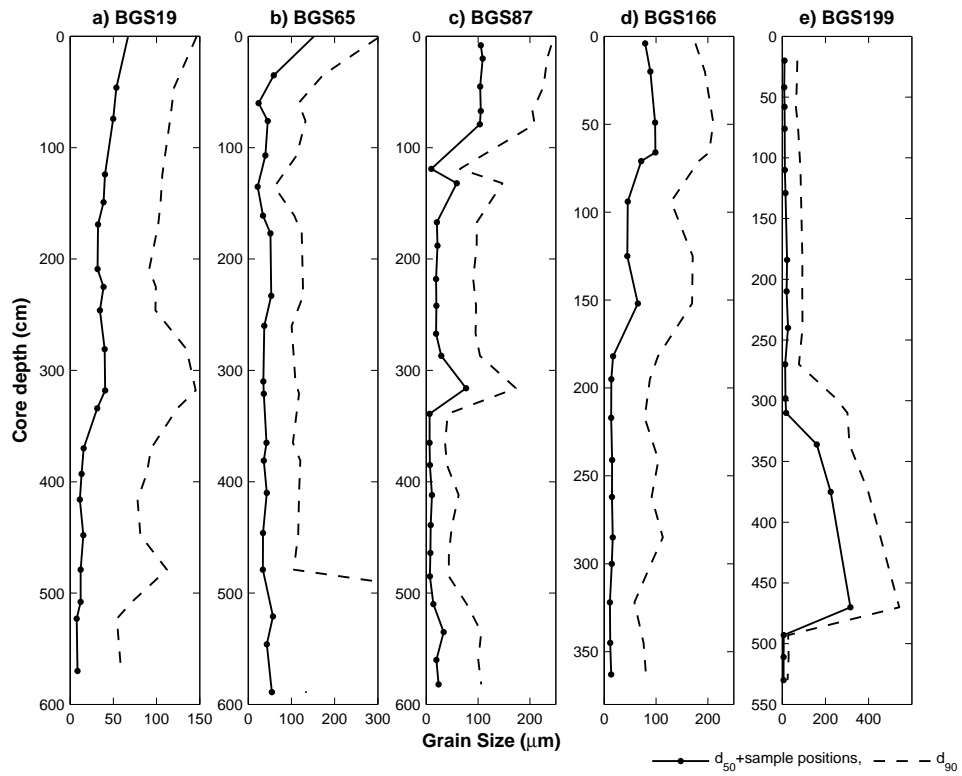
Figure 5.7: Observed grain size profiles for the five BGS vibrocores, showing d_{50} (solid line) and d_{90} (dashed line), both in µm. Note the varying core depths.
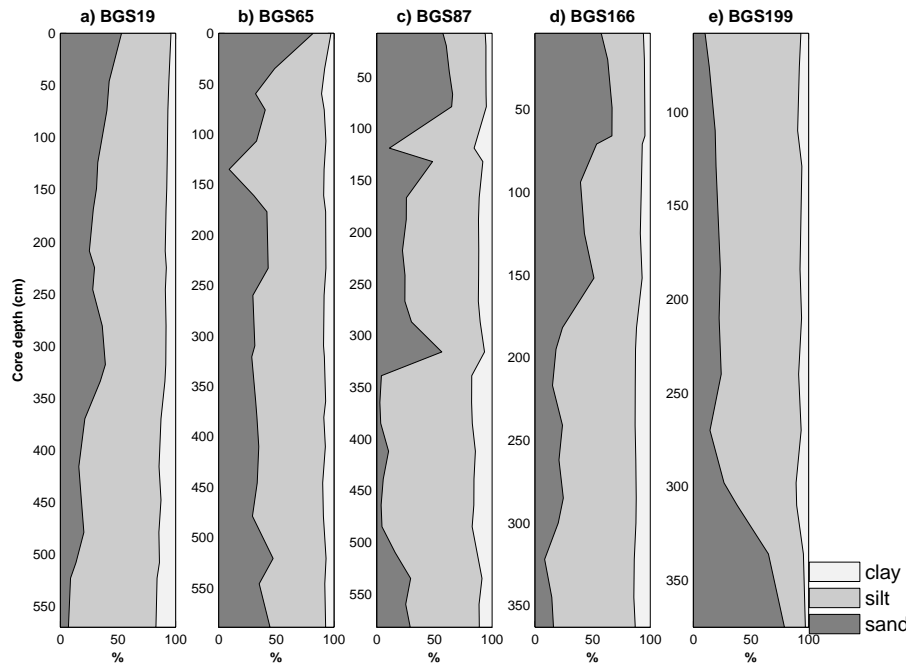
Figure 5.8: Sand (dark grey), silt (medium grey) and clay (light grey) content of the five BGS vibrocores. Note the varying core depths. Only the dated extent of BGS199 is included.

5.2 Radiocarbon dating results

A total of 17 samples from BGS19, BGS65, BGS87 and BGS166 were analysed at the NERC Radiocarbon Dating Facility (12 samples) and at the Atmosphere and Ocean Research Institute, University of Tokyo (5 samples). The positions of these samples within each core are shown in Figure 5.9, and details of the samples and the resulting radiocarbon dating data are presented in Table 5.3. Sample material was dependent upon material availability, and different species were not collected to account for changing water depths. The existing radiocarbon dates for BGS199 are shown in Table 5.4. The ranges given in the tables were output by the online version of the OxCal software (Bronk, 2013), the calculations being based on the conventional radiocarbon age and the standard deviations ($\pm 1\sigma$) reported in the results from the laboratories. The OxCal software (v4.2) uses the Intcal13 and Marine13 calibration curves of Reimer et al (2013). The appropriate Marine Reservoir Corrections (ΔR) for each core (which is dependent upon core location) were obtained using the online 14CHRONO Marine Reservoir Effect database and were based upon correction values published by Harkness (1983) and by Butler et al (2009). These ΔR values were subsequently applied to the calibrated ages, resulting in the corrected, calibrated radiocarbon dates for each sample, i.e. yr cal BP (as detailed in Table 5.3).

5.3 Core age-depth models

The corrected, calibrated ^{14}C dates were used to generate age-depth models for each of the cores (Figures 5.10 to 5.13) and have been applied to the grain size profiles to display change of grain size with time, rather than with core depth. The models are based on linear interpolation between the dated core depths, where the depths of the samples used in the model were taken to be the mid-point of the sample slices.

The ^{14}C dating results for the range finder samples taken from BGS166 suggest significant reworking of the sample ($\sim$13100-13400 yr cal BP for both 0.01 m and 1.63 m sample depths). An age-depth model for this core is thus not presented and BGS166 is not used for the model-data comparison in Chapter 7. Where paired datings of molluscs and forams from the same level was carried out, only one of each pair of the dates was used for constructing the age-depth models, and the selections were made as follows:

- *BGS19, 0.49 m sample depth:* The age of the mollusc (*Venus casina*) was *ca.* 1200

Table 5.3: Radiocarbon dating results for BGS19, BGS65, BGS87 and BGS166. Samples marked with a * were analysed at AORI, Japan, the remainder were analysed at the NERC Radiocarbon Dating Facility. Where bivalve-foram paired samples were taken, the selected date is in bold.

Core ID	Stratigraphic position (m down core)	Material	Sample weight (mg)	$\delta^{13}C_{PDB} \pm 0.1$‰	Conventional radiocarbon age (yr BP)	ΔR offset (years)	Corrected (calibrated) age (yr cal BP) (Intcal13 and Marine13)
+54/-05/19	0.49	Ammonia batavus	17.0	-0.2	1771 ±37	-72	**1178-1325**
+54/-05/19	0.49	Venus casina	58.5	0.2	2721 ± 41	-72	2246-2531
+54/-05/19	3.18*	Venus casina	37.0	-	4630 ± 35	-72	4713-4885
+54/-05/19	3.70*	Corbula gibba	7.5	-	5530 ± 30	-72	5772-5922
+54/-05/19	3.93	Corbula gibba	18.1	1.5	6504 ± 38	-72	6830-7068
+54/-05/65	0.00	Corbula gibba	19.8	1.4	7418 ±38	-72	7718-7888
+54/-05/65	5.89	Ammonia batavus	5.9	-0.8	11938 ±45	-72	**13207-13428**
+54/-05/65	5.89	Abra sp.	3.0	-0.6	11511 ±44	-72	12751-13054
+53/-06/87	0.20	Ammonia batavus	5.5	-0.8	2981 ± 37	1	**2695-2841**
+53/-06/87	0.20	Abra prismatica	6.3	0.4	477 ± 37	1	n/a-228
+53/-06/87	0.79*	Corbula gibba	21.6	-	3600 ± 25	1	3408-3575
+53/-06/87	1.32*	Abra nitida	8.2	-	4615 ± 30	1	4777-4942
+53/-06/87	5.82	Corbula gibba	35.7	1.2	7871 ± 37	1	8236-8414
+56/-09/166	0.01	Cibicides	9.7	0.9	11865 ± 46	-29	13191-13416
+56/-09/166	0.01	Venus casina	2.7	-	9842 ± 88	-29	10533-11021
+56/-09/166	1.52	Cibicides	11.6	0.9	11832 ± 46	-29	13161-13390

Table 5.4: Radiocarbon dating results for BGS199. The Marine Reservoir Effect (ΔR) for the location of this core is -15 years (Harkness, 1983) and has been applied to the dates calibrated using Intcal13 and Marine13.

Core ID	Stratigraphic position (m down core)	Material	$\delta^{13}C_{PDB} \pm 0.1$‰	Conventional radiocarbon age (yr BP)	Corrected (calibrated) age (yr cal BP) from Scourse et al (2002)	Corrected (calibrated) age (yr cal BP) (Intcal13 and Marine13)
+51/-07/199	0.50-0.51	*Bulimina marginata*	0.0	3010 ± 75	2650-2990	2600-2978
+51/-07/199	1.05-1.06	*Bulimina marginata*	0.1	3320 ± 50	2980-3320	2999-3308
+51/-07/199	1.55-1.56	*Bulimina marginata*	0.2	3765 ± 55	3510-3860	3541-3837
+51/-07/199	2.05-2.06	*Bulimina marginata*	-0.1	4675 ± 55	4760-5120	4771-5055
+51/-07/199	2.45-2.46	*Bulimina marginata*	0.0	5795 ± 60	6090-6300	6020-6333
+51/-07/199	2.75-2.76	*Bulimina marginata*	0.0	6210 ± 60	6460-6800	6471-6788
+51/-07/199	3.05-3.06	*Bulimina marginata, Quinqueloculina seminulum, Ammonia batavus*	0.0	7575 ± 70	7850-8180	7881-8175
+51/-07/199	3.35-3.36	*Quinqueloculina seminulum*	-0.1	8855 ± 115	9030-9790	9252-9857
+51/-07/199	4.20-4.30	*Spisula elliptica*	2.3	11570± 100	13210-12860	12784-13253
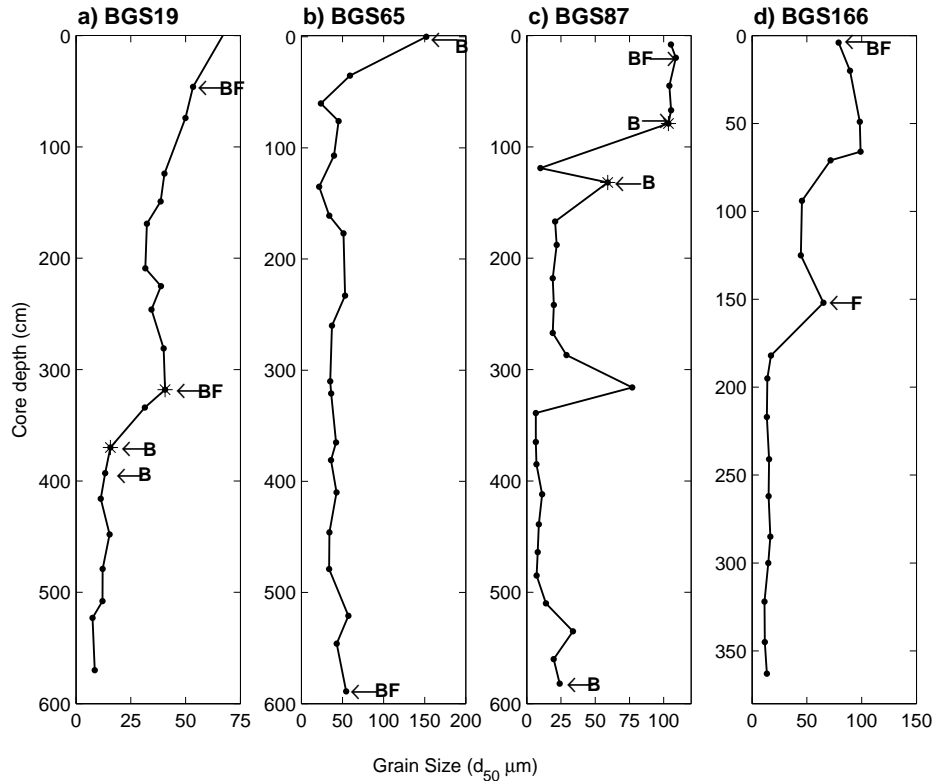
Figure 5.9: Position of radiocarbon dating samples for BGS19, BGS65, BGS87 and BGS166. The arrows indicate the positions of the samples on the grain size profiles, and labels describe the type of sample, where B=bivalve only sample, F=foraminifera only sample and BF=paired bivalve-foram sample. The stars indicate samples analysed at AORI.

years older than the age of the foram sample. It is possible that the mollusc had been transported or reworked *post-mortem* to reside in an apparently older position down core. If the mollusc was reworked, it is likely that a fraction of the foram sample was also reworked and hence the foram-derived radiocarbon date is also too old by an uncertain amount. Since the weight of the foram sample was considerable (17 mg), and hence a large number of (monospecific) specimens was used in comparison with the single mollusc, the foram date (1178-1325 yr cal BP) for this sample depth was used in the age-depth model.

- *BGS65, 5.89 m sample depth:* The foram date (13207-13428 yr cal BP) was older than the mollusc date (12751-13504 yr cal BP) from the same level. A foram-generated ^{14}C date can appear older than a date obtained from a bivalve from the same level due to the tendency for reworking and resuspension/transport of forams in comparison with larger molluscs (Heier-Nielsen et al, 1995). This discrepancy, however, could

also be due to the burrowing of the slightly younger infaunal mollusc species *Abra* sp. (Petersen, 1918), or a combination of both these factors. There was evidence of bioturbation throughout sections of this core and further, the mollusc specimen was incomplete and hence a full identification was not possible. For these reasons, the foram-derived ^{14}C date was used for the core base in the age-depth model.

- *BGS87, 0.20 m sample depth:* The ^{14}C date (2695-2841 yr cal BP) from the foram sample at 0.20 m was considerably older than the mollusc-derived (*Abra prismatica*) date (present day-228 yr cal BP). Again, a possible combination of burrowing of the mollusc species (Petersen, 1918), or reworking of the forams are the likely cause, there being indications of bioturbation within the core sample. It was not possible to sample nearer the top of this core due to lack of suitable material. Since the *Abra* community are known to burrow (Petersen, 1918), and because the foram sample was monospecific, containing more specimens in the one sample, the foram sample for this level was used in constructing the age-depth model for BGS87.

The dated section of BGS19 was aged between approximately 2400 and 6900 yr cal BP. The corresponding grain size profile from within this date range displayed a generally coarsening-upwards, with a slight inversion of this trend between 3000 and 5000 yr cal BP; however, these changes in grain sizes were minimal, the median grain size varying within the classification of silt (4-63 μm) between 7000 and 2000 yr cal BP. The age-depth model for BGS65 is crude, there being very few levels with suitable and sufficient material for dating. A surface sample from BGS65 was dated, along with a sample from 5.89 m, just 0.20 m from the core base; thus a longer section of the core was dated than for BGS19. BGS65 was chosen for analysis because the grain size did not appear to change considerably along the length of the core, ranging within the size classification for silt between 14000 and 7000 cal yr BP and thus there was no need to try and resolve specific features within the dated extent of the grain size profile. The age-constrained grain size profile for BGS87 displayed an overall coarsening upwards between ∼8500 and ∼1500 cal yr BP, although there was no significant change until ∼3500 yr cal BP, after when the grain size increased from a silt to a fine sand. The most interesting (dated) variation in grain size was in BGS199 (∼11000 to ∼ 3000 cal yr BP). The results from the PSA show a significant fining-upwards until ∼8000 yr cal BP, after when the grain size remained relatively constant. This core has a higher resolution age-depth model than any other core.
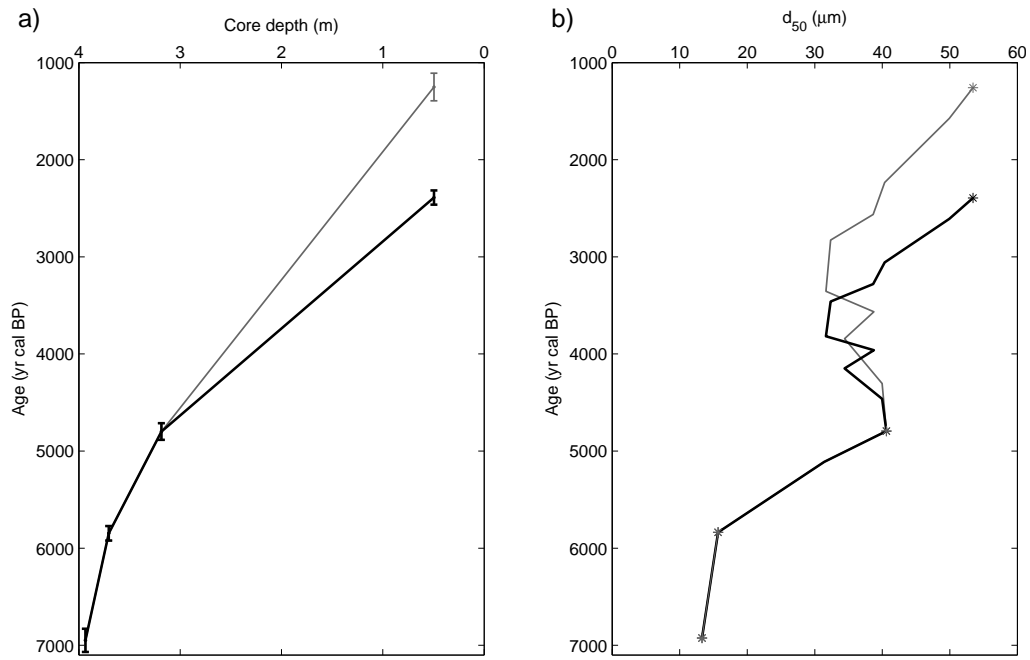
Figure 5.10: a) Age-depth curve and b) interpolated age-grain size profile for BGS19, based on corrected, calibrated ages (with 2σ error bar shown in panel a). In both a) and b), the curve/profiles are generated using the preferred bivalve-foram sample (black line) and for the bivalve-foram sample not used (grey line).
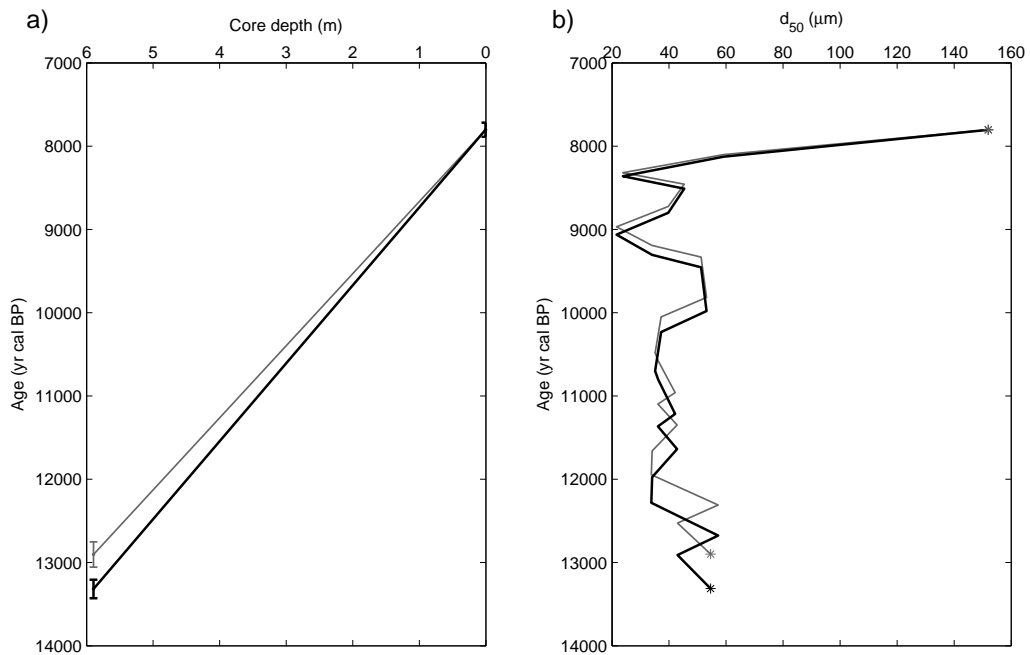
Figure 5.11: a) Age-depth curve and b) interpolated age-grain size profile for BGS65, based on corrected, calibrated ages (with 2σ error bar shown in panel a). In both a) and b), the curve/profiles are generated using the preferred bivalve-foram sample (black line) and for the bivalve-foram sample not used (grey line).
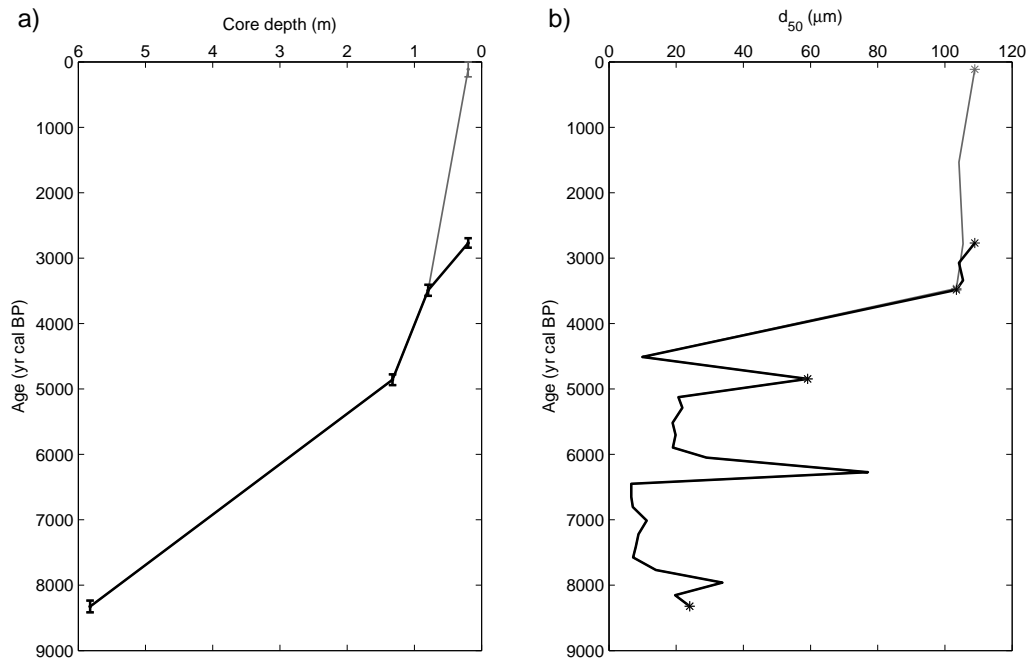
Figure 5.12: a) Age-depth curve and b) interpolated age-grain size profile for BGS87, based on corrected, calibrated ages (with 2σ error bar shown in panel a). In both a) and b), the curve/profiles are generated using the preferred bivalve-foram sample (black line) and for the bivalve-foram sample not used (grey line).
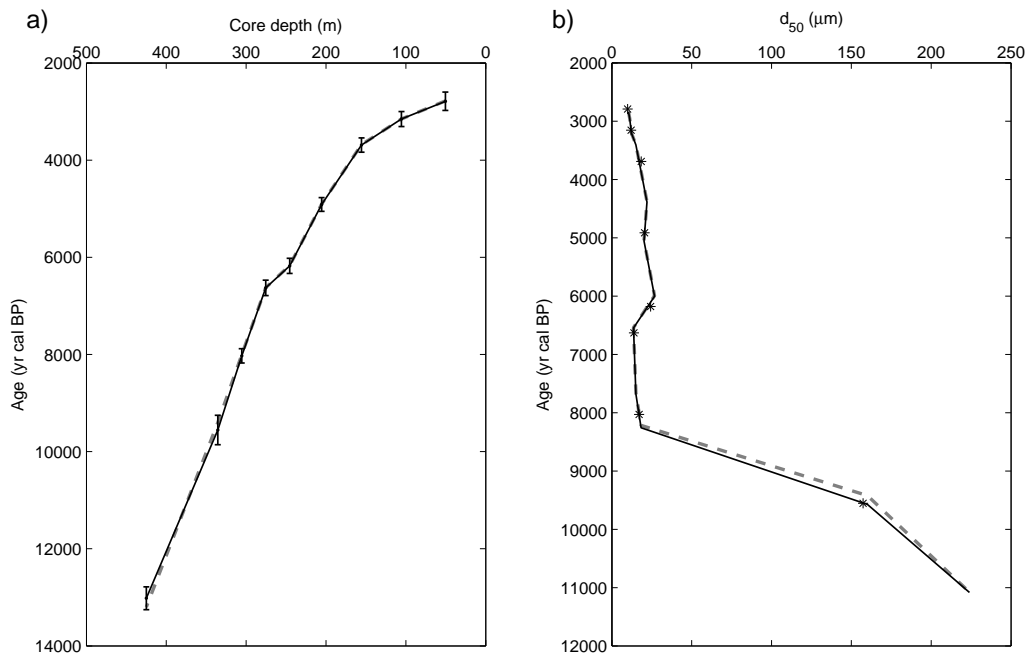
Figure 5.13: a) Age-depth curve and b) interpolated age-grain size profile for BGS199, based on corrected, calibrated ages (with 2σ error bar shown in panel a). The dashed grey lines show the age-depth curve and age-grain size profiles for BGS199 constructed using Intcal98 and Marine98 (using OxCal online), the calibration curves used by Scourse et al (2002).

5.4   Summary points

- Grain size profiles have been generated for five NWESS cores using laser diffractometry methods, and new age-depth models, of varying resolutions, have been developed for three of these cores. The three new age-depth models (BGS19, BGS65 and BGS87) complement the existing higher-resolution age-depth model developed by Austin and Scourse (1997) and Scourse et al (2002) for BGS199, a vibrocore taken from the Celtic Deep.

- The range finder dates for BGS166 were inconclusive, suggesting that significant mixing (by either physical or biological processes) has occurred at that site.

- In the first instance, range finder dates were obtained for the four previously undated cores, using samples from as close as possible to the core tops and bases. Subsequent samples from levels in-between were then sent for radiocarbon dating, to increase the resolution of the age-depth models.

6 Modelling the evolution of seasonal stratification: 21 ka BP - present

In this chapter, outputs from the new palaeotidal models are used to calculate how the positions of tidal mixing fronts (Section 2.4.1) have changed on the NWESS since 21 ka BP. Tidal mixing fronts are interesting in this context since the timing of stratification onset at the location of BGS199 in the Celtic Sea has been used as proxy data to constrain palaeotidal model simulations (Austin and Scourse, 1997; Scourse et al, 2002; Uehara et al, 2006). Prior to this work, this was the only attempt at constraining shelf sea palaeotidal model simulations.

6.0.1 Modelled mean position of tidal mixing fronts on the NWESS

The NWESS are tidally energetic with significant tidal currents, which are strongly linked to seasonal stratification (Simpson et al, 1974). Further to the work of Simpson et al (1974) and Simpson and Bowers (1981), Bowers and Simpson (1987) inferred from infrared satellite imagery that the locations of the tidal mixing fronts are consistent with a critical contour at 250 m^{-2} s^{-3}, when the tidal current speed used is the modelled depth-averaged amplitude of the tidal stream of the M_2 tidal constituent. It is most common to use the $\log_{10}$ value, and thus the equation becomes:

$$\chi = \log_{10}\left(\frac{h}{|u|^3}\right) \tag{6.1}$$

where $\chi < 2.4$ are tidally-mixed waters, h is the water depth and $|u|$ is the modelled amplitude of the depth-averaged M_2 tidal current speed. This more recent (log) value developed by Bowers and Simpson (1987) was used in the calculations for the mean position of the tidal mixing fronts presented here (shown as a black contour on Figure 6.1), and the focus is on the output from the *ROMS+Bradley* palaeotidal model simulations.

The modelled present-day mean position of the tidal mixing fronts (Figure 6.1) was in close agreement with those presented in previous studies (e.g Pingree and Griffiths, 1978; Simpson and Bowers, 1981; Bowers and Simpson, 1987; Holt and Umlauf, 2008). Also illustrated in Figure 6.1 is the transitional water (where $1.9 < \chi < 2.9$), which indicates modulation in the position of the tidal mixing fronts due to seasonal heating (Pingree and Griffiths, 1978).
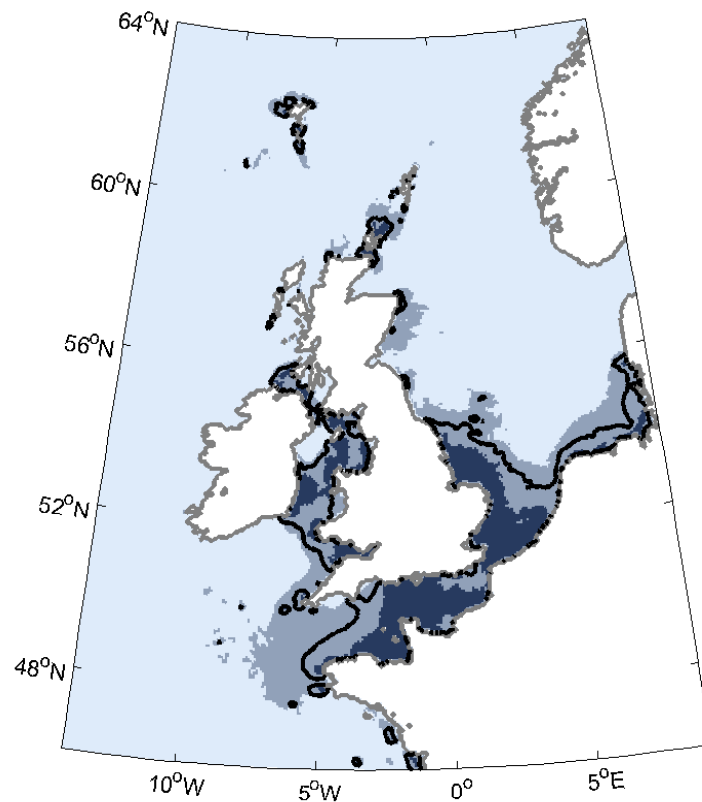
Figure 6.1: Predicted location of the present-day tidal mixing fronts on the NWESS. The dark blue area indicates regions that are vertically well mixed throughout the year ($\chi < 1.9$), the lighter blue indicates transitional water ($1.9 < \chi < 2.9$) and the very light blue indicates seasonally-stratified water ($\chi > 2.9$), i.e. areas which would be stratified during the summer months. The black line is the critical contour of $\chi = 2.4$, developed by Bowers and Simpson (1987).

6.0.2 Changes in the modelled mean position of tidal mixing fronts: 21 ka BP - present

Uehara et al (2006) used earlier values of Pingree and Griffiths (1978) to define the location of tidal mixing fronts on the NWESS at various time slices, having adapted the critical contour for application to the model output of tidal current speed for five tidal constituents.

The positions of tidal mixing fronts for a number of time slices predicted by *ROMS+Bradley* are shown in Figure 6.2, which are plotted using the critical contour of $\chi = 2.4$, which is given as a black line shown in Figure 6.1). There was a significant increase in the extent of mixed waters on the shelf with the rapid flooding of the NWESS between 21 and 15 ka BP. A peak in the areal extent of tidally-mixed waters on the shelf was reached at 15 ka BP, which decreased in extent from 12 ka BP onwards, as the position of the tidal mixing fronts migrate landwards with increasing sea levels. In the Uehara et al (2006) simulations, the ratio of tidally-mixed to total shelf area has remained relatively constant over the last five thousand years. In the *ROMS+Bradley* simulations, the extent of tidally mixed waters has fluctuated within this time, primarily due to more extensive mixed waters in the southern North Sea in comparison to the present-day. The model outputs suggest, however, that the ratio of mixed to stratified waters has not changed significantly in the last 7 ka, with the area of mixed water between 7-8 % of the stratified area. The variation in the area of the tidally-mixed water in comparison to present-day is presented in Figure 6.3.

The south-western section of the NWESS remained tidally-mixed until 9 ka BP, after which the front shifted north-eastwards into the English Channel. This main frontal system separated into two at 8 ka BP; one section migrated into the inner Celtic Sea and the Irish Sea, and the other into the western English Channel. This division of the front happened 1 ka earlier than was simulated by Uehara et al (2006). The position of the tidal mixing front in the Irish Sea has not changed significantly since 9 ka BP. After 14 ka BP, seasonally-stratified areas began to appear in the Celtic Sea, the majority of which is seasonally-stratified at the present-day. The front in the North Sea migrated south with rising sea levels, and the area of mixed water in this region decreased from 8 ka BP onwards.

6.1 Modelled seasonal stratification at the marine sediment core locations

The changes in front positions in the Irish and Celtic Seas predicted by the *ROMS+Bradley* simulations are shown in Figure 6.4, and the core locations are given for reference. The predicted changes at each of the core locations is shown in Figure 6.5, from the LGM to present-day, for both the *ROMS+Bradley* and the *ROMS+Lambeck* simulations.

The predicted changes in stratification at the location of the cores varied between simulations, particularly when a transitional zone was not considered (Figures 6.5 and 6.6). The focus is on the results which incorporate a transition zone.
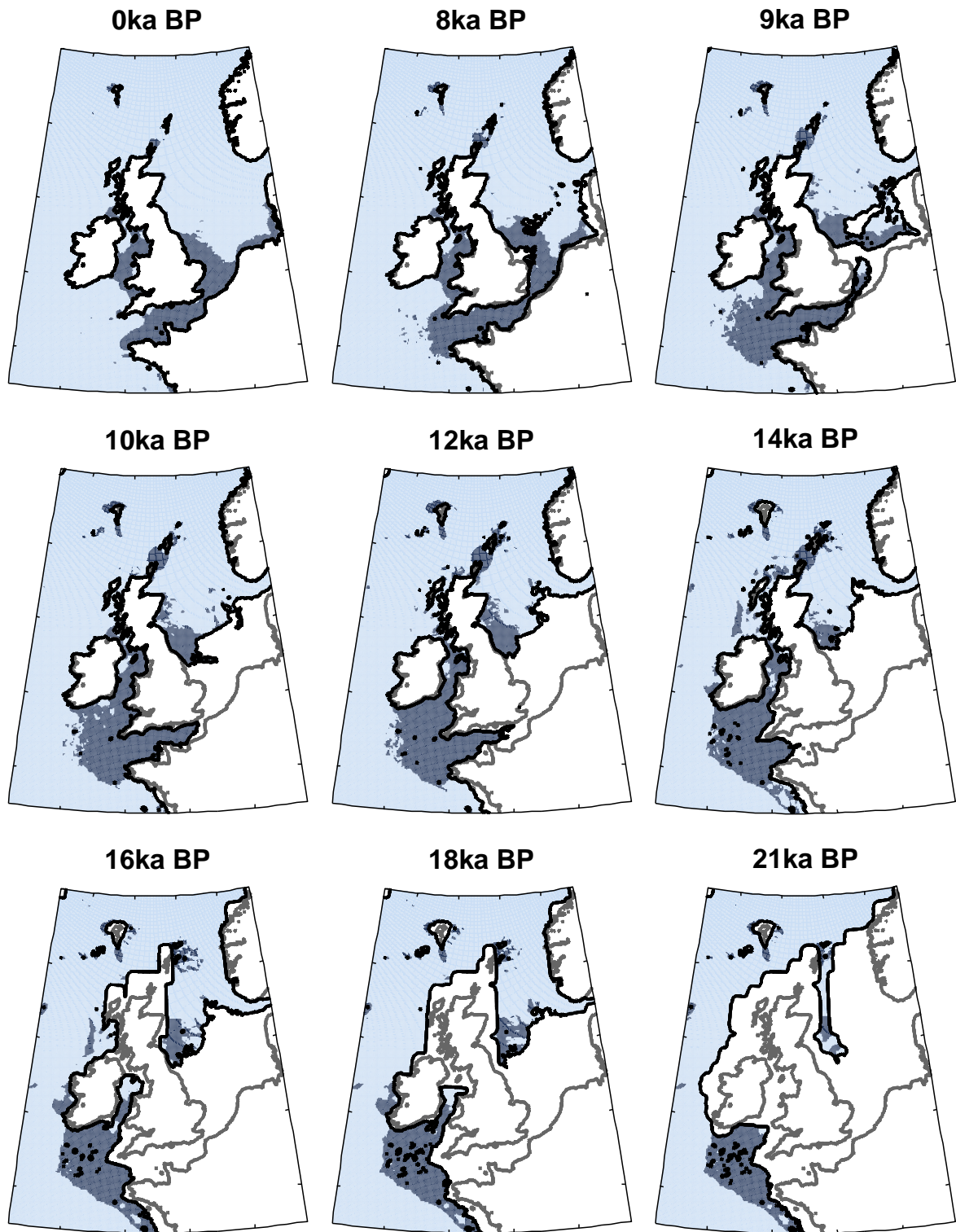
Figure 6.2: Predicted locations of the tidal mixing fronts on the NWESS, for selected modelled time slices. The dark blue area indicates vertically well-mixed water, the critical contour of which was plotted at $\chi = 2.4$. The light blue area represents seasonally-stratified water. The white areas are land/ice and the present-day coastline is given for reference (grey line).
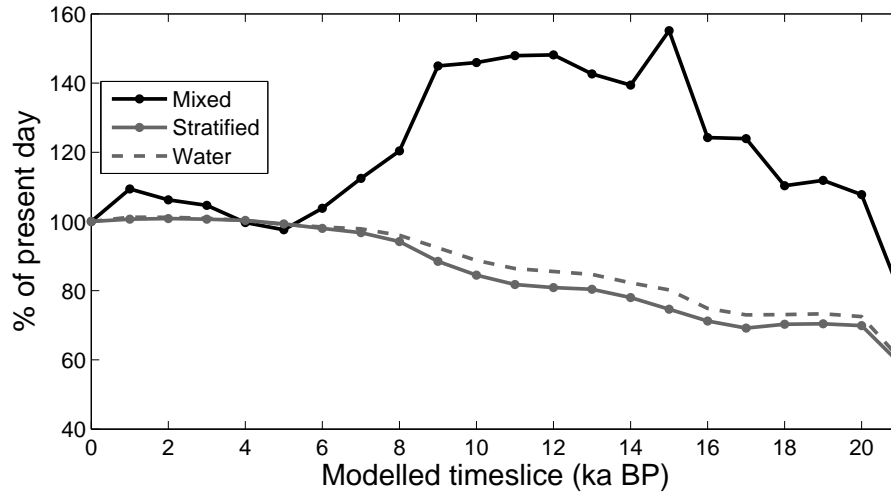
Figure 6.3: Changes in the modelled (*ROMS+Bradley*) area of water (dashed grey line), seasonally-stratified water (grey line) and tidally-mixed water (black line) within the model domain for various time slices, shown as % of present-day.

The *ROMS+Bradley* and *ROMS+Lambeck* simulations predicted that the location of BGS19 remained transitional since 8 ka BP and 9 ka BP, respectively (Figure 6.5a). Prior to this, the site was not inundated in *ROMS+Lambeck*, whereas in *ROMS+Bradley* there were fluctuations between stratified (15-14 ka BP) and mixed (10-9 ka BP). There was discrepancy between the simulation predictions for the present-day stratification at BGS65, with *ROMS+Bradley* predicting the change from stratified to transitional water at 14 ka BP, which is 3 ka earlier than *ROMS+Lambeck*. Similarly, at the site of BGS87, the transition from tidally-mixed to stratified occurred 3 ka BP earlier in the *ROMS+Bradley* simulations (between 15 and 14 ka BP), than in *ROMS+Lambeck*. Using the output of *ROMS+Bradley*, BGS166 was predicted to remain stratified, with the exception of between 16-14 ka BP when it was transitional; however, *ROMS+Lambeck* output predicted that this location transitioned to being tidally-mixed and transitional between 18 and 12 ka BP, and remained stratified from 11 ka BP onwards.

Previously published geological proxy data were used by Uehara et al (2006) for comparison with model predictions of the timing of stratification at the site of BGS199. Austin and Scourse (1997) used data from stable isotopes and foraminifera from BGS199 to estimate that this region of the Celtic Sea became progressively seasonally-stratified in the early Holocene. Scourse et al (2002) further constrained the date at which the site of BGS199 transitioned from tidally-mixed to seasonally-stratified to between 8990 and 8440 yr cal BP ($8720\pm2\sigma$). Uehara et al (2006) estimated that the timing of onset of stratification at the core site occurred between 10 and 8 ka BP. In contrast, the *ROMS+Lambeck* simulations estimated an earlier data of stratification, between 10 and 9 ka BP. The *ROMS+Bradley*
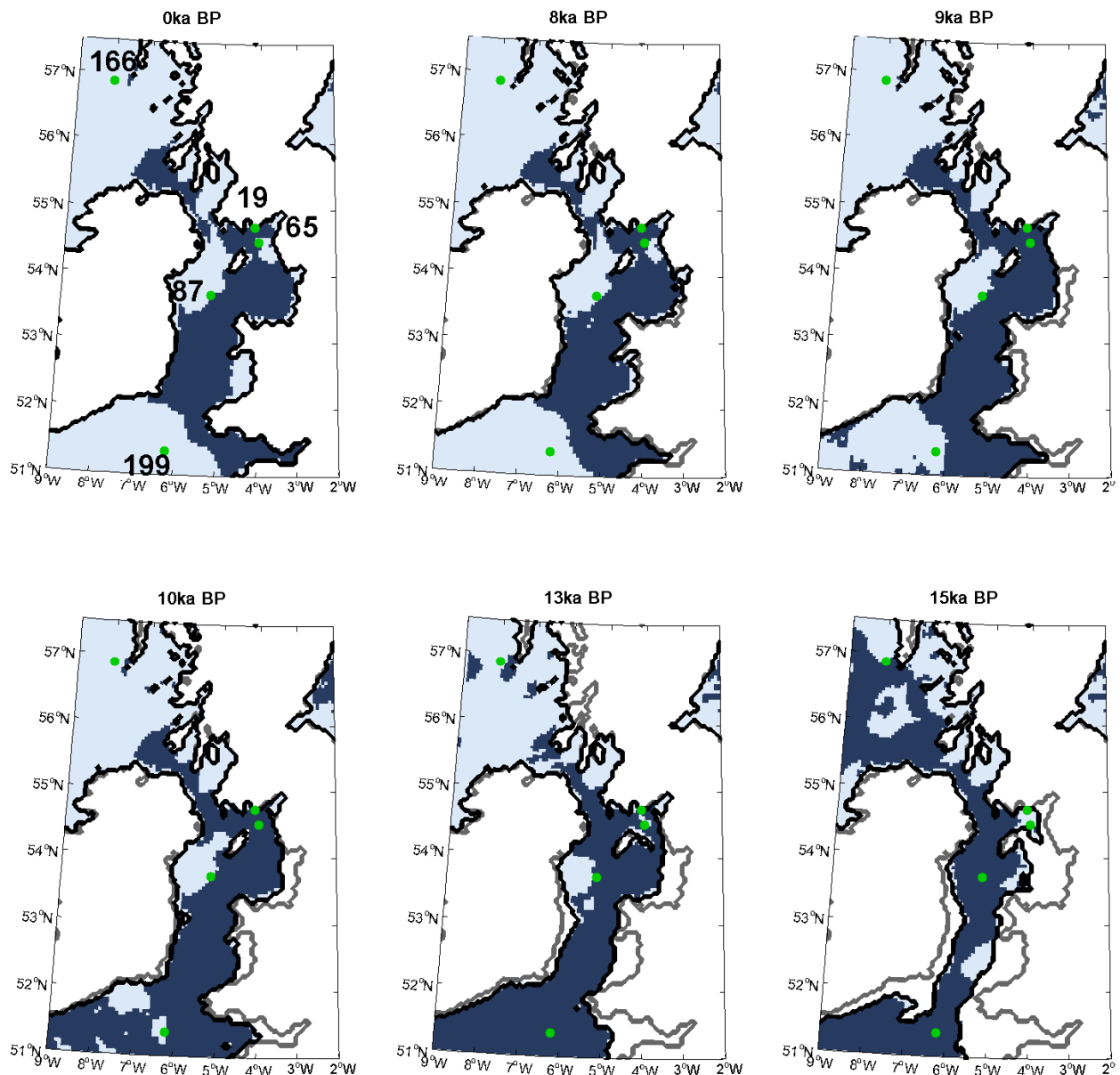
Figure 6.4: Predicted location of the tidal mixing fronts in the Celtic and Irish Seas, for various modelled time slices (*ROMS+Bradley*). The dark blue area indicates vertically well-mixed water, and the light blue area indicates regions of seasonally stratified water, the critical contour of which was plotted at $\chi = 2.4$. The white areas are land/ice and the present-day coastline is given for reference (grey line). The green dots indicate the core sites, which are labelled in the present-day panel.

simulations estimated the transition from tidally-mixed to seasonally-stratified at BGS199 to have happened earlier still, between 11 and 10 ka BP. Despite the differences in the timing of the onset of stratification at BGS199 between the observational data and the model results, both indicate that since 9 ka BP, the site has remained seasonally-stratified.
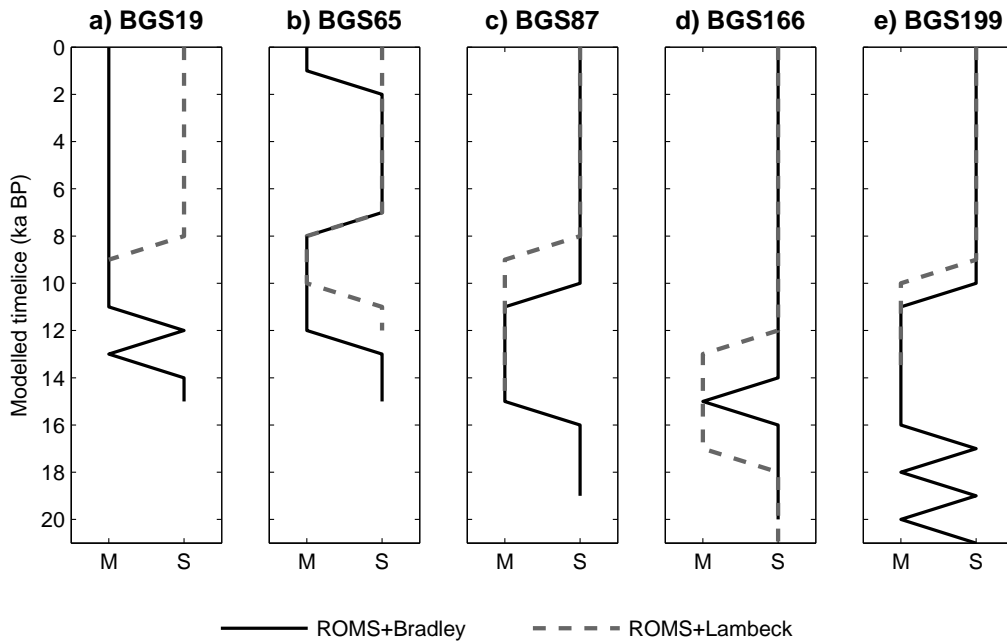
Figure 6.5: Evolution of stratification at the core sites for *ROMS+Bradley* (solid black line) and *ROMS+Lambeck* (dashed grey line) simulations, where M = tidally-mixed water ($\chi < 2.4$) and S = seasonally-stratified ($\chi > 2.4$).
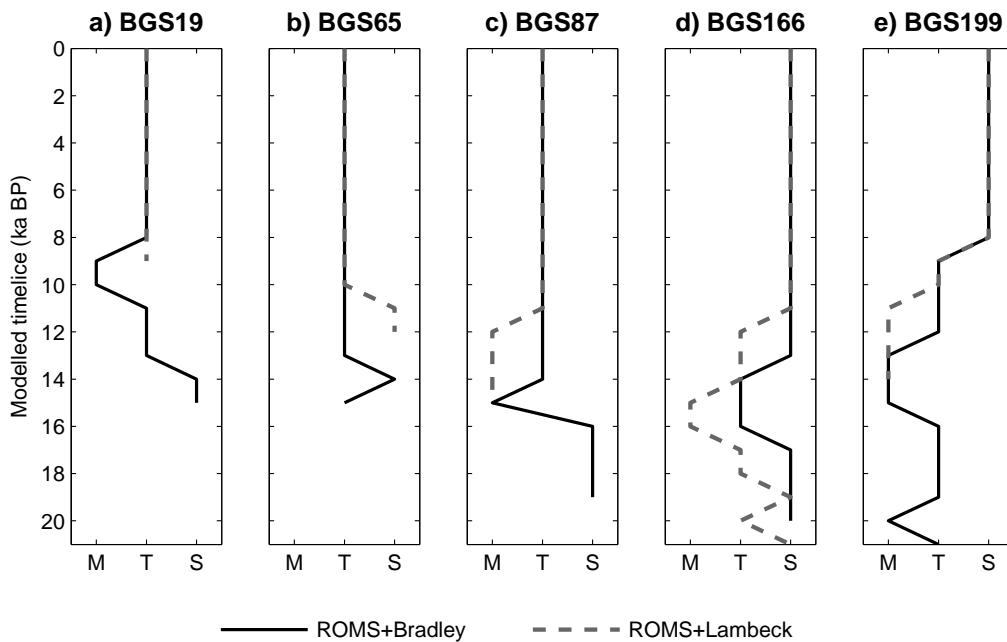
Figure 6.6: Evolution of stratification at the core sites for *ROMS+Bradley* (solid black line) and *ROMS+Lambeck* (dashed grey line) simulations, where M = tidally-mixed water ($\chi < 1.9$), T = transitional water ($1.9 < \chi < 2.9$) and S = seasonally-stratified ($\chi > 2.9$).

These predicted differences in stratification are sensitive to the definition of the tidal mixing front, i.e. to the value of the critical contour. The variations in the predicted values of the stratification parameter at the site of BGS199 are shown in Figure 6.7. For *ROMS+Bradley* and *ROMS+Lambeck*, the core site was calculated to be 'transitional'

between 12-9 ka BP and 11-9 ka BP, respectively. After 8 ka BP, the water at the core site was stratified, which is consistent with the observational data. Further, the value of the stratification parameter was very similar for both simulations from 8 ka BP onwards.

The predicted differences in timing of stratification onset between the models, when using the same values of the critical contour, are largely due to differences in water depths at the core sites, a result of different GIA models. Additionally, even for the same water depth, small variations in modelled tidal current amplitudes can influence the value of the stratification parameter since it is dependent upon u^3. The comparison of these model results with observational data is inconclusive with regard to defining which palaeotidal model simulation is superior; however, given the sensitivity of the stratification parameter, this ought not overshadow the fact that the new *ROMS+Bradley* is considered an improvement on existing palaeotidal models which use older GIA models of the region to derive palaeotopographies.
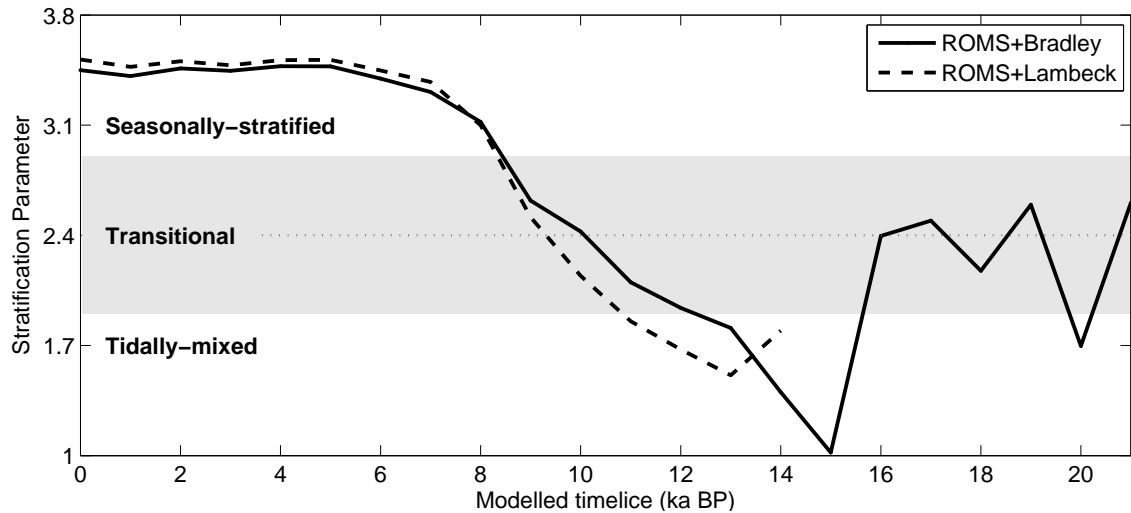
Figure 6.7: Variation in the stratification parameter (χ) at the site of BGS199 from 21 ka BP to present-day for *ROMS+Bradley* (solid black line) and *ROMS+Lambeck* (dashed black line). The grey area highlights the value of $1.9 < \chi < 2.9$, indicting seasonal fluctuations in the position of the tidal mixing front. The critical contour $\chi = 2.4$ is given by the dotted grey line.

6.2 Summary points

- The position of tidal mixing front can be predicted from model outputs of tidal current speeds. The location of tidal mixing fronts have been calculated for the present-day (Figure 6.1), and for the time slices of the palaeotidal model (Figure 6.2), using the theory of Bowers and Simpson (1987). These calculations successfully predicts the observed (present-day) mean location of the tidal mixing fronts on the NWESS.

- There is considerable variation in the timing of onset of stratification at the core locations predicted by different palaeotidal models (Figure 6.6). Despite the difference in timing that the location of BGS199 becomes transitional, both the *ROMS+Bradley* and *ROMS+Lambeck* palaeotidal models predict that the site became stratified between 9 and 8 ka BP, which is in agreement with the observational data for the location (Scourse et al, 2002).

- Modelling the onset of stratification at point locations is interesting in this context since the observed timing of stratification onset at the site of core BGS199 has been used to validate a palaeotidal model (Scourse et al, 2002; Uehara et al, 2006).

- For sites near the front (i.e. 'transitional'), using the critical contour to define whether the water is seasonally-stratified or tidally-mixed is very sensitive to the model resolution, since the tidal mixing front is generally around 5 km wide (Simpson et al, 1974). Further, the exact position of the front is sensitive to the value of the critical contour used, and to the model output used to calculate the position of this contour. Thus, inclusion of a 'transitional zone' ($\chi = 2.4 \pm 1$) is important when considering specific sites such as core locations.

7 Using seabed sediment data to validate a new palaeotidal model of the NWESS

In this chapter the results of the ROMS palaeotidal model are presented alongside output from existing palaeotidal models, and are compared with core grain size data, the analysis of which is presented in Chapter 5. The focus is on the newly-developed ROMS palaeotidal model (*ROMS+Bradley*), which incorporated the most up-to-date palaetopographic datasets of the region.

7.1 Comparing two GIA models for the region

There is a comprehensive relative sea level database for the British Isles, which plays an important role in developing GIA models for the region (Lambeck, 1995, 1996; Peltier, 2002a; Shennan et al, 2000b; Bradley et al, 2011). The relative sea level signal for the region is complex due to the effects of local (British-Irish) and non-local (Fennoscandian and Laurentide) ice sheets. Differences in GIA model configuration can significantly alter predicted relative sea level patterns, which in turn can impact on outputs from palaeotidal model with palaeotopographies based on different GIA models. The most up-to-date GIA model for the region (Bradley et al, 2011) was used in the new ROMS palaeotidal model simulations, and was available for the NWESS at a spatial resolution of approximately 1/12 degree. The Lambeck GIA model (Lambeck, 1995; Uehara et al, 2006) was also regional, but was of lower resolution at 0.7 and 0.15 degrees in longitude and latitude, respectively. All palaeotidal model simulations considered here which used the Lambeck model, incorporated a revised version of the GIA model of Lambeck (1995), which had been updated using improved ice-sheet models and ice extents (Lambeck and Purcell, 2001; Lambeck and Chappell, 2001), as well as improved solutions of formulating isostasy

(Lambeck et al, 2003). Details of these revisions were described by Uehara et al (2006). The differences in land/ice and water boundaries generated using these two GIA models for selected time slices are shown in Figure 7.1. Despite the large differences in palaeoto-pographies, the *ROMS+Lambeck* model is still interesting to consider since it can be used to compare with palaeotidal model outputs which use the same hydrodynamic model but different GIA model (*ROMS+Bradley*), and to compare with other palaeotidal models developed using different hydrodynamic models but the same GIA model (*KUTM+Lambeck* and *POLCOMS+Lambeck*).

The Bradley model is the first GIA model of the region to include all available relative sea level data for both Britain and Ireland, and brings together a number of recent works on GIA in the region (Milne et al, 2006; Shennan et al, 2006b; Brooks et al, 2008b; Bradley et al, 2009). The most up-to-date advancements in GIA sea-level modelling were used in the sea level model component of the Bradley model, which solves the generalised sea-level equation (Milne and Mitrovica, 1998; Mitrovica et al, 2001; Mitrovica and Milne, 2003; Kendall et al, 2005). Palaeotidal corrections were only applied to five localities of the SLIPs used to constrain the Bradley GIA model, using output of Uehara et al (2006). Fewer SLIPs were used by Lambeck (1995) as evidence for past sea levels, none of which were corrected for temporal changes in tidal amplitudes.

In both GIA models, the ice sheet model was relatively low resolution, at 1/2 degree in longitude and 1/4 degree in latitude. The 25 km spatial resolution ice model GB-3 developed by Lambeck (1993) was used in the Lambeck model. The local ice sheet model used in Bradley was constrained using more data than previous GIA models for the area, using reconstructions by Shennan et al (2006b) and Brooks et al (2008b). The global model of Bassett et al (2005) was used for the non-local ice-melt signal, although it was tuned to fit more relative sea level data and the BIIS component of the model was removed. The Bradley model thus takes into account more recent field data regarding the extent of the ice sheet which were not available at the time of the development of the Lambeck model.

The choice of parameters used in the earth model component varies between GIA models, including ranges in lithospheric thicknesses and in values of viscosity structure of the upper and lower mantle. The Bradley model was set with an upper mantle viscosity of 5×10^{20} Pa s, a lower mantle viscosity of 3×10^{22} Pa s and lithospheric thickness of 71 km. The lithosphere was set to have high viscosity, at 10^{43} Pa s. In comparison, the lithosphere in the earth component of the Lambeck model was 65 km thick and was of considerably

lower viscosity (10^{25}) than in the Bradley model. The optimum upper mantle viscosity in the Lambeck model was similar to the Bradley model, at 4-5 x 10^{20}, below which (i.e. deeper than 670 km) the viscosity was also set at least one order of magnitude higher.

It is likely that the ice coverage in the lower resolution Lambeck runs is overestimated by interpolating the low resolution ice sheet model onto the palaeotidal model grid. This was also the case in the Bradley run, but efforts were made to reduce the effects of the interpolation (as described in Section 3.5). The increased isostatic depression caused by the thicker and more extensive LGM ice sheets in the ice model used by Bradley et al (2011) will have resulted in higher relative sea level in comparison to the Lambeck simulations. This can be seen in Figure 7.1, where between 20 and 11 ka BP, the areal extent of the shelf seas was considerably greater in the Lambeck palaeotopographies. After 8 ka BP, there was no significant difference between the palaeotopographies generated by the two models. The land/ice extended further south in the Lambeck simulations until 13 ka BP. In contrast, at 21 ka BP, the land/ice mask extended considerably further north on the western shelf in the Bradley simulations. The northern section of the North Sea flooded considerably earlier according to the Bradley GIA model.

7.2 Palaeotidal model output for the NWESS

In this section the regional output of the *ROMS+Bradley* model are presented and compared with the output of Uehara et al (2006) and Neill et al (2010). Model output at the specific core locations are presented in Section 7.3.

7.2.1 Sea-level change

The evolution of the NWESS since 21 ka BP according to the Bradley GIA model can be seen from the selection of the palaeotopographies given in Figure 7.2. Figure 7.2 suggests that at 21 ka BP much of the NWESS was either land or ice, and the majority of the shelf that was submerged had water depths <50 m. Following initially rapid deglaciation, a significant area of the NWESS was submerged by 20 ka BP, with water depths of up to 150 m. By 15 ka BP, the response of the unloading of the Fennoscandian Ice Sheet was apparent, with areas of the southern North Sea re-emerging as land. This response was also apparent in the northern North Sea, where water was shallower at 15 ka BP than during earlier times (e.g. 18 ka BP). Between 9 and 8 ka BP, the English Channel opened, and much of the North Sea was submerged. On the whole, the present-day coastline had emerged by 6 ka BP, with little eustatic sea-level rise in the last several thousand years.

The significant variability in the relative sea level curves at various locations (Figure 7.3) around the British Isles can be seen clearly in Figure 7.4. This figure also illustrates how different GIA models can influence the timing of emergence of coastlines, e.g. for Arisaig, in western Scotland (Figure 7.3a and 7.4a). The relative sea level curves at the sites are discussed in more detail here, with focus on the curves generated by the GIA model of Bradley et al (2011).

At Arisaig, in western Scotland, which was near to the centre of loading of the BIIS, there was rapid relative sea-level fall during early deglaciation, in concurrence with the rapid retreat of the ice sheet. With the exception of 13 ka BP, when there was a relative sea-level rise at this site, likely due to the ice sheet re-advance during the Younger Dryas, this relative sea-level fall in western Scotland continued until 11 ka BP. After 11 ka BP, the signal from the eustatic sea-level rise dominated and there was a relative sea-level rise, before relative sea-level fall to the present day, attributable to ongoing GIA. Sites b, e and f were a medium distance from the centre of loading of the BIIS, in comparison to the other sites. At these three sites, the GIA signal had the dominant influence on the relative sea level curves between 21 ka BP and 15 ka BP, after when the eustatic sea-level rise became the dominant signal, causing relative sea-level rise at these three sites until around 8 ka BP. There was overall relative sea-level rise at the two southern-most sites (Figure 7.4c and d) since 21 ka BP, as these sites are further from the centre of loading of the BIIS and Fennoscandian Ice Sheet than the other sites for which relative sea level curves are considered.
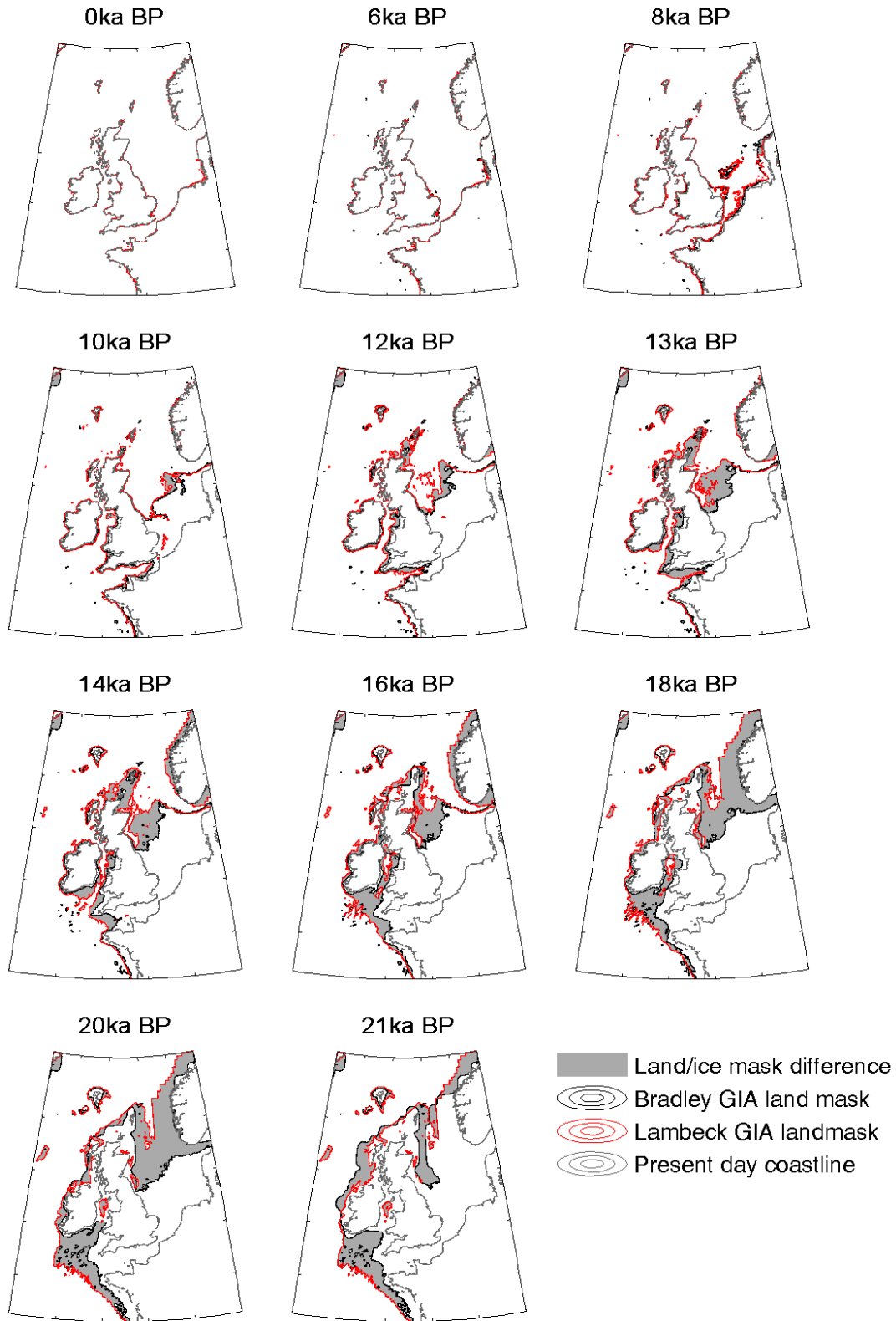
Figure 7.1: Difference between the land/ice and sea boundaries for model palaeotopographies generated using the Bradley and Lambeck GIA models. Black line: the land/ice masks for the *ROMS+Bradley* simulations, with a minimum model water depth of 10 m. Red line: the land/ice mask used by Uehara et al (2006) and in the *ROMS+Lambeck* simulations, with a minimum water depth of 6 m and interpolated onto the higher resolution ROMS computational grid. The grey fill highlights the difference between the two masks and the present-day coastline is given for reference (grey line).

0ka BP **8ka BP** **10ka BP**

12ka BP **14ka BP** **15ka BP**

18ka BP **20ka BP** **21ka BP**

0–50 50–100 100–150 150–200 >200
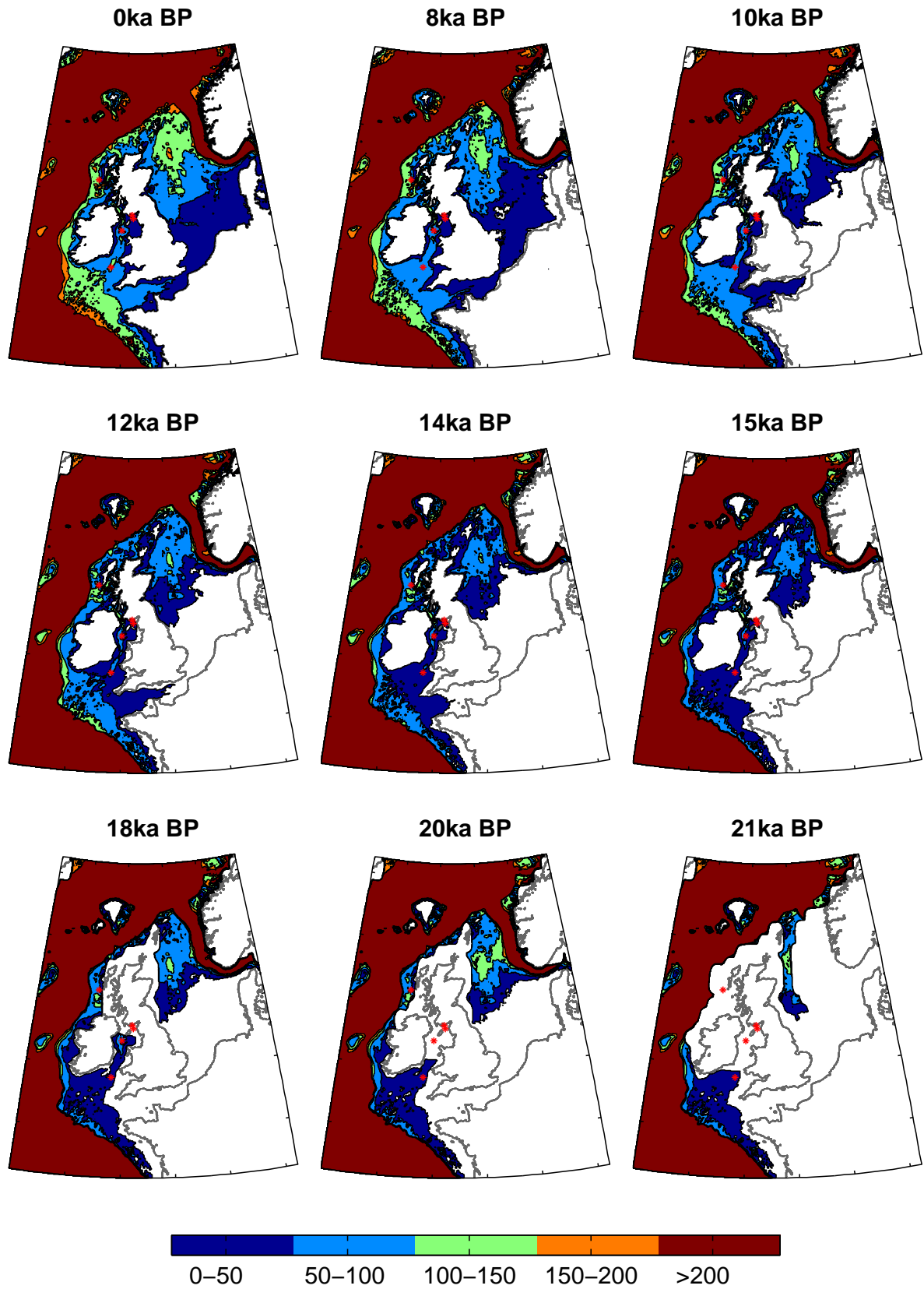
Figure 7.2: Palaeobathymetries for selected time slices using the GIA model of Bradley et al (2011), with water depths of 0-50 m (dark blue), 50-100 m (light blue), 100-150 m (green), 150-200 m (orange) and >200 m (red) plotted. The red markers indicate the core sites. The white areas are land/ice and the present-day coastline is given for reference (grey line).
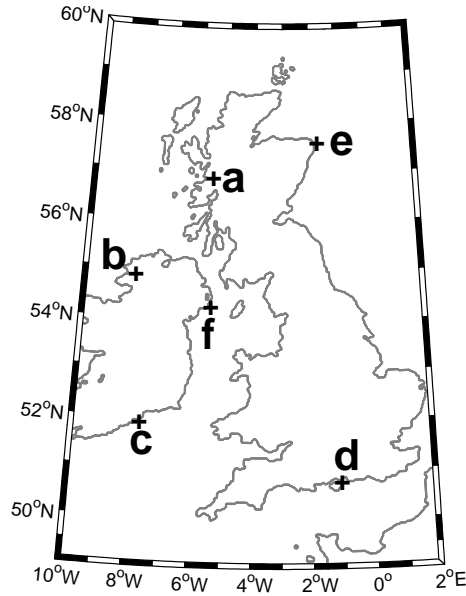
Figure 7.3: Locations of sites a-f, for which relative sea level curves are given in Figure 7.4.
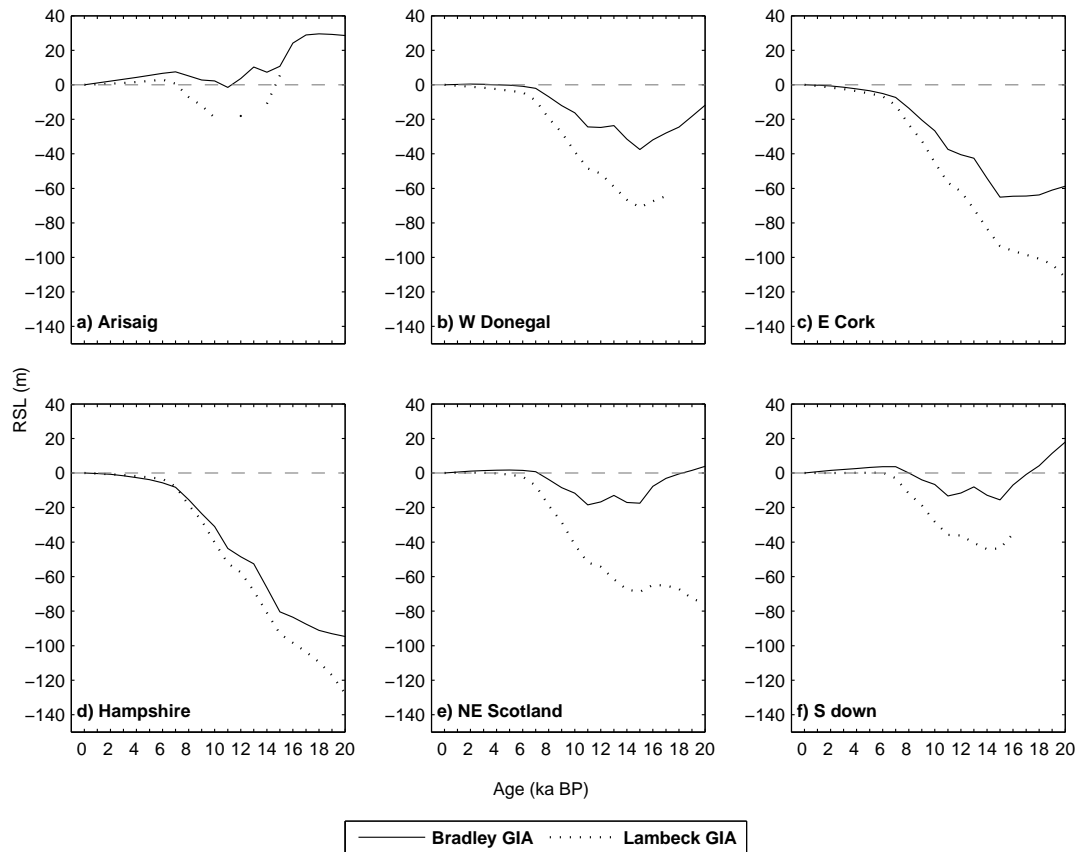
Figure 7.4: Relative sea level curves for a number of sites using the Bradley (solid line) and Lambeck (dotted line) GIA models. Where points are missing for the Lambeck models, the sites were ice-covered. The site locations are shown in Figure 7.3. Note the varying depths scales (RSL = relative sea level) for each plot, the present-day sea level is given for reference (grey dashed line).

7.2.2 Changes in M_2 tidal elevation amplitudes

Figure 7.5 shows the evolution of M_2 tidal elevation amplitude and phase since 21 ka BP, for a number of selected time slices. In concurrence with the findings of Egbert (2004) and Uehara et al (2006), high M_2 amplitudes were observed on the margin of the eastern North Atlantic during deglaciation. Along the palaeo-coastline between Britain and northern France (between 47 and 50°N), M_2 amplitude reached a maximum of ~4 m at 20 ka BP, and remained in excess of 2.5 m until the English Channel fully connected with the North Sea between 9 and 8 ka BP. The split of this area of high M_2 amplitude into the Bristol Channel and along the Brittany coast happened earlier in the *ROMS+Bradley* simulations (after 14 ka BP) than in the Lambeck simulations (after 12 ka BP) (Uehara et al, 2006). During this period, the areas of high M_2 amplitudes migrated along the northern shore of France as it was submerged, into the mouth of the English Channel, reaching amplitudes in excess of 4.5 m in the Bay of Biscay (northern France) at 10 ka BP. Increasing M_2 amplitudes were found in the southern Irish Sea after 14 ka BP, with the appearance of the Bristol Channel. Here the M_2 amplitude reached a maximum of 4.5 m at 10 ka BP, before decreasing to <4 m between 5 and 6 ka BP after which the M_2 amplitude increased to the present-day value of ~4.4 m.

As the enclosed Irish Sea was flooded, the M_2 amplitudes remained <1 m until 16 ka BP. Between 16 ka BP and 15 ka BP, the North Channel opened and connected the Irish Sea and the Malin Shelf/North Atlantic, and the maximum M_2 amplitude in the eastern Irish Sea doubled from 1.3 m to 2.6 m. The degenerate amphidromic point (tidal node) to the south of Ireland moved further north during deglaciation and moved progressively eastwards after 12 ka BP, to its present-day position near the eastern Irish coast (it remains degenerate). These results for the northern Celtic Sea and Irish Sea differ with respect to the pattern and timings of the results presented by Uehara et al (2006), due to the timings of submergence of the shelf in this area. In contrast to the Lambeck simulations, in the *ROMS+Bradley* simulations, the northern Celtic Sea remained flooded from 21 ka BP to the present-day.

There were also areas of high M_2 amplitude along the western Irish coast, which peaked in excess of 3.5 m at 19 ka BP, and remained >2.5 m until 12 ka BP, and >2 m until 10 ka BP. Uehara et al (2006) found that the M_2 amplitudes in this area were >2.5 m until 10 ka BP. During deglaciation, there were also high M_2 amplitudes along the north-western extent of the palaeo-coastlines on the shelf, along what is now the west coast of Scotland. From 21 - 11 ka BP these were >2.5 m and were particularly high (>3 m) and

migrated north between 16 and 12 ka BP, with a maximum M_2 amplitude of $\sim$4 m at 15 ka BP. In comparison, M_2 amplitudes remained >2.5 m until 10 ka BP in this area in the *KUTM+Uehara* palaeotidal model simulations.

The amphidromic point in the eastern North Sea was degenerate between 21 and 15 ka BP, with the exception of at 20 ka BP. After 15 ka BP, it moved progressively southeast as the North Sea deepened - at the same time the tidal amplitude along the eastern coast of Great Britain increased - and has remained in its approximate present-day location since 8 ka BP. Further, the present-day amphidromic point in the southern North Sea/northern English Channel appeared at 8 ka BP, which is 1 ka earlier than in the Lambeck case, and shifted eastwards to its present-day position by *ca.* 6 ka BP. As found by Uehara et al (2006), there were no significant changes in M_2 amplitude from 6 ka BP to present (*ROMS+Bradley*).

7.2.3   Changes in S_2 tidal elevation amplitudes

S_2 tidal elevation amplitudes remained <1 m across the entire model domain between 21 and 17 ka BP (Figure 7.6), after when there was an increase in S_2 amplitude along the west coast of Ireland, west of Scotland and along the north coast of France, as well as in the extending English Channel. In the region of the English Channel, the S_2 amplitude generally continued increasing until the present-day value of 1.6 m. A maximum S_2 amplitude of 0.9 m was observed along the western Irish coast at 17 ka BP; the maximum present-day S_2 amplitude in this region is 0.6 m. The S_2 amplitude west of Scotland reached a maximum of 1.2 m 2 ka later (at 15 ka BP) than the maximum west of Ireland. The higher S_2 amplitude continued to migrate north along the Scottish coast and down the east coast of the British Isles and into the North Sea after 11 ka BP. Since 9 ka BP, the S_2 tidal amplitude was higher along the east coast of Great Britain than along the western coasts of Ireland, Northern Ireland and Scotland. The overall trend in evolving S_2 amplitudes in the Bristol Channel was an increase from 21 ka BP to the present-day value of 1.4 m, having been >1m since 10 ka BP.

An S_2 amphidromic point appeared in the North Sea at 15 ka BP, and migrated south eastwards with the flooding of the North Sea to its present-day location in the German Bight. The S_2 amphidromic point in the English Channel followed a similar pattern of evolution as the M_2 amphidromic point in the region, emerging after 9 ka BP and migrating eastwards slightly to its present-day position.
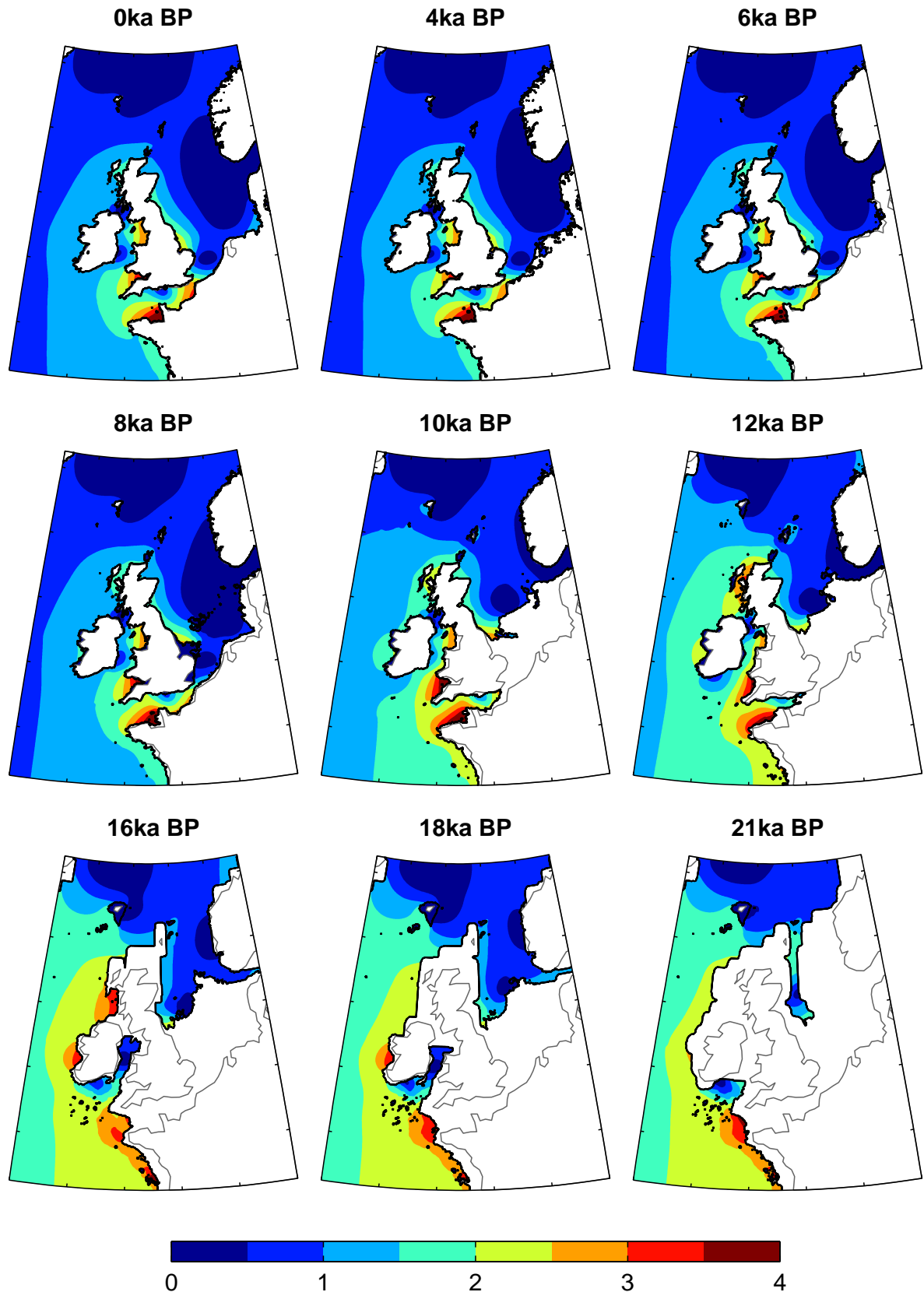
Figure 7.5: Modelled M$_2$ tidal amplitudes (colour scale, 0-4 m) and phases (dashed lines) for selected time slices from the *ROMS+Bradley* simulations. The black line is the palaeo-coastline, the white areas are land/ice and the present-day coastline is given for reference (grey line).
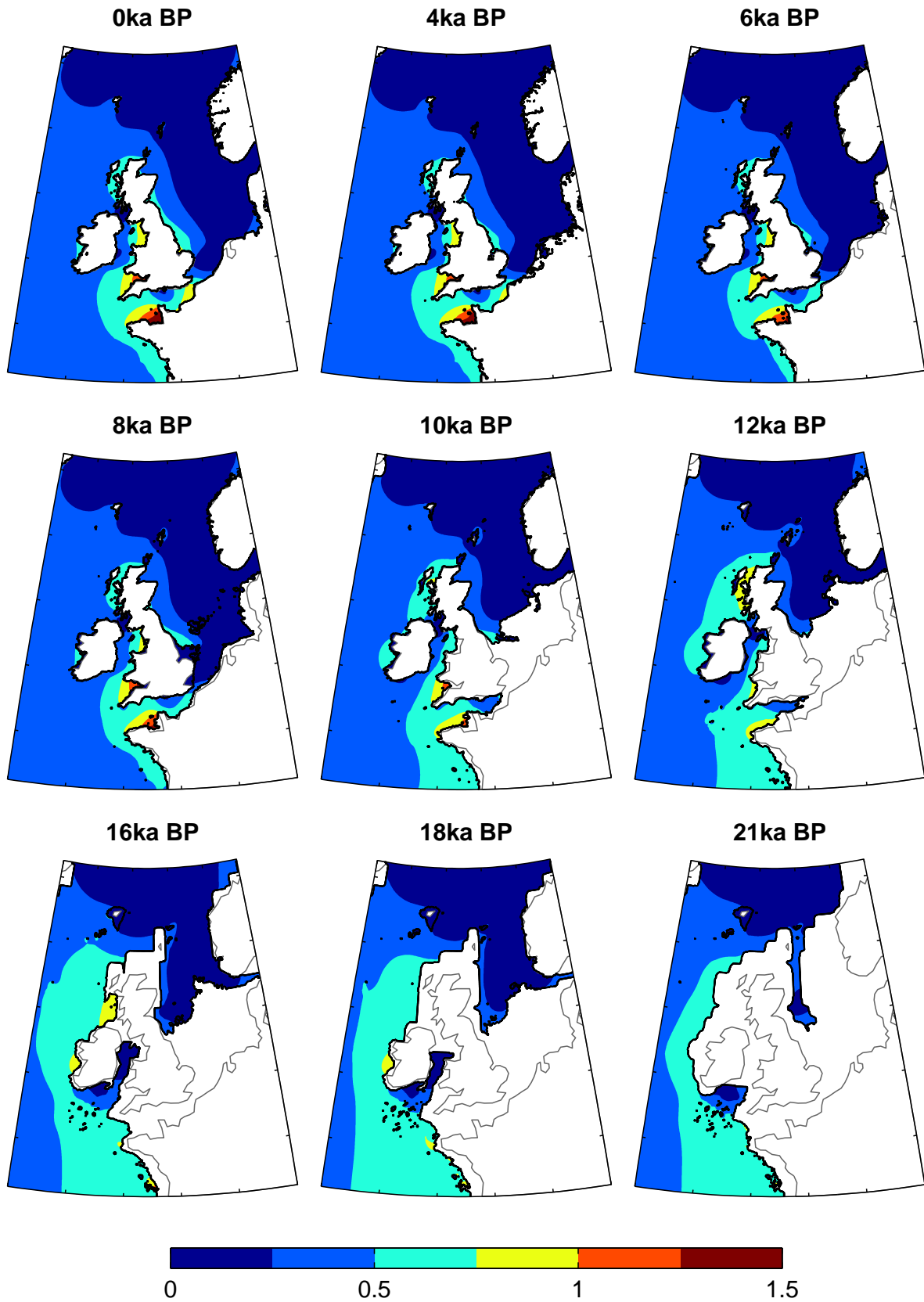
Figure 7.6: Modelled S_2 tidal elevation amplitudes (colour scale, 0-1.5 m) and phases (dashed lines) for selected time slices from the *ROMS+Bradley* simulations. The black line is the palaeo-coastline, the white areas are land/ice and the present-day coastline is given for reference (grey line).

7.2.4 Changes in BSS

The regions of high BSS on the NWESS have moved position considerably since the LGM, with increasing water depths and the changes in extent of the shelf seas. At present, regions of particularly high BSS are found in the Irish Sea and the North Channel, along the English Channel, near the Wash (east coast of Great Britain) and around the Orkney- and Faroe Isles. The peak modelled (near-bed) BSS for selected time slices during the deglaciation are presented in Figure 7.7.

Between 21 and 12 ka BP, there was a region of high peak BSS in the southern Celtic Sea. The water depth was <70 m, and a maximum BSS of 16 N m^{-2} was observed in this region at 21 ka BP (which relates to a current speed of 1.6 m s^{-1}). This region of high tidal currents in the southern Celtic Sea migrated northeast (onto the shelf) with rising sea levels, into the English and Bristol Channels as they formed. A clear divide in high BSS occurred in this region after 10 ka BP, moving into the English Channel and the Irish Sea. There were high tidal current speeds in the northern Irish Sea with the opening of the North Channel (between 16 and 15 ka BP) as the gateway between the Irish Sea and the North Atlantic, peaking at 18 N m^{-2} ($\sim$ 2.5 m s^{-1} bottom current speed) at 12 ka BP. Before 15 ka BP, high BSS in this region were confined to the Celtic Sea and were not observed in the enclosed Irish Sea.

High BSS were also observed at 21 ka BP south and west of the Faroe Isles (maximum of 24 N m^{-2}), and remained high until 16 ka BP. The minimum present-day water depth for the same region south of the Faroes is 120 m (in comparison to <20 m at 21 ka BP), and the peak BSS in the region is significantly lower (maximum of 2.4 N m^{-2}). There was also an area of divergence northwest of the Faroe Isles, most apparent before 14 ka BP, across the Faroe-Scotland ridge. The area of high BSS north of Scotland (around what is now Orkney) has decreased since the region was first submerged between 16 and 15 ka BP. There are still particularly high BSS south of Orkney, where peak modelled tidal current speeds are >3.5 m s^{-1} (i.e. BSS >35 N m^{-2}).

Between 21 and 12 ka BP, there was high BSS along the western shelf break, in particular along the edge of the Malin Shelf and west of Ireland, due to the flooding of the shelf in this region. The palaeotopography at 21 ka BP (Figure 7.2) shows the BIIS extended out to the shelf break in this area. As the North Sea flooded, an area of high BSS developed after 14 ka BP, southwest of Dogger Bank and along the north of the palaeo-coastline. BSS remained high along the east coast of the Great Britain at this latitude, in the area of the Wash.
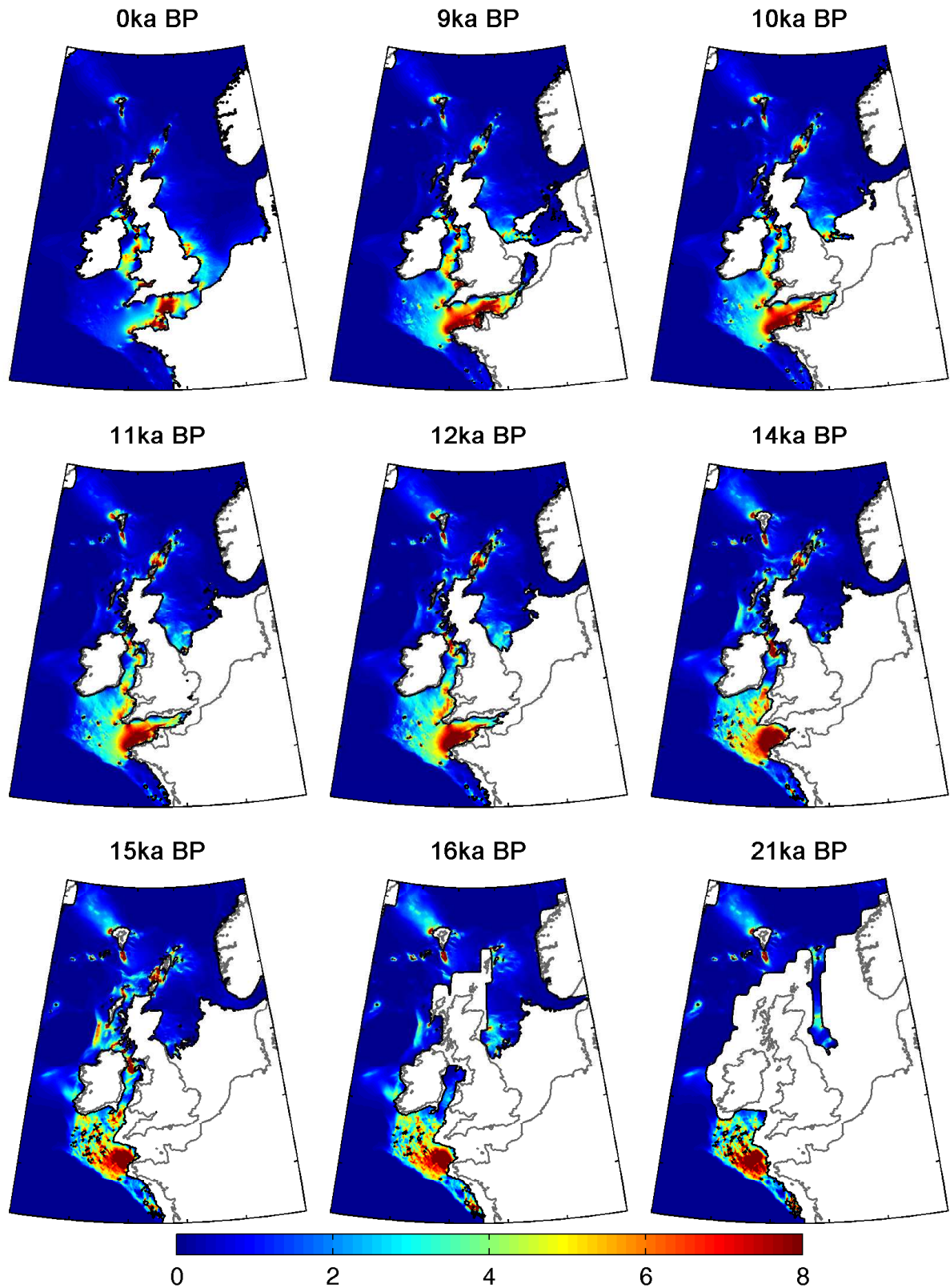
Figure 7.7: Magnitude of modelled peak near-bed BSS for selected time slices. The colour scale denotes the magnitude of the BSS (0-8 N m^{-2}, increasing red to blue). The black line is the palaeo-coastline, the white areas are land/ice and the present-day coastline is given for reference (grey line).

Figure 7.8 illustrates the differences in modelled BSS for the *ROMS+Lambeck* and *KUTM+Lambeck* simulations, the outputted BSS from these two models being near-bed and depth-averaged, respectively. At 21 ka BP, there were higher tidal current speeds in the southern Celtic Sea and along the southwestern margin of the shelf in the *ROMS+Lambeck* simulations. In many areas of the shelf the BSS was higher in the *KUTM+Lambeck* runs (blue areas in Figure 7.8). By taking the mean difference across the entire domain, the modelled present-day peak BSS was on average 0.5 N m^{-2} higher in the output from *KUTM+Lambeck* than from *ROMS+Lambeck*. This is most obvious across the Faroe-Scotland Ridge (and around the Faroe Isles) for all time slices, as well as west of Scotland during deglaciation (21-11 ka BP). Higher BSS evolved in the English Channel for the *ROMS+Lambeck* simulations, and remain so in the southern North Sea at the present-day.
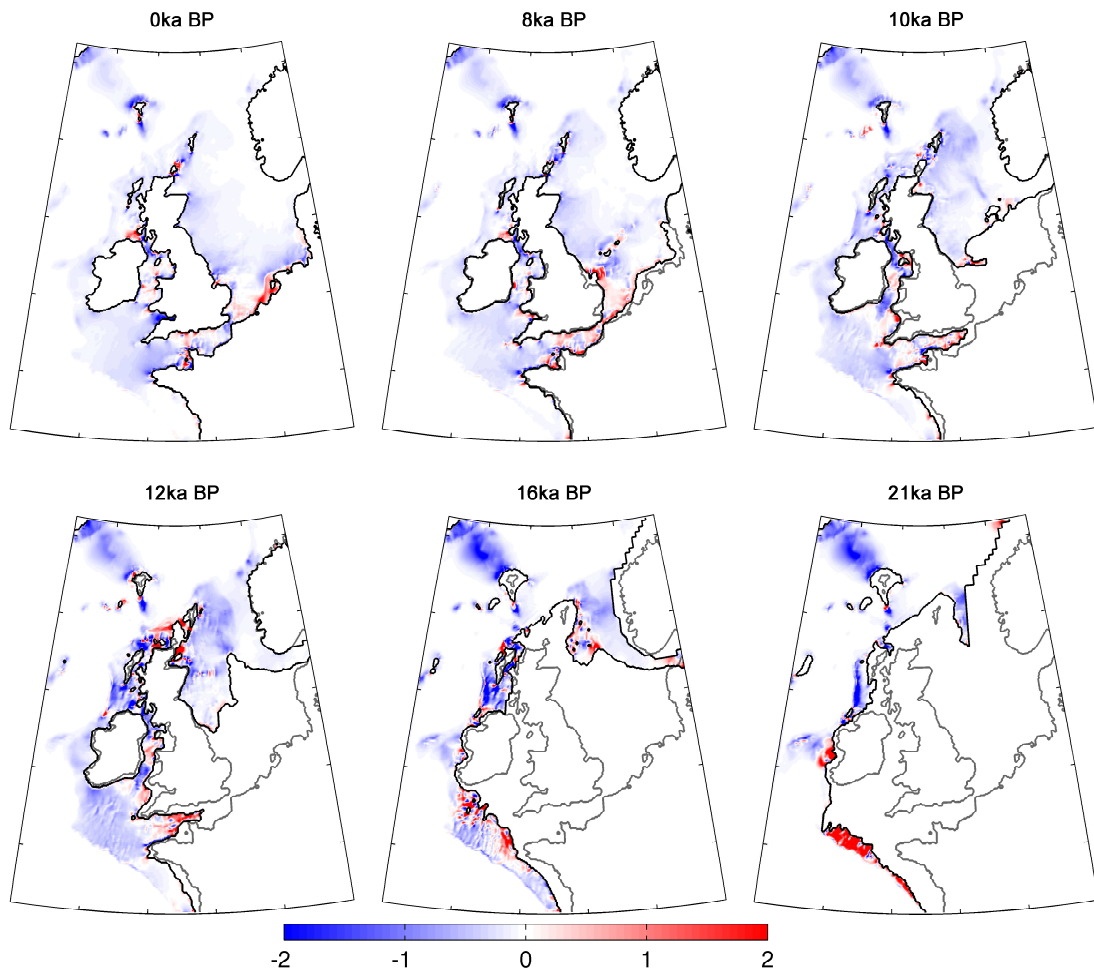
Figure 7.8: Difference between peak near-bed BSS output from *ROMS+Lambeck* and *KUTM+Lambeck* models, for selected time slices. The colour scale denotes the magnitude of the difference in BSS (and is set to saturate at ± 2 N m^{-2}) of the *ROMS+Lambeck* minus *KUTM+Lambeck*. The black line is the palaeo-coastline, the white areas are land/ice and the present-day coastline is given for reference (grey line).

7.3 Palaeotidal model output at the marine sediment core locations

The output from the palaeotidal model at the locations of the five cores are presented here, first for the *ROMS+Bradley* model, the outputs of which are then compared with existing palaeotidal model outputs, as well as with the new *ROMS+Lambeck* palaeotidal model output.

7.3.1 New *ROMS+Bradley* palaeotidal model

Figure 7.9 shows the changes in relative sea level at each of the core sites for 1 ka time slices since 21 ka BP. According to the Bradley GIA model, the locations of BGS19 and BGS65, in the eastern Irish Sea, were inundated between 16 and 15 ka BP. The relative sea level signals for these two core sites are similar, although the overall change in relative sea level at BGS65 since 15 ka BP was almost double that at BGS19 (which is further north). The relative sea level fall, resulting from the continued isostatic rebound from the retreat of the BIIS, is obvious at both sites since 7 ka BP. This is also apparent in the relative sea level signal at BGS87, although to a lesser extent, as it is situated further south in the Irish Sea, and thus further from the centre of loading of the BIIS. At the site of BGS166 between 20 and 15 ka BP, the relative sea level signal was dominated by the rapid glacial-isostatic rebound in the region, shown as a fall in relative sea level, after when the eustatic sea-level rise dominated. The relative sea level signal at BGS199 reflects most strongly the eustatic sea level rise since the LGM, with an overall increase in water depth of ∼80 m.
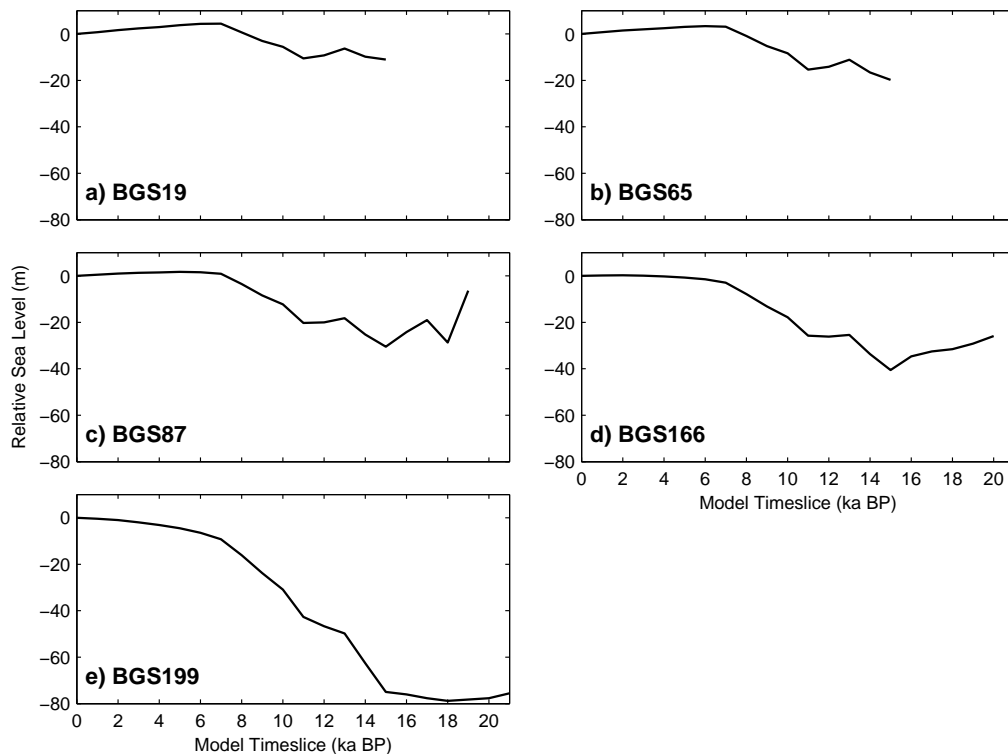
Figure 7.9: Model predictions of relative sea level at the five selected core sites from 21 ka BP to present, from the Bradley GIA model (Bradley et al, 2011).

The modelled evolutions of BSS at each of the five core locations are shown in Figure 7.10. At BGS19 and BGS65, there was an overall increase in BSS with time, in contrast

to an overall decreased BSS at the sites of BGS87, BGS166 and BGS199. The pattern of changes in BSS at BGS19 and BGS65 are similar, with maximum peak BSS of 1.4 and 1.6 N m^{-2} observed at both locations, respectively, at 9 ka BP. Since these core sites were inundated (between 16 and 15 ka BP), the BSS has remained higher at BGS65 than at BGS19, despite the deeper water at the location of BGS65 (Figure 7.11).
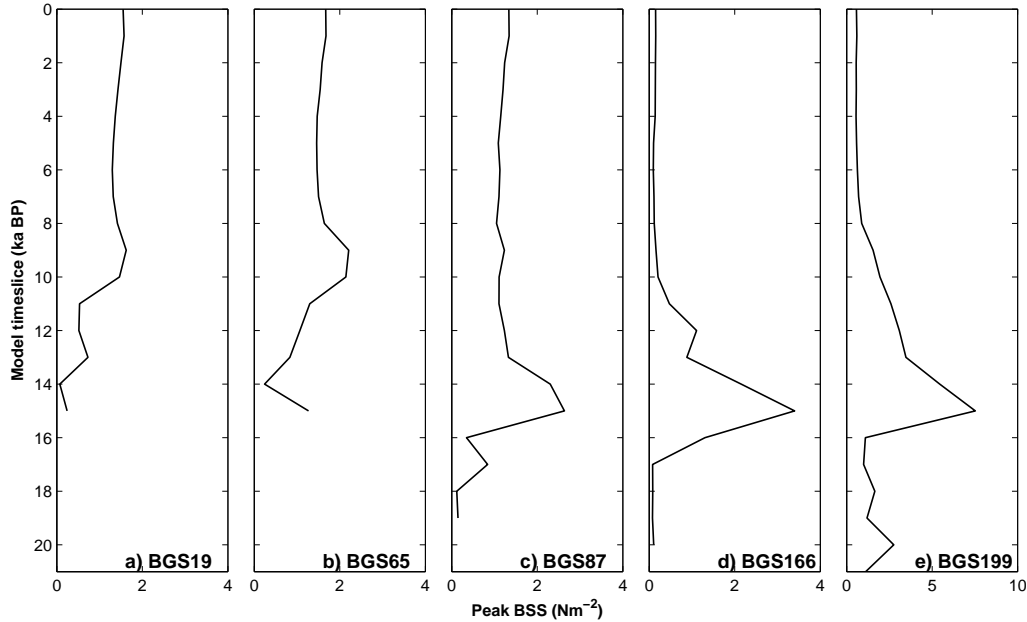
Figure 7.10: Modelled evolution of peak BSS (in N m^{-2}) at each of the core sites, plotted in 1 ka time slices from the LGM to present-day. Note the different scale for BGS199.

After the site of BGS87 was inundated (between 20-19 ka BP) and until 16 ka BP, the BSS was <1 N m^{-2}. Between 16 and 12 ka BP, the peak BSS at BGS87 was significantly higher, reaching a maximum of 2.6 N m^{-2} at 15 ka BP (which is coincident with the timing of the opening of the North Channel). This timing of the peak BSS at 15 ka BP was mirrored in the modelled BSS evolutions at BGS166 and BGS199, where the maximum modelled BSS were 3.4 N m^{-2} and 5.4 N m^{-2}, respectively. The BSS modelled at the site of BGS87 was not seen to change considerably after 12 ka BP ($\sim$ 1 N m^{-2}). Similarly, the magnitude of the peak BSS at BGS199 has been <1 N m^{-2} since 9 ka BP. The relative sea level fall at BGS19, BGS65 and BGS87 since 7 ka BP is reflected in the slight increase in BSS at each of the sites during this time.

7.3.2   Palaeotidal model comparison

It is important to note that the resolution of *ROMS+Bradley* model was twice as high as the other palaeotidal models, and so defining the core locations will have been more accurate. Figure 7.11 illustrates how the Bradley and Lambeck GIA models affected the

changing water depths at each of the core sites. The overall patterns of evolving magnitudes of BSS at the five core sites were similar in all the palaeotidal model simulations considered, although the magnitude and timing of the changes varied between models (Figure 7.12). The peak in simulated bed shear stress at 15 ka BP, most obvious at the locations of BGS87, BGS166 and BGS199, is likely due to the opening of the North Channel and hence the tide would have been able to propagate through the Irish Sea, and northwards through the North Channel onto the Malin Shelf.
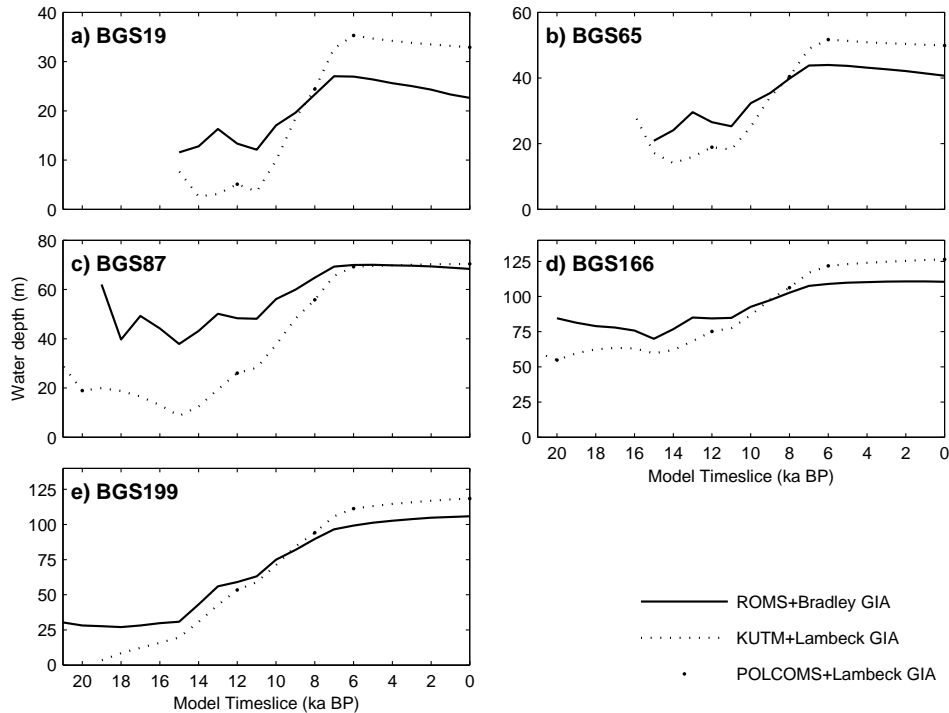
Figure 7.11: Water depths at the five core site for 1 ka time slices from the LGM to present-day, showing *ROMS+Bradley* (solid line), and the water depths in the *KUTM+Lambeck* and *POLCOMS+Lambeck* models (dotted line, with points showing the time slices of the *POLCOMS+Lambeck* palaeotidal model).

The timing of submergence of the site of BGS19 (15 ka BP) was consistent between palaeotidal models. Despite the similar pattern of changes in BSS at this core site between palaeotidal model simulations, the output from *ROMS+Bradley* were found to be consistently higher than for the models which incorporated the Lambeck GIA model. There were also greater fluctuations in the BSS output from the *ROMS+Bradley* model, in particular before 9 ka BP. The outputs of BSS from the different palaeotidal models at the site of BGS65 were more comparable than at BGS19 (with the exception of *POLCOMS+Lambeck*, the outputs from which were consistently lower), with approximately the same magnitude maximum peak BSS being output by three models at 9 ka BP (~ 2.2 N m^{-2}).

For BGS87 the output of the various palaeotidal models for 9 ka BP to present-day
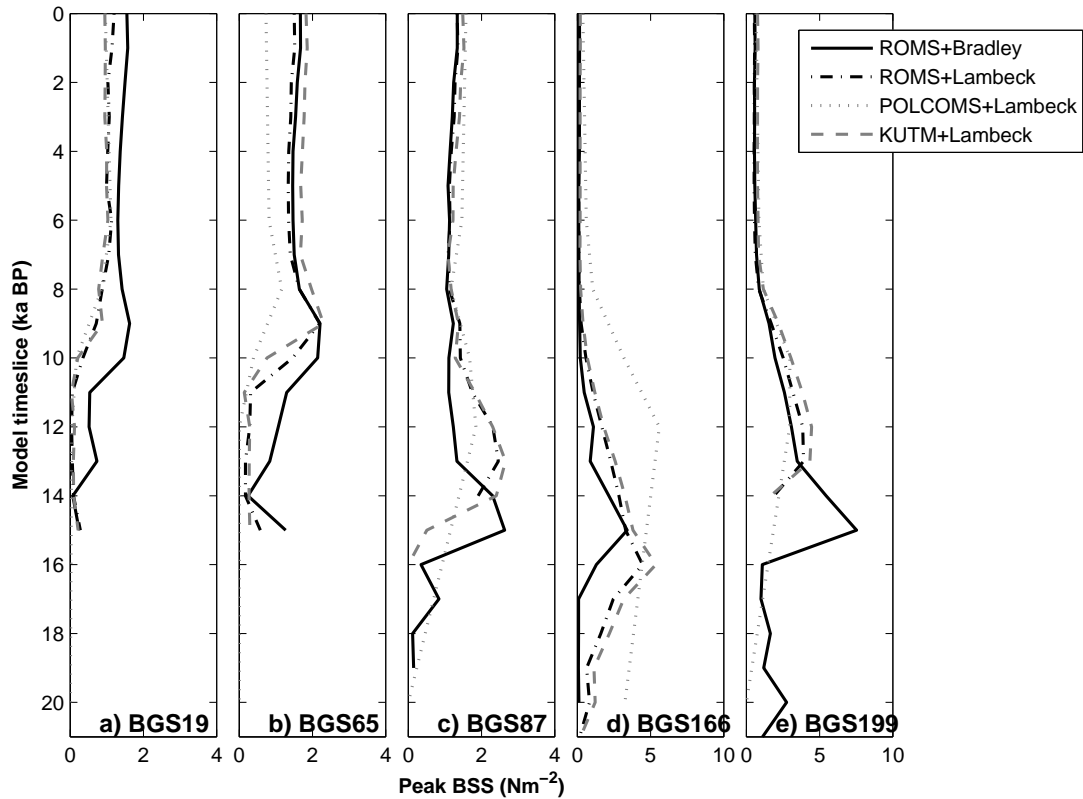
Figure 7.12: Modelled evolution of peak BSS (in N m^{-2}) at each of the core sites for *ROMS+Bradley* (solid black line), *ROMS+Lambeck* (dashed black line), *POL-COMS+Lambeck* (dotted grey line) and *KUTM+Lambeck* (dashed grey line). Note the different scale for BGS166 and BGS199.

were of similar magnitude. The peak BSS observed at this core site occurred 2 ka earlier in the *ROMS+Bradley* simulations than in the other palaeotidal model output. The *ROMS+Bradley* simulations suggested no significant change in BSS at BGS87 since 13 ka BP, and in the Lambeck simulations since 9 ka BP.

The increase in BSS at the site of BGS166 in the early stages of deglaciation happened much earlier in the model runs with the Lambeck GIA model. In contrast, the BSS remained low until 17 ka BP for *ROMS+Bradley*. In contrast to the differences at BGS87, the peak BSS from the *ROMS+Bradley* at BGS166 was observed 1 ka BP later (i.e. at 15 ka BP) than in the other palaeotidal models, after when the general trend in decreasing BSS was observed in all simulations.

The modelled evolution of BSS at BGS199 followed a similar pattern to that in BGS166,

the peak BSS being observed in *ROMS+Bradley* earlier by 2-3 ka, and considerably higher (5.4 N m^{-2}) than in the other output from palaeotidal models which incorporated the Lambeck GIA model (i.e. ~ 4 N m^{-2}). In contrast to the Lambeck GIA runs, this core site remained inundated throughout all *ROMS+Bradley* simulations.

7.4 Comparing observed grain size evolutions and modelled BSS

The grain size evolution profiles for the dated extent of four cores are plotted in combination with the modelled BSS evolutions at the core sites in Figure 7.13. The results for BGS166 are not included in this section, as it was not possible to generate an age-depth model for this core. The trends in evolving grain size and BSS over time are described below, and the significance of the trends are illustrated in the regression analysis plots in Figure 7.14. No single palaeotidal model had a consistently better fit with the trends in observed changes in grain size, thus the focus is on output from the new *ROMS+Bradley* palaeotidal model.
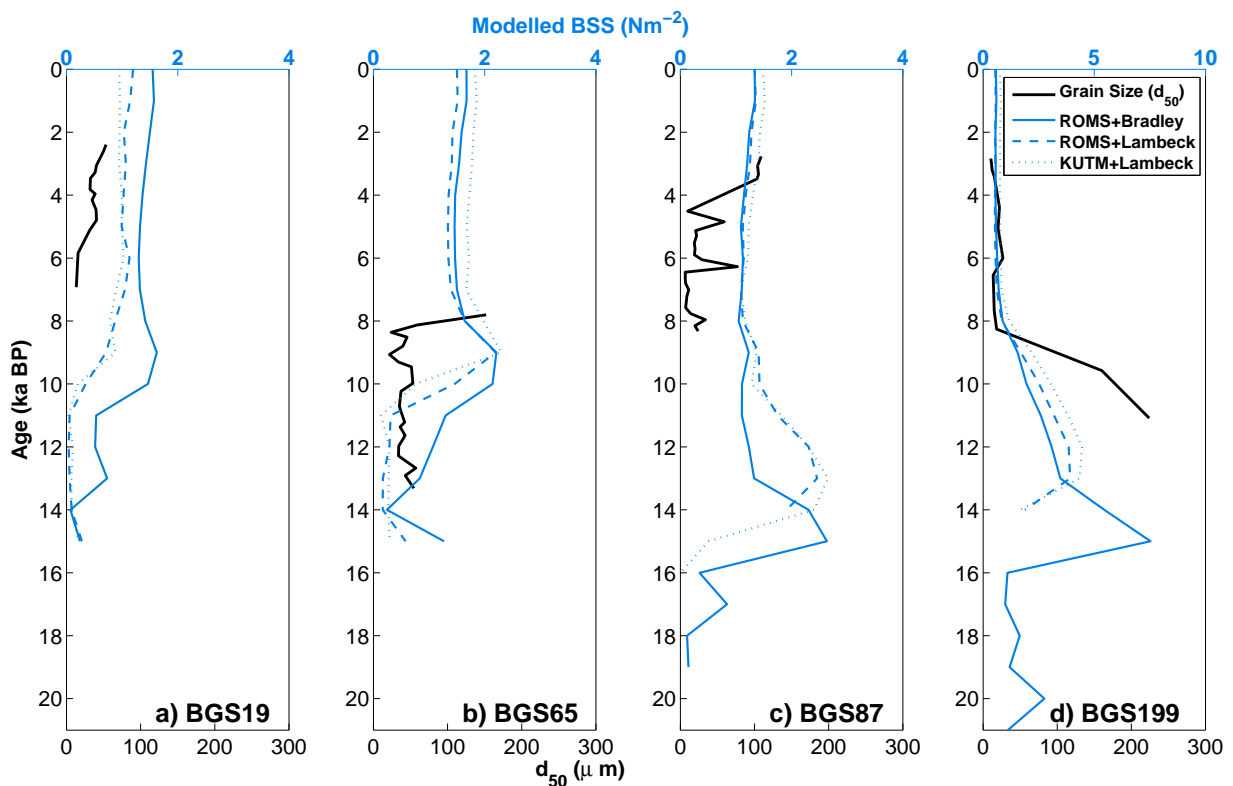
Figure 7.13: Comparison of changes in modelled BSS (blue lines and axis, *ROMS+Bradley*=solid, *ROMS+Lambeck*=dashed, *KUTM+Lambeck*=dotted) at the core sites and observed median grain sizes (solid black lines) within the dated extents of the cores. The scales for peak BSS and grain size are consistent, with the exception of BGS199.

For BGS19, the increase in modelled BSS between *ca.* 7 and 2 ka BP was mirrored in the general coarsening of observed core sediments. However, the modelled increase in BSS during this time was very slight, from 1.1 to 1.2 N m^{-2}, and the observed median grain size remained <63 μm, which is within the Wentworth classification for mud. The correlation between the observed grain size and modelled BSS for BGS19 are statistically highly significant, i.e. the r^2 value was greater than that for the 1% correlation coefficient for a sample size of 6 (Figure 7.14a).

A sharp increase in modelled BSS at BGS65 occurred between 11 and 9 ka BP, during which time no major change in grain size was observed. At *ca.* 8 ka BP, however, there was a significant increase in median grain size, from a mud (<63 μm) to a sand, as a d_{50} of 150 μm was observed in the top sample of the core (which was dated to 8 ka BP). The timing of this major change in observed grain size in BGS65 did not correlate well with the modelled changes in BSS, as can be seen from the poor correlation coefficient shown in Figure 7.14b.

Although the correlation between the observed median grain size and modelled BSS for the dated extent of BGS87 was not statistically significant ($r^2 < 0.5$), the fluctuations in both the data and model output were only slight. The grain size within BGS87 between *ca.* 8 and 3 ka BP (which was almost the entire length of the core) only varied within the *very fine sand and mud* category of the GSTCP, i.e. <125 μm. Similarly, the model variations in BSS within this period were only small (between 1 and 1.2 N m^{-2}).

As was found for BGS19, a very significant model-data correlation ($r^2 > 0.9$) was observed for the dated extent of BGS199 (*ca.* 13 to 3 ka BP, Figure 7.14d). There were, however, discrepancies in the timing of the major changes in both the observed grain size and modelled BSS in this core/at this core location. A significant fining of median grain size was observed between *ca.* 11 and 8 ka BP, from fine sand to mud, and the mud continued for the remainder of the dated core extent.

7.4.1   Reconstructing observed grain size evolutions using modelled BSS

The GSTCP developed in Chapter 4 was applied to the palaeotidal model outputs of BSS. The grain size predictions based on the modelled BSS at each core location, for the model time slices within the age models for each core section, could thus be compared with the observed grain sizes, as presented in Figure 7.15. The focus remained on the first-order relationship, and thus the observed grain sizes and the predicted grain sizes were converted to sediment classifications, as in the development of the GSTCP, namely very fine sand
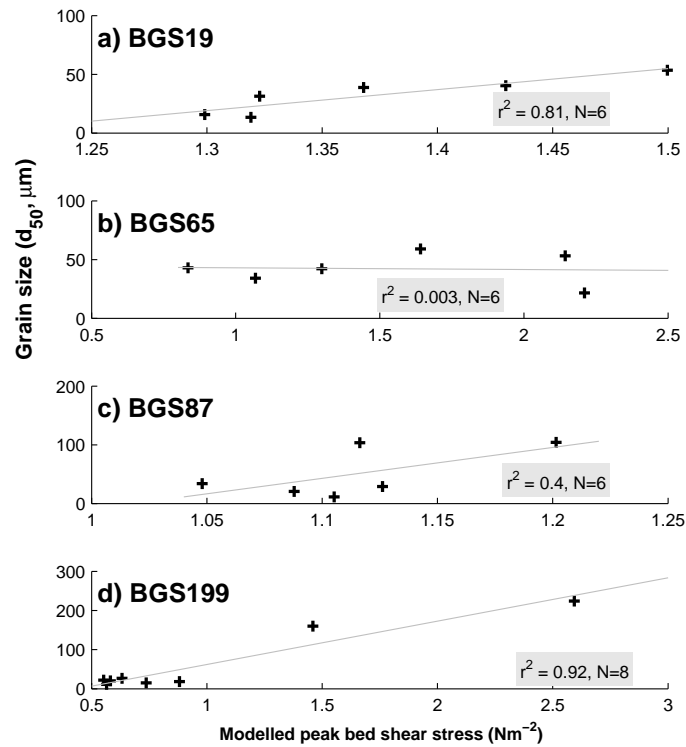
Figure 7.14: Correlation between observed median grain size (d_{50}) from the dated extents of the four sediment cores and the modelled peak BSS at the core locations for the corresponding time slices. The critical correlation coefficient for the 5 % coefficients are $r^2 = 0.5$ (n=6) and $r^2 = 0.4$ (n=8) and for the 1% coefficients are $r^2 = 0.7$ (n=6) and $r^2 = 0.6$ (n=8), respectively. Note the varying scales.

and mud (<125 µm), fine sand (125-250 µm), medium sand (250-500 µm), coarse sand (500-1000 µm), very coarse sand (1000-2000 µm) and gravel (>2000 µm).

The GSTCP over-predicted the grain sizes at all four locations. Interestingly, in each case, reducing the predicted grain size by a factor 10 (and then classifying the grain size) produced a better fit with the observed grain sizes. These results are also included in Figure 7.15.

The median grain size in the dated extent of BGS19 was very fine sand and mud. According to the GSTCP, very fine sand and mud is found in areas with BSS <0.25 N m^{-2}. The modelled BSS for the corresponding time slices was >1.5 N m^{-2}. There was poor correlation between changes in patterns of observed grain size and modelled BSS at BGS65, however, the observed variations in both were low. The grain size produced by the GSTCP, in this case coarse sand, did not correlate well with the observed grain sizes (very fine sand and mud). Similarly, applying the GSTCP to the BSS outputs of BGS87 between 8 and 2 ka BP over-estimated (coarse sand) the grain size in comparison to the observed grain sizes, which remained finer than fine sand. The isolated observed peak of fine sand at *ca.* 6.3 ka BP was not reflected in the model output for 7 nor 6 ka BP, and
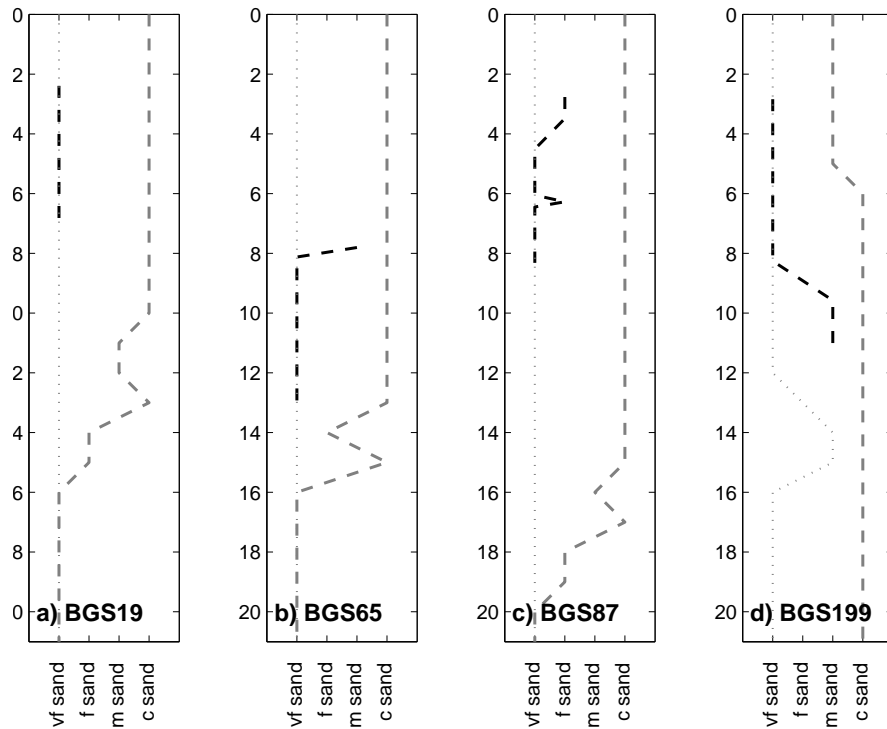
Figure 7.15: Evolutions of classifications of observed grain sizes (dashed black lines) and classifications of grain sizes calculated using the GSTCPs for peak BSS (dashed grey lines) for BGS19, BGS65, BGS87 and BGS199. The thin grey dotted lines show the grain size classification predicted by decreasing the results of the GSTCP by a factor 10. The labels on the x axes refer to clay, very fine sand and mud, fine sand, medium sand and coarse sand.

neither was the observed coarsening of grain size between 4 and 5 ka BP mirrored in the GSTCP results.

Despite the strong correlation between the trends in changing modelled BSS and observed grain size at BGS199 (between 11 and 2 ka BP), it was not possible to reconstruct the observed grain size evolution using the GSTCP. Between 10 and 8 ka BP, the observed grain size decreased from a medium sand to a very fine sand and mud. A change from coarse sand to medium sand predicted by the GSTCP occurred considerably later, between 6 and 5 ka BP. Using a much reduced GSTCP (i.e. using the BSS divided by 10), generated the observed changes in grain size more successfully, although the fining from coarse sand to very fine sand and mud was predicted too early, between 14 and 12 ka BP.

To explore whether the misfits between the modelled and observed grains size evolution profiles were due to spatial inaccuracies in the palaeotidal model set-up, a 'nearest-neighbour' approach was taken. The BSS output in the eight grid cells surrounding the model grid cell which was closest to the core location were compared (Figure 7.16). Con-

sistently, similar trends in BSS evolution were observed in all grid cells surrounding the core sites, with most variability in the areas surrounding BGS19, most likely due to the proximity of this core site to the coast (and the shallow water).
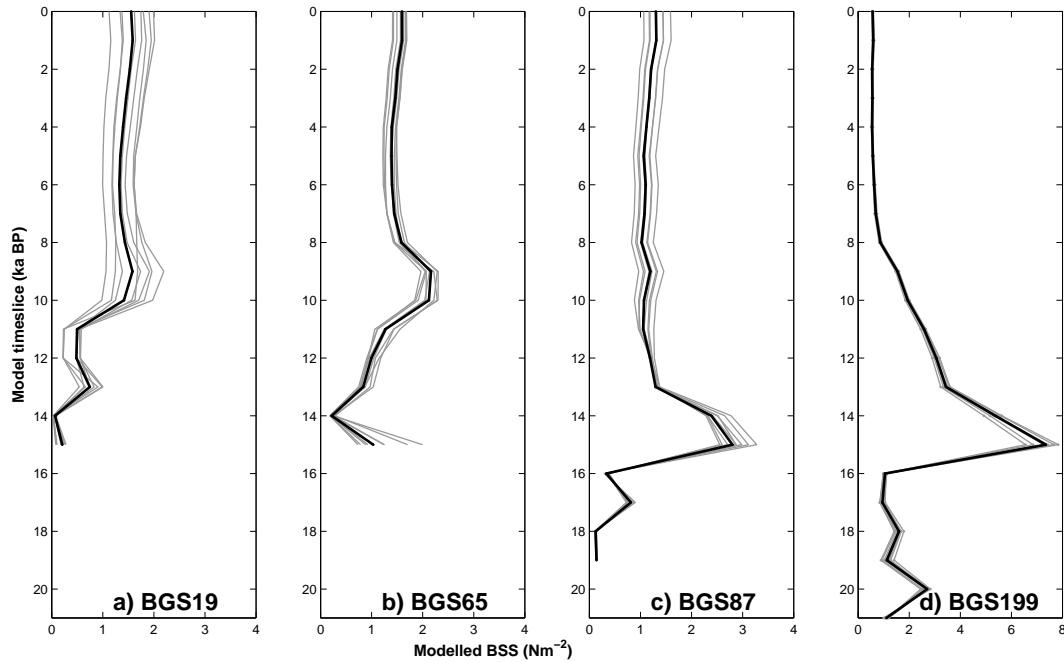
Figure 7.16: Modelled BSS evolution at the core sites (black line) and in the eight model grid cells surrounding the core site (grey lines).

7.5 Predicting past seabed sediment distribution on the NWESS

Despite the limitations of the applying the GSTCP to palaeotidal model output of BSS at specific core locations, the GSTCP has been shown to reproduce the large-scale (regional) patterns of present-day seabed sediment type. The output from the regional palaeotidal model for each time slice has been used to generated predictive maps of past seabed sediment classifications on the NWESS, a selection of which are presented in Figure 7.17.

The predicted seabed sediment distributions on the shelf did not change considerably from 6 ka BP onwards. Coarse sands and gravels are predicted to have been present in the region of high BSS in the Celtic Sea and west of northern France at 21 ka BP. This area of coarse sediments followed the region of high BSS as it migrated northwards into the Irish Sea (after 15 ka BP) and eastwards into the opening English Channel. Despite the higher BSS predicted west of Ireland and Scotland during deglaciation, these were predicted to only be high enough to transport sediments up to medium sand. According to the proxy, fine sands and very fine sands might be found in these regions at the present-day.

The Faroe Islands are located on the Greenland-Scotland Ridge, the section of this ridge
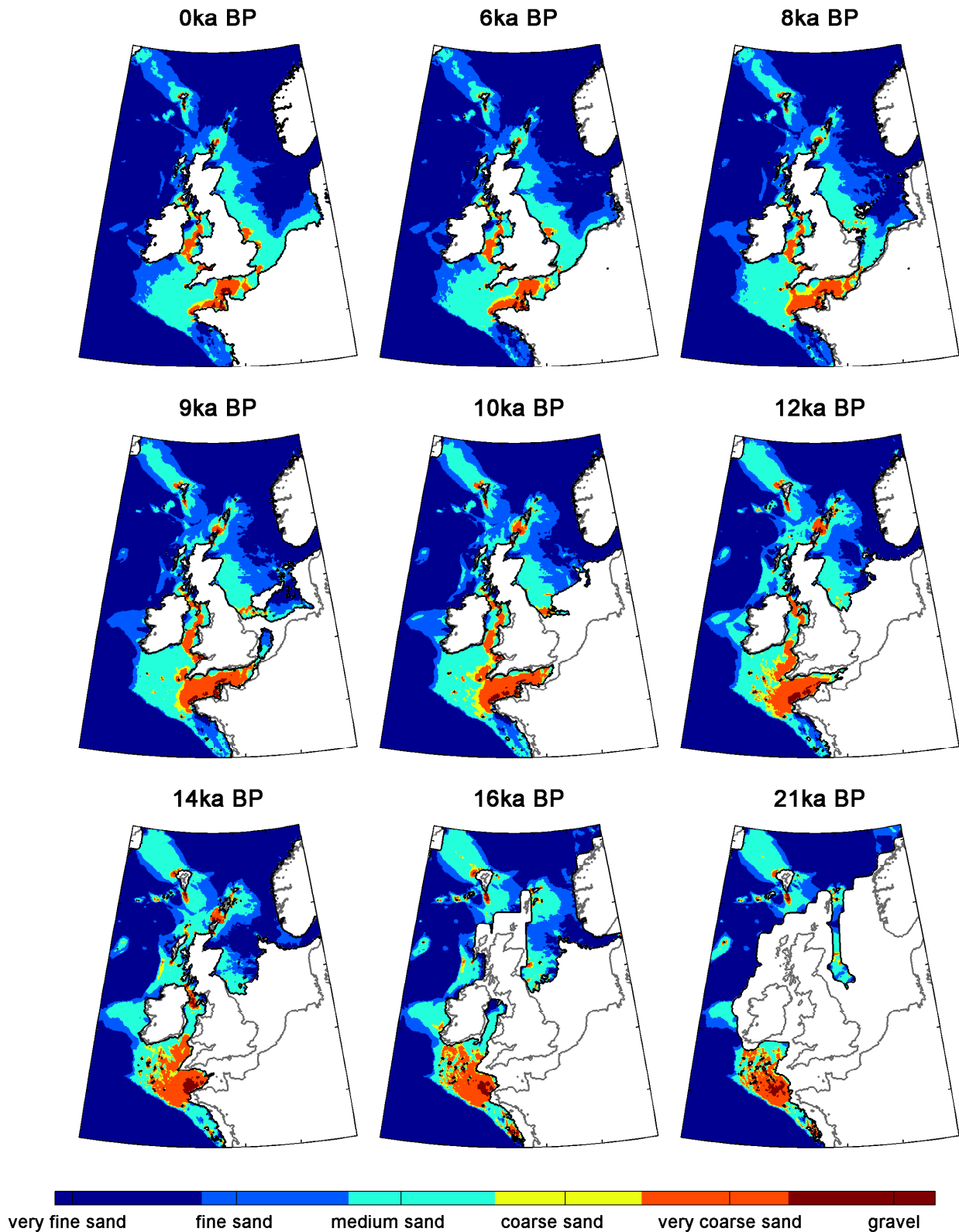
Figure 7.17: NWESS seabed sediment type predicted by the GSTCP for various time slices since the LGM. The black line is the palaeo-coastline, the white areas are land/ice and the present-day coastline is given for reference (grey line).

extending south of the Faroe Islands is referred to as the Faroe-Scotland Ridge, north and south of which are the Norwegian Sea and the North Atlantic Ocean, respectively. The GSTCP predicts a fining of seabed sediment sediments over the Faroe-Scotland Ridge since deglaciation, from medium sand with patches of coarse sand between 21 and 15 ka BP, to predominantly medium sand until 8 ka BP, to mainly fine sand with patches of medium sand at present.
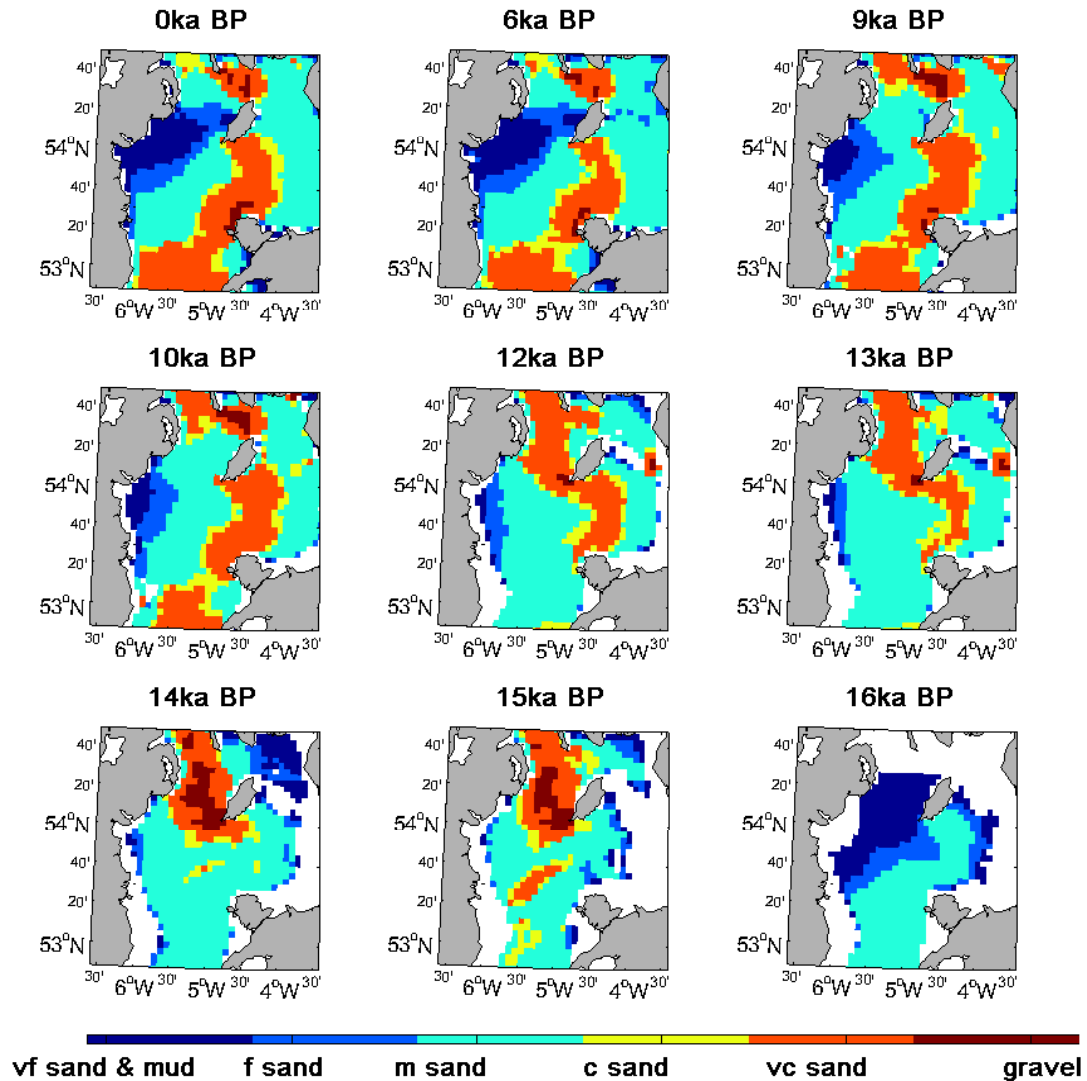
Figure 7.18: Seabed sediment type predicted by the GSTCP for various time slices since the LGM, for the region of the present-day Western Irish Sea Mud Belt. For reference, the grey areas show the present-day land, and the white areas are land/ice.

As described in Section 7.2.4, the flooding of the Irish Sea and the opening of the North Channel resulted in large changes in BSS in the Irish Sea. The predicted effect of these changing currents on the seabed sediment type are shown in Figure 7.18. The low

tidal amplitudes and tidal currents in the area prior to 15 ka BP indicate that predicted currents were only strong enough to transport sediments finer than medium sand. The GSTCP predicted that after 15 ka BP, there was an area of coarse sands and gravel in the western Irish Sea, which migrated northwards until 11 ka BP, after when it shifted eastwards to form the present-day area of coarser sediments north of the Isle of Man. After 15 ka BP, there was predicted to be an area of fine sediments along the emerging east coast of Ireland. This suggests that significant quantities of finer sediments would have only started accumulating in the western Irish Sea after 11 ka BP. By 10 ka BP, this area of mud and fine sands were extending eastwards into the western Irish Sea, reaching the Isle of Man between 8 and 7 ka BP, thus forming the Western Irish Sea Mud Belt. The extent of this muddy area has remained relatively constant since 6 ka BP.

7.6   Discussion

On the whole, the fluctuations in grain sizes within the cores were subtle and much of the dated extent of the cores had grain sizes finer than those used to develop the GSTCP. The changes in modelled BSS and observed grain sizes were not well correlated. Furthermore, the GSTCP did not resolve the fluctuations in the observed grain sizes and consistently over-predicted the sediment core grain sizes. At this point it should be noted that the GSTCP was developed based on a sediment dataset which had been sieved, whereas the particle size analysis of the sediment cores was conducted on a laser particle sizer, where the former has a bias towards coarser sediments (Poizot et al, 2008). The results presented here indicate the first order GSTCP, which was shown to successfully reproduce large-scale seabed sediment patterns (Chapter 4), does not successfully reproduce observed sediment grain sizes at the core locations. There is likely to be significant local variations in both hydrodynamic and sedimenotological processes, which the GSTCP, when applied to palaeotidal model output of BSS, cannot reproduce. The proxy is thus considered to not be suitable for application to sediment cores as a proxy for past tidal current conditions. The fine sediments in the core samples highlight that the proxy would benefit from further work on quantifying the relationship between modelled BSS and fine (cohesive) seabed sediments. Higher resolution (palaeo) tidal models would also be beneficial for better resolution of small scale variations in hydrodynamics.

Although there were slight differences in the modelled BSS between the different palaeotidal model simulations, the overall trend in changes at each core site were similar between models. It is unlikely that all of the palaeotidal models were under-performing

to such a degree that this could explain the discrepancy between the changes in grain size and modelled BSS. The differences in the relative sea level at the core sites between the different palaeotidal models is evident in the modelled BSS. For examples, BGS19 is very close to the present-day coastline and was taken from considerably shallower water (26 m) than BGS65 (48 m), although the relative sea level curves indicate that both core sites were inundated between 16 and 15 ka BP (Figure 7.9). Between 15 and 7 ka BP, the relative sea level at BGS65 was almost double that at BGS19, after when the GIA signal from the BIIS was slightly greater at BGS19 (resulting in relative sea level fall). These relative sea level signals are consistent with BGS19 having been taken from a site further north than BGS65, closer to the centre of loading of the BIIS.

The difference between the age-depth models for BGS19 and BGS65 is interesting given their proximity to each other. Such a large difference is not seen in the model output of BSS, as a very similar pattern of changing BSS is seen in the locations of BGS19 and BGS65. This highlights the fact that it is unlikely that a tidal model of this spatial resolution is resolving local-scale variations in tidal dynamics. The dated extent of BGS19 was fine ($<100\mu m$), with a slight increase in grain size with time observed. These fluctuations in grain size were too fine to be resolved by the GSTCP, despite the fact that there was a very slight increase in modelled BSS at the core site after 6 ka BP. The fine sediments in BGS19 are likely to display some cohesive behaviour, which was not accounted for in the calculation of the GSTCP. The *ROMS+Bradley* tidal model simulated slightly higher BSS at BGS19 than the other palaeotidal models, likely a result of the shallower water depth at this core site from 8 ka BP onwards.

There was very little correlation between changes in modelled BSS and observed grain size at BGS65, which could be a result of the site of BGS65 not actually being tidally dominated, or perhaps it is so close to the shore that consideration should be made of the sediment influx to the area. In the core top sample taken from BGS65, the sediment is coarser than in the majority of the core. This is consistent with the visual observations; the core top was unconsolidated, and contained some pebbles and shell fragments. The unconsolidated nature of the top section of the core supports the idea that significant sediment reworking may have occurred, or that the sample may have been disturbed prior to sampling, and hence that the radiocarbon age of the allochthonous mollusc sample is erroneously old. The presence of this coarser material could suggest that finer sediments may have been washed away by higher tidal energies more recently, exposing older sediments which have been sorted by the currents. The modelled BSS at this core site does increase

slightly from 6 ka BP onwards, increasing from ~ 1.3 N m^{-2} (at 6 ka BP) to ~ 1.6 N m^{-2} (at 1 ka BP), likely a result of the decreasing water depth. Further, the sediment in the area of BGS65 may have been deposited and eroded a number of times, thus affecting the apparent age of the surface deposits; however, without higher resolution radiocarbon analysis of the core, it is difficult to draw a conclusion as to how far down the core this apparent mixing has an effect.

BGS65 is relatively poorly age-constrained, having only been dated at the core top and bottom, but the extent of BGS65 is older than the entire dated length of BGS19 ($\sim$4 m). Based on the radiocarbon age of the single mollusc sample (*Corbula gibba*), sedimentation at the location of BGS65 appears to have stopped over 7000 years ago. This apparently old surface sediment may be an indication of either deposition of a terrestrial source of ^{14}C known to influence radiocarbon ages in the area (Benoit et al, 1979), or due to reworking of older marine deposits (Kershaw, 1986). A further possibility is that there has been net erosion at this site since 7 ka BP, thus removing the sedimentary record, although this is unlikely given the minimal increase in modelled BSS since 7 ka BP, and since the coastal embayments in the eastern Irish Sea have previously been considered to be acting as a sediment sink (Aston and Stanners, 1982; Kirby et al, 1983; Kershaw, 1986).

BGS87 was taken from water 72 m deep in the middle of the Irish Sea, in an area which was flooded 4 ka earlier (between 20 and 19 ka BP) than the core sites further north (BGS19 and BGS65). In BGS87, no material suitable for radiocarbon dating existed above 0.2 m, which was dated to *ca.* 2750 yr cal BP. Most of the sediment within the dated extent of BGS87 was within the mud fraction and thus is likely to display cohesive behaviour. Very little variation in modelled BSS was seen at this core site within the last 8 ka, and this was observed in all of the three palaeotidal models considered. The GSTCP significantly over predicted the grain size at BGS87 (coarse sand) between 8 and 2 ka BP. The grain size evolution profile of BGS87 suggests a considerable change in either the hydrodynamics, or the sediment supply, within the last 3.5-2.5 ka, which is equivalent to the top 1.5 m of the core. There is an overall increase in modelled BSS of about 0.3 N m^{-2} from 8 ka BP to present-day, and this general increasing trend is displayed in the grain size profile for this core, although the changes in both BSS and grain size are minimal. At the site of BGS87, there is little modelled change in water depth (relative sea level) during the last 8 ka, which corresponds to the majority of the dated extent of this core. It is likely that the coarsening of sediments within the last 3 ka was due to factors other than the shallower water.

An opposite grain size evolution is observed in BGS199 in comparison with the three other cores, with an obvious upwards fining sequence before 8 ka BP. BGS199 shows the greatest grain size variation, which is mirrored in the considerable decrease in modelled BSS at the site prior to 8 ka BP. There has been ongoing relative sea level rise at the site of BGS199 since 15 ka BP, whereas there has been a relative sea level fall at each of the three other core sites since 7 ka BP. Since there is no grain size data from this core deeper than 4.25 m, which is interpolated to being at *ca.* 11 ka BP, it is not possible to deduce whether timing of the change in grain size at this core lags behind the change in modelled BSS, which decreased since 15 ka BP. Both observed grain size and modelled BSS have remained relatively consistent from 8 ka BP onwards. The relationship between changing modelled BSS and grain size at this core site suggests that changing tidal dynamics have a more dominant effect than at any of the other core sites considered. Further, the site of BGS199 is modelled to shift from being transitionally-stratified to seasonally stratified between 9 and 8 ka BP, and the change in tidal dynamics that caused this appear to be reflected in the (upwards fining) grain size profile, since coarser sediments tend to be found under mixed waters (Scourse et al, 2002). Each of the three remaining core sites are modelled to be transitional for the model time slices relating to the dated core extents.

7.7   Summary points

- The GIA model of Bradley et al (2011) generated significantly different patterns of relative sea level change on the NWESS than the revised GIA model of Lambeck (1995), which had been incorporated into existing palaeotidal models of the region. The differences in the GIA models were most pronounced between 21 ka BP and 11 ka BP.

- The overall pattern in the changing M_2 and S_2 elevation amplitudes modelled by the *ROMS+Bradley* palaeotidal model was similar to existing palaeotidal model output, although there were differences in the timings of the major changes. The enlarged M_2 tidal amplitudes observed along the western extent of the palaeo-coastline during the early deglacial period are consistent with the findings of previous modelling studies for North Atlantic megatides during the LGM, e.g. Egbert (2004).

- Using different GIA model output in the generation of palaeotidal model bathymetric grids can have a considerable impact on the magnitude of modelled BSS. Further, BSS computed using depth-averaged or near-bed tidal current speeds vary, although using

the depth-averaged tidal current magnitudes did not consistently produce higher calculated BSS.

- Between 21 and 16 ka BP, the region with the most intense BSS was the shallow southwestern area of the shelf (the present-day southern Celtic Sea). This area of high BSS migrated northeast into the emerging English Channel, and subsequently northwards into the Irish Sea after the North Channel opened between 16 and 15 ka BP. High BSS have been found in the region of the Orkney Isles, north of Scotland, since the area deglaciated between 16 and 15 ka BP.

- The overall trends in modelled BSS evolution at the core locations were consistent between palaeotidal models, although the timing and magnitude of significant changes varied. With the exception of at the site of BGS19, the BSS output by the four palaeotidal models at each of the core locations was comparable from 8 ka BP onwards. At BGS19, the BSS modelled by *ROMS+Bradley* was consistently higher than the BSS output by other palaeotidal models.

- The general trends in observed (median) grain size evolutions at BGS19, BGS87 and BGS199 were seen in the modelled evolutions of BSS for the time slices relating to the dated extents of the cores. No correlation between changing grain size and modelled BSS was found for BGS65, although variations in both were low.

- Applying the GSTCP to the model output of BSS consistently over-predicted the observed median grain size. Reducing the observed grain size by a factor 10 produced a better fit.

- Despite the limitations of the GSTCP for reproducing observed sediment classifications at specific sites, the GSTCP was applied to the regional model output of BSS to generate predictive maps of seabed sediment distribution on the shelf since the LGM. These maps suggest that the Western Irish Sea Mud Belt began forming after 14 ka BP, and had reached its approximate present-day spatial extent by 6 ka BP.

8 Discussion

8.1 An updated palaeotidal model for the NWESS

A new three-dimensional palaeotidal model for the NWESS has been developed, which incorporates the latest GIA model output available for the region, and driven by evolving palaeotidal boundary conditions. Using palaeotidal model output for 1 ka time slices, from 21 ka BP to the present-day, the influence of changing sea levels on the tidal dynamics on the shelf are compared with previous palaeotidal model output. The main influence on the timings and magnitude of changes to tidal dynamics is relative sea level, since considerable differences were found between palaeotidal models of the region which incorporated the GIA models of Lambeck (1995) and Bradley et al (2011). Although a proxy for regional grain size distribution was developed for the present-day using modelled near-bed BSS, this proxy did not replicate the observed sediment grain size evolutions in a number of shelf sea sediment cores. The palaeotidal models thus do not reflect all of the changes in sediment dynamics that have occurred since the LGM.

Since the tides over the NWESS are dominated by the semi-diurnal constituents, forcing the tidal model with M_2, S_2 and N_2 tidal constituents is considered appropriate. The non-linear M_4 overtide (the first harmonic of S_2), the interaction of which with M_2 is important for sediment transport on the shelf (Pingree and Griffiths, 1979), is also included in the model output of BSS. Pingree and Griffiths (1979) demonstrated that most sand transport occurs in response to the maximum current speed over a tidal cycle, where they considered the interaction between M_2 and M_4 tidal currents. Incorporating the S_2 tidal constituent alongside M_2 produces spring-neap modulation, where in general peak spring tides induce the highest BSS.

Uehara et al (2006) demonstrated that when applying boundary forcing to a palaeotidal model, consideration of changes to ocean tides ('ocean-tide') is important and provides a better fit with observations of the positions of tidal mixing fronts than when no changes in ocean tides are considered (i.e. 'fixed' at present-day values). The sensitivity of tidal mod-

els to model input and the actual model set-up is illustrated here by comparing two models with 'ocean-tide' forcing. This is demonstrated when comparing the *ROMS+Lambeck* BSS with those generated by Uehara et al (2006) (*KUTM+Lambeck*, Figure 7.8). At this point it should be noted that the forcing at the model boundaries was different between the two models, since the *ROMS+Lambeck* was forced with the output of Uehara et al (2006), who forced the 1/12° shelf model at the boundaries with low-resolution (1/2°) global tides. Tidal models are often forced with various combinations of tidal constituents, and the calculation for the location of the tidal mixing front is dependent upon tidal constituents, as well as on the model output being used, e.g. depth-averaged or surface current speeds. The sensitivity of the stratification parameter demonstrates that using the timing of stratification onset is not a sensitive proxy for quantifying which palaeotidal model simulations are superior, in particular when the observational data are sourced from a single core location, such as by Austin and Scourse (1997) and Scourse et al (2002).

Another significant consideration when making inter-model comparisons is the nature of the output, such as whether BSS is calculated using near-bed or depth-averaged tidal current speeds, and whether spatially-varying drag coefficients are used either as model input, or for calculating BSS from model output. For considering tidal-induced sediment transport, the modelled near-bed BSS is favoured over BSS calculated using depth-averaged tidal currents speeds, since the latter make assumptions about the vertical distribution of velocity. These results, combined with those of Uehara et al (2006), indicate relative sea level to be of larger influence on the timing and magnitude of changes to shelf sea tidal dynamics (since the LGM), rather than the hydrodynamic model used, as illustrated in Figure 7.12. In essence, incorporating the most up-to-date (and most well-constrained) GIA model output in the model palaeotopographies is of more importance than considering which hydrodynamic model to use. With this in mind, and considering the palaeotidal model developed here has more extensive output than that presented by Uehara et al (2006), this new palaeotidal model *ROMS+Bradley* is an improvement on existing palaeotidal models. The differences in the temporal and spatial changes in the tides between *ROMS+Bradley* and *KUTM+Lambeck* simulations are significant where the latter has been used to support observational evidence, such as the evolution of the Celtic Sea mega 'linear tidal sand ridges' (Scourse et al, 2009b) and the formation of sediment waves in the Irish Sea (Van Landeghem et al, 2009).

Van Landeghem et al (2009), who used the palaeotidal model output of Uehara et al (2006), found that use of the 'fixed' boundary conditions provided a better fit with ob-

served directions of bottom BSS vectors in the Irish Sea (15 ka BP to present-day). The predicted BSS direction was sensitive to the GIA model used (i.e. Peltier (1994); Lambeck (1995)) and there are shown to be further differences when comparing the *ROMS+Bradley* simulations. For example, Van Landeghem et al (2009) reported a reversal in the peak BSS vector direction in the southern Irish Sea between 9 and 8 ka BP (*KUTM+Lambeck*, 'ocean-tide'), whereas this is simulated by *ROMS+Bradley* to happen earlier, between 11 and 10 ka BP (Figure 8.1). That the BSS vectors in the southern Irish Sea have been directed southwest for longer in the new palaeotidal model is more consistent with the observed bedload transport direction, since Van Landeghem et al (2009) reported opposing observed and predicted BSS vector directions in this region before 9 ka BP (note the shift from a region of convergence at 15 ka BP, to divergence after 9 ka BP, highlighted in Figure 8.1). The *POLCOMS+Lambeck* simulations are only available for 2 ka time slices, and so are not compared here. These results highlight the sensitivity of palaeotidal models to changes in ocean forcing and relative sea level and indicate that using a better-constrained GIA model, and more realistic 'ocean-tide' forcing in palaeotidal models provides a better fit with the observational data of Van Landeghem et al (2009) than the palaeotidal models that existed at the time, in particular when the unrealistic 'fixed' boundary was used.

The tidal elevation amplitudes output by *ROMS+Bradley* in the northwest Celtic Sea, in the vicinity of the linear tidal sand ridges, is considerably smaller during early deglaciation than those modelled by Uehara et al (2006). The northern extent of the sand ridges extend into this area of lower amplitudes, which had correspondingly lower BSS. This new palaeotidal model solution poses a problem with regards defining the origin of the sand ridges, which are proposed by Scourse et al (2009b) to have formed by high (tidal-induced) BSS remobilising sediments between 20 and 12 ka BP (or until 10 ka BP in the southerly region). In addition to these differences in the BSS magnitude, the area largely remained marine throughout deglaciation in the Bradley simulations, whereas the relative sea level was considerably lower in the Celtic Sea in the Lambeck simulations. The grounding line of the Irish Sea Ice Stream are thought to be further south into the Celtic Sea (Scourse et al, 1990) than is represented by these palaeotopographies. This is likely due to the low-resolution ice sheet models used for deducing the location of the ice-water boundary in the model palaeobathymetric grids.
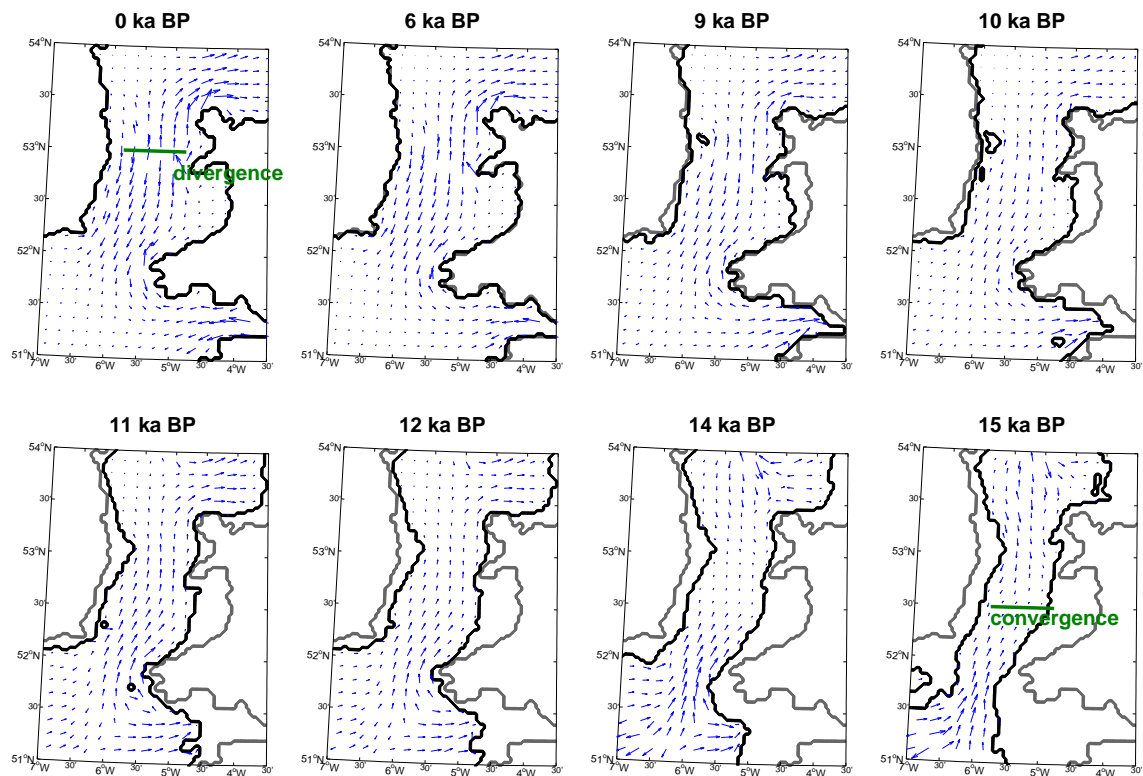
Figure 8.1: Modelled peak BSS vectors in the Irish Sea, for various time slices since the LGM (*ROMS+Bradley*). The smaller vectors indicate BSS <4 N m^{-2} and the longer arrows are BSS >4 N m^{-2}. The black outline indicates the extent of land/ice, and the present-day coastline is given for reference (grey line). A region of divergence (bed load parting) is highlighted at the present-day, and a region of convergence is highlighted at 15 ka BP (green lines).

8.1.1 Using palaeotidal model output to constrain SLIPs

Fundamental to constraining GIA models are SLIPs, which tend to form at or around mean high water spring tide (MHWST), rather than at the palaeo mean sea level (Shennan et al, 2002, 2006b). Together with this reference water level, the 'indicative range' is considered, which is the likely range over which the sediment has been deposited, thus defining the 'indicative meaning' of the SLIP. MHWST varies with tidal amplitude, which is influenced by relative sea level changes (Gehrels et al, 1995; Shennan et al, 2000a; Uehara et al, 2006; Neill et al, 2010), therefore it is incorrect to assume that tidal range has not changed over time. Correcting SLIPs for palaeo-changes in MHWST is thus critical for constraining their indicative meaning. Figure 8.2 shows the changes in MHWST at Arisaig, on the west coast of Scotland (location in Figure 7.4), which is the location of the most extensive SLIP record for the British Isles (Shennan et al, 2006b), with over 16 ka of data. This figure

revises the MHWST evolution curve presented by Neill et al (2010), which was developed using the Lambeck GIA model and the POLCOMS tidal model (three-dimensional, 1/12 degree), for a water grid cell near to the location of Arisaig. Shown in Figure 8.2 are the modelled evolution of MHWST, which is the $M_2 + S_2$ tidal elevation amplitude, output by three different palaeotidal model simulations. Between 18 ka BP and 8 ka BP, there were large differences between simulated tidal elevation amplitudes and relative sea level. The large tidal amplitudes were due to the large tides along the western extent of the BIIS during early deglaciation (Figures 7.5 and 7.6). The large decrease in relative sea level (i.e. sea level fall) during early deglaciation was due to the rapid GIA caused by the decrease in loading from the diminishing BIIS.

Figure 8.2 highlights the differences between the modelled MHWST (tidal amplitudes) at the nearest grid cell to Arisaig for the different palaeotidal model s, and which is the correction that could be applied to the Arisaig SLIP to adjust for evolving changes in tidal amplitudes. The actual distance from the location of Arisaig varies with model resolution, with the modelled land/ice and water mask, and with different GIA models. Again, it is assumed that *ROMS+Bradley* is the preferred palaeotidal model , since it is of higher spatial resolution (1/24 degree), and incorporates the latest advancements in GIA modelling for the region.
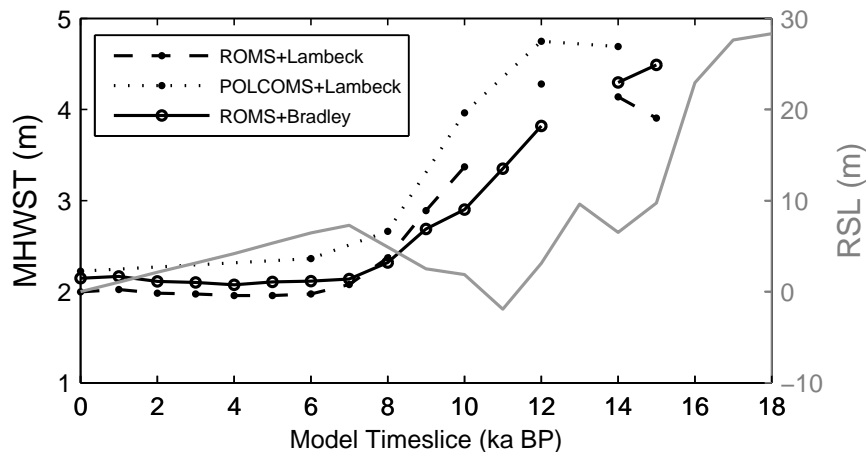
Figure 8.2: Changes in modelled MHWST (black lines, left axis) from the model grid cell nearest to Arisaig, plotted as the amplitude of the $M_2 + S_2$ tidal constituent elevations. Three different model outputs are plotted, as indicated by the legend (*ROMS+Bradley*, *ROMS+Lambeck* and *POLCOMS+Lambeck*). The grey line is the relative sea level curve from the GIA model of Bradley et al (2011) (right axis, RSL = relative sea level). Missing MHWST data points are indicative of the site being emerged (i.e. land/ice).

Constraining SLIPs with MHWST corrections is a somewhat iterative process, whereby

SLIPs are used to constrain a GIA model, the output of which is used as input for a palaeotidal model , and subsequently the output of the palaeotidal model is necessary for correcting the SLIPs from their *in situ* position. As proposed by Neill et al (2010), one way to approach this problem would be using split calibration verification methods, whereby only a portion of the SLIPs are used to constrain GIA model output, which are used to construct palaeobathymetric grids for the palaeotidal model (this is standard practice for many model calibrations). A tidal correction could then be applied to the remaining portion of the SLIPs using the palaeotidal model output, and the corrected SLIPs could be used to further constrain the GIA output. Regardless of this circularity, the outputs of this palaeotidal model are better-suited for such an application, since they are higher resolution (and so the core sites and the locations of SLIPs can be defined with more accuracy), and incorporate an improved GIA model for the British Isles.

8.2 Relationship between modelled BSS and observed seabed sediment grain size

The grain size tidal current proxy (GSTCP) is a first order approximation based on the model output of BSS (near-bed), using a 1 km model grid resolution and a limited number of sediment classifications. The GSTCP is based on several key assumptions, namely:

1. Tidal-induced BSS dominates long-term sediment transport processes in the Irish Sea and on the NWESS.

2. Sediment supplies are unlimited and unsorted.

3. The presence of a residual near-bed flow, since it is the peak BSS that is considered, and areas of zero residual (e.g. at bed load partings) are not accounted for.

4. The present-day seabed sediment distribution in the Irish Sea is a product of recent tidal current speeds, i.e. the present-day steady-state has been achieved over several thousand years, as indicated by the minimal relative sea level change and minimal modelled BSS changes (e.g. in the last 8 ka).

5. Ripples, dunes and varying grain size are not accounted for, since a constant drag coefficient is selected in the model (0.003).

Despite these assumptions, the GSTCP is able to define and differentiate between the dominant present-day sediment classifications (mud, sand and gravel) in the Irish Sea on

a regional scale (present-day). The GSTCP is essentially an attempt at deriving critical threshold values for sediments in the field, which are highly variably in terms of hydrodynamics and sediment dynamics. Although tidal-induced currents dominate sediment transport in many regions of the NWESS, other factors, the significance of which vary temporally and spatially, play considerable roles in determining sediment dynamics (e.g. waves). Rather than there being a definitive threshold condition to define which current speeds displace certain grain sizes, a range of threshold values exist (Paphitis, 2001) due to the complexity and stochastic nature of the factors which can influence sediment transport. This range is not specifically accounted for in the GSTCP, which further highlights the need to consider the GSTCP as a predictor of *large-scale* patterns in seabed sediment type.

Predicting (albeit large-scale) patterns in seabed sediment type on regional scales using tidal model output has several key applications, including physical (e.g. morphodynamic) modelling and biological studies, where information regarding the approximate distribution of seabed sediments is important. Knowledge of the physical properties of an area, including energy regime, topography and substrate type, is essential for predictive habitat mapping, which is used to predict the biological community on the seabed. A tool for predicting large-scale distributions of seabed sediments is very valuable, facilitating higher-resolution research to focus on areas of interest, rather than first having to collect data from an entire region. In addition to this present-day application of the GSTCP, it can be used to generate predictive maps for seabed sediment evolution over various timescales, useful for morphodynamic modelling and for consideration of the evolution of present-day bedforms. Future work should focus on the relationship between grain size of mixed seabed sediment classes and bed shear stresses, as well as on combined tidal- and wave-induced bed shear stresses.

Defining empirical curves for the threshold of sediment motion (e.g. Hjulstrom, 1935; Shields, 1936; Miller et al, 1977) is notoriously difficult, as there is considerable scatter in the data (Miller et al, 1977; Paphitis, 2001). Although these threshold curves are simple to use, they remain severely restricted by the conditions under which they were developed and as such, are not applicable to regional model output such as from the NWESS. Furthermore, the Irish Sea is an interesting region in terms of tidal dynamics, due to the tides entering this semi-enclosed water body concurrently from the north and the south. The unique and complex features of the overall circulation of the region will have added complexity to quantifying the relationship between modelled BSS and seabed sediment classification.

Predicting (albeit *large-scale*) patterns in seabed sediment type on regional scales using tidal model output has several key applications, including physical (e.g. morphodynamic) modelling and biological studies (e.g. habitat mapping). Knowledge of the physical properties of an area, including energy regime, topography and substrate type, is essential for predictive habitat mapping, which is used to predict the biological community on the seabed (e.g. Countryside Council for Wales, 2007). An ability to predict the seabed sediment type without requiring extensive observational data of an area is valuable for such applications. In addition to this present-day application of the GSTCP, it can be used to generate predictive maps for seabed sediment evolution over various timescales (e.g. Figure 7.17), useful for morphodynamic modelling and for consideration of the evolution of present-day bedforms.

In the majority of regional-scale hydrodynamic modelling, spatially-varying bed roughness is not accounted for, since extensive observational data regarding seabed sediment type are required for the model set-up. The bottom drag in tidal models is usually described using linear or quadratic friction laws, often using a constant drag coefficient (Pingree and Griffiths, 1979; van der Molen et al, 2004; Uehara et al, 2006; Neill et al, 2010; Davies et al, 2011). Using model output of BSS to predict seabed sediment type is another iterative problem, since varying bottom roughness due to variations in grain size can feedback on tidal energetics, such as BSS and dissipation (Aldridge and Davies, 1993; Nicolle and Karpytchev, 2007; Kagan et al, 2012). Incorporating spatially-varying drag coefficients in tidal models is important, since it can influence sediment transport properties through impacting on calculations of velocity and hence BSS. The ability to calculate varying model drag coefficient is dependent upon varying the bottom roughness, which is defined as a function of median grain size (e.g Li and Amos, 2001; Warner et al, 2005, 2008b). These feedback effects are clearly greater on the near-bed tidal current speeds than on the depth-averaged tidal currents. Of more significance in terms of bed roughness are larger-scale modulations in bottom roughness such as dunes and ripples (Kagan et al, 2012), however, overlying such features is variability in grain roughness. In the past, inputting the bottom roughness for calculating varying drag coefficients has been dependent upon observational seabed sediment data (e.g. Warner et al, 2008a; Wu et al, 2011), or on roughness lengths predicted by model (morphodynamic) subroutines (Li and Amos, 2001). Further, where comprehensive regional seabed sediment maps exist, it is possible to input variable bed roughness into tidal models (e.g. Nicolle and Karpytchev, 2007), although in this case the issue of estimating a median grain size of a mixed sediment class remains. A GSTCP

addresses the limitations of the above factors, by predicting spatially-varying median grain size on a regional scale.

8.3   Validating palaeotidal model outputs with grain size data

8.3.1   Marine core sediment data

Central to the model-data comparison are new seabed sediment sequences from NWESS sediment cores. Although the GSTCP resolves the seabed sediment patterns on a regional scale, it cannot be applied to seabed sediment cores because of large local variations in hydrodynamic and sedimentological properties. The first-order GSTCP does not resolve the subtle variations in observed BSS evolution at each core site. The overall trends in fluctuations of modelled BSS and observed seabed sediment grain size are consistent in three of the four core sites considered (BGS19, BGS87 and BGS199), although the predicted grain sizes are too large. It is possible that the small variations in seabed sediment grain size were too small to be attributable to the modelled changes in BSS, and so the attempt at using the GSTCP for predicting sediment grain size at the core locations is considered unsuccessful. Future work should incorporate more data on seabed sediment grain size and should this proxy be developed further, work needs to be done on attributing a median grain size to mixed sediment classifications. Considering that this geological proxy has not been successful in validating modelled past BSS, there remains the need to develop a proxy for past tidal current conditions on shelf seas.

The present-day seabed sediment data are based on grab samples, which are generally 10-15 cm of the surface sediment. Further, the sediment samples were prepared in different ways: the present-day seabed sediment sample data are based on sieving, whereas the sediment core grain size data were obtained through laser particle diffractometry. The difference in sediment sampling methods add a level of discrepancy between the sediment datasets (Poizot et al, 2008, and references therein), and could contribute to the GSTCP overestimating observed (past) grain sizes. Sediment sampling via grab sampling is biased towards the coarse fraction, since much of the fine fraction can be misplaced during grab sampling. Furthermore, due to the non-sphericity of sediments particles, the sieves can retain sediment which are coarser than the diameter corresponding the sieve mesh size (Matthews, 1991).

Another considerable restriction is the palaeotidal model resolution, since the model-data comparison is based on comparing vibrocore samples (of diameter ~8 cm) with the

model output from the grid cell (with area ~ 30 km^2) nearest to the core site. A higher-resolution tidal model would be better-suited to extracting model output from a specific location for model-data comparison. With this in mind, a higher resolution ($\sim$1.1 km) tidal model was used for defining the GSTCP; however, this model resolution was still low relative to the specific locations of the seabed sediment grab samples. Another consideration is the degree to which the core data can be considered representative of the dominant sediment type, or stratigraphy, in the areas from which they were collected. To highlight this, the locations of BGS19, BGS65 and BGS87 are shown in Figure 8.3, and overlay the DigSBS250 map for the area. The seabed sediment at BGS19 and BGS65 is defined as '*gravel, sand and silt*' in the DigSBS250 map, whereas observed d_{50} of the core tops at these two sites were classified as *very fine sand* and *fine sand*, respectively. Similarly, the DigSBS250 map classifies the sediment at BGS87 as *sandy mud*, whereas the observed d_{50} is *very fine sand*. To overcome this limitation would be for extensive grain size and radiocarbon analysis of many more seabed sediment grab samples and marine sediment cores, which would be very expensive. Furthermore, a comprehensive study into spatial variations in sedimentary facies, morphological features and sub-environments is essential for furthering our knowledge of the sedimentology of the region.
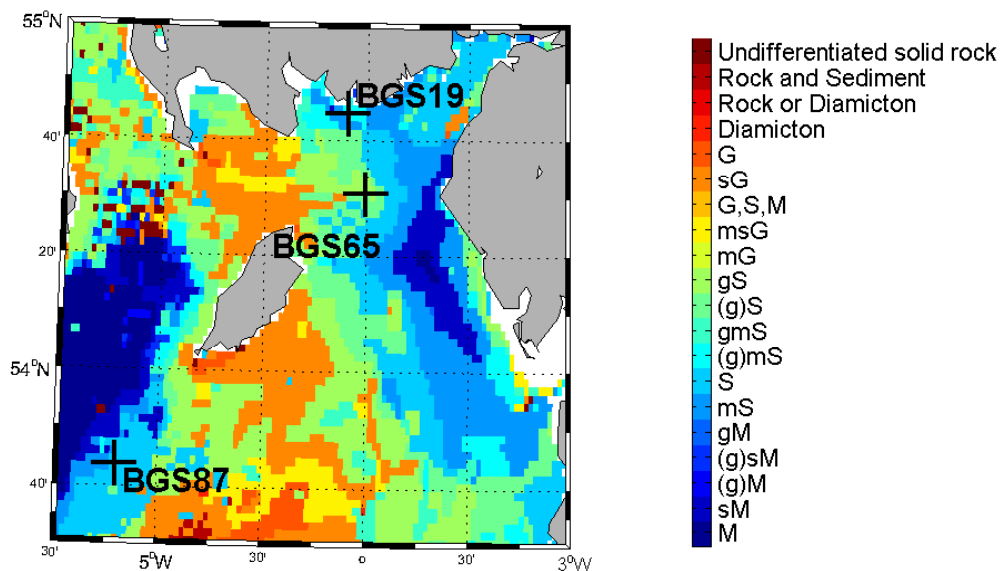
Figure 8.3: DigSBS250 map of the northern Irish Sea, showing the sites of BGS19, BGS65 and BGS87.

An interesting point to note is the discrepancy between the modelled water depths at the core sites (Figure 7.11), which differ considerably from the recorded water depths in the BGS core logs. This point highlights the difference in the present-day bathymetries

used in the *ROMS+Bradley* and the *ROMS+Lambeck* simulations, which were derived from GEBCO and a combination of sources (Uehara et al, 2006), respectively. Despite these differences, both tidal models were considered to provide reasonable RMS errors, when validated using observations (Section 3.4.5). None of the simulations incorporated 'wetting and drying', and the minimum water depths were 10 m in *ROMS+Bradley*, and 6 m in *KUTM+Lambeck* and *ROMS+Lambeck*. It might be expected that signals from these different water depths may account for some of the present-day differences between peak BSS at the core sites (Figure 7.12); however, the correlation between differences in water depths and differences in peak BSS are not consistent. For example, at BGS19, the present-day water depth in the Lambeck simulations is ∼10 m deeper than in the Bradley simulations, and as expected, the modelled peak BSS is higher in the latter. In contrast, at BGS19, the peak BSS is higher in the *ROMS+Bradley* (deeper) than in *KUTM+Lambeck* (shallower), which may be a product of the near-bed BSS output from *ROMS+Bradley*.

8.3.2 Exploring stratigraphic misfits

Mitchener and Torfs (1996) reported a transition from cohesionless to cohesive behaviour of sediments with mud content (by weight) between 3 and 15 %. Although sediment samples with mud content in excess of this range were not explicitly removed during development of the GSTCP, mud samples from areas with high BSS (>10 N m^{-2}) were removed (such as in the Bristol Channel), in an attempt to address this problem. There is a significant mud content ('clay' plus 'silt', Figure 5.8) in each of the cores, including the top half of BGS199. The median grain sizes of much of the sediment core samples are <63 μm (Figure 5.7), indicating that at least 50 % of these samples are in the mud range, and therefore are likely to exhibit cohesive behaviour. This is likely to contribute to the mismatch between predicted and observed grain sizes in the core samples.

There are inherent uncertainties linked to the linear-interpolation (regression) of the age-depth models, although it is a well-established method (e.g. Kershaw, 1986; Stuiver et al, 1998; Scourse et al, 2002; Blaauw, 2012). The linear interpolation omits any consideration of varying sedimentation rates, as well as assuming no erosion. In reality, temporal and spatial variations in deposition and erosion rates exist, hence there may be hiatuses in the geological record which are not accounted for in the linear interpolation. Where turbulent mixing and peak BSS are high in concurrence, net sediment erosion is likely to occur, thus producing gaps in the sediment record. Although this is important to note, it is not likely that this will have contributed significantly to the misfits between the predicted

and observed grain sizes. This suggests, once again, that the stratigraphic record is too spatially variable to be used on scales such as sediment cores, and that the relationship must only be used on regional scales. Further, wave action is not accounted for, and the influence of this is likely to have changed over space and time (Neill et al, 2009b).

Deducing the depths to which mixing of the core sample (by either physical or biological processes) has an effect is impossible without radiocarbon dating more material from various core depths. Many shelf sediment sequences from the region have been found to be heavily bioturbated (Kershaw et al, 1983; Scourse et al, 2002), which effects the age-depth profiles. Higher resolution age-depth models would reduce these mixing and sediment deposition errors considerably, by further constraining the sediment accumulation rates.

9 Conclusions and further work

9.1   Conclusions

Sediment dynamics over the northwest European shelf seas (NWESS) have been subject to considerable change due to the evolution of tidal dynamics, resulting from significant sea level rise since the LGM. Large-scale sediment dynamics over the NWESS are dominated by tidal-induced bed shear stress (BSS); the overarching aim of this research was to deduce whether seabed sediment grain size can be used as a proxy for tidal-induced BSS. Although a correlation ($r^2 = 0.38$, N=242) was found between present-day seabed sediment type and modelled peak BSS magnitude, this relationship does not resolve more subtle fluctuations observed in the grain size data across a range of shelf sea sediment cores. When applied to the Irish Sea, this 'grain size tidal current proxy' (GSTCP) is successful in defining and differentiating between the large-scale pattern of seabed sediment grain size distribution. An ability to estimate the large-scale spatial variability of seabed sediment type in the absence of extensive observational data is valuable for many applications. For example, in some physical (e.g. morphodynamic) models (including those applied to palaeo-time slices), knowledge of seabed sediment type is important for inputting spatially-varying bed roughness, and in biological studies, an ability to estimate the distribution of seabed sediment would greatly benefit habitat mapping (e.g. scallop dredging).

A new palaeotidal model has been developed, which uses the latest glacial isostatic adjustment (GIA) model for the region for deriving palaeotopographies. There were shown to be noticeable changes in modelled tidal current conditions when the outputs from this palaeotidal model were compared with existing palaeotidal models, which incorporated older GIA models for the region. Use of the most up-to-date and well constrained GIA model is important in order to reproduce past relative sea levels as accurately as possible, which can significantly alter tidal dynamics of shelf seas. Work on constraining GIA models to produce better fit with observational data on relative sea levels is ongoing, as significant uncertainties remain in the inputs to GIA models (i.e. the ice-, earth- and sea-level models

used as inputs).

Due to the complexity of sediment dynamics and the resulting complex environmental signature which the geological record holds, the core stratigraphies predicted by applying the GSTCP to the palaeotidal model output do not replicate the observed grain size. The proxy does not resolve the intricacies of the actual sediment dynamics, since only tidal-induced sediment transport processes are considered, and the proxy is shown to not be sensitive enough to be used for constraining palaeotidal model output at point locations. The inability of the proxy to predict specific grain size on such small spatial scales ought not eclipse the fact that, in many areas of the Irish Sea, the proxy does indeed identify the regional trends. The proxy can be used to approximate the large-scale sediment distribution over the NWESS for the present-day, and has been applied to palaeotidal model output to predict the evolution of large-scale patterns in sediment dynamics across the shelf over the last 21 ka.

The failure of the GSTCP to derive the observed grain sizes highlights the shortcomings of the approach, and the proxy is considered effectively unsuitable for constraining palaeotidal model output in this context. The main limitations are the lack of consideration of sediment availability, the limited spatial extent of the geological data (i.e. few sediment cores) and the absence of additional physical processes such as wave-induced BSS, baroclinic flows and wetting and drying. There remains the need to develop new proxies for past hydrodynamic conditions on the shelf seas, which can be used to constrain numerical model output on regional scales.

9.2   Suggestions for future work

More comprehensive modelling studies are the basis for unravelling the complexity of how the main physical mechanisms (tidal currents and waves) have evolved since the LGM. A more refined GSTCP could be developed with more extensive present-day seabed sediment data from the NWESS, representing a wide range of sedimentary environments and ratios of wave-tide induced BSS. Using more data, such as incorporating extensive sediments data from the North Sea (e.g. from the North Sea Benthos Survey, Basford, 1993), it would be possible to develop the proxy to predict a greater number of seabed sediment classifications, such that smaller variations in grain size could be resolved by model outputs, as well as enhanced predictions of areas likely to contain mixed sediment (including those with high mud content). A recent attempt to quantify the relationship between combined wave- and current-induced disturbances and seabed sediment type on the NWESS has been carried

out by Aldridge et al (2014), and includes an attempt at quantifying a median grain size of mixed seabed sediment samples. Despite this recent work, the response of mixed sediments to BSS is not sufficiently known and quantified to make relationship predictions between BSS and grain size of heterogeneous sediments. Further work is needed on understanding small- and regional scale sedimentary processes, both for the present day and for the geological record, before more geological observational data are able to be used as proxies for past hydrodynamic conditions.

A higher-resolution tidal model would also help improve the proxy, by eliminating the need to combine nearby seabed sediment samples into the same model grid cell (and to interpolate these to the grid centre), as was done in Chapter 4. Further, applying the GSTCP to a higher-resolution palaeotidal model would enable the core sites (and seabed sediment sample sites) to be located more precisely. As discussed, a key application of the new palaeotidal model output generated here is for correcting SLIPs. The model output are readily available for use by the GIA and sea-level community for correcting the indicative meaning of SLIPs for changes in tidal ranges. Future palaeotidal modelling studies ought to reflect changes in GIA models by updating the palaeobathymetries. A study focussing on quantifying the relative contribution of palaeotidal model inputs (e.g. tidal forcing, GIA model, tidal constituents, hydrodynamics) would be beneficial to future palaeotidal model developments. An iterative approach would be needed for quantifying differences (such as the impact on tidal elevation amplitudes) between hydrodynamic models (e.g. ROMS vs POLCOMS), and subsequently between different model inputs within the same hydrodynamic models.

The consideration of wave-induced sediment transport is central to developing this proxy further since waves also play a significant role in coastal and shelf scale sediment transport. In the first instance, the ROMS subroutine could be implemented, using grain size information to run a bedform predicting algorithm, which feeds back to the hydrodynamics within the model (Soulsby and Whitehouse, 2005). Again, knowledge of spatially-varying grain sizes is needed. The hydrodynamics output from the palaeotidal model could also be applied to sediment transport and morphodynamic formulae, including feedback between the evolving bed and the morphodynamics, where possible. Such an approach would consider the spatial (as well as the temporal) gradients in BSS, which is in contrast with the point-specific approach used here. Further still, the tidal model would be well-suited to model coupling with wind-, wave- and morphodynamic models, such as is possible using COAWST (Coupled-Ocean-Atmosphere-Wave- Sediment Transport Model-

ing System, Warner et al, 2010). This comprehensive modelling system enables dynamic feedback between the models through multi-way model coupling. Although this model coupling (which is extremely computationally expensive) is possible for the present-day, work needs to be done on improving palaeowind datasets for input to palaeowind/wave models. Past changes in global ice volumes have had implications for global and regional wind conditions as well as for sea levels, which have in turn influenced wave dynamics. Existing palaeowind datasets are of limited spatial scale (several degrees latitude/longitude), and limited temporal scales (e.g. monthly means), which are insufficient for using the wind fields for forcing palaeowave models. To date, only present-day wind fields have been used to force palaeowave models (e.g. Neill et al, 2009b). This coupled model approach would help quantify interactions between seabed sediment and the physical processes that control sediment dynamics, over a large scale.

References

Aldridge J, Parker E, Bricheno L, Green SL, van der Molen J (2014) Assessment of the Physical Disturbance of the Northern European Continental Shelf Seabed by Waves and Currents. Submitted to Continental Shelf Research

Aldridge JN (1997) Hydrodynamic Model Predictions of Tidal Asymmetry and Observed Sediment Transport Paths in Morecambe Bay. Estuarine, Coastal and Shelf Science 44(1):39–56

Aldridge JN, Davies AM (1993) A High-Resolution Three-Dimensional Hydrodynamic Tidal Model of the Eastern Irish Sea. Journal of Physical Oceanography 23(2):207–224, DOI 10.1175/1520-0485(1993)023<0207:AHRTDH>2.0.CO;2

Arbic BK, Garrett C (2010) A coupled oscillator model of shelf and ocean tides. Continental Shelf Research 30(6):564–574, DOI 10.1016/j.csr.2009.07.008

Arbic BK, Karsten RH, Garrett C (2009) On tidal resonance in the global ocean and the back-effect of coastal tides upon open-ocean tides. Atmosphere-Ocean 47(4):239–266, DOI 10.3137/OC311.2009

Aston SR, Stanners DA (1982) The transport to and deposition of Americium in intertidal sediments of the Ravenglass Estuary and its relationship to Plutonium. Environmental Pollution Series B, Chemical and Physical 3(1):1–9, DOI 10.1016/0143-148X(82)90038-6

Austin RM (1991) Modelling Holocene tides on the NW European continental shelf. Terra Nova 3:276–288

Austin WEN, Scourse JD (1997) Evolution of seasonal stratification in the Celtic Sea during the Holocene. Journal of the Geological Society 154(2):249–256, DOI 10.1144/gsjgs.154.2.0249

Aviso (2012) FES2012 was produced by Noveltis, Legos and CLS Space Oceanography Division and distributed by Aviso, with support from Cnes (http://www.aviso.altimetry.fr/). URL http://www.aviso.oceanobs.com/no_cache/en/data/products/auxiliary20-products/global-tide-fes2004-fes99/description-fes2012/print.html?sword_list%252525255B0%252525255D=fes2012

Bailard JA (1981) An energetics total load sediment transport model for a plane sloping beach. Journal of Geophysical Research 86(C11):10,938, DOI 10.1029/JC086iC11p10938

Baker AC (1991) Tidal Power. Peter Peregrinus Ltd, London

Barnett TP (1990) Recent changes in sea level and their possible causes. Climatic Change 5(1):15–38, DOI 10.1007/BF00144678

Basford D (1993) The ICES North Sea benthos survey: the sedimentary environment. ICES Journal of Marine Science 50(1):71–80, DOI 10.1006/jmsc.1993.1008

Bassett SE, Milne GA, Mitrovica JX, Clark PU (2005) Ice sheet and solid Earth influences on far-field sea-level histories. Science 309(5736):925–8, DOI 10.1126/science.1111575

Beckmann A, Haidvogel DB (1993) Numerical Simulation of Flow around a Tall Isolated Seamount. Part I: Problem Formulation and Model Accuracy. Journal of Physical Oceanography 23(8):1736–1753, DOI 10.1175/1520-0485(1993)023<1736:NSOFAA>2.0.CO;2

Belderson R, Pingree R, Griffiths D (1986) Low sea-level tidal origin of Celtic Sea sand banks - evidence from numerical modelling of M2 tidal streams. Marine Geology 73:99–108

Benoit GJ, Turekian KK, Benninger LK (1979) Radiocarbon dating of a core from Long Island Sound. Estuarine and Coastal Marine Science 9(2):171–180

Blaauw M (2012) Out of tune: the dangers of aligning proxy archives. Quaternary Science Reviews 36:38–49, DOI 10.1016/j.quascirev.2010.11.012

Blott SJ, Pye K (2001) GRADISTAT: a grain size distribution and statistics package for the analysis of unconsolidated sediments. Earth Surface Processes and Landforms 26:1237–1248

Blumberg AF, Mellor GL (1987) Three-Dimensional Coastal Ocean Models, Coastal and Estuarine Sciences, vol 4. American Geophysical Union, Washington, D. C., DOI 10.1029/CO004

Blyth-Skyrme V, Lindenbaum C, Verling E, Van Landeghem K, Robinson K, Mackie A, Darbyshire T (2008) Broad-scale biotope mapping of potential reefs in the Irish Sea (north-west of Anglesey). JNCC Report No. 423. Tech. rep.

Boulton GS, Smith GD, Jones AS, Newsome J (1985) Glacial geology and glaciology of the last mid-latitude ice sheets. Journal of the Geological Society 142(3):447–474, DOI 10.1144/gsjgs.142.3.0447

Bowen D, Rose J, McCabe A, Sutherland D (1986) Correlation of Quaternary glaciations in England, Ireland, Scotland and Wales. Quaternary Science Reviews 5

Bowers D, Simpson J (1987) Mean position of tidal fronts in European-shelf seas. Continental Shelf Research 7(1):35–44

Bradley SL (2011) Using sea-level and land motion data to develop an improved glacial isostatic adjustment model for the British Isles. PhD thesis

Bradley SL, Milne GA, Teferle FN, Bingley RM, Orliac EJ (2009) Glacial isostatic adjustment of the British Isles: new constraints from GPS measurements of crustal motion. Geophysical Journal International 178(1):14–22, DOI 10.1111/j.1365-246X.2008.04033.x

Bradley SL, Milne GA, Shennan I, Edwards R (2011) An improved glacial isostatic adjustment model for the British Isles. Journal of Quaternary Science 26(5):541–552, DOI 10.1002/jqs.1481

Bradwell T, Stoker MS, Golledge NR, Wilson CK, Merritt JW, Long D, Everest JD, Hestvik OB, Stevenson AG, Hubbard AL, Finlayson AG, Mathers HE (2008) The northern sector of the last British Ice Sheet: Maximum extent and demise. Earth-Science Reviews 88(3-4):207–226, DOI 10.1016/j.earscirev.2008.01.008

Bronk C (2013) OxCal online, v4.2. URL http://c14.arch.ox.ac.uk/embed.php?File=oxcal.html

Brooks AJ, Edwards RJ (2006) The Development of a sea-level database for Ireland. Irish Journal of Earth Sciences 24(1):13–27

Brooks AJ, Bradley SL, Edwards RJ, Milne GA, Horton B, Shennan I (2008a) Correspondence, Comment: Postglacial relative sea-level observations from Ireland and their role in glacial rebound modelling. Journal of Quaternary Science 23(8):817–820, DOI 10.1002/jqs

Brooks AJ, Bradley SL, Edwards RJ, Milne GA, Horton B, Shennan I (2008b) Postglacial relative sea-level observations from Ireland and their role in glacial rebound modelling. Journal of Quaternary Science 23(2):175–192, DOI 10.1002/jqs

Brown E, Colling A, Park D, Phillips J, Rothery D, Wright J (2006) Waves, Tides and Shallow Water Processes, 2nd edn. Butterworth Heinemann, in association with The Open University, Oxford.

Butler PG, Scourse JD, Richardson CA, Wanamaker AD, Bryant CL, Bennell JD (2009) Continuous marine radiocarbon reservoir calibration and the 13C Suess effect in the Irish Sea: Results from the first multi-centennial shell-based marine master chronology. Earth and Planetary Science Letters 279:230–241

Campbell L (2005) Practical Sand Transport Modelling. Tech. rep.

Carr SJ, Holmes R, van der Meer JJM, Rose J (2006) The Last Glacial Maximum in the North Sea Basin: micromorphological evidence of extensive glaciation. Journal of Quaternary Science 21(2):131–153, DOI 10.1002/jqs.950

Chiverrell RC, Thomas GSP (2010) Extent and timing of the Last Glacial Maximum (LGM) in Britain and Ireland: a review. Journal of Quaternary Science 25(4):535–549, DOI 10.1002/jqs.1404

Church J, Clark P, Cazenave A, Gregory J, Jevrejeva S, Levermann A, Merrifield M, Milne G, Nerem R, Nunn P, Payne A, Pfeffer W, Stammer D, Unnikrishnan A (2013) Sea Level Change. In: Stocker T, Qin D, Plattner GK, Tignor M, Allen S, Boschung J, Nauels A, Xia Y, Bex V, Midgley P (eds) In: Climate Change 2013: The Physical Science Basis. Contribution of Working Group I to the Fifth Assessment Report of the Intergovernmental Panel on Climate Change, Cambridge University Press, Cambridge, United Kingdom and New York, NY, USA.

Clark CD, Hughes AL, Greenwood SL, Jordan C, Sejrup HP (2012) Pattern and timing of retreat of the last British-Irish Ice Sheet. Quaternary Science Reviews 44:112–146, DOI 10.1016/j.quascirev.2010.07.019

Clark PU, Mix AC (2002) Ice sheets and sea level of the Last Glacial Maximum. Quaternary Science Reviews 21(1-3):1–7, DOI 10.1016/S0277-3791(01)00118-4

Clark PU, Dyke AS, Shakun JD, Carlson AE, Clark J, Wohlfarth B, Mitrovica JX, Hostetler SW, McCabe AM (2009) The Last Glacial Maximum. Science 325(5941):710–4, DOI 10.1126/science.1172873

Coastal and Marine Research Centre (2008) ADFISH: Application of Seabed Acoustic Data in Fish Stocks Assessment & Fishery Performance. URL http://www.cmrc.ie/projects/adfish-application-of-seabed-acoustic -data-in-fish-stocks-assessment–fishery-performance.html

Countryside Council for Wales (2007) HABMAP. URL www.ccgc.gov.uk/landscape–wildlife/habitats–species/habmap.aspx

Courant R, Friedrichs KO, Lewy H (1928) Ueber die partiellen Differenzengleichungen der mathematischen Physik. Mathematische Annalen 100:32–74

Darwin G (1880) On the Tidal Friction of a Planet Attended by Several Satellites, and on the Evolution of the Solar System. Proceedings of the Royal Society of London 31:322–325

Davies AM, Jones JE (1990) Application of a three-dimensional turbulence energy model to the determination of tidal currents on the northwest European Shelf. Journal of Geophysical Research 95(C10):18,143, DOI 10.1029/JC095iC10p18143

Davies AM, Xing J, Jones JE (2011) A model study of tidal distributions in the Celtic and Irish Sea regions determined with finite volume and finite element models. Ocean Dynamics 61(10):1645–1667, DOI 10.1007/s10236-011-0428-1

Deschamps P, Durand N, Bard E, Hamelin B, Camoin G, Thomas AL, Henderson GM, Okuno J, Yokoyama Y (2012) Ice-sheet collapse and sea-level rise at the Bølling warming 14,600 years ago. Nature 483(7391):559–64, DOI 10.1038/nature10902

Egbert G, Ray R (2000) Significant dissipation of tidal energy in the deep ocean inferred from satellite altimeter data. Nature 405(6788):775–8, DOI 10.1038/35015531

Egbert GD (2003) Semi-diurnal and diurnal tidal dissipation from TOPEX/Poseidon altimetry. Geophysical Research Letters 30(17):1907, DOI 10.1029/2003GL017676

Egbert GD (2004) Numerical modeling of the global semidiurnal tide in the present day and in the last glacial maximum. Journal of Geophysical Research 109(C3):C03,003, DOI 10.1029/2003JC001973

Egbert GD, Erofeeva SY (2002) Efficient Inverse Modeling of Barotropic Ocean Tides. Journal of Atmospheric and Oceanic Technology 19(2):183–204, DOI 10.1175/1520-0426(2002)019<0183:EIMOBO>2.0.CO;2

Egbert GD, Ray RD (2001) Estimates of M2 tidal energy dissipation from TOPEX/Poseidon altimeter data. Journal of Geophysical Research 106(C10):22,475, DOI 10.1029/2000JC000699

Egbert GD, Bennett AF, Foreman MGG (1994) TOPEX/POSEIDON tides estimated using a global inverse model. Journal of Geophysical Research 99(C12):24,821, DOI 10.1029/94JC01894

Emery K, Dietz R (1941) Gravity coring instrument and mechanics of sediment coring. Bulletin of the Geological Society of America 52:1685–1714

Everest JD, Bradwell T, Stoker M, Dewey S (2013) New age constraints for the maximum extent of the last British-Irish Ice Sheet (NW sector). Journal of Quaternary Science 28(1):2–7, DOI 10.1002/jqs.2603

Eyles N, Marshall McCabe A (1989) The Late Devensian (22,000 BP) Irish Sea Basin: The sedimentary record of a collapsed ice sheet margin. Quaternary Science Reviews 8(4):307–351, DOI 10.1016/0277-3791(89)90034-6

Fairbanks RG (1989) A 17,000-year glacio-eustatic sea level record: influence of glacial melting rates on the Younger Dryas event and deep-ocean circulation. Nature 342:637–642

Farrell WE, Clark JA (1976) On Postglacial Sea Level. Geophysical Journal of the Royal Astronomical Society 46(3):647–667, DOI 10.1111/j.1365-246X.1976.tb01252.x

Flather RA (1976) A tidal model of the north-west European continental shelf. Memoires de la Society Royal des Sciences de Liege 6 series(10):141–164

Folk R (1954) The distinction between grain size and mineral composition in sedimentary rock nomenclature. Journal of Geology 62(4):344–359

Folk R, Ward W (1957) Brazos River bar: a study in the significance of grain size parameters. Journal of Sedimentary Petrology 27:3–26

Gehrels W, Belknap DF, Pearce BR, Gong B (1995) Modeling the contribution of M2 tidal amplification to the Holocene rise of mean high water in the Gulf of Maine and the Bay of Fundy. Marine Geology 124(1-4):71–85, DOI 10.1016/0025-3227(95)00033-U

Gehrels WR (2010) Sea-level changes since the Last Glacial Maximum: an appraisal of the IPCC Fourth Assessment Report. Journal of Quaternary Science 25(1):26–38, DOI 10.1002/jqs.1273

Gehrels WR, Milne GA, Kirby JR, Patterson R, Belknap DF (2004) Late Holocene sea-level changes and isostatic crustal movements in Atlantic Canada. Quaternary International 120(1):79–89, DOI 10.1016/j.quaint.2004.01.008

Gibbard PL, Head MJ, Walker MJC (2010) Formal ratification of the Quaternary System/Period and the Pleistocene Series/Epoch with a base at 2.58 Ma. Journal of Quaternary Science 25(2):96–102, DOI 10.1002/jqs.1338

Green J, Simpson JH, Legg S, Palmer MR (2008) Internal waves, baroclinic energy fluxes and mixing at the European shelf edge. Continental Shelf Research 28(7):937–950, DOI 10.1016/j.csr.2008.01.014

Green JAM, Green CL, Bigg GR, Rippeth TP, Scourse JD, Uehara K (2009) Tidal mixing and the Meridional Overturning Circulation from the Last Glacial Maximum. Geophysical Research Letters 36(15):L15,603, DOI 10.1029/2009GL039309

Griffiths SD, Peltier WR (2008) Megatides in the Arctic Ocean under glacial conditions. Geophysical Research Letters 35(8):L08,605, DOI 10.1029/2008GL033263

Gyllencreutz R, Mahiques MM, Alves DVP, Wainer IKC (2010) Mid- to late-Holocene paleoceanographic changes on the southeastern Brazilian shelf based on grain size records. The Holocene 20(6):863–875, DOI 10.1177/0959683610365936

Haidvogel D, Arango H, Budgell W, Cornuelle B, Curchitser E, Di Lorenzo E, Fennel K, Geyer W, Hermann A, Lanerolle L, Levin J, McWilliams J, Miller A, Moore A, Powell T, Shchepetkin A, Sherwood C, Signell R, Warner J, Wilkin J (2008) Ocean forecasting in terrain-following coordinates: Formulation and skill assessment of the Regional Ocean Modeling System. Journal of Computational Physics 227(7):3595–3624, DOI 10.1016/j.jcp.2007.06.016

Haidvogel DB, Arango HG, Hedstrom K, Beckmann A, Malanotte-Rizzoli P, Shchepetkin AF (2000) Model evaluation experiments in the North Atlantic Basin: simulations in nonlinear terrain-following coordinates. Dynamics of Atmospheres and Oceans 32(3):239–281

Hall P, Davies AM (2004) Modelling tidally induced sediment-transport paths over the northwest European shelf: the influence of sea-level reduction. Ocean Dynamics 54(2):126–141, DOI 10.1007/s10236-003-0070-7

Harkness DD (1983) The extent of natural 14C deficiency in the coastal environment of the United Kingdon. Proc First Int Symp C-14 and Archaeology PACT 8:351–364

Harris P, Collins M (1991) Sand transport in the Bristol Channel: bedload parting zone or mutually evasive transport pathways? Marine Geology 101(1):209–216

Hashemi MR, Neill SP (2014) The role of tides in shelf-scale simulations of the wave energy resource. Renewable Energy 69:300–310, DOI 10.1016/j.renene.2014.03.052

Heier-Nielsen S, Conradsen K, Heinemeier J, Knudsen K, Nielsen H, Rud N, Sveinbjornsdottir A (1995) Radiocarbon dating of shells and foraminifera from the Skagen core, Denmark: evidence reworking. Radiocarbon 37:119–130

Hinton A (1995) Holocene tides of The Wash, U.K.: The influence of water-depth and coastline-shape changes on the record of sea-level change. Marine Geology 124(1-4):87–111, DOI 10.1016/0025-3227(95)00034-V

Hjulstrom F (1935) Study of the morphological activity of rivers as illustrated by the Furis. Bulletin of the Geological Institutions of the University of Uppsala 25:221–527

Holmes R, Tappin D (2005) DTI Strategic Assessment Area 6 , Irish Sea , seabed and surficial geology and processes. British Geological Survey Commissioned Report, CR/05/057. Tech. Rep. May

Holt J, Umlauf L (2008) Modelling the tidal mixing fronts and seasonal stratification of the Northwest European Continental shelf. Continental Shelf Research 28(7):887–903, DOI 10.1016/j.csr.2008.01.012

Horvath H (2009) Gustav Mie and the scattering and absorption of light by particles: Historic developments and basics. Journal of Quantitative Spectroscopy and Radiative Transfer 110(11):787–799, DOI 10.1016/j.jqsrt.2009.02.022

Hubbard A, Bradwell T, Golledge N, Halld A, Pattonb H, Sugdend D, Cooperc R, Stokerc M (2009) Dynamic cycles, ice streams and their impact on the extent, chronology and deglaciation of the British-Irish ice sheet. Quaternary Science Reviews 28:758– 776

Jackson DI, Jackson AA, Evans D, Wingfield RTR, Barnes RP, Arthur MJ (1995) The geology of the Irish Sea. (HMSO.). Tech. rep.

Jarke J (1956) Eine neue Bodenkarte der sudlichen Nordsee. Deutsche Hydrographische Zeitschrift 9(1):1–9, DOI 10.1007/BF02019424

Jeffreys H (1920) Tidal friction in shallow seas. Philosophical Transactions of the Royal Society, London, Series A pp 239–264

Kagan BA, Sofina EV, Rashidi E (2012) The impact of the spatial variability in bottom roughness on tidal dynamics and energetics, a case study: the M2 surface tide in the North European Basin. Ocean Dynamics 62(10-12):1425–1442, DOI 10.1007/s10236-012-0571-3

Kendall RA, Mitrovica JX, Milne GA (2005) On post-glacial sea level - II. Numerical formulation and comparative results on spherically symmetric models. Geophysical Journal International 161(3):679–706, DOI 10.1111/j.1365-246X.2005.02553.x

Kershaw P (1986) Radiocarbon dating of Irish Sea sediments. Estuarine, Coastal and Shelf Science 23(3):295–303, DOI 10.1016/0272-7714(86)90029-6

Kershaw PJ, Swift DJ, Pentreath RJ, Lovett MB (1983) Plutonium redistribution by biological activity in Irish Sea sediments. Nature 306(5945):774–775, DOI 10.1038/306774a0

Kirby R, Parker W, Pentreath R, Lovett M (1983) Sedimentation studies relevant to low-level radioactive effluent dispersal in the Irish Sea. Part III. An evaluation of possible mechanisms for the incorporation of radionuclides into marine sediments. Tech. rep., Institute of Oceanographic Sciences Report 178, Wormley, UK

Knebel HJ, Poppe LJ (2000) Seafloor Environments within Long Island Sound: A Regional Overview. Journal of Coastal Research 16(3):533–550

Kozachenko M, Fletcher R, Sutton G, Monteys X, Van Landeghem, K, Wheeler A, Lassoued Y, Cooper A, Nicoll C (2008) A geological appraisal of marine aggregate resources in the southern Irish Sea. Technical report produced for the Irish Sea. Technical report produced for the Irish Sea Marine Aggregates Initiative (IMAGIN) project funded under the INTERREG IIIA Programme. Tech. rep.

Kuchar J, Milne G, Hubbard A, Patton H, Bradley S, Shennan I, Edwards R (2012) Evaluation of a numerical model of the British-Irish ice sheet using relative sea-level data: implications for the interpretation of trimline observations. Journal of Quaternary Science 27(6):597–605, DOI 10.1002/jqs.2552

Lambeck K (1993) Glacial rebound of the British Isles-I. Preliminary model results. Geophysical Journal International 115(3):941–959, DOI 10.1111/j.1365-246X.1993.tb01503.x

Lambeck K (1995) Late Devensian and Holocene shorelines of the British Isles and North Sea from models of glacio-hydro-isostatic rebound. Journal of the Geological Society 152(3):437–448, DOI 10.1144/gsjgs.152.3.0437

Lambeck K (1996) Glaciation and sea-level change for Ireland and the Irish Sea since Late Devensian/Midlandian time. Journal of the Geological Society 153(6):853–872, DOI 10.1144/gsjgs.153.6.0853

Lambeck K, Chappell J (2001) Sea level change through the last glacial cycle. Science 292(5517):679–86, DOI 10.1126/science.1059549

Lambeck K, Purcell AP (2001) Sea-level change in the Irish Sea since the Last Glacial Maximum: constraints from isostatic modelling. Journal of Quaternary Science 16(5):497–506, DOI 10.1002/jqs.638

Lambeck K, Smither C, Johnston P (1998) Sea-level change, glacial rebound and mantle viscosity for northern Europe. Geophysical Journal International (134):102–144

Lambeck K, Esat TM, Potter EK (2002) Links between climate and sea levels for the past three million years. Nature 419(6903):199–206, DOI 10.1038/nature01089

Lambeck K, Purcell A, Johnston P, Nakada M, Yokoyama Y (2003) Water-load definition in the glacio-hydro-isostatic sea-level equation. Quaternary Science Reviews 22(2-4):309–318, DOI 10.1016/S0277-3791(02)00142-7

Lambeck K, Anzidei M, Antonioli F, Benini A, Esposito A (2004) Sea level in Roman time in the Central Mediterranean and implications for recent change. Earth and Planetary Science Letters 224(3-4):563–575, DOI 10.1016/j.epsl.2004.05.031

Lambeck K, Woodroffe CD, Antonioli F, Anzidei M, Gehrels WR, Jacques L, Wright AJ (2010) Paleoenvironmental Records, Geophysical Modeling, and Reconstruction of Sea-Level Trends and Variability on Centennial and Longer Timescales. In: Church JA, Woodworth PL, Aarup T, Wilson WS (eds) Understanding Sea-Level Rise and Variability, Wiley-Blackwell, Hoboken, NJ, USA, chap 4, pp 61–121, DOI 10.1002/9781444323276

van Landeghem KJ, Wheeler AJ, Mitchell NC (2009) Seafloor evidence for palaeo-ice streaming and calving of the grounded Irish Sea Ice Stream: Implications for the interpretation of its final deglaciation phase. Boreas 38(1):119–131, DOI 10.1111/j.1502-3885.2008.00041.x

Lewis SE, Wust RA, Webster JM, Shields GA (2008) Mid-late Holocene sea-level variability in eastern Australia

Li MZ, Amos CL (2001) SEDTRANS96: the upgraded and better calibrated sediment-transport model for continental shelves. Computers & Geosciences 27(6):619–645, DOI 10.1016/S0098-3004(00)00120-5

Lowe J, Rasmussen S, Björck S, Hoek W, Steffensen J, Walker M, Yu Z (2008) Synchronisation of palaeoenvironmental events in the North Atlantic region during the Last Termination: a revised protocol recommended by the INTIMATE group. Quaternary Science Reviews 27(1-2):6–17, DOI 10.1016/j.quascirev.2007.09.016

Malvern Instrument Wordwide (2012) A Basic Guide to Particle Characterization. Tech. rep.

Marchesiello P, McWilliams JC, Shchepetkin A (2001) Open boundary conditions for long-term integration of regional oceanic models. Ocean Modelling 3(1-2):1–20, DOI 10.1016/S1463-5003(00)00013-5

Marks KM, Smith WHF (2006) An Evaluation of Publicly Available Global Bathymetry Grids. Tech. Rep. 1, DOI 10.1007/s11001-005-2095-4

Matthews M (1991) The effect of grain shape and density on the size measurement. In: Syvitski J (ed) In: Principles, Methods and Application of Particle Size Analysis., Cambridge Univ. Press, New York, pp 22–23

McCabe A, Clark P, Smith D, Dunlop P (2007) A revised model for the last deglaciation of eastern Scotland. Journal of the Geological Society 164(2):313–316, DOI 10.1144/0016-76492006-120

McCave I, Manighetti B, Beveridge N (1995a) Circulation in the glacial North Atlantic inferred from grain-size measurements. Nature 374:149–151

McCave IN, Manighetti B, Robinson S (1995b) Sortable silt and fine sediment size/composition slicing: Parameters for palaeocurrent speed and palaeoceanography. Paleoceanography 10(3):593–610

McCave IN, Hall IR, Bianchi GG (2006) Laser vs. settling velocity differences in silt grain-size measurements: estimation of palaeocurrent vigour. Sedimentology 53(4):919–928, DOI 10.1111/j.1365-3091.2006.00783.x

Michels KH (2000) Inferring Maximum Geostrophic Current Velocities in the Norwegian-Greenland Sea from Settling-Velocity Measurements of Sediment Surface Samples: Methods, Application, and Results. Journal of Sedimentary Research 70(5):1036–1050, DOI 10.1306/101599701036

Miller MC, McCave IN, Komar PD (1977) Threshold of sediment motion under unidirectional currents. Sedimentology 24(4):507–527, DOI 10.1111/j.1365-3091.1977.tb00136.x

Milne G (2008) How the climate drives sea-level changes. Astronomy and Geophysics 49(2):2.24–2.28

Milne GA, Mitrovica JX (1998) Postglacial sea-level change on a rotating Earth. Geophysical Journal International 133(1):1–19, DOI 10.1046/j.1365-246X.1998.1331455.x

Milne GA, Shennan I, Youngs BAR, Waugh AI, Teferle FN, Bingley RM, Bassett SE, Cuthbert-Brown C, Bradley SL (2006) Modelling the glacial isostatic adjustment of the UK region. Philosophical transactions Series A, Mathematical, physical, and engineering sciences 364(1841):931–48, DOI 10.1098/rsta.2006.1747

Milne GA, Gehrels WR, Hughes CW, Tamisiea ME (2009) Identifying the causes of sea-level change. Nature Geoscience 2(7):471–478, DOI 10.1038/ngeo544

Mitchell AJ, Uličný D, Hampson GJ, Allison PA, Gorman GJ, Piggott MD, Wells MR, Pain CC (2010) Modelling tidal current-induced bed shear stress and palaeocirculation in an epicontinental seaway: the Bohemian Cretaceous Basin, Central Europe. Sedimentology 57(2):359–388, DOI 10.1111/j.1365-3091.2009.01082.x

Mitchener H, Torfs H (1996) Erosion of mud/sand mixtures. Coastal Engineering 29(1-2):1–25, DOI 10.1016/S0378-3839(96)00002-6

Mitrovica JX, Milne GA (2003) On post-glacial sea level: I. General theory. Geophysical Journal International 154(2):253–267, DOI 10.1046/j.1365-246X.2003.01942.x

Mitrovica JX, Milne GA, Davis JL (2001) Glacial isostatic adjustment on a rotating earth. Geophysical Journal International 147(3):562–578, DOI 10.1046/j.1365-246x.2001.01550.x

Mix AC, Edouard B, Ralph S (2001) Environmental processes of the ice age: land, oceans, glaciers (EPILOG). Quaternary Science Reviews 20:627–657

van der Molen J (2002) The influence of tides, wind and waves on the net sand transport in the North Sea. Continental Shelf Research 22(18-19):2739–2762, DOI 10.1016/S0278-4343(02)00124-3

van der Molen J, Gerrits J, de Swart H (2004) Modelling the morphodynamics of a tidal shelf sea. Continental Shelf Research 24(4-5):483–507, DOI 10.1016/j.csr.2003.12.001

National Geophysical Data Center (2001) ETOPO2 Global 2 minute Elevations. Boulder, Colorado, USA: U.S. Department of Commerce, National Oceanic and Atmospheric Administration.

National Tidal and Sea Level Facility (2012) Real-time data - UK National Tide Gauge Network. URL http://www.ntslf.org/data/uk-network-real-time

Neill SP, Hashemi MR (2013) Wave power variability over the northwest European shelf seas. Applied Energy 106:31–46, DOI 10.1016/j.apenergy.2013.01.026

Neill SP, Scourse JD (2009) The formation of headland/island sandbanks. Continental Shelf Research 29(18):2167–2177, DOI 10.1016/j.csr.2009.08.008

Neill SP, Litt EJ, Couch SJ, Davies AG (2009a) The impact of tidal stream turbines on large-scale sediment dynamics. Renewable Energy 34(12):2803–2812

Neill SP, Scourse JD, Bigg GR, Uehara K (2009b) Changes in wave climate over the northwest European shelf seas during the last 12,000 years. Journal of Geophysical Research 114(C6):C06,015, DOI 10.1029/2009JC005288

Neill SP, Scourse JD, Uehara K (2010) Evolution of bed shear stress distribution over the northwest European shelf seas during the last 12,000 years. Ocean Dynamics 60(5):1139–1156, DOI 10.1007/s10236-010-0313-3

Nicholls R, Hoozemans F, Marchand M (1999) Increasing flood risk and wetland losses due to global sea-level rise: regional and global analyses. Global Environmental Change 9:S69–S87, DOI 10.1016/S0959-3780(99)00019-9

Nicholls RJ (2011) Planning for the impacts of sea level rise. Oceanography 24(2):144–157, DOI 10.5670/oceanog.2011.34

Nicolle A, Karpytchev M (2007) Evidence for spatially variable friction from tidal amplification and asymmetry in the Pertuis Breton (France). Continental Shelf Research 27(18):2346–2356, DOI 10.1016/j.csr.2007.06.005

Ó Cofaigh C, Evans DJ (2007) Radiocarbon constraints on the age of the maximum advance of the British-Irish Ice Sheet in the Celtic Sea. Quaternary Science Reviews 26(9-10):1197–1203, DOI 10.1016/j.quascirev.2007.03.008

Oliver PG, Holmes AM, Killeen IJ, Turner JA (2010) Marine Bivalve Shells of the British Isles (Mollusca: Bivalvia). Amgueddfa Cymru - National Museum Wales. URL http://naturalhistory.museumwales.ac.uk/britishbivalves/

Pantin HM (1991) Seabed sediments around the United Kingdom: their bathymetric and physical environment, grain size, mineral composition and associated bedforms. Tech. rep., British Geological Survey Marine Geology Series research report, SB/90/1

Paphitis D (2001) Sediment movement under unidirectional flows: an assessment of empirical threshold curves. Coastal Engineering 43(3-4):227–245, DOI 10.1016/S0378-3839(01)00015-1

Pawlowicz R, Beardsley B, Lentz S (2002) Classical tidal harmonic analysis including error estimates in MATLAB using T_TIDE. Computers & Geosciences 28(8):929–937

Peltier WR (1994) Ice Age Palaeotopography. Science 265(5159):195–201

Peltier WR (1996) Mantle Viscosity and Ice-Age Ice Sheet Topography. Science 273(5280):1359–1364, DOI 10.1126/science.273.5280.1359

Peltier WR (2002a) Global glacial isostatic adjustment: palaeogeodetic and space-geodetic tests of the ICE-4G (VM2) model. Journal of Quaternary Science 17(5-6):491–510, DOI 10.1002/jqs.713

Peltier WR (2002b) On eustatic sea level history: Last Glacial Maximum to Holocene. Quaternary Science Reviews 21(1-3):377–396, DOI 10.1016/S0277-3791(01)00084-1

Petersen C (1918) The sea-bottom and its production of fish food. Rep Danish biol Sta 25(1)

Pingree RD, Griffiths DK (1978) Tidal fronts on the shelf seas around the British Isles. Journal of Geophysical Research 83(C9):4615, DOI 10.1029/JC083iC09p04615

Pingree RD, Griffiths DK (1979) Sand transport paths around the British Isles resulting from M2 and M4 tidal interactions. Journal of the Marine Biology Association UK 59:497–513

Poizot E, Méar Y, Biscara L (2008) Sediment Trend Analysis through the variation of granulometric parameters: A review of theories and applications. Earth-Science Reviews 86(1-4):15–41, DOI 10.1016/j.earscirev.2007.07.004

Provost C, Lyard F (1997) Energetics of the M2 barotropic ocean tides: an estimate of bottom friction dissipation from a hydrodynamic model. Progress in Oceanography 40(1-4):37–52, DOI 10.1016/S0079-6611(97)00022-0

Pugh DT (1987) Tides, Surges and mean sea-level, vol 5. John Wiley & Sons, Ltd., Chichester, DOI 10.1016/0264-8172(88)90013-X

Rasmussen SO, Andersen KK, Svensson AM, Steffensen JP, Vinther BM, Clausen HB, Siggaard-Andersen ML, Johnsen SJ, Larsen LB, Dahl-Jensen D, Bigler M, Röthlisberger R, Fischer H, Goto-Azuma K, Hansson ME, Ruth U (2006) A new Greenland ice core chronology for the last glacial termination. Journal of Geophysical Research 111(D6):D06,102, DOI 10.1029/2005JD006079

Reimer PJ, Bard E, Bayliss A, Beck JW, Blackwell PG, Bronk C, Caitlin R, Hai EB, Edwards RL (2013) IntCal13 and Marine13 radiocarbon age calibration curves 0 - 50,000 years cal BP. Radiocarbon 55(4)

Rippeth TP, Scourse JD, Uehara K, McKeown S (2008) Impact of sea-level rise over the last deglacial transition on the strength of the continental shelf CO2 pump. Geophysical Research Letters 35(24):L24,604, DOI 10.1029/2008GL035880

Roberts M, Scourse J, Bennell J, Huws D, Jago C, Long B (2011) Late Devensian and Holocene relative sea-level change in North Wales, UK. Journal of Quaternary Science 6(2)

Robinson K, Darbyshire T, Van Landeghem K, Lindenbaum C, McBreen F, Creavan S, Ramsay K, Mackie A, Mitchell N, Wheeler A, Wilson J, O'Beirn F (2009) Habitat Mapping for Conservation and Management of the Southern Irish Sea (HABMAP) I: Seabed Surveys. Studies in Marine Biodiversity and Systematics from the National Museum of Wales. Tech. rep.

Roelvink J (2006) Coastal morphodynamic evolution techniques. Coastal Engineering 53(2-3):277–287, DOI 10.1016/j.coastaleng.2005.10.015

Rohlf FJ, Robert RS (1936) Statistical Tables, 3rd edn. W. H. Freeman and Company

Scott DB, Greenberg DA (1983) Relative sea-level rise and tidal development in the Fundy tidal system. Canadian Journal of Earth Sciences 20(10):1554–1564, DOI 10.1139/e83-145

Scourse JD, Austin RM (1995) Palaeotidal modelling of continental shelves: marine implications of a land-bridge in the Strait of Dover during the Holocene and Middle Pleistocene. Geological Society, London, Special Publications 96(1):75–88, DOI 10.1144/GSL.SP.1995.096.01.07

Scourse JD, Austin WEN, Bateman RM, Catt JA, Evans CDR, Robinson JE, Young JR (1990) Sedimentology and micropalaeontology of glacimarine sediments from the Central and Southwestern Celtic Sea. Geological Society, London, Special Publications 53(1):329–347, DOI 10.1144/GSL.SP.1990.053.01.19

Scourse JD, Austin WEN, Long BT, Assinder DJ, Huws D (2002) Holocene evolution of seasonal stratification in the Celtic Sea: refined age model, mixing depths and foraminiferal stratigraphy. Marine Geology 191:119–145

Scourse JD, Haapaniemi AI, Colmenero-Hidalgo E, Peck VL, Hall IR, Austin WE, Knutz PC, Zahn R (2009a) Growth, dynamics and deglaciation of the last British-Irish ice sheet: the deep-sea ice-rafted detritus record. Quaternary Science Reviews 28(27-28):3066–3084, DOI 10.1016/j.quascirev.2009.08.009

Scourse JD, Uehara K, Wainwright A (2009b) Celtic Sea linear tidal sand ridges, the Irish Sea Ice Stream and the Fleuve Manche: Palaeotidal modelling of a transitional passive margin depositional system. Marine Geology 259(1-4):102–111, DOI 10.1016/j.margeo.2008.12.010

Sejrup HP, Hjelstuen BO, Dahlgren KTr, Haflidason H, Kuijpers A, Nygå rd A, Praeg D, Stoker MS, Vorren TO (2005) Pleistocene glacial history of the NW European continental margin. DOI 10.1016/j.marpetgeo.2004.09.007 <http://dx.doi.org/10.1016/j.marpetgeo.2004.09.007>

Shchepetkin AF, McWilliams JC (2005) The regional oceanic modeling system (ROMS): a split-explicit, free-surface, topography-following-coordinate oceanic model. Ocean Modelling 9(4):347–404, DOI 10.1016/j.ocemod.2004.08.002

Shennan I, Horton B (2002) Holocene land- and sea-level changes in Great Britain. Journal of Quaternary Science 17(5-6):511–526, DOI 10.1002/jqs.710

Shennan I, Lambeck K, Flather RA, Horton BP, Mcarthur J, Innes J, Lloyd J, Rutherford M, Wingfield R (2000a) Modelling western North Sea palaeogeographies and tidal changes during the Holocene. Holocene Land-Ocean Interaction and Environmental Change around the North Sea, Geological Society, Special Publications 166:299–319

Shennan I, Lambeck K, Horton B, Innes J, Lloyd J, Mcarthur J, Purcell T, Rutherford M (2000b) Late Devensian and Holocene records of relative sea-level changes in northwest Scotland and their implications for glacio-hydro-isostatic modelling. Quaternary Science Reviews 19:1103–1135

Shennan I, Peltier W, Drummond R, Horton B (2002) Global to local scale parameters determining relative sea-level changes and the post-glacial isostatic adjustment of Great Britain. Quaternary Science Reviews 21(1-3):397–408, DOI 10.1016/S0277-3791(01)00091-9

Shennan I, Bradley S, Milne G, Brooks A, Bassett S, Hamilton S (2006a) Invited Review: Relative sea-level changes, glacial isostatic modelling and ice-sheet reconstructions from the British Isles since the Last Glacial Maximum. Journal of Quaternary Science 21(6):585–599, DOI 10.1002/jqs

Shennan I, Hamilton S, Hillier C, Hunter A, Woodall R, Bradley S, Milne G, Brooks A, Bassett S (2006b) Relative sea-level observations in western Scotland since the Last Glacial Maximum for testing models of glacial isostatic land movements and ice-sheet reconstructions. Journal of Quaternary Science 21(6):601–613, DOI 10.1002/jqs

Shields A (1936) Application of similarity principles and turbulence research to bedload movement. Tech. rep., Hydrodynamics Laboratory, California Institute of Technology

Signell RP, List JH, Farris AS (2000) Bottom Currents and Sediment Transport in Long Island Sound: A Modeling Study. Journal of Coastal Research 16(3):551–566

Simpson J, Bowers D (1981) Models of stratification and frontal movement in shelf seas. Deep Sea Research Part A Oceanographic Research Papers 28(7):727–738

Simpson J, Hunter J, Bowden K (1974) Fronts in the Irish Sea. Nature 250:404–406

Smith WH (1997) Global Sea Floor Topography from Satellite Altimetry and Ship Depth Soundings. Science 277(5334):1956–1962, DOI 10.1126/science.277.5334.1956

Soulsby R, Whitehouse R (1997) Threshold of Sediment Motion in Coastal Environments. Pacific Coasts and Ports '97: Proceedings of the 13th Australasian Coastal and Ocean Engineering Conference and the 6th Australasian Port and Harbour Conference 1:145–150

Soulsby RL (1997) Dynamics of Marine Sand. Thomas Telford, London

Soulsby RL, Whitehouse RJ (2005) Prediction of Ripple Properties in Shelf Seas. Mark 2 Predictor for Time Evolution. Tech. rep., HR Wallingford, Wallingford, UK

Sperazza M, Moore JN, Hendrix MS (2004) High-resolution particle size analysis of naturally occurring very fine-grained sediment through laser diffractometry. Journal of Sedimentary Research 74(5):737–743

Steffen H, Wu P (2011) Glacial isostatic adjustment in Fennoscandia - A review of data and modeling. Journal of Geodynamics 52(3-4):169–204, DOI 10.1016/j.jog.2011.03.002

Stern N (2007) Stern Review on the Economics of Climate Change. Cambridge University Press, Cambridge

Stuiver M, Polach HA (1977) Discussion of reporting of 14C data. Radiocarbon 19(3):355–363

Stuiver M, Pearson GW, Braziunas T (1986) Radiocarbon age calibration of marine samples back to 9000 cal yr BP. Radiocarbon 28(2B):980–1021

Stuiver M, Reimer P, Bard E, Beck JW, Burr G, Hughen KA, Kromer B, McCormac G, van der Plicht J (1998) INTCAL98 radiocarbon age calibration, 24,000-0 cal BP. Radiocarbon 40(3):1041–1083

Tebble N (1966) British Bivalve Seashells. A Handbook for Identification. Trustees of the British Museum (Natural History), London

Teferle FN, Bingley RM, Orliac EJ, Williams SDP, Woodworth PL, McLaughlin D, Baker TF, Shennan I, Milne Ga, Bradley SL, Hansen DN (2009) Crustal motions in Great Britain: evidence from continuous GPS, absolute gravity and Holocene sea level data. Geophysical Journal International 178:23–46, DOI 10.1111/j.1365-246X.2009.04185.x

Thomas M, Sündermann J (1999) Tides and tidal torques of the world ocean since the Last Glacial Maximum. Journal of Geophysical Research 104(C2):3159, DOI 10.1029/1998JC900097

Uehara K, Saito Y, Hori K (2002) Paleotidal regime in the Changjiang (Yangtze) Estuary, the East China Sea, and the Yellow Sea at 6 ka and 10 ka estimated from a numerical model. Marine Geology 183(1-4):179–192, DOI 10.1016/S0025-3227(01)00255-9

Uehara K, Scourse JD, Horsburgh KJ, Lambeck K, Purcell AP (2006) Tidal evolution of the northwest European shelf seas from the Last Glacial Maximum to the present. Journal of Geophysical Research 111(C9):C09,025, DOI 10.1029/2006JC003531

Umlauf L, Burchard H (2003) A generic length-scale equation for geophysical turbulence models. Journal of Marine Research 61(2):235–265, DOI 10.1357/002224003322005087

Uncles RJ (1983) Modeling Tidal Stress, Circulation, and Mixing in the Bristol Channel as a Prerequisite for Ecosystem Studies. Canadian Journal of Fisheries and Aquatic Sciences 40(S1):s8–s19, DOI 10.1139/f83-265

Uncles RJ, Stephens JA (2007) SEA 8 Technical Report - Hydrography. Tech. rep., Plymouth Marine Laboratory, Prospect Place, Plymouth, Devon PL1 3DH, UK

US Geological Survey (2013) Nomenclature. URL http://pubs.usgs.gov/of/2006/1195/htmldocs/nomenclature.htm

Van Landeghem KJ, Uehara K, Wheeler AJ, Mitchell NC, Scourse JD (2009) Post-glacial sediment dynamics in the Irish Sea and sediment wave morphology: Data-model comparisons. Continental Shelf Research 29(14):1723–1736, DOI 10.1016/j.csr.2009.05.014

Vermeer M, Rahmstorf S (2009) Global sea level linked to global temperature. Proceedings of the National Academy of Sciences of the United States of America 106(51):21,527–32, DOI 10.1073/pnas.0907765106

Ward SL, Green JAM, Pelling HE (2012) Tides, sea-level rise and tidal power extraction on the European shelf. Ocean Dynamics pp 1153–1167, DOI 10.1007/s10236-012-0552-6

Warner JC, Sherwood CR, Arango HG, Signell RP (2005) Performance of four turbulence closure models implemented using a generic length scale method. Ocean Modelling 8(1-2):81–113, DOI 10.1016/j.ocemod.2003.12.003

Warner JC, Butman B, Dalyander PS (2008a) Storm-driven sediment transport in Massachusetts Bay. Continental Shelf Research 28(2):257–282, DOI 10.1016/j.csr.2007.08.008

Warner JC, Sherwood CR, Signell RP, Harris CK, Arango HG (2008b) Development of a three-dimensional, regional, coupled wave, current, and sediment-transport model. Computers & Geosciences 34(10):1284–1306, DOI 10.1016/j.cageo.2008.02.012

Warner JC, Armstrong B, He R, Zambon JB (2010) Development of a Coupled Ocean-Atmosphere-Wave-Sediment Transport (COAWST) Modeling System. Ocean Modelling 35(3):230–244, DOI 10.1016/j.ocemod.2010.07.010

Wessel Pl, Smith WHF (1996) A global, self-consistent, hierarchical, high-resolution shoreline database. Journal of Geophysical Research 101(B4):8741, DOI 10.1029/96JB00104

Wilson JG, Mackie ASY, O'Connor BDS, Rees EIS, Darbyshire T (2001) Benthic Biodiversity in the southern Irish Sea 2. The South-West Irish Sea Survey (SWISS). Studies in Marine Biodiversity and Systematics from the National Museum of Wales. BIOMÔR Reports 2(1). Tech. rep.

Wu Y, Chaffey J, Greenberg Da, Colbo K, Smith PC (2011) Tidally-induced sediment transport patterns in the upper Bay of Fundy: A numerical study. Continental Shelf Research 31(19-20):2041–2053, DOI 10.1016/j.csr.2011.10.009

Appendix 1: ROMS CPP options

```
/* Momentum equations. */
#define UV_ADV
#define UV_COR
#define UV_VIS2
#define UV_QDRAG

    /* Tracer equations. */
#define TS_U3HADVECTION
#define TS_A4VADVECTION
#define TS_DIF2
#define SALINITY

    /* Pressure gradient algorithm. */
#define DJ_GRADPS

    /* Model configuration. */
#define SOLVE3D
#define MASKING
#define SPHERICAL
#define STATIONS

    /* Analytical fields. */
#define ANA_SMFLUX
#define ANA_BSFLUX
#define ANA_BTFLUX
#define ANA_SSFLUX
#define ANA_STFLUX
#define ANA_FSOBC
#define ANA_INITIAL
#define ANA_M2OBC

    /* Mixing schemes. */
#define MIX_S_UV
#define GLS_MIXING
#define MIX_S_TS

    /* Tidal forcing. */
#define SSH_TIDES
#define UV_TIDES
#define RAMP_TIDES
```

Appendix 2: ROMS physical input parameters

```
!!  ROMS/TOMS Standard Input parameters.
!
!svn $Id: ocean_rainy_high.in 102 2009-01-08 16:06:18Z iant $
!========================================================= Hernan G. Arango ===
!  Copyright (c) 2002-2008 The ROMS/TOMS Group                               !
!    Licensed under a MIT/X style license                                    !
!    See License_ROMS.txt                                                    !

! Application title.

        TITLE = NWESS pal 16kyr 1/24 test case

! C-preprocessing Flag.

    MyAppCPP = NWESS1

! Input variable information file name.  This file needs to be processed
! first so all information arrays can be initialized properly.

!     VARNAME = /homedir/ospa1a/trunk/ROMS/External/varinfo.dat
      VARNAME = //home/sophie.ward/roms/nwess1/varinfo.dat
     Ngrids = 1

! Grid dimension parameters. See notes below in the Glossary for how to set
! these parameters correctly.

          Lm == 623           ! 623 Number of I-direction INTERIOR RHO-points
          Mm == 859           ! 859 Number of J-direction INTERIOR RHO-points
           N == 10            ! Number of vertical levels

        Nbed = 0              ! Number of sediment bed layers

         NAT = 2              ! Number of active tracers (usually, 2)
         NPT = 0              ! Number of inactive passive tracers
         NCS = 0              ! Number of cohesive (mud) sediment tracers
         NNS = 0              ! Number of non-cohesive (sand) sediment tracers

! Domain decomposition parameters for serial, distributed-memory or
! shared-memory configurations used to determine tile horizontal range
! indices (Istr,Iend) and (Jstr,Jend), [1:Ngrids].

       NtileI ==  12                          ! I-direction partition
       NtileJ ==   4                          ! J-direction partition

! Set lateral boundary conditions keyword. Notice that a value is expected
! for each boundary segment per nested grid for each state variable.
!
!   Keyword    Lateral Boundary Condition Type
!
!                   W      S      E      N
!                   e      o      a      o
!                   s      u      s      r
!                   t      t      t      t
!                   h             h
!
!                   1      2      3      4

   LBC(isFsur) ==  Cha    Cha    Cha    Cha       ! free-surface
   LBC(isUbar) ==  Fla    Fla    Fla    Fla       ! 2D U-momentum
   LBC(isVbar) ==  Fla    Fla    Fla    Fla       ! 2D V-momentum
   LBC(isUvel) ==  Gra    Gra    Gra    Gra       ! 3D U-momentum
   LBC(isVvel) ==  Gra    Gra    Gra    Gra       ! 3D V-momentum
   LBC(isMtke) ==  Gra    Gra    Gra    Gra       ! mixing TKE

   LBC(isTvar) ==  Gra    Gra    Gra    Gra \     ! temperature
                   Gra    Gra    Gra    Gra       ! salinity


! Time-Stepping parameters.

       NTIMES == 5000     ! 43200
           DT == 60.0d0    ! time step (s) 2160 steps per day, 90 steps per hour.
      NDTFAST == 10        ! 2D timestep 40/10 is 4.0 seconds.

! Model iteration loops parameters.

         ERstr =  1
         ERend =  1
        Nouter =  1
        Ninner =  1
    Nintervals =  1

! Number of eigenvalues (NEV) and eigenvectors (NCV) to compute for the
! Lanczos/Arnoldi problem in the Generalized Stability Theory (GST)
! analysis. NCV must be greater than NEV (see documentation below).

          NEV =  2                               ! Number of eigenvalues
          NCV =  10                              ! Number of eigenvectors

! Input/Output parameters.
```

```
        NRREC == 0
   LcycleRST == F
        NRST == 64800  ! 30 days.
        NSTA == 60      ! 10 minutes.
        NFLT == 90
       NINFO == 90      ! 1 hour.

! Output history, average, diagnostic files parameters.

      LDEFOUT == T
        NHIS == 60      ! 1 hour.
     NDEFHIS == 0
      NTSAVG == 60
        NAVG == 60
     NDEFAVG == 0
      NTSDIA == 1
        NDIA == 10
     NDEFDIA == 0


! Output tangent linear and adjoint models parameters.

   LcycleTLM == F
        NTLM == 72
     NDEFTLM == 0
   LcycleADJ == F
        NADJ == 72
     NDEFADJ == 0
        NSFF == 72

! Output check pointing GST restart parameters.

     LrstGST =  F                         ! GST restart switch
  MaxIterGST = 500                        ! maximun number of iterations
        NGST = 10                         ! check pointing interval

! Relative accuracy of the Ritz values computed in the GST analysis.

    Ritz_tol = 1.0d-15

! Harmonic/biharmonic horizontal diffusion of tracer: [1:NAT+NPT,Ngrids].

        TNU2 == 2*10.0d0                  ! m2/s
        TNU4 == 2*0.0d0                   ! m4/s

! Harmononic/biharmonic, horizontal viscosity coefficient: [Ngrids].

       VISC3 == 5.0d0                     ! m2/s
       VISC4 == 8.0d+12                    ! m4/s

! Vertical mixing coefficients for active tracers: [1:NAT+NPT,Ngrids]

     AKT_BAK == 1.0d-6                     ! m2/s

! Vertical mixing coefficient for momentum: [Ngrids].

     AKV_BAK == 1.0d-5                     ! m2/s

! Turbulent closure parameters.

     AKK_BAK == 5.0d-6                     ! m2/s
     AKP_BAK == 5.0d-6                     ! m2/s
      TKENU2 == 0.0d0                      ! m2/s
      TKENU4 == 0.0d0                      ! m4/s

! Generic length-scale turbulence closure parameters.

       GLS_P == 3.0d0                      ! K-epsilon
       GLS_M == 1.5d0
       GLS_N == -1.0d0
     GLS_Kmin == 7.6d-6
     GLS_Pmin == 1.0d-12

     GLS_CMU0 == 0.5477d0
       GLS_C1 == 1.44d0
       GLS_C2 == 1.92d0
      GLS_C3M == -0.4d0
      GLS_C3P == 1.0d0
     GLS_SIGK == 1.0d0
     GLS_SIGP == 1.30d0

! Constants used in surface turbulent kinetic energy flux computation.

  CHARNOK_ALPHA == 1400.0d0        ! Charnok surface roughness
 ZOS_HSIG_ALPHA == 0.5d0           ! roughness from wave amplitude
       SZ_ALPHA == 0.25d0          ! roughness from wave dissipation
      CRGBAN_CW == 100.0d0         ! Craig and Banner wave breaking

! Constants used in momentum stress computation.
```

```
       RDRG == 2.5d-04                       ! m/s
      RDRG2 == 3.0d-03                        ! nondimensional
        Zob == 0.02d0                         ! m
        Zos == 0.02d0                         ! m

! Height (m) of atmospheric measurements for Bulk fluxes parameterization.

      BLK_ZQ == 10.0d0                        ! air humidity
      BLK_ZT == 10.0d0                        ! air temperature
      BLK_ZW == 10.0d0                        ! winds

! Minimum depth for wetting and drying.

       DCRIT == 0.10d0                        ! m

! Various parameters.

       WTYPE == 1
     LEVSFRC == 15
     LEVBFRC == 1

! Vertical S-coordinates parameters, [1:Ngrids].
       Vtransform == 1.0
      THETA_S == 6.0d0                        ! set0 0 < THETA_S < 20
      THETA_B == 0.5d0                        ! set 1 0 < THETA_B < 1
       TCLINE == 10.0d0                       ! m

! Mean Density and Brunt-Vaisala frequency.

        RHO0 =  1025.0d0                      ! kg/m3
     BVF_BAK =  1.0d-5                         ! 1/s2

! Time-stamp assigned for model initialization, reference time
! origin for tidal forcing, and model reference time for output
! NetCDF units attribute.

! TIDE_START = 1/7/2009 (tide phase origin) - 1/7/2009 (TIME_REF) = 0 days.

      DSTART =  0.0d0                          ! days
  TIDE_START =  0.0d0                          ! days
    TIME_REF =  20000101.0d0                   ! yyyymmdd.dd


! Nudging/relaxation time scales, inverse scales will be computed
! internally, [1:Ngrids].

       TNUDG == 2*0.0d0                        ! days
       ZNUDG == 0.0d0                          ! days
      M2NUDG == 0.0d0                          ! days
      M3NUDG == 0.0d0                          ! days

! Factor between passive (outflow) and active (inflow) open boundary
! conditions, [1:Ngrids]. If OBCFAC > 1, nudging on inflow is stronger
! than on outflow (recommended).

      OBCFAC == 0.0d0                          ! nondimensional

! Linear equation of State parameters:

          R0 == 1027.0d0                       ! kg/m3
          T0 == 12.5d0                         ! Celsius
          S0 == 32.0d0                         ! PSU
       TCOEF == 1.7d-4                         ! 1/Celsius
       SCOEF == 0.0d0                          ! 1/PSU

! Slipperiness parameter: 1.0 (free slip) or -1.0 (no slip)

      GAMMA2 == -1.0d0

! Starting (DstrS) and ending (DendS) day for adjoint sensitivity forcing.
! DstrS must be less or equal to DendS. If both values are zero, their
! values are reset internally to the full range of the adjoint integration.

       DstrS == 0.0d0                          ! starting day
       DendS == 0.0d0                          ! ending day

! Starting and ending vertical levels of the 3D adjoint state variables
! whose sensitivity is required.

       KstrS == 1                              ! starting level
       KendS == 1                              ! ending level

! Logical switches (TRUE/FALSE) to specify the adjoint state variables
! whose sensitivity is required.

Lstate(isFsur) == F                            ! free-surface
Lstate(isUbar) == F                            ! 2D U-momentum
Lstate(isVbar) == F                            ! 2D V-momentum
Lstate(isUvel) == F                            ! 3D U-momentum
```

```
Lstate(isVvel) == F                              ! 3D V-momentum

! Logical switches (TRUE/FALSE) to specify the adjoint state tracer
! variables whose sensitivity is required (NT values are expected).

Lstate(isTvar) == F F                            ! tracers

! Stochastic optimals time decorrelation scale (days) assumed for
! red noise processes.

    SO_decay == 2.0d0                            ! days

! Logical switches (TRUE/FALSE) to specify the state surface forcing
! variable whose stochastic optimals is required.

SOstate(isUstr) == F                             ! surface u-stress
SOstate(isVstr) == F                             ! surface v-stress

! Logical switches (TRUE/FALSE) to specify the surface tracer forcing
! variable whose stochastic optimals is required (NT values are expected).

SOstate(isTsur) == F F                           ! surface tracer flux

! Stochastic optimals surface forcing standard deviation for
! dimensionalization.

SO_sdev(isUstr) == 1.0d0                          ! surface u-stress
SO_sdev(isVstr) == 1.0d0                          ! surface v-stress
SO_sdev(isTsur) == 1.0d0 1.0d0                    ! NT surface tracer flux

! Logical switches (TRUE/FALSE) to activate writing of fields into
! HISTORY output file.

Hout(idUvel) == T                                ! 3D U-velocity
Hout(idVvel) == T                                ! 3D V-velocity
Hout(idWvel) == F                                ! 3D W-velocity
Hout(idOvel) == F                                ! omega vertical velocity
Hout(idUbar) == T                                ! 2D U-velocity
Hout(idVbar) == T                                ! 2D V-velocity
Hout(idFsur) == T                                ! free-surface
Hout(idBath) == F                                ! time-dependent bathymetry

Hout(idTvar) == F F                              ! temperature and salinity

Hout(idUsms) == F                                ! surface U-stress
Hout(idVsms) == F                                ! surface V-stress
Hout(idUbms) == T                                ! bottom U-stress
Hout(idVbms) == T                                ! bottom V-stress

Hout(idUbrs) == T                                ! bottom U-current stress
Hout(idVbrs) == T                                ! bottom V-current stress
Hout(idUbws) == F                                ! bottom U-wave stress
Hout(idVbws) == F                                ! bottom V-wave stress
Hout(idUbcs) == F                                ! bottom max wave-current U-stress
Hout(idVbcs) == F                                ! bottom max wave-current V-stress

Hout(idUbot) == F                                ! bed wave orbital U-velocity
Hout(idVbot) == F                                ! bed wave orbital V-velocity
Hout(idUbur) == T                                ! bottom U-velocity above bed
Hout(idVbvr) == T                                ! bottom V-velocity above bed

Hout(idW2xx) == F                                ! 2D radiation stress, Sxx component
Hout(idW2xy) == F                                ! 2D radiation stress, Sxy component
Hout(idW2yy) == F                                ! 2D radiation stress, Syy component
Hout(idU2rs) == F                                ! 2D radiation U-stress
Hout(idV2rs) == F                                ! 2D radiation V-stress
Hout(idU2Sd) == F                                ! 2D U-Stokes velocity
Hout(idV2Sd) == F                                ! 2D V-Stokes velocity

Hout(idW3xx) == F                                ! 3D radiation stress, Sxx component
Hout(idW3xy) == F                                ! 3D radiation stress, Sxy component
Hout(idW3yy) == F                                ! 3D radiation stress, Syy component
Hout(idW3zx) == F                                ! 3D radiation stress, Szx component
Hout(idW3zy) == F                                ! 3D radiation stress, Szy component
Hout(idU3rs) == F                                ! 3D U-radiation stress
Hout(idV3rs) == F                                ! 3D V-radiation stress
Hout(idU3Sd) == F                                ! 3D U-Stokes velocity
Hout(idV3Sd) == F                                ! 3D V-Stokes velocity

Hout(idWamp) == F                                ! wave height
Hout(idWlen) == F                                ! wave length
Hout(idWdir) == F                                ! wave direction

Hout(idTsur) == F F                              ! surface net heat and salt flux
Hout(idLhea) == F                                ! latent heat flux
Hout(idShea) == F                                ! sensible heat flux
Hout(idLrad) == F                                ! longwave radiation flux
Hout(idSrad) == F                                ! shortwave radiation flux
Hout(idevap) == F                                ! evaporation rate
Hout(idrain) == F                                ! precipitation rate
```

```
Hout(idDano) == F                               ! density anomaly
Hout(idVvis) == F                               ! vertical viscosity
Hout(idTdif) == F                               ! vertical T-diffusion
Hout(idSdif) == F                               ! vertical Salinity diffusion
Hout(idHsbl) == F                               ! depth of surface boundary layer
Hout(idHbbl) == F                               ! depth of bottom boundary layer
Hout(idMtke) == F                               ! turbulent kinetic energy
Hout(idMtls) == F                               ! turbulent length scale

 Hout(inert) == F                               ! inert passive tracers

! Logical switches (TRUE/FALSE) to activate writing of exposed sediment
! layer properties into HISTORY output file.  Currently, MBOTP properties
! are expected for the bottom boundary layer and/or sediment models:
!
!   Hout(idBott(isd50)),  isd50 = 1     ! mean grain diameter
!   Hout(idBott(idens)),  idens = 2     ! mean grain density
!   Hout(idBott(iwsed)),  iwsed = 3     ! mean settling velocity
!   Hout(idBott(itauc)),  itauc = 4     ! critical erosion stress
!   Hout(idBott(irlen)),  irlen = 5     ! ripple length
!   Hout(idBott(irhgt)),  irhgt = 6     ! ripple height
!   Hout(idBott(ibwav)),  ibwav = 7     ! wave excursion amplitude
!   Hout(idBott(izdef)),  izdef = 8     ! default bottom roughness
!   Hout(idBott(izapp)),  izapp = 9     ! apparent bottom roughness
!   Hout(idBott(izNik)),  izNik = 10    ! Nikuradse bottom roughness
!   Hout(idBott(izbio)),  izbio = 11    ! biological bottom roughness
!   Hout(idBott(izbfm)),  izbfm = 12    ! bed form bottom roughness
!   Hout(idBott(izbld)),  izbld = 13    ! bed load bottom roughness
!   Hout(idBott(izwbl)),  izwbl = 14    ! wave bottom roughness
!   Hout(idBott(iactv)),  iactv = 15    ! active layer thickness
!   Hout(idBott(ishgt)),  ishgt = 16    ! saltation height
!
!                                  1 1 1 1 1 1 1
!              1 2 3 4 5 6 7 8 9 0 1 2 3 4 5 6

Hout(idBott) == F F F F F F F F F F F F F F F F

! Generic User parameters, [1:NUSER].

        NUSER =  0
         USER =  0.d0

! NetCDF-4/HDF5 compression parameters for output files.

  NC_SHUFFLE = 1                    ! if non-zero, turn on shuffle filter
  NC_DEFLATE = 1                    ! if non-zero, turn on deflate filter
   NC_DLEVEL = 1                    ! deflate level [0-9]

! Input NetCDF file names, [1:Ngrids].

     GRDNAME == grid_nwess.nc
     ININAME == ini_nwess.nc
     ITLNAME == ocean_itl.nc
     IRPNAME == ocean_irp.nc
     IADNAME == ocean_iad.nc
     CLMNAME == ocean_clm.nc
     BRYNAME == bry_nwess.nc
     FWDNAME == ocean_fwd.nc
     ADSNAME == ocean_ads.nc

     NFFILES == 1                             ! number of forcing files

     FRCNAME == tides_nwess.nc

! Output NetCDF file names, [1:Ngrids].

     GSTNAME == output/ocean_gst.nc
     RSTNAME == output/ocean_rst.nc
     HISNAME == ocean_his.nc
     TLMNAME == output/ocean_tlm.nc
     TLFNAME == output/ocean_tlf.nc
     ADJNAME == output/ocean_adj.nc
     AVGNAME == output/ocean_avg.nc
     DIANAME == output/ocean_dia.nc
     STANAME == ocean_sta.nc
     FLTNAME == output/ocean_flt.nc

! Input ASCII parameter filenames.

     APARNAM =  ROMS/External/s4dvar.in
     SPOSNAM =  stations.in
     FPOSNAM =  ROMS/External/floats.in
     BPARNAM =  ROMS/External/bioFasham.in
     SPARNAM =  sediment.in
     USRNAME =  ROMS/External/MyFile.dat
```

182

Appendix 3: Laser particle sizing results tables